UNIVERSITY OF ALBERTA

HYDRAULIC RESPONSE OF A FRACTURE ZONE TO EXCAVATION-INDUCED SHEAR

by
DWAYNE D. TANNANT

©

A THESIS
SUBMITTED TO THE FACULTY OF GRADUATE STUDIES AND RESEARCH
IN PARTIAL FULFILMENT OF THE REQUIREMENTS FOR THE DEGREE OF
DOCTOR OF PHILOSOPHY

DEPARTMENT OF CIVIL ENGINEERING

EDMONTON, ALBERTA
FALL 1990

National Library
of Canada

Canadian Theses Service

Ottawa, Canada
K1A 0N4

Bibliothèque nationale
du Canada

Service des thèses canadiennes

The author has granted an irrevocable non-exclusive licence allowing the National Library of Canada to reproduce, loan, distribute or sell copies of his/her thesis by any means and in any form or format, making this thesis available to interested persons.

The author retains ownership of the copyright in his/her thesis. Neither the thesis nor substantial extracts from it may be printed or otherwise reproduced without his/her permission.

L'auteur a accordé une licence irrévocable et non exclusive permettant à la Bibliothèque nationale du Canada de reproduire, prêter, distribuer ou vendre des copies de sa thèse de quelque manière et sous quelque forme que ce soit pour mettre des exemplaires de cette thèse à la disposition des personnes intéressées.

L'auteur conserve la propriété du droit d'auteur qui protège sa thèse. Ni la thèse ni des extraits substantiels de celle-ci ne doivent être imprimés ou autrement reproduits sans son autorisation.

ISBN 0-315-65019-2

UNIVERSITY OF ALBERTA
RELEASE FORM

NAME OF AUTHOR: DWAYNE D. TANNANT
TITLE OF THESIS: HYDRAULIC RESPONSE OF A FRACTURE ZONE TO EXCAVATION-INDUCED SHEAR

DEGREE: DOCTOR OF PHILOSOPHY
YEAR GRANTED: FALL 1990

Permission is hereby granted to THE UNIVERSITY OF ALBERTA to reproduce single copies of this thesis and to lend or sell such copies for private, scholarly or scientific research purposes only.

The author reserves other publication rights, and neither the thesis nor extensive extracts from it may be printed or otherwise reproduced without the author's written permission.

(Signed) Dwayne Tannant
(Permanent Address) Geomechanics Research Cntr
Laurentian University
Sudbury, Ont. P3E 2C6

Dated Aug. 27 1990

THE UNIVERSITY OF ALBERTA

FACULTY OF GRADUATE STUDIES AND RESEARCH

The undersigned certify that they have read, and recommend to the Faculty of Graduate Studies and Research for acceptance, a thesis entitled HYDRAULIC RESPONSE OF A FRACTURE ZONE TO EXCAVATION-INDUCED SHEAR submitted by DWAYNE D. TANNANT in partial fulfilment of the requirements for the degree of DOCTOR OF PHILOSOPHY.

Dr. P.K. Kaiser ....
Supervisor

Dr. D. Chan ....
Co-Supervisor

Dr. D. Cruden ....
(chairman)

Dr. D. Elsworth ......Derek Elsworth......
(external examiner)

Dr. T. Hrudey ......T. Hrudey......

Dr. D. Schmitt ....

Date ......27/05/90......

ABSTRACT

The hydro-mechanical response of a fracture zone to tunnel excavation was investigated. Field data from the Room 209 tunnel at the Underground Research Laboratory of Atomic Energy of Canada Limited showed an unexpected transmissivity reduction as a tunnel face intersected a fracture zone. The observed hydraulic response could not be interpreted with conventional normal stress - fracture closure models. However, the similarity between shear stress development near a tunnel face and the measured hydraulic behaviour in the Room 209 fracture zone lead to the hypothesis that shear stresses or displacements were responsible for the excavation-induced transmissivity reductions.

The primary object of this thesis is to assess and validate of the mechanism or concept of shear-induced transmissivity reduction in fracture zones by comparison of field data from Room 209 with finite element predictions. A phenomenological relationship between shear displacement and transmissivity change was introduced based on the geometric structure of flow paths in en echelon fracture zones. Extensive numerical modelling was undertaken to simulate the hydro-mechanical response in the Room 209 fracture zone. Shear displacements were generated at different excavation stages as the tunnel face passed through the fracture zone. The shear displacements were determined with a three-dimensional finite element model using linear-elastic joint elements. The shear displacements were generally less than 1 mm with the largest displacements present during fracture zone intersection. The shear displacements and the shear displacement - transmissivity relationship were then used to generate transmissivity distributions in the fracture zone. The transmissivity distributions were transferred to a two-dimensional finite element seepage model to predict the hydraulic response.

Seepage analyses were made for various tunnel-face positions and provided predictions of steady-state heads, inflows, and ratios of flow to head drop at packer locations. The predicted response varied depending on the shear displacement distribution. The excavation-dependent variation in hydraulic response closely matched field measurements, showing a significant transmissivity reduction as the fracture zone was intersected.

The correspondence between measured and predicted hydraulic response supports the hypothesis of fracture zone transmissivity reduction due to excavation-induced shear displacements and provides a new mechanism for the interpretation of hydraulic responses in fracture zones.

ACKNOWLEDGEMENTS

I wish to express my sincerest thanks to Dr. Peter Kaiser. He has and continues to provide the inspiration conducive to excellence in rock engineering. Peter and the staff of the Geomechanics Research Centre maintained a simulating and productive research environment for the final year's work on my thesis. Dr. Dave Chan has been of greatest assistance during the early struggles with software and supercomputer problems and his co-supervision was appreciated. The Geotechnical Group at the University of Alberta are commended for their excellence and dedication to geotechnique.

Tai Wong could answer most of my Mac questions as well as a host of others. I shall teach others what he has taught me. My thanks extend to my many friends and colleagues from the Dept. of Civil Engineering at U of A, especially Elisabeth Hivon and John Mckay. I extend a sincere thanks to Sean Maloney and David Wood for their constructive comments on the text of the thesis.

Derek Martin and others at AECL were most cooperative in providing information necessary for this thesis. The Supercomputer staff at the University of Calgary were helpful in resolving computing difficulties with the Cyber computers.

Financial support has been provided by the Natural Sciences and Engineering Research Council of Canada, Atomic Energy of Canada Limited, Geomechanics Research Centre, and Petro-Canada.

TABLE OF CONTENTS

1 INTRODUCTION 1

1.1 Description of Problem 3

1.2 Scope of Thesis 5

2 REVIEW OF FRACTURE ZONES AND FRACTURE PROPERTIES FOR FINITE ELEMENT MODELLING 7

2.1 Introduction 7

2.2 The Morphology of Fracture Zones in Igneous Intrusive Rock Masses 8
  2.2.1 Primary Fractures 8
  2.2.2 Secondary Fractures 13

2.3 Fracture Zone Morphology and Numerical Modelling 16

2.4 Modelling Geomechanical Fracture Behaviour 16
  2.4.1 Normal Deformation and Normal Fracture Stiffness 17
  2.4.2 Shear Deformation 22
    2.4.2.1 Shear Strength 23
    2.4.2.2 Shear Stiffness 25
  2.4.3 Determination of Normal and Shear Stiffnesses for Joint Elements 26

2.5 Finite Element Models for Fractured Rock 27
  2.5.1 Equivalent Rock Mass Models 27
  2.5.2 Discrete Joint Element Models 29

2.6 Modelling Hydraulic Behaviour of Single Fractures 31
  2.6.1 Hydraulic Models Based on the Parallel Plate Model 33
  2.6.2 Validity of the Cubic Flow Law 34
    2.6.2.1 Laminar Flow Assumption 35
    2.6.2.2 Aperture Determination 35
    2.6.2.3 Normal Stress and Tortuosity 36
    2.6.2.4 Limitations of the Cubic Flow Law 37

2.7 Using Transmissivities in Finite Element Seepage Programs 38

3 SHEAR DISPLACEMENT - TRANSMISSIVITY RELATIONSHIP 40

3.1 Background 40

3.2 Fracture Zone Flow Model 44

3.3 Parallel Plate Flow Model and Fracture Zone Transmissivity 47

3.4 Transmissivity - Shear Displacement Relationship 49

3.5 Parametric Study of the Transmissivity - Shear Displacement Relationship. 51
  3.5.1 Primary Fracture Orientation 51
  3.5.2 Shear Direction 53
  3.5.3 Initial Ratio of Primary to Secondary Fracture Aperture 54
  3.5.4 Angle Between Primary and Secondary Fractures 55
  3.5.5 Initial Aperture Ratios in Natural Fracture Zones 56

3.6 Conclusions 57

4 FLOW FROM A FRACTURE ZONE INTO A CIRCULAR OPENING 59

4.1 Shear Displacement and Transmissivity Determination 59

4.2 Quarter Mesh Results 60
  4.2.1 Constant Transmissivity Solution 62
  4.2.2 Effect of Internal Fracture Zone Structure 63
  4.2.3 Effect of Non-Axisymmetric Shear Displacement Distributions 68

4.3 Circular Mesh Results 70
  4.3.1 Interpretation of Q/ΔH Measured from Packer Tests 72
  4.3.2 Seepage Simulations with a Constant Transmissivity Distribution 74
    4.3.2.1 Response to Borehole Drilling and Excavation 74
    4.3.2.2 Effect of Blast-holes and Excavation Opening on Simulated Fluid Withdrawal Tests 76
  4.3.3 Rings of Low Transmissivity Around the Excavation 78

4.4 Summary 80

5 HYDRO-MECHANICAL RESPONSE OF THE ROOM 209 FRACTURE ZONE 82
5.1 Introduction 82
5.2 Room 209 Excavation Response Experiment 83
5.2.1 Hydro-Geologic Setting 83
5.2.2 Instrumentation 86
5.2.3 Measured Response to Tunnel Excavation 87
5.3 Previous Numerical Simulations of Room 209 (Elimination of Normal Stress - Fracture Closure Model) 89
5.4 Geomechanical Finite Element Model of Room 209 94
5.4.1 Finite Element Mesh and Coordinate System 94
5.4.2 In Situ State of Stress 98
5.4.3 Material Properties 99
5.4.4 Excavation Sequence 102
5.5 3-D Finite Element Results 102
5.5.1 Tunnel Wall Displacements 103
5.5.1.1 Closures and Convergence 106
5.5.2 Shear Displacements in the Fracture Zone 107
5.6 Room 209 Seepage Modelling 111
5.6.1 Finite Element Mesh and Boundary Conditions 111
5.6.2 Transmissivity Models 114
5.6.2.1 Constant Transmissivity Distribution 115
5.6.2.2 Pre-Excavation Transmissivity Match 115
5.6.2.3 Pilot Excavation with Pre-Excavation Transmissivities 117
5.6.2.4 Matching Post-Pilot Transmissivities 117
5.6.2.5 Slash Excavation with Pilot Transmissivities 117
5.6.2.6 Matching Post-Slash Transmissivities 117
5.6.3 Hydraulic Response in the Fracture Zone 118
5.6.3.1 Steady-State Heads at Packers 121
5.6.3.2 Packer Test Q/ΔH Values 122
5.6.3.3 Flows into the Blast-Holes, Pilot, and Slash 122
5.6.3.4 Summary 123

5.6.4 Transmissivity Distributions Based on Shear Displacements....... 123
5.6.4.1 Transmissivity Distributions and Seepage Modelling........ 127
5.6.4.2 Flows into the Tunnel........ 130
5.6.4.3 Steady-State Heads........ 130
5.6.4.4 Fluid Withdrawal Tests........ 133

6 CONCLUSIONS AND RECOMMENDATIONS........ 141

6.1 Shear - Transmissivity Relationship........ 142

6.2 Shear Displacement Distributions........ 143

6.3 Interpretation of Field Hydraulic Monitoring Data........ 143

6.4 Recommendations........ 144
6.4.1 Field Work........ 144
6.4.2 Numerical Models........ 145

7 REFERENCES........ 146

Appendix A - Killarney Fracture Zones........ 164

Appendix B - Application of Barton-Bandis Equations to Data from Room 209........ 171

B.1 Determination of Normal and Shear Stiffnesses........ 172
B.1.1 Normal Stiffness........ 173
B.1.2 Shear Stiffness........ 174

B.2 Implications........ 174

Appendix C - Parallel Plate Analogy for Flow in a Single Fracture........ 176

Appendix D - Displacements Around a Circular Opening........ 179

Appendix E - Steady-State Radial Flow into a Circular Opening........ 182

Appendix F - Effect of Additional Boreholes on Q/ΔH Determined at a Borehole........ 183

Appendix G - Measured Hydraulic Response at Room 209........ 186

LIST OF TABLES

Table 5.1 Orientation of Room 209 and fracture zone 96
Table 5.2 Resource usage on the Cyber computers 97
Table 5.3 In situ stresses 98
Table 5.4 In situ fracture zone stresses 98
Table 5.5 Excavation sequence 102
Table 5.6 Wall closures and convergence 106
Table A.1 Summary of fracture zone characterization 169
Table B.1 Barton-Bandis empirical equations 171
Table B.2 Additional empirical relationships (after Barton and Bakhtar, 1983) 172
Table B.3 Rock and fracture parameters 172
Table G.1 Borehole interference test results (after Lang et al., 1986) 186
Table G.2 Steady-state pressure heads at packed-off locations during pilot excavation (after Lang et al., 1987b) 187
Table G.3 Steady-state pressure heads at packed-off locations during slash excavation (after Lang et al., 1987b) 187
Table G.4 Fluid withdrawal test data during pilot excavation (after Lang et al., 1987b) 188
Table G.5 Fluid withdrawal test data during slash excavation (after Lang et al., 1987b) 188
Table G.6 Estimated flow rates (after Lang et al., 1987b) 189

LIST OF FIGURES

Figure 1.1 Similarity in excavation-dependent changes in measurements of Q/ΔH and development of shear stresses near an excavation face 4
Figure 2.1 Displacement modes at fracture propagation front 9
Figure 2.2 Fracture zone characterization and terminology 10
Figure 2.3 Fracture zone structures based on primary fracture trace orientation 11
Figure 2.4 Secondary fracturing near en echelon fractures 15
Figure 2.5 Pre-peak stress - displacement relationships for fractures 18
Figure 3.1 Examples of excavation-dependent fracture conductivity decreases 42
Figure 3.2 Evolution of fracture zone flow model 45
Figure 3.3 Fracture zone flow model 46
Figure 3.4 Effect of primary fracture orientation on transmissivities during shear 52
Figure 3.5 Effect of shear direction on transmissivity 54
Figure 3.6 Effect of aperture ratio and shear direction on transmissivity 55
Figure 3.7 Effect of angle between primary and secondary fractures on transmissivity 56
Figure 4.1 Fracture zone perpendicular to the opening axis................................ 59
Figure 4.2 Quarter-mesh and boundary conditions 61
Figure 4.3 Head profile for constant transmissivity case 63
Figure 4.4 Shear displacement at full fracture closure versus primary fracture orientation 64
Figure 4.5 Shear displacement and transmissivity profiles for varying amounts of shear and hydrostatic stress conditions 66
Figure 4.6 Head profiles for fracture zones with varying shear and different primary fracture orientations under hydrostatic stress conditions 67
Figure 4.7 Effect of fracture zone geometry and shear displacement distribution on flows into a circular opening 68
Figure 4.8 Effect of shear distribution on transmissivity and resulting head profiles.. 69
Figure 4.9 Circular finite element mesh showing opening and nodes representing blast-holes and packer 71
Figure 4.10 Head profiles after excavation of blast-holes and opening and during packer testing plus values of Q/ΔH from the packer tests 75
Figure 4.11 Flows into blast-holes and excavated opening 76
Figure 4.12 Location of a low transmissivity ring around opening 78

Figure 4.13 Head profiles and inflows for opening with different transmissivity rings and results from simulated packer tests 79
Figure 5.1 Location of the Underground Research Laboratory 82
Figure 5.2 Cross-section through Lac du Bonnet Batholith 83
Figure 5.3 Plan and section of Room 209 showing fracture zone and packer locations 85
Figure 5.4 Extent of Room 209 fracture zone 86
Figure 5.5 Hydraulic interconnection from borehole interference testing (after Kozak and Davison, 1986) 88
Figure 5.6 Measured Q/ΔH values at Room 209 packer locations 90
Figure 5.7 Development of shear stresses at the crown and springline as a function of the face position (after Pelli, 1987) 91
Figure 5.8 Normal stress changes in the plane of the Room 209 fracture zone after excavation of the slash (after Chan et al., 1987) 92
Figure 5.9 Comparison between measured heads at packer locations around Room 209 and heads predicted by a normal stress - fracture closure hydraulic model (after Kaiser et al., 1987) 93
Figure 5.10 Three-dimensional finite element mesh and cross-section of the inner part of the mesh 95
Figure 5.11 Longitudinal section through finite element mesh showing joint elements and slice orientations 96
Figure 5.12 Reduced modulus zones and locations for displacement and stress determination 100
Figure 5.13 Radial displacements along the tunnel at the north and south walls and the roof and floor during pilot excavations 104
Figure 5.14 Radial displacements along the tunnel at the north and south walls and the roof and floor during slash excavations 105
Figure 5.15 Maximum shear displacement magnitudes in the fracture zone during pilot excavations 108
Figure 5.16 Maximum shear displacement magnitudes in the fracture zone during slash excavations 110
Figure 5.17 Two-dimensional finite element mesh for seepage analyses 112
Figure 5.18 Inner part of finite element seepage mesh showing nodes representing packer locations and excavation perimeter 113
Figure 5.19 Trial and error matched transmissivity (aperture) distributions 116

Figure 5.20 Comparison between measured and predicted steady-state heads at the packer locations for different transmissivity distributions 119
Figure 5.21 Comparison between measured and predicted Q/ΔH at the packer locations for different transmissivity distributions 120
Figure 5.22 Predicted and measured (estimated) inflows into the Room 209 tunnel from the fracture zone 121
Figure 5.23 Modified inner part of finite element seepage mesh showing pilot and slash and nodes representing packer locations 124
Figure 5.24 Initial or Development Room transmissivity (aperture) distribution 126
Figure 5.25 Transmissivity (aperture) distributions during pilot excavation based on shear displacements 128
Figure 5.26 Transmissivity (aperture) distributions during slash excavation based on shear displacements 129
Figure 5.27 Specific discharges into Room 209 at different excavation steps and total inflows 131
Figure 5.28 Measured and predicted steady-state heads at all packers for all excavation steps 132
Figure 5.29 Measured and predicted heads at packer locations versus excavation step 134
Figure 5.30 North and roof predicted head profiles 135
Figure 5.31 Measured and predicted values of Q/ΔH versus time or excavation sequence 136
Figure 5.32 Measured and predicted Q/ΔH at the north and roof packers (showing predicted Q/ΔH if there were no transmissivity changes due to excavation) 138
Figure A.1 Killarney fracture zone #1 165
Figure A.2 Killarney fracture zone #2 166
Figure A.3 Mean fracture orientations of Killarney fracture zones 1 to 4 167
Figure A.4 Mean fracture orientations of Killarney fracture zones 5 to 8 168
Figure A.5 Killarney fracture zone #1 flow paths 170
Figure B.1 Normal stiffness versus normal stress for fractures in the Room 209 fracture zone 175
Figure C.1 Parallel plate model for fluid flow in a fracture 176
Figure D.1 Radial displacements around a circular opening 181
Figure F.1 Two wells in a circular confined aquifer 183

1 INTRODUCTION

Understanding and predicting the hydro-mechanical response of fracture zones is an important issue in many civil and mining engineering projects. Water-bearing fracture zones are common features in most tunnelling operations. In conventional civil engineering and mining operations the presence of water-bearing fractures may demand remedial measures to limit the quantity of inflow, reduce the hydraulic pressures and ensure tunnel stability. The engineer is mainly concerned with the stability of underground openings and pumping requirements. The precise hydro-mechanical response in the fracture zone may not be a primary concern. However, at nuclear waste repository sites located in igneous intrusive rock, fractures are the dominant structural features and the principal conduits along which potentially contaminated groundwater can migrate. Furthermore, the presence of joints or fractures can dramatically affect the mechanical behaviour of the rock mass. When tunnelling for nuclear waste repository sites, understanding the hydro-mechanical response of water-bearing fracture zones is crucial for assessing the influence of tunnel excavation on the long term isolation of nuclear waste.

Before embarking upon a discussion of shear displacements and hydraulic response of fracture zones it is necessary to set down some basic definitions. Water-bearing 'fracture zones' are near-planar sections of rock mass containing a series of hydraulically inter-connected, individual fractures. The fracture 'aperture' is the space between opposing fracture faces which is present because of contacting asperities. Fracture 'permeability' describes the fluid conductive qualities of the fracture and is a function of the fracture aperture. 'Hydraulic conductivity' or simply 'conductivity' reflects a combination of the conductive properties of the fluid and the fracture. Fracture 'transmissivity' is given by the hydraulic conductivity multiplied by the fracture aperture. Since the hydraulic conductivity is itself a function of aperture, conductivity or aperture changes are associated with changes in transmissivity. Since fracture 'transmissivity' is a description of the ability for a fracture to conduct water, this term is used through the thesis. However, 'permeability' and 'hydraulic conductivity' or 'conductivity' also describe flow properties of a fracture and are sometimes used interchangeably with the term 'transmissivity' when appropriate. More precise mathematical definitions of these terms are given later.

Excavation through a water-bearing fracture zone alters the in situ stresses, induces displacements, and changes hydraulic boundary conditions in the fracture zone. The influence of stresses or displacements on the hydro-mechanical response will depend on the properties of individual fractures including the interaction between fractures within the fracture zone. Shear displacements are commonly induced by the excavation. The engineer needs to know the effect of excavation on the fracture zone transmissivity. Traditionally, decreases in the transmissivity of in situ fractures have been explained by increases in normal stress on the fractures. This explanation is valid for single fractures. However, fracture zones create a complex flow network that is dominated by the geometric arrangement of the fractures within this zone. Shear displacements in fracture zones may be as important as normal stress - fracture closure for reducing transmissivities.

Increases in fracture conductivity can occur as an excavation passes a fracture or fracture zone. The increase in fracture conductivity is commonly caused by blast damage which loosens the rock around the opening. In cases where careful blasting or mechanical excavation are used to create an opening, fracture conductivity decreases have been noted (Montazer et al., 1982; Wilson et al., 1983; Lang et al., 1987a,b; see Section 3.1). Simple analyses of the stress redistributions around circular openings have indicated a potential for both fracture closure or fracture opening depending on the orientation of the fractures relative to the opening (Kelsall et al., 1984; Pusch, 1989). Fractures which are oriented roughly perpendicular to the axis of the opening can experience a permeability decrease towards the opening.

The influence of tunnelling-induced stress changes and displacements on the hydro-mechanical response of water-bearing fractures has been examined by conducting elaborate, full scale experiments in various crystalline rock bodies (Montazer et al., 1982; Wilson et al., 1983; Kelsall et al., 1984; Egger, 1988; Pusch, 1989; and Lang, 1989). However, only a few cases exist where numerical modelling has been used to analyse and predict the hydro-mechanical behaviour of excavation responses in fractured rock (Chan et al., 1987; Barton and Makurat, 1989; Kaiser et al., 1987, 1989). The near-field numerical modelling of repository sites has necessitated development of realistic models capable of simulating fluid flow within the fracture zones.

This thesis examines the mechanism of shear-induced transmissivity reduction and assesses whether this mechanism provides a plausible explanation for measured excavation-dependent transmissivity reductions in an intersected fracture zone. Verification of shear-induced transmissivity reductions in fracture zones provides a new means for the prediction and the interpretation of hydraulic responses.

Numerical simulation was selected as the approach to modelling and assessing the mechanism of shear-induced transmissivity reduction in fracture zones. Numerical models are flexible and relatively inexpensive compared to physical models. In addition, the availability of different finite element codes at the University of Alberta made the use of finite element models attractive. One problem with using numerical models is the determination of the necessary constitutive relationships and material parameters. These problems are addressed throughout the thesis.

It must be noted that flow through fracture zones is an extremely complex phenomena and any numerical model will have limitations. It can not be expected that a numerical model, which will always have inherent simplifications and assumptions, will correctly simulate all features of flow through a fracture zone. However, models which account for some of the more important aspects of flow in fracture zones can provide insight into the complex behaviour of fracture zones subject to shear.

This thesis reveals that shear displacements in fracture ~~zones~~ can, under certain circumstances, dominate the hydraulic response of fracture zones. Therefore, future predictions of influence of excavations on the hydraulic response of fracture zones should give consideration to shear induced as well as normal stress induced changes in fracture zone transmissivity.

1.1 Description of Problem

An excavation response experiment performed at Room 209 of Atomic Energy of Canada Limited's (AECL), Underground Research Laboratory (URL) located near Pinawa, Manitoba (Lang, 1989), provided an opportunity to develop a finite element model to simulate a pilot and slash excavation of a tunnel through a prominent fracture zone and to evaluate the model's performance against field measurements (Kaiser et al., 1987; 1989). This modelling effort showed that the hydraulic response of this fracture zone could not be explained by normal stress-dependent fracture behaviour (see Section 5.3) and provided the impetus to improve the hydraulic modelling component of the excavation response simulation.

The Room 209 excavation response experiment involved carefully controlled blasting through a fracture zone oriented roughly perpendicular to the tunnel. Field measurements demonstrated an excavation-dependent decrease in transmissivity in a narrow zone adjacent to the tunnel wall (Lang et al., 1987b). The decrease in transmissivity was partially recovered as the excavation face proceeded past the fracture zone (Fig. 1.1a). The characteristic trends in ratios of flow to head drop ($Q/\Delta H$) at packer locations which showed a maximum decrease when the excavation face was near the fracture zone, are similar to the shear stress development which peaks near the excavation face (Pelli, 1987). Shear stresses also return toward their pre-excavation values as the excavation face proceeds (Fig. 1.1b). This similarity in excavation-dependent behaviour indicated that shear stresses or displacements might be responsible for the observed hydraulic response in the Room 209 fracture zone.

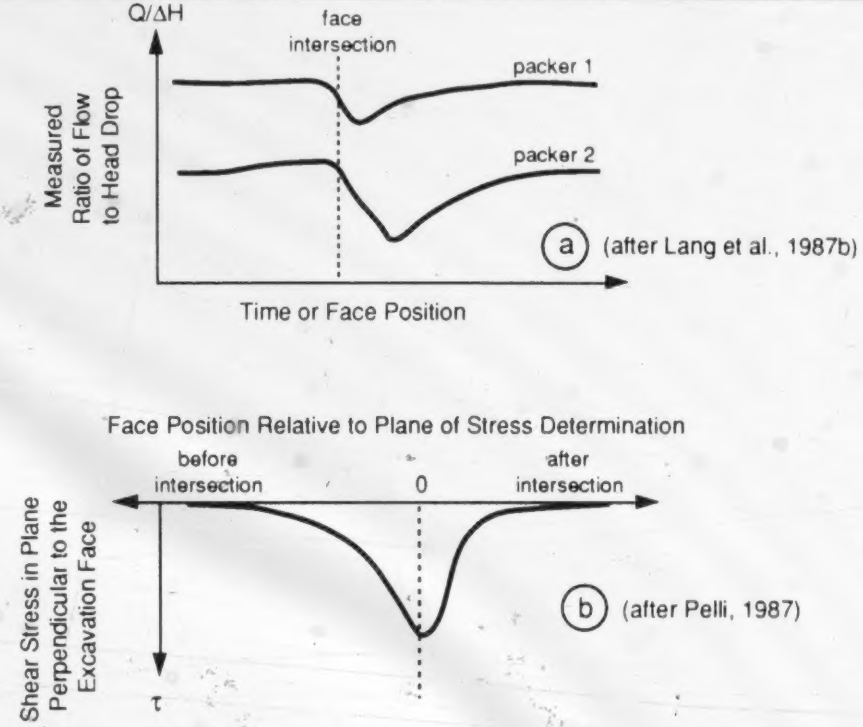

Figure 1.1 Similarity in excavation dependent changes in measurements of Q/ΔH and development of shear stresses near an excavation face

Other possible explanations for the observed hydraulic response at Room 209 include turbulent flow and fracture blockage by rock particles from blasting or sheared asperities. However, these alternatives do not provide a mechanism consistent with the excavation-dependent recoveries of Q/ΔH. Furthermore, while turbulent flow may increase the hydraulic gradient near an opening, it is not possible for turbulent flow to generate the extremely high hydraulic gradients which exist near the wall of the Room 209 tunnel. The high pressure gradients (approximately 1 MPa/m) near the opening would likely remove crushed rock particles which were generated during the excavation process. The changes in the normal stress on the fracture zone (Kaiser et al., 1989) could not explain, in a consistent manner, all the observed changes in transmissivity around the tunnel. Only shear displacements which cut off flow channels in the fracture zone seem likely to provide the necessary mechanism for resisting the high pressure gradients.

1.2 Scope of Thesis

The hypothesis of fracture zone transmissivity reduction and partial recovery based on shear displacements constitutes the focus of this thesis. The purpose of this thesis is not to provide a perfect shear displacement - transmissivity change model but to demonstrate, using field data and numerical models, that the concept of an excavation-dependent, shear-induced reduction in transmissivity is a valid mechanism to explain the observed hydraulic response a fracture zone.

It is recognized that normal stress - fracture closure can play an important role in the hydraulic response of fractures and certain fracture zones. This thesis, by concentrating on the influence of shear displacements, does not imply that normal stress effects are irrelevant. Instead, the thesis demonstrates that shear displacements can dominate the hydraulic response in certain fracture zones. By examining the influence of shear displacements alone, a conclusive assessment of shear-induced transmissivity changes can be made without additional uncertainties and complexities introduced by examining both shear and normal stress - fracture closure.

The development of the shear-induced transmissivity model required the establishment of a phenomenological relationship between shear and transmissivity change. The starting point to establish this relationship was an examination of fracture zone morphology. The morphology of fracture zones typically encountered in igneous intrusive rock masses is presented in Section 2. This thesis explores the hydraulic response of pre-existing fracture zones. Fracture initiation and propagation are not examined. Section 2 also includes a review of the mechanical and hydraulic properties of individual fractures. The applicability and limitations of the parallel plate analogue for fracture flow are discussed in Section 2.6.

Fracture zone morphology and specifically the orientations of primary fractures within fracture zones are used in Section 3 to establish an idealized fracture zone flow model and a relationship between shear displacement and transmissivity change in a fracture zone. A parametric study of the shear displacement - transmissivity relationship is presented in Section 3.5.

The primary research tools were two finite element programs. One program, SAGE (Chan, 1986) was used for 3-D modelling of shear displacements and the other program, SEEP (Guther, 1972) was used for 2-D flow modelling in the fracture zone. A brief summary of finite element techniques for representing fracture zones is presented in Section 2. The fracture zone response was restricted to pre-peak strengths and elastic behaviour; post-peak, time-dependent, and thermal effects were ignored. The analyses of fracture deformation and fracture flow were uncoupled and seepage forces in the fracture zone were disregarded. These simplifications should not limit the applicability of the numerical model when applied to analysis of excavations through naturally occurring fracture zones in competent rock at moderate to low stress levels. In these conditions, the yield strength of fractures in crystalline rock may not be exceeded (Kaiser et al., 1989) and since excavation is rapid, time-dependent and thermal effects are minimal.

Fluid flow is presumed to obey a linear relationship between head drop and flow. It is recognized that tortuosity and contact between opposite sides of a fracture can exercise control over the flow through a fracture (especially at high normal stresses) and these effects have been observed in small scale laboratory specimens. However, it is unclear whether they constitute a dominant influence at the scale of naturally occurring fracture zones. Therefore, to simplify the analysis, a parallel plate representation for fluid flow was assumed appropriate at the single fracture scale.

The shear displacement - transmissivity relationship was used with simple shear displacement distributions and finite element seepage analyses in Section 4 to examine the flow into circular openings. This section highlights the need to understand changes in hydraulic boundary conditions when assessing data from packer tests.

Section 5 presents the results from a comprehensive finite element analysis of the hydromechanical response in the Room 209 fracture zone. In this case history, the effects of fracture zone shear displacements on the changes in transmissivity are examined in detail. Shear displacements in the fracture zone were generated with a 3-D finite element model while various 2-D finite element models were used to simulate the hydraulic response. The excavation-dependent changes in transmissivity and the resulting hydraulic response in the fracture zone were found to correspond with the measured responses when a shear-dependent transmissivity was used. The correspondence between measured and predicted hydraulic response supports the hypothesis of fracture zone transmissivity reduction based on excavation-induced shear displacements.

2 REVIEW OF FRACTURE ZONES AND FRACTURE PROPERTIES FOR FINITE ELEMENT MODELLING

2.1 Introduction

Rock masses encountered near the surface of the earth typically contain several systems of discontinuities as evidence of their origin and response to long term tectonic stresses. These discontinuities may have diverse origins and characteristics and include features such as bedding planes, solution and vesicular cavities, and various forms of failure surfaces. When dealing with igneous intrusive rock masses, the hydraulically prominent discontinuities are almost exclusively dominated by failure surfaces. These include faults and shear zones which have experienced lateral movement (shearing displacements) along the plane of failure and typically contain infillings of clay or breccia; joints, which tend to occur in sub-parallel sets and are often discontinuous within their own planes; and fractures which generally encompasses all types of failure surfaces. Fracture zones, measuring 10 to 100 m in length are of greater extent than joints and typically consist of several closely spaced, often interconnected, joints or fractures with minimal infilling.

Technically, the word 'joint' is restricted to those fractures with field evidence for dominantly opening displacements, i.e. displacements are perpendicular to the fracture surface (Pollard and Aydin, 1988). Faults refer to large scale failure or rupture surfaces which have experienced shearing displacements. Normally faults are much larger features than joints. In this thesis, the term 'fracture' is adopted to describe the near planar failure surfaces commonly found in igneous intrusive rock masses. This term is appropriate for structural features displaying any combination of opening and shearing displacements and has a more generic meaning than the word 'joint'. The term 'joint' is employed in connection with finite element joint or interface models to conform to the convention of its original usage (Goodman et al., 1968).

Fracture zones are often conduits for groundwater and can range from structures that are tight and dry to wide, highly permeable zones that may contain large volumes of water. Fracture zones which have experienced appreciable shear often contain fine-grained gouge material that greatly reduces their permeability. In fact, large gouge-rich shear zones or faults may be dominant zones of flow restriction in a rock mass. In contrast, fracture zones consisting of hydraulically connected, relatively clean fractures can act as the principal conduit for groundwater in a rock mass. By their very nature, these fracture zones have experienced only limited shear, often involve tensile opening, and contain numerous, individual, smaller fractures confined to a narrow region. This thesis is concerned with fracture zones consisting of hydraulically connected, unfilled fractures.

When an excavation intersects a fracture zone the stresses in the fractures are altered by the presence of the excavation. Furthermore, the fluid boundary conditions are radically changed. These two processes involve a complex interaction which leads to a new steady-state flow condition and stresses in the fracture zone. In cases where the change in fluid pressure results in significant changes in effective stress a coupled process ensues between fluid pressures, stresses, displacements, and fracture transmissivity.

A framework for analysing the hydro-mechanical response of a fracture zone is divided into a review of: 1) the morphology of fracture zones; 2) the mechanical properties of fractures; 3) the hydraulic properties of fractures. Each of these three topic areas is followed by a discussion of the application of finite element numerical models to modelling of the hydro-mechanical response of fracture zones.

2.2 The Morphology of Fracture Zones in Igneous Intrusive Rock Masses

This thesis concentrates on the hydro-mechanical behaviour of fracture zones typically encountered in igneous intrusive rock masses. The dominant fractures within these zones are on the order of a few metres in length. To understand the hydro-mechanical behaviour of fracture zones, one must know the geometric structure of the fractures within a fracture zone as well as their individual hydraulic and mechanical characteristics. The fracture geometry depends on the fracture genesis and the mechanical interaction with neighbouring fractures. It is not the intent of this thesis to describe the fracture process since it is the ultimate fracture zone structure, which is evident in the field, that is of primary interest. Any reader interested in understanding the fracture formation process may refer to *Fracture Mechanics of Rock* edited by B.K. Atkinson (1987). A historical perspective of fracture formation and corresponding morphological characteristics was presented by Pollard and Aydin (1988).

2.2.1 Primary Fractures

Various systems of terminology have been adopted to describe the geometry and pattern of fractures and secondary features within fracture zones. Generally, the terminology may be grouped into descriptions based on geometric or kinematic relationships between the various components in the fracture zone. Petit (1987) used a geometrical terminology to describe the position of fractures in a shear context and did not refer to the formation mechanism. Morgenstern and Tchalenko (1967), Gamond (1983), Atkinson (1987), and Pollard and Aydin (1988) presented a kinematic terminology which used the displacement components near the fracture front to define three modes of fracture generation. Figure 2.1 shows the commonly accepted fracture generation modes.

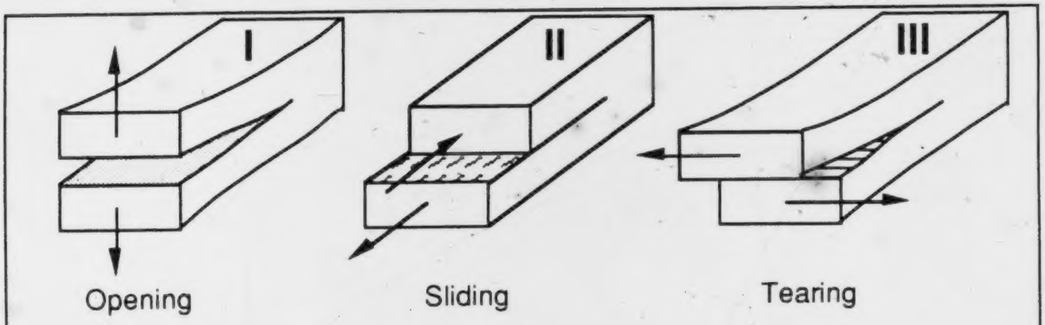

Figure 2.1 Displacement modes at fracture propagation front

Mode I involves opening displacements perpendicular to the fracture surface. Shear displacements occurring parallel to the fracture surface are classified as Mode II displacements if the shearing is perpendicular to the fracture front or Mode III displacement if the shearing is parallel to the propagation front. Generally, joints are associated with Mode I displacement while faults are associated with the shearing modes.

Essentially all former systems for classification of fracture arrangements depend on a known or inferred stress field and directions of displacement associated with the creation of the constituent fractures. Excavation-induced stresses, however, may be completely different from those which originally generated the fracture system. The stress field and displacement directions associated with generation of the fracture system are not important for the purposes of this thesis. Instead, the response of pre-existing fracture zones to excavation-induced change in stress and hydraulic boundary conditions is examined. Therefore, a characterization is required which is not based on kinematics or the original stress field at the time of fracture creation. A flow chart for a purely geometrical characterization of fracture zones is presented in Figure 2.2. This figure also gives the terminology and symbols used for geometric characterization of fractures. A fracture zone characterization scheme based on the overlap (o) and the inclination of primary fractures (α) within a fracture zone has been developed and is presented in Figure 2.3.

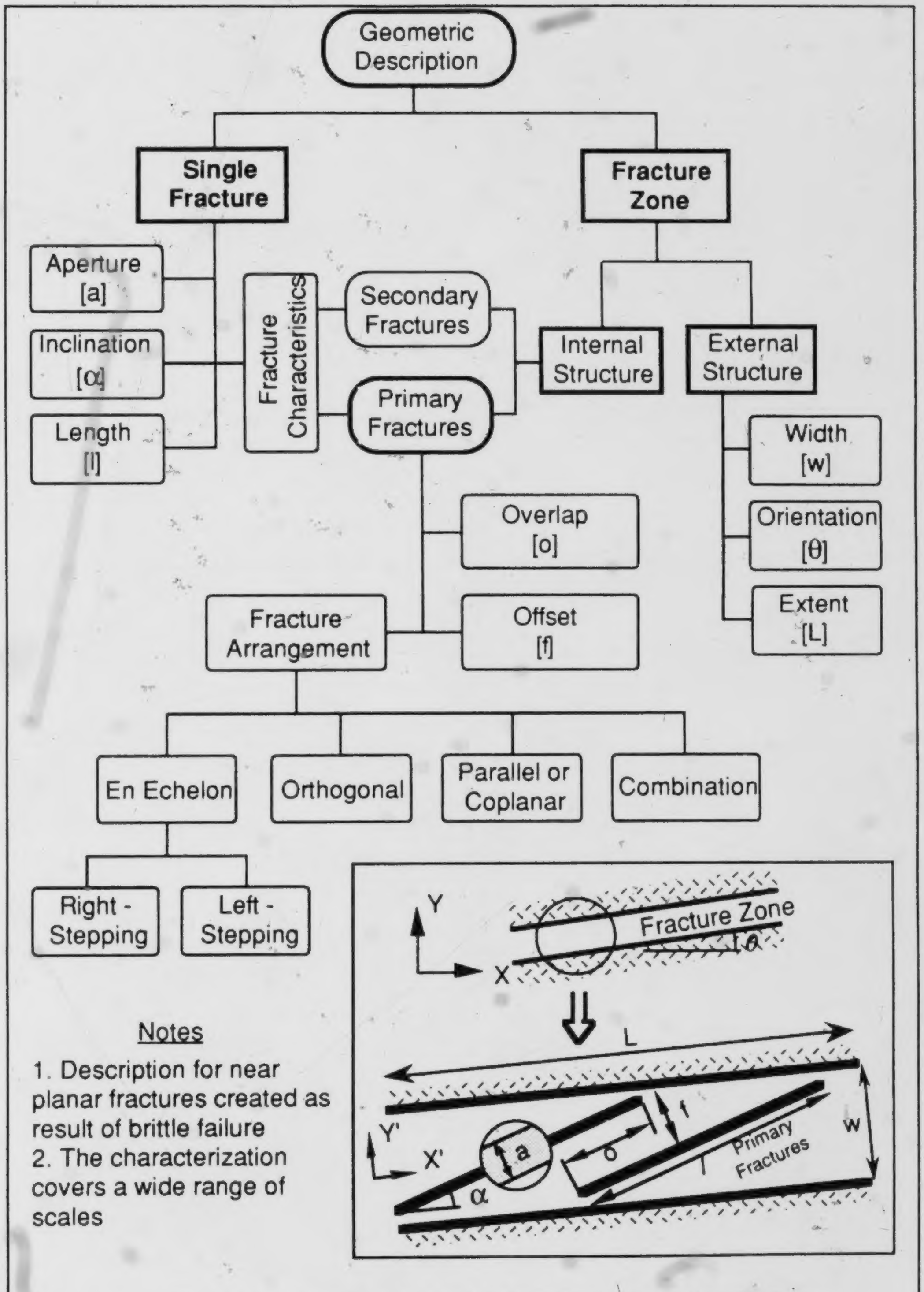

Notes

1. Description for near planar fractures created as result of brittle failure
2. The characterization covers a wide range of scales

Figure 2.2 Fracture zone characterization and terminology

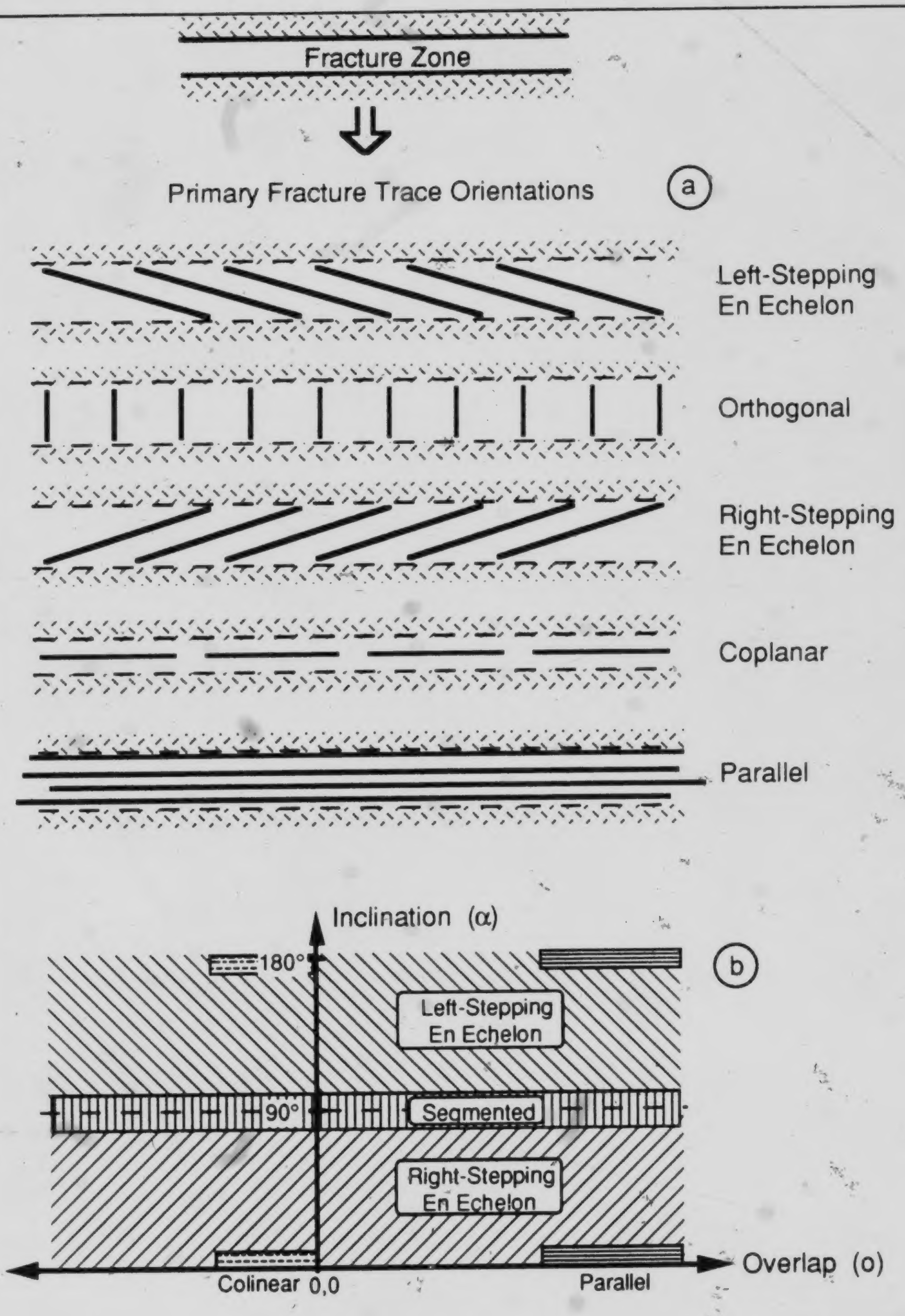

Figure 2.3 Fracture zone structure based on primary fracture trace orientation

The orientations of the primary fractures represented in Figures 2.2 and 2.3 are for the fracture traces. The angle between the trace of the fracture zone boundary and the primary fracture traces (α) will be maximum when the plane of section in which the the traces are seen is perpendicular to the line of intersection between the primary fractures and fracture zone. The maximum angle (α) is needed to classify the fracture zone structures. Therefore the fracture zone must be seen in two non-parallel sections to properly characterize it (analogous to the 'apparent dip problem'). Otherwise the primary fracture inclination, overlap, and offset will depend on the point of view. The distinction between right and left stepping fractures applies to traces as seen on the earth's surface. In the underground environment, the lack of a reference system for the point of view means that a stepped fracture zone seen from opposite directions could be characterized as either right or left stepping.

An important step when analysing the hydro-mechanical response of a fracture zone is the characterization of the fracture zone. The flow chart shown in Figure 2.2 provides a means for fracture zone characterization. The first critical distinction exists between fracture zones which may be characterized (and modelled) as a single fracture and those comprised of multiple, interconnected, individual fractures. The hydro-mechanical response of a fracture zone having more than one discrete fracture depends greatly on the interaction and arrangement of the fractures in the zone. Since the interaction between various fractures can potentially dominate the hydro-mechanical response of the zone, it is important to determine which types of internal fracture arrangements are most common in fracture zones present in igneous intrusive rock.

The morphology of fractures differs between the various types of host rock. The geometry (surface morphology, shape, dimension, spacing, and pattern) of fractures generated in rock masses containing dominant depositional or structural features is often controlled by these features. For example, most joints within layered sedimentary rocks are oriented perpendicular to the layering and are roughly orthogonal. Similarly, joints produced by cooling of a lava flow or by desiccation of a sediment layer are rectangular in shape and are usually perpendicular to the flow surface or sediment layer. In contrast, igneous intrusive rock masses tend to be relatively homogeneous, therefore initiation and subsequent formation of fractures is largely controlled by the evolution of the stress field.

Fracture patterns in homogeneous host materials often display remarkably similar geometries at scales ranging from micrometers in granite (Kranz, 1979) to a few millimetres for shear zones in clay (Morgenstern and Tchalenko, 1967; and Tchalenko,

1970) to tens of kilometres along earthquake faults (Bonilla, 1979; Deng et al., 1986; Naylor et al., 1986; and Sibson, 1986). These fractures or shear zones typically display en echelon arrangements of fractures. The similarity of fracture structures over widely varying scales has allowed researchers to interpret the geometry, kinematics, and stress fields of natural faults based on laboratory experiments (Gamond, 1983; Hempton and Neher, 1986; Naylor et al., 1986; and Petit, 1988). Even the structure of mining-induced fracture zones reveal geometric characteristics which coincide with natural fracture zones (Gay and Ortlepp, 1979; McGarr et al., 1979; and Wallace and Morris, 1979).

Field evidence indicates that faults and fracture zones in massive rock masses commonly have en echelon arrangements of fractures (Deng et al. 1986; Sibson, 1986). Similarly, mining-induced fault zones have displayed en echelon fracture patterns (Gay and Ortlepp, 1979). Experimental deformation of rock and other materials has also generated en echelon fracture patterns (Morgenstern and Tchalenko, 1967; Tchalenko, 1970; Petit, 1988). These field and experimental studies indicate that fracture zones rarely develop by the propagation of a single isolated fracture. More commonly, a fracture zone develops by the progressive incorporation and amalgamation of newly formed and pre-existing fracture segments of varying sizes and orientations. These fracture segments typically form en echelon arrangements with individual segments sub-parallel to the general trend of the fracture zone. The en echelon patterns are called either left-stepping or right-stepping when viewed along the trend of the fracture zone and noting whether one must step to the left or right to reach the next segment (Fig. 2.3). This characteristic occurrence of en echelon fracture patterns has been observed in granitic rock by Everitt (per. comm., 1988) and Segall and Pollard (1983a,b).

2.2.2 Secondary Fractures

Fracture zones acting as conduits for groundwater must contain a hydraulically interconnected array of fractures or exhibit significant intergranular permeability. The fracture patterns established earlier for igneous intrusive rock masses refer to the prominent fractures existing in the fracture zone (called primary fractures). Besides the primary fractures which often exhibit an en echelon array, smaller secondary fractures typically transect the rock mass between the primary fractures. These secondary fractures have been observed at the microscopic (Kranz, 1979) and macroscopic scales (McGarr et al., 1979; Segall and Pollard, 1980; Sibson, 1986; Gamond, 1987; Petit, 1987, 1988; Kemeny and Long, 1989; see also Appendix A).

The geometric arrangement of the secondary fractures is not well established although their orientation appears related to the geometry of the primary fractures and the direction of shear during the generation of the fracture zone (Kranz, 1979; Segall and Pollard, 1980). For a given shear direction (or given stress field) the stress state in the regions near closely spaced fracture tips differ markedly between left- and right-stepping en echelon fracture patterns. The stress state in these regions can lead to secondary extensional and/or shear failures near the en echelon fracture tips. Extensional failure is expected when local tensile stresses exceed the tensile strength of the rock. The generation of high local differential stresses may lead to shear failure when the magnitude of the differential stresses exceed some failure criterion. Figure 2.4 summarizes the findings of Segall and Pollard (1980) who examined the stress states near pairs of en echelon fracture tips using a two-dimensional elastic model. For en echelon fracture segments subject to right lateral shear (Fig. 2.4), the secondary fracturing showed the following characteristics. For left-stepping en echelon segments: 1) short tensile cracks may form outside the step (Fig. 2.4a); 2) the line linking the ends of the two segments is nearly perpendicular to the local maximum compressive stress and is therefore an unfavourable orientation for secondary fracturing; 3) secondary fractures may form ahead of and parallel to the segments; and 4) left lateral secondary shear fractures may form within the step oriented at approximately 45° to 60° to the segments. For right-stepping en echelon segments: 1) tensile fracturing may occur between the segments, possibly linking the segments; 2) shear fractures may form within the step at orientations parallel to the segments and at orientations ranging from 55° to 75° to the segments. Although this thesis is not concerned with the formation processes in a fracture zone, Figure 2.4 does show a potential range in the orientations of the sub-fractures between en echelon primary fractures and illustrates how primary fractures could be hydraulically connected.

Appendix A presents a detailed description of a series of fracture zones occurring in a quartz monzonite rock mass. The surface traces of fractures within the fracture zone display the characteristic en echelon pattern. Data from eight fracture zones showed that the primary fractures are inclined at angles between 9° and 41° degrees to the trend of the fracture zone and the secondary fractures were near perpendicular to the primary fractures (angles between the primary and secondary fractures ranged from 49° to 87°).

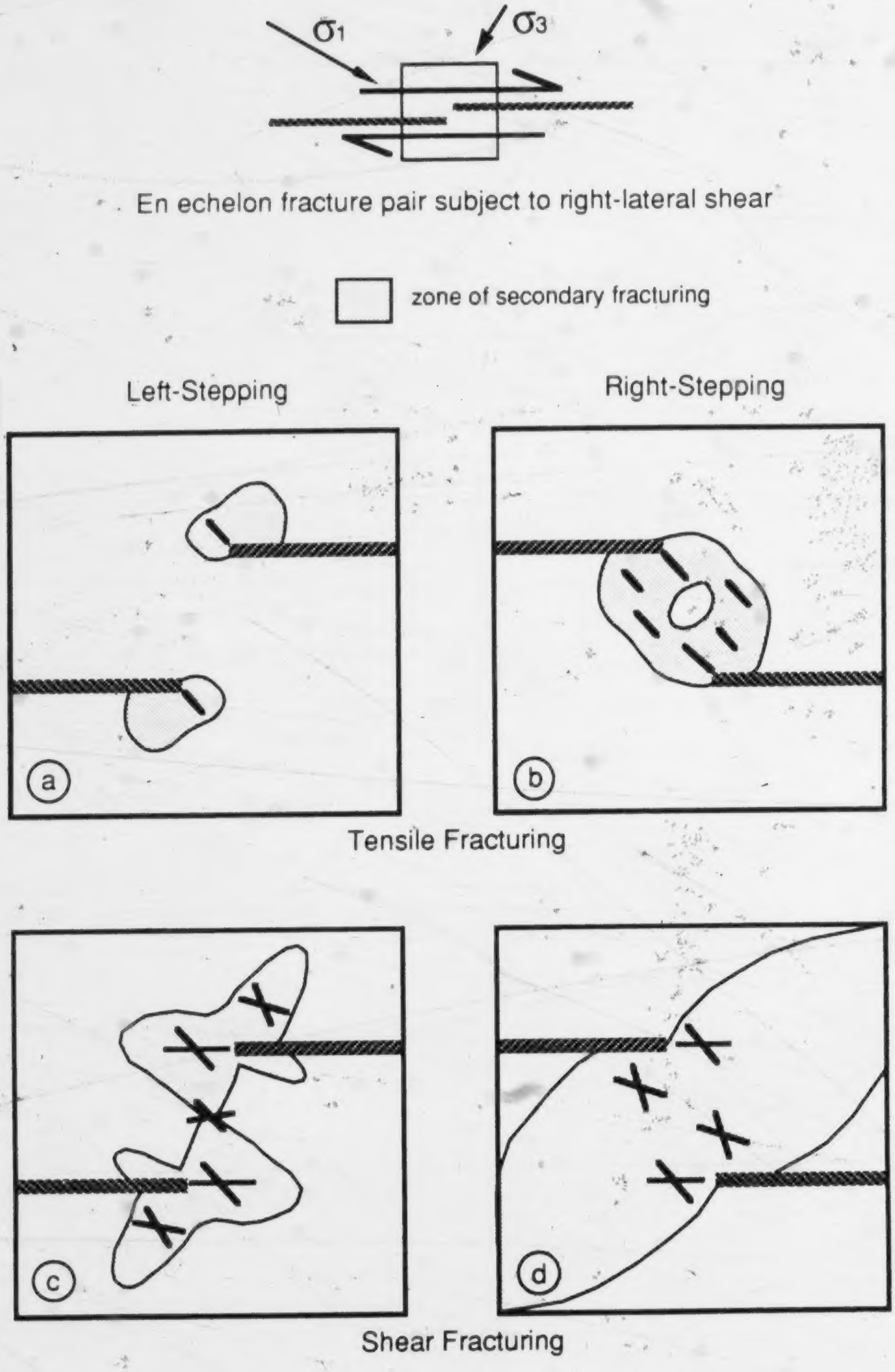
σ1
σ3
En echelon fracture pair subject to right-lateral shear
zone of secondary fracturing
Left-Stepping
Right-Stepping
a
b
Tensile Fracturing
c
d
Shear Fracturing

Figure 2.4 Secondary fracturing near en echelon fractures

2.3 Fracture Zone Morphology and Numerical Modelling

When numerically modelling the hydro-mechanical response of a rock mass containing a fracture zone it is important to choose an appropriate numerical representation of the fracture zone. The relative scale of an excavation opening to the individual fractures is a vital criterion for selecting an adequate numerical model and constitutive relationship. For example, the simulation of a 10 cm diameter borehole intersecting a fracture zone composed of 3 m long, individual fractures may be best modelled with joint elements representing each individual fracture. However, a 3 m diameter tunnel intersecting the same fracture zone may be modelled with joint elements which represent the fracture zone as a whole. The constitutive relationships used for the joint elements would then depend on the properties of the individual fractures and their geometric relationship to each other. The choice between representing a fracture zone with joint elements for each individual fracture or by joint elements encompassing the whole zone depends on: 1) the scale of the problem being analysed; 2) the detail to which the geometry and properties of fractures within the fracture zone are known; and 3) the availability of adequate computational resources for numerical modelling.

Structural geologists can provide accurate maps of the fracture traces on an excavation surface. However, rarely is the internal structure of a fracture zone determined accurately before an excavation exposes the zone. Determination of the orientation and extent of a fracture zone can often prove difficult. This lack of structural information limits the degree of sophistication of finite element models to the representation of only the fracture zone and not its constituent fractures. Nevertheless, joint elements representing the fracture zone can employ constitutive relationships which, to some degree, account for the internal fracture zone structure. The typical en echelon structure observed for fracture zones found in massive or crystalline rock is used as a basis for developing a simple flow model in Section 3.

2.4 Modelling Geomechanical Fracture Behaviour

The geomechanical behaviour of a fracture or fracture zone may be described by constitutive relationships for normal displacement versus normal stress, shear displacement versus shear stress, coupled displacements and stresses such as dilation, and a criterion for shear strength. Most constitutive laws for fracture deformability are obtained from examination of measured responses of fractures or from the surface profiles of rock fractures. For adequate modelling of fracture behaviour, constitutive relationships for both shear and normal loading are required. If more complex deformation phenomena such as coupled shear displacement and fracture dilation or contraction are relevant, then the constitutive model must account for these components of deformation. Nonlinear relationships between aperture, conductivity and flow rate may cause dramatic coupling between the hydraulic and mechanical fracture behaviour. Therefore, both the stress/deformation and the hydraulic responses in fractures must be reflected by an appropriate choice of the constitutive relationship.

The constitutive relationships must also be conducive to implementation into finite element joint elements. Joint elements require explicit relationships for the components of the element stiffness matrix, $\begin{bmatrix} K_{nn} & K_{ns} \\ K_{sn} & K_{ss} \end{bmatrix}$. Where K_{nn} is the normal stiffness, K_{ss} is the shear stiffness, and K_{ns} and K_{sn} are stiffness terms linking normal displacements with shear stress and shear displacements with normal stress.

Various constitutive relationships have been developed to describe the deformational behaviour of fractures, however, this thesis is only concerned with relationships applicable to rough, clean, relatively unfilled fractures of the type found in permeable fracture zones. These types of fractures can exist in either ‘mated’ or ‘unmated’ form, where mated fractures display a juxtaposition between peaks and their respective depressions in the fracture surfaces. Mated fractures are most commonly associated with fractures that were created in tension and have never been subjected to shear displacements.

The deformation phenomena observed in fractures can be more readily understood when examined separately as normal and shear displacements. The terms normal and shear displacements implicitly refer to the relative displacements occurring within the fracture unless otherwise noted. Figure 2.5 presents plots of relationships between fracture displacements, stresses, and stiffnesses.

2.4.1 Normal Deformation and Normal Fracture Stiffness

The normal stress-closure behaviour of fractures has been described by many researchers. Three different approaches have formed the basis for development of normal closure models. One approach is based on the theoretical application of elastic contact theories to fracture surface profiles (Greenwood and Williamson, 1966; Walsh and Grosenbaugh, 1979; Swan, 1983; Johnson, 1983; Gerrard, 1985; Brown and Scholz, 1985, 1986; and Hopkins et al.,1987). This approach begins by characterizing the fracture's topography using a simple profilometer, followed by prediction of the normal mechanical behaviour using an elastic contact theory. Another approach is based on describing the observed normal stress-closure deformations and explaining these in terms of phenomenological relationships or elasto-plastic deformations (Gangi, 1978; Tsang and Witherspoon, 1981, 1982, 1983). Both approaches implicitly assume the applied shear stress is zero.

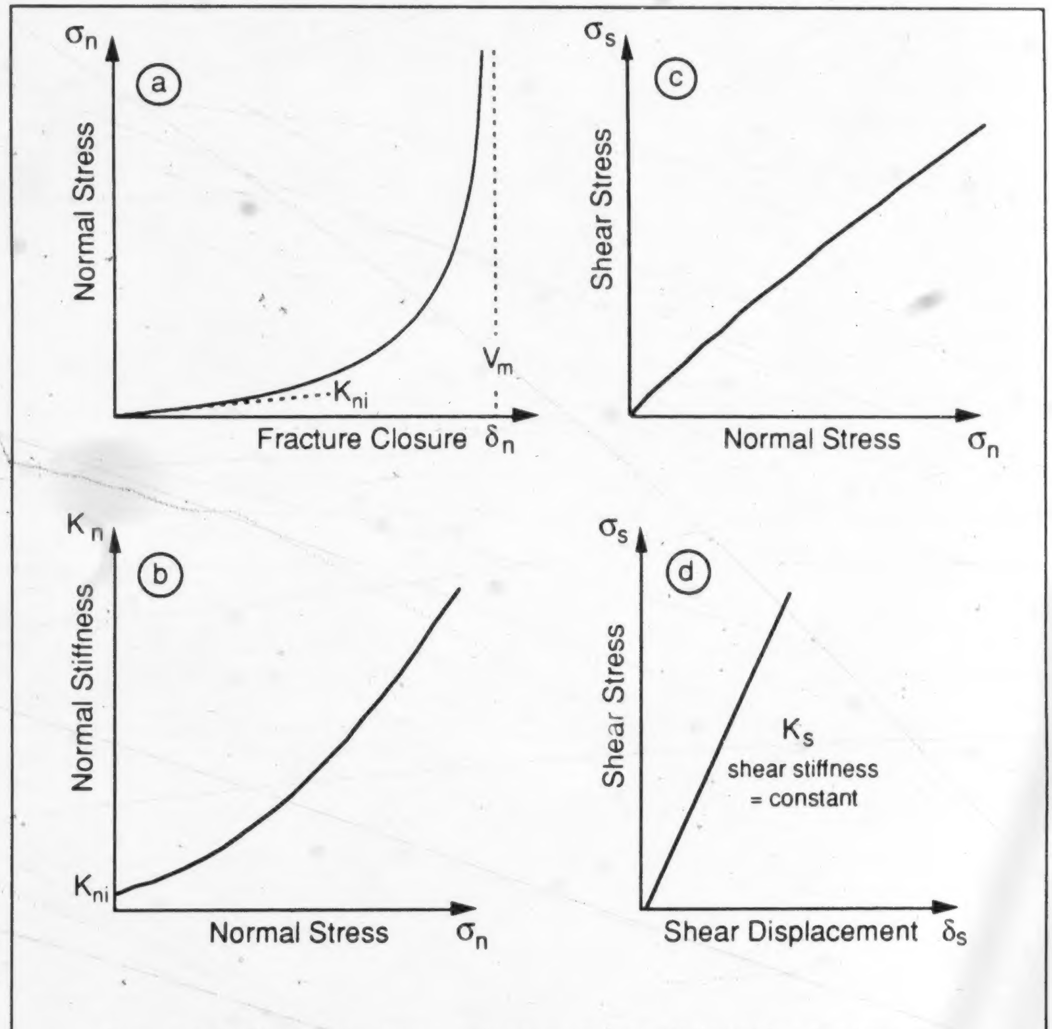

Figure 2.5 Pre-peak stress - displacement relationships for fractures

A third approach involves empirical description of observed normal stress-closure behaviour of fractures. The simplicity of this method eliminates the need to conduct profilometer characterization of the fracture surface or perform elaborate normal stress-closure testing on undisturbed fracture specimens. The empirical relationships may be extrapolated to different dimension scales and need the least fracture characterization input. Furthermore, recent modelling of fractured rock masses has shown that empirical relationships provide adequate quantitative representation of fracture behaviour (Lee, 1983; Bandis et al., 1985a,b; Olofsson, 1985; Barton and Makurat, 1989; Skinas et al., 1990; Vik and Johansen, 1990). One drawback of empirical relationships is that they do not provide an explanation for the basic mechanisms behind the observed behaviour. This thesis adopts the empirical approach for defining the normal stress-closure behaviour of fractures.

The first joint or fracture models used to analyse deformation behaviour of jointed rock masses used linear stress-deformation relationships (Goodman et al., 1968; Mahtab and Goodman, 1970). However, the normal stress-closure relationship for fractures was noted by many researchers to be strongly non-linear, especially at low normal stresses (Goodman, 1969; Goodman and St. John, 1979; Bandis et al., 1981, 1983; Barton, 1986; Yoshinaka and Yamabe, 1986).

Goodman (1974) described fracture normal deformation by observing that the maximum closure of a fracture should be less than its aperture and that an open fracture has no tensile resistance. Goodman's experimental data showed that the closure under increasing normal stress varies in a hyperbolic manner:

$$\sigma_n = \left(\frac{\delta_n}{V_m - \delta_n} \right) \sigma_i + \sigma_i \qquad [2.1]$$

where σ_n is the normal stress, δ_n is the fracture closure, V_m is the maximum fracture closure, and σ_i is the initial seating stress. The normal fracture stiffness, K_n (required for the joint element) is given as:

$$K_n = \frac{\partial \sigma_n}{\partial \delta_n} \qquad [2.2]$$

It is generally assumed that changes in normal stress do not induce shear displacements. Using Equations 2.2 and 2.1, the normal stiffness is:

$$K_n = \frac{\sigma_i V_m}{(V_m - \delta_n)^2} \qquad [2.3]$$

Goodman (1976) subsequently proposed a new hyperbolic relation in a dimensionless form:

$$\frac{\sigma_n - \sigma_i}{\sigma_i} = C\left(\frac{\delta_n}{V_m - \delta_n}\right)^t \qquad [2.4]$$

where C and t are curve fitting parameters. To obtain these parameters, values of σ_i and V_m must be known. The maximum closure can be extrapolated from normal stress versus closure curves. However, estimating the seating pressure is arbitrary and the relationship is sensitive to the assumed value of σ_i. Because of the fitting parameters, the equation for normal stiffness is more complex:

$$K_n = t\,C\,\sigma_i\,V_m \frac{\delta_n^{\,t-1}}{(V_m - \delta_n)^{t+1}} \qquad [2.5]$$

As the fracture closure approaches V_m, the fracture stiffness approaches infinity. This expression for normal stiffness will generate numerical problems if used in a joint element. This model calls for the estimation of four parameters. Elliott et al. (1985) showed a range of values for t and C in granitic fractures ($0.6 \le t \le 1.3$, and $1.2 \le C \le 22$). Elliott's data also suggests that it may be incorrect to arbitrarily choose $t = C = 1.0$, which is the case for Goodman's first hyperbolic relationship. The variability and difficulty in determining the parameters for both of Goodman's hyperbolic relationships demonstrates the problematic nature of defining accurate constitutive models.

Bandis et al. (1983) presented another empirical hyperbolic function which described their laboratory data on natural interlocked fractures better than the Goodman formula (Fig. 2.5a):

$$\sigma_n = \frac{\delta_n}{a - b\,\delta_n} \qquad [2.6]$$

where a and b are parameters defined by the values of initial normal stiffness (K_{ni}) and maximum fracture closure (V_m):

$$K_{ni} = \frac{1}{a} \quad \text{and} \quad V_m = \frac{a}{b} \qquad [2.7]$$

These values uniquely define the hyperbolic stress-closure relation for a fracture. The fracture normal stiffness can be expressed as:

$$K_n = \frac{a}{(a - b\,\delta_n)^2} \qquad [2.8]$$

or as a function of K_{ni} and V_m:

$$K_n = \frac{K_{ni}}{\left(1 - \frac{\delta_n}{V_m}\right)^2} \qquad [2.9]$$

The above relationships for the normal stiffness of fractures are strongly dependent upon the fracture closure. For numerical implementation into joint elements, the normal stiffness may be more conveniently expressed in terms of normal stress (Fig. 2.5b) instead of fracture closure. By substitution of δ_n as:

$$\delta_n = \frac{\sigma_n\, a}{1 + \sigma_n\, b} = \frac{\sigma_n V_m}{K_{ni} V_m + \sigma_n} \qquad [2.10]$$

Equation 2.9 becomes:

$$K_n = \frac{K_{ni}}{\left(1 - \frac{\sigma_n}{V_m K_{ni} + \sigma_n}\right)^2} \qquad [2.11]$$

In this form, it is immediately apparent that the normal stiffness is normal stress dependent.

The Bandis normal stress-closure model does not explicitly consider the initial stress level at which K_{ni} and V_m are determined. Since these parameters are stress level dependent themselves, the relationship can be improved by addition of a stress correction term which accounts for the initial seating stress (σ_i) (Wei and Hudson, 1986):

$$(\sigma_n - \sigma_i) = \frac{\delta_n}{a - b\,\delta_n} \qquad [2.12]$$

One positive feature for the Bandis relationship is that the curve fitting parameters, a and b, relate directly to physical properties of the fracture. The Goodman (1976) model is equivalent to this relationship if: $t = 1$, and $C = 1/\sigma_i b$. Therefore, the Bandis et al. (1983) model is a special case of the Goodman model.

Other researchers have proposed logarithmic normal stress-closure relationships (Yoshinaka and Yamabe, 1986). Logarithmic normal stress-closure functions generate linear relationships between normal stiffness and stress which are significantly different from the non-linear normal stiffness relationships obtained from the hyperbolic normal stress-closure expressions. In general, the hyperbolic normal closure relationships are found to better represent fracture behaviour than the logarithmic functions.

Barton et al. (1985) observed that in situ fractures respond to normal loading in a manner similar to the third or fourth loading cycles of laboratory samples. This is attributed to the removal of sampling disturbances (reduction of hysteresis) by repeated loading cycles. When considering unloading and reloading Goodman (1976) suggested that the unloading response of fractures is similar to intact rock. However, Bandis et al. (1983) noted that the unloading curves are also hyperbolic and are described by the same equation as the loading curves. Fracture unloading displayed strong hysteresis, with the nonrecoverable displacements reducing with subsequent loading cycles.

For this thesis, the Bandis et al. (1983) hyperbolic normal stress-closure relationship (Equation 2.6) has been adopted for representation of the in situ fracture behaviour. Equation 2.11 defines the normal stiffness for use in joint elements.

2.4.2 Shear Deformation

Shear displacements in fractures can be conveniently separated into pre-peak and post-peak responses (the peak being related to the shear strength). When dealing with competent igneous intrusive rock masses and typical excavation geometries one finds that the stresses induced in a fracture because of an excavation often fall below the peak strength. Most experimental, theoretical, and numerical work on the shearing response of fractures has concentrated on post-peak behaviour. Typical features which have been introduced include joint dilation, pre-failure yielding, visco-plastic behaviour, strain hardening and softening, asperity surface degradation, nonassociative, and anisotropic response (For examples, see: Gerrard, 1985; Olofsson, 1985; Pande, 1985; Plesha, 1985, 1987; Desai and Fishman, 1987; Desai, 1988). Most of these models have been validated by comparisons with laboratory data from fractures that have been sheared well beyond peak. The pre-peak behaviour has seldom been carefully tested and has been neglected or simplified in these constitutive models. However, this thesis is motivated by a class of problems in which the fractures do not exceed their yield strength, thus shearing is dominated by the pre-peak behaviour and a proper constitutive model only needs features related to pre-peak fracture behaviour.

A constitutive model for the shearing behaviour of fractures generally requires relationships for: 1) shear stress versus normal stress (shear strength or failure/yield criterion); 2) shear stress versus shear displacement (fracture shear stiffness); 3) shear displacement or stress versus normal displacement (dilation or contraction).

2.4.2.1 Shear Strength

A failure criterion for rock fractures in its simplest form can be expressed as:

$$F = \mu N \tag{2.13}$$

where μ is the coefficient of friction and F and N are the shear and normal forces acting on the fracture. For discontinuities having inherent shear strength, a Mohr - Coulomb failure criterion for the shear strength (τ_p) of fractures is more appropriate:

$$\tau_p = c + \sigma_n \tan\phi \tag{2.14}$$

where c is the inherent shear strength of the fracture, σ_n is the normal stress on the fracture, and ϕ is the angle of friction ($\mu = tan\phi$). Both c and ϕ are not true constants but depend on many factors. The shear strength of rock fractures is sensitive to the normal stress level, degree of surface roughness, compressive strength of the rock (asperities), displacement history, degree of weathering, mineralogy, and the presence of water. Non-linear shear strength envelopes are well accepted as a fundamental characteristic for non-planar rock fractures. A bilinear relationship presented by Patton (1966) accounted for the influence of fracture asperities on the shear strength at lower normal stress levels. Several empirical power relationships have been used to fit the distinctively curved shear strength envelopes observed in laboratory tests (Jaeger, 1971).

More recently, Bock (1979), Heuze (1979), Heuze and Barbour (1982), Gerrard (1985; 1986), and Plesha (1987) among others, have presented alternative relationships to describe the shearing behaviour of fractures. However, the most widely adopted relationships are those introduced by Ladanyi and Archambault (1969) and Barton (1976).

Ladanyi and Archambault (1969) proposed a formulation for the shear strength of fractures which accounts for shearing through asperities:

$$\tau_p = \frac{\sigma_n(1 - a_s)(v + \tan\phi_r) + a_s S_r}{1 - (1 - a_s)v \tan\phi_r} \tag{2.15}$$

where:

a_s = the shear area ratio giving the proportion of fracture area sheared through the asperities;

v = rate of dilation at the instant of peak shear strength;

S_r = shear strength of the asperities.

Ladanyi and Archambault also developed empirical relationships for the shear area ratio and the rate of dilation:

$$a_s = 1 - (1 - \sigma_n/\sigma_T)^{k_1} \quad \text{and} \quad v = \tan i\,(1 - \sigma_n/\sigma_T)^{k_2} \qquad [2.16]$$

where i is the dilation angle, σ_T is the brittle-ductile transition pressure and $k_1 \cong 1.5$ and $k_2 \cong 3$ to 4. The rate of change of normal displacement with increasing shear displacement at low constant normal stress is v. Subsequently, Ladanyi and Archambault (1980) modified these equations as follows:

$$a_s = 1 - (1 - \sigma_n/\sigma_c)^{0.75} \quad \text{and} \quad v = \tan i\left[1 - (\sigma_n/\sigma_c)^{0.25}\right]^{1.75} \qquad [2.17]$$

where σ_c is the unconfined compressive strength of the rock. The Patton and the Ladanyi and Archambault models are ways of describing the shape of the failure envelope. These models however, do not account for pre-sliding behaviour and explicit relationships between increments of stress and displacement are not obtainable.

Barton (1976) presented an empirical relation for the peak shear strength (τ_p) of fractures (Fig. 2.5c):

$$\tau_p = \sigma_n \tan\left[JRC \,\log\left(\frac{JCS}{\sigma_n}\right) + \phi_r\right] \qquad [2.18]$$

where *JRC* is the fracture roughness coefficient, *JCS* is the fracture wall compressive strength, and ϕ_r is the residual friction angle. A study of fracture behaviour by Barton and Choubey (1977) has shown that the parameters in this equation can be easily determined and that the relationship is sufficiently accurate for most applications. This equation has also been the basis for defining yield functions in the context of elasto-plastic constitutive relationships (Pande, 1985). When used as a yield function, the parameters *JRC* and *JCS*, are no longer constants reflecting the peak strength condition but vary in response to deformation in the fracture thereby simulating changes in mobilized shear strength. Furthermore, these parameters account for scale effects since both are size dependent.

Lee (1983) modified Barton's (1976) formulae by letting the *JCS* equal the shear strength of intact rock. This led to a better match between laboratory and in situ shear strength values and more realistic predictions of asperity angles at very low and very high normal stresses. Using the shear strength of intact rock as the *JCS* value had the advantage of eliminating the need to perform somewhat subjective Schmidt hammer tests but then *JCS* becomes a function of normal stress as well.

Barton's (1976) shear strength equation has been chosen for this thesis. The equation adequately reflects the normal-stress dependent nature of shear strength, scale effects, and has the advantage of being dependent on only a few relatively easy to determine parameters.

2.4.2.2 Shear Stiffness

Measured pre-peak portions of different shear stress - shear displacement (τ -δ_s) curves show both linear and non-linear behaviour. Linear pre-peak relationships between shear stress and shear displacement have been proposed by Goodman et al. (1968) and Goodman and St. John (1979). In these cases the shear stiffness (K_s) is expressed as:

$$K_s = constant \qquad [2.19]$$

Hyperbolic functions have been used by many researchers (Kulhawy, 1975; Hungr and Coates, 1978; Janardhanam and Kane, 1985; Yoshinaka and Yamabe, 1986) to describe the non-linear behaviour of sheared fractures in the pre-peak range. Kulhawy (1975) gave the following formula:

$$\tau = \frac{\delta_s}{\frac{1}{K_{si}} + \frac{R_f\ \delta_s}{\tau_p}} \qquad [\ 2.20]$$

from which the following relationship for shear stiffness was developed:

$$K_s = K_{si}\left(1 - \frac{\tau\ R_f}{\tau_p}\right)^2 \qquad [2.21]$$

in which K_{si} = initial tangent shear stiffness; δ_s = shear displacement; τ = mobilized shear stress; τ_p = peak shear strength calculated using a suitable failure criterion; and R_f = failure ratio (τ/τ_{ult}).

Bandis et al. (1983) found that hyperbolic equations such as Equation 2.20 offered good representation of the pre-peak shear behaviour of their test data irrespective of the fracture type and normal stress level. These relationships show the importance of the initial stiffness and maximum closure.

Barton and Choubey (1977) suggested the following empirical relationship to describe the shear stiffness:

$$K_s = \frac{100}{L}\ \sigma_n \tan\left[JRC\ \log\left(\frac{JCS}{\sigma_n}\right) + \phi_r\right] \qquad [2.22]$$

where L is the fracture length, introduced to allow for scale effects on K_S, and *JRC* and *JCS* are the fracture parameters described earlier. Lee (1983) found that a slightly modified version of this relation adequately described the pre-yield stiffness of bedding planes at Mount Isa. Equation 2.22 was modified (Barton and Bakhtar, 1983) to better account for the shear displacement required for peak shear stress mobilization. The shear stiffness in the pre-peak range was given as:

$$K_s = \frac{\tau_p}{\delta_{(peak)}} = \frac{\sigma_n}{\delta_{(peak)}} \tan\left[JRC \log\left(\frac{JCS}{\sigma_n}\right) + \phi_r \right] \qquad [2.23]$$

where σ_n is the normal stress at peak shear displacement. The peak shear displacement for strong unweathered joints was given by the following empirical equation:

$$\delta_{(peak)} = \frac{L}{500}\left(\frac{JRC}{L}\right)^{.33} \qquad [2.24]$$

Note, the relationship for shear stiffness (Eqn. 2.23) gives a constant value for the shear stiffness in the pre-peak region (Fig. 2.5d). Equations 2.23 and 2.24 have been chosen to represent fracture shear stiffness in this thesis.

2.4.3 Determination of Normal and Shear Stiffnesses for Joint Elements

The Barton and Bandis group of empirical relations (Eqns. 2.6, 2.18, and 2.23) offer simple yet realistic expressions of fracture behaviour under normal and shear loading conditions. These relations are based on the most readily measured or estimated parameters. They can be incorporated into numerical analyses ranging from simple linear elastic analysis to models which progressively modify the normal and shear stiffness values by incremental or iterative procedures to simulate nonlinear stress-deformation behaviour in fractured rock.

Even with the simplicity associated with the Barton and Bandis equations, it is difficult to obtain sufficiently accurate estimates of *JRC* and *JCS* as well as stress levels and apertures for in situ fracture conditions. In cases where the fractures are highly stressed in situ, the strong nonlinearities commonly observed in the laboratory, using disturbed fracture specimens and lower normal stress levels, are less important and linear stress-displacement relationships may be sufficient for modelling the mechanical response of the fracture.

Joint elements used for finite element analyses require values of K_{nn} and K_{ss}. These may be determined directly from Equations 2.11 and 2.23. For this thesis the off-diagonal stiffness terms, K_{ns} and K_{sn} are assumed negligible and are set to zero. Using zero off-diagonal stiffnesses is a common practice since these values are extremely difficult to measure and when measured they are typically much smaller than the diagonal terms under pre-peak strength conditions. An example of the application of the Barton-Bandis equations for determination of joint element stiffness values is presented in Appendix B.

2.5 Finite Element Models for Fractured Rock

Numerical simulations of fractured rock masses have, in general, followed two approaches: 1) statistical models where the geometry of the fracture system is represented by proper statistical distributions; and 2) deterministic models where the geometry of the fracture system is assumed or is known. The first approach uses the properties of the fracture system to generate an 'equivalent' rock mass material. This approach eliminates the need to use discrete joint elements in the rock mass model and is most appropriate in situations where well defined and uniformly spaced fractures predominate. Furthermore, the size of the opening should be large compared to the fracture spacing. The other approach involves modelling each individual fracture separately within the rock mass. Discrete joint models are applicable to geological settings where only a few fractures dominate the behaviour of the rock mass.

A different approach to the modelling of jointed rock masses is the use of distinct elements (Kafritsas et al., 1984; Lemos et al. 1985; Cundall and Fairhurst, 1986; Cundall, 1987). The distinct element method is a recognized discontinuum modelling approach with joints regarded as boundary interactions between blocks of rock.

The following presents a brief review of the alternative numerical methods for incorporating the influence of fractures in finite element analyses of fractured rock masses. This discussion is biassed to methods applicable for modelling the behaviour of rock masses containing single or multiple fractures or joint sets. Nevertheless, the synopsis also includes equivalent rock mass models.

2.5.1 Equivalent Rock Mass Models

Zienkiewicz et al. (1970) introduced a stratified (laminar) rock mass model where all nonlinear phenomena are confined to normal and tangential stresses in the stratification planes. Malina (1970) also derived the formulation for a stratified finite element model. The strength of the material as well as the friction and cohesion along discontinuities were described by a Mohr-Coulomb envelope. If the strength is exceeded, irreversible sliding or discontinuity opening occurs along the one representative stratification surface within the element. Similar models for fractured media were presented by Serrano Gonzalez and Soriano (1986) and Blanford et al. (1987) which allowed generation of an equivalent continuum constitutive relationship for a rock mass containing a series of planar discontinuities of different orientation.

Equivalent rock mass models may be capable of determining the state of stress on an arbitrarily oriented plane (fracture) within the element, but the proper displacement patterns are generated only in a regional sense. No displacement discontinuities are generated. The various deformation modes are handled by appropriate stress redistribution schemes.

Olofsson (1985) modified the multi-laminate model to include recoverable, linearly stress-dependent normal and shear joint deformations as well as unrecoverable or plastic deformations governed by a yield surface dependent upon the applied stress field and the total plastic deformation. These equivalent material models are only applicable for evenly spaced and continuous joints. The spacing of these joints must be smaller than the minimum dimension of the underground opening. Phenomena such as beam effects in a stratified roof or interlocking structures in cross-jointed rock are not simulated by the model.

Carr (1985) extended the multi-laminate model to geologic settings where the fractures are less frequent. The fracture orientations are specified to exist at the Gauss integration points within the continuum mesh. These locations can be associated with element types enabling analysis of either ubiquitous or interspersed fracture systems. With this continuum model, when a fracture reaches failure the entire stiffness matrix is modified. The fracture density in the rock mass model simply depends on the spacing of the Gauss points. Although this model allows modelling of more variable fracture spacings than previous multi-laminate models, it is still not well suited for analysis of very sparse fracture systems or single fractures transecting an otherwise continuous medium.

Equivalent rock mass models have been successfully used to model the far-field conditions. In many analyses, the far-field is simulated with boundary integral formulations. Sofianos and Watson (1986) utilized a linear elastic orthotropic rock mass model in the far-field.

A major limitation with these methods is that in the near-field the nonlinear behaviour of each individual joint and the kinematic constraints imposed by a system of discontinuities on the rock mass can not be readily duplicated.

2.5.2 Discrete Joint Element Models

Various finite element models have been developed to simulate the presence of discrete fractures or joints in a rock mass. Most of these are descendants of the basic joint element developed by Goodman et al. (1968). They are based on explicit simulation of discontinuous displacement behaviour with relative displacements instead of strains being used in their formulations. The joint elements may be called zero-thickness elements. However, Desai et al. (1984) presented the development of a thin-layer element for joints which essentially represents a solid element of finite thickness between two bodies. This model is not based on relative displacements and is more closely associated with some equivalent rock mass models. The joint models based on relative displacements contrast the multi-laminar (or equivalent rock mass) models which represent essentially quasi-continuum conditions.

Goodman et al. (1968) first introduced a discrete finite element interface or joint element based on relative displacements between the two joint halves. This element was extended to three-dimensional models by Mahtab and Goodman (1970). Heuze et al. (1971) made further modifications to the 'Goodman' joint element by changing the solution procedure to allow for variable stiffnesses and no tension analyses by using a stress transfer scheme. Goodman and Dubois (1972) implemented the capability for dilation modelling in the Goodman joint element. Dilatancy was incorporated through off-diagonal stiffness terms in the element stiffness matrix and by using a load or stiffness perturbation technique to update the stresses. The off-diagonal stiffness terms depend only on the intrinsic properties of normal and shear stiffness relative to a local joint plane and the geometry of the asperities. Joint contractancy was also discussed in their paper. The zero-thickness joints can be made to dilate or contract without reference to an initial joint aperture since opening or closure is defined through the joint stiffnesses by relative nodal displacements.

The joint element originally developed by Goodman et al. (1968) was formulated from a simple, rectangular, two-dimensional, linear element. Although this element is implicitly based on relative displacements, it uses eight displacement degrees-of-freedom. This element allows adjacent, continuous elements to penetrate into each other. Ghaboussi et al. (1973) modified this element by transforming displacement degrees-of-freedom of one side of the joint into relative displacements between the two sides of the joint. Only one side of the joint is recognized explicitly in the mesh; the opposite side is considered to belong to one of the contiguous blocks as an internal feature. This allowed the joint element to use four relative displacement degrees-of-freedom in its formulation. The presence of the joint element involved expanding the stiffness matrix of a block on one side of the joint. The use of relative displacement degrees-of-freedom also resolves some numerical difficulties associated with the presence of stiff joint elements as shown by Wilson (1977). Ghaboussi et al. (1973) allowed elastic-plastic deformations within their joint model and the Goodman and Dubois (1972) type dilatancy. In their elastic-plastic formulation Ghaboussi et al. (1973) use an associated plastic flow rule which may improperly predict dilation since friction is, generally, non-associated.

Herrmann (1978) used a two-dimensional contact element to model the bond between reinforcement and concrete. This element is a variation of earlier developed joint elements and defines three distinct behavioural regimes i.e., nonslip, slip, and separation modes and uses the analogy of normal and tangential springs between the contacting surfaces.

Goodman and Dubois (1972) noted that the definition of joint stiffness coefficients from direct shear tests become ambiguous when dilatancy, contractancy, or coupled shear displacement occur unless the stiffness of the shear box and the testing machine is specified. Heuze (1979) provided an alternative to the Goodman and Dubois (1972) model for joint dilation. This model accounts for the stiffness of the structure transverse to the joint. Heuze's model contains no off-diagonal stiffness terms and accounts for the effects of dilation by specifying that the increment in normal stress is equivalent to the product of the increment in normal displacement and the transverse stiffness. In practical terms, the determination of representative values of either the off-diagonal stiffnesses for the Goodman and Dubois (1972) model or the transverse stiffnesses for the Heuze (1979) model proves very difficult and neither model can be seen more appropriate for dilation modelling.

The application of joint elements was extended to three-dimensional analyses. Heuze and Barbour (1982) developed an axisymmetric joint element as an extension of a two-dimensional formulation. Van Dillen and Ewing (1981) developed a three-dimensional joint element with the dilation and slip expressed in terms of plasticity theory. A non-associated flow rule was used which enabled the freedom to specify slip and dilation behaviour separately but also generated a non-symmetric stiffness matrix. No details were presented concerning this element's formulation. Beer et al. (1985) also presented a general formulation for an isoparametric three-dimensional joint element. Their stiffness matrix only contained the diagonal stiffness terms and did not account for dilation or contraction effects. Carol et al. (1985) provided formulation for a sixteen-node isoparametric joint element.

The joint elements derived from the basic Goodman joint elements were incompatible with eight-node quadrangular and six-node triangular isoparametric elements since they only have four nodes and display linear displacement distributions. The Goodman element also did not make use of shape functions. Instead, the displacement variables were referred to the mid-point of the element which is considered constant in length. Carol and Alonso (1983) improved this element by formulating a six-node isoparametric joint element. The constitutive matrix is made symmetric by neglecting the off-diagonal stiffness terms, but dilation effects were still included by using a technique similar to that of Heuze (1979). Carol et al. (1985) further extended this formulation to a sixteen-node isoparametric joint element for use in three-dimensional finite element programs. A new definition of the yield surface was proposed which allowed some numerical advantages while still fitting well with experimental data.

The three-dimensional element formulated by Carol et al. (1985) was selected for finite element representation of the fracture zone in this thesis. The element was implemented and tested in the finite element code SAGE (Chan and Chen, 1988). Although this element allows for fracture yielding and dilation, these features were not used in this thesis. A finite element study of the Room 209 fracture zone using the yielding joint element (Kaiser et al., 1987) showed that the joint elements did not yield except at a few very limited locations near the excavation face as the face passed through the fracture zone.

2.6 Modelling Hydraulic Behaviour of Single Fractures

Most investigations of hydro-mechanical fracture behaviour have been conducted on single fractures. It is therefore appropriate to begin the examination of flow through fracture zones by looking at flow through single fractures. The influence of normal fracture displacement (fracture closure and dilation) has been comprehensively examined whereas far less research (Ohnishi and Goodman, 1974; Maini and Hocking, 1977; Makurat, 1985; Teufel, 1987) has been directed to understanding the effects of shear displacement on the hydraulic response of a fracture.

Many researchers (Gale, 1977; Neuzil and Tracy, 1981; Elsworth, 1984; Long et al., 1985; Smith et al., 1985; Andersson and Dverstorp, 1987; Dershowitz and Einstein, 1987; Witherspoon and Long, 1987; Chen et al., 1989; Yang et al., 1989) have examined the hydro-mechanical behaviour of hypothetical or idealized fractures and fracture systems. Laboratory and field studies have also been conducted (Louis and Maini, 1970; Jouanna, 1972; Jones, 1975; Gale 1977, 1982a, 1987a; Kranz et al., 1979; Witherspoon et al., 1979, 1980; Tsang and Witherspoon, 1981, 1983, 1985; Bandis et al., 1985b; Elliott et al., 1985; Raven and Gale, 1985; Pyrak-Nolte et al., 1987; Ryan et al., 1987; Sundaram et al., 1987; Jung, 1989). These efforts have established important properties of flow through individual fractures and fracture networks.

Two general approaches have been adopted for numerical modelling the influences of stress and deformation-dependent permeability* on the hydraulic properties of fractured rock. One approach involves direct determination of relationships between permeability and applied stresses usually based on flow tests through fractured rock. The other approach uses empirical or theoretical relationships between applied stresses and fracture deformation. A model for flow through a fracture with a variable aperture is then used to relate the stress-dependent deformation to fracture permeability. The second approach generates a two-stage mechanical-hydraulic model. When applying finite element techniques to the analysis of mechanical-hydraulic fracture behaviour either approach may be adopted. However, when significant non-recoverable displacements are expected, a two-staged hydro-mechanical model which utilizes the displacements to estimate permeability changes is more convenient. This is especially true when off-diagonal terms in joint element stiffness matrices are used. This overview will concentrate on the two-stage hydro-mechanical model. Implicit throughout this thesis is the assumption that the permeability of the fractures is considerably greater than that of the rock matrix so that flow through the rock can be neglected.

Relationships for the mechanical (or stress-displacement) behaviour of fractures have been presented earlier. The parallel plate model for the hydraulic behaviour of fractures presented next, makes use of aperture changes derived from the mechanical properties of fractures.

---

* Throughout this thesis 'permeability' is used to denote an intrinsic fracture property (dimensions L^2). 'Hydraulic conductivity' accounts for both fluid properties and permeability (dimensions L/T).

2.6.1 Hydraulic Models Based on the Parallel Plate Model

The most basic equation for flow in a fracture assumes that the fluid flow is governed by Darcy's law where the hydraulic conductivity is derived by idealizing the fracture as a parallel plate opening. The derivations are based on the Navier-Stokes equation for single-phase, laminar flow of a viscous incompressible fluid (known as plane Poiseuille flow). Appendix C presents a derivation for single fracture hydraulic conductivity (K_f) which is expressed as:

$$K_f = \frac{\rho g}{12\,\mu}\,a^2 \qquad [2.25]$$

where ρ is the fluid density, g is the gravitational acceleration, μ is the dynamic viscosity, and a is the fracture aperture. Note that many researchers used the dimension a as the width of one half of the parabolic velocity distribution. The intrinsic fracture permeability is given by $k_f = a^2/12$. The flow through a single fracture for saturated one-dimensional laminar flow is given by:

$$Q = -\,K_f \nabla h\; a \qquad [2.26]$$

where ∇ is the del operator ($\partial/\partial x$). After substituting the expression for fracture hydraulic conductivity:

$$Q = -\,\frac{\rho g}{12\,\mu}\,a^3\,\nabla h \qquad [2.27]$$

where Q is the fracture flow (flow per unit length of fracture) and h is the hydraulic head. Equation 2.26 is essentially a statement of Darcy's Law for fluid flow. Equation 2.27 shows that the flow through a fracture is a function of the aperture cubed (hence, called the 'cubic flow law'). In the case of radial flow, the flow may be expressed as:

$$Q = -\frac{2\,\pi}{\ln(R/r)}\,\frac{\rho g}{12\,\mu}\,a^3\,\nabla h \qquad [2.28]$$

where R and r are the outer and inner radii of flow.

The parallel plate flow equation accurately describes laminar flow between two parallel plates. However, fractures and joints in rock have uneven walls and variable apertures. In fact, flow in a fracture under compressive stress is possible only because the fracture walls are uneven and the contact of opposing asperities resists the compressive stresses. Nevertheless, the parallel plate model has been extended to rough, partially contacting, fracture surfaces by assuming that:

1. Surface roughness has little effect on the flow which can be considered to be laminar.
2. The length of the flow path is approximately the same as the length of the fracture in the

direction of the hydraulic gradient.
3. Flow occurs over nearly all the fracture area.

2.6.2 Validity of the Cubic Flow Law

Witherspoon et al. (1980) assessed the validity of the cubic law for fluid flow in deformable rock fractures. They found that the cubic law was valid for fractures closing under stress regardless of the rock type. The effect of deviations from the ideal parallel plate model only cause an apparent reduction in flow. This could be accounted for by a simple empirical reduction factor (f).

$$\frac{Q}{\nabla h} = \frac{1}{f}\, c\, a^3 \qquad [2.29]$$

where c is a parameter describing the fluid properties and flow conditions (see Eqn. 2.27 or 2.28). Some field and laboratory investigations (Pratt et al., 1977; Kranz et al., 1979 and Makurat, 1985) found that predictions based on the parallel plate model did not adequately match experimental results. However, Gale (1977) reviewed earlier experimental results which concluded that the cubic flow relation was not valid and pointed out that the cubic law was valid if better estimates of the apertures had been used. Experimental evidence has shown that even when a fracture under normal stress reaches an asymptotic closure indicating that the fracture is essentially mechanically closed, there still exists flow through the fracture (Pratt et al., 1977; Witherspoon et al., 1980, 1981; Raven and Gale, 1985; Pyrak-Nolte et al., 1987). The cubic law can be modified to include the effect of this irreducible flow (Pyrak-Nolte et al., 1987):

$$Q = Q_0 + c\, a^3\, \nabla h \qquad [2.30]$$

Incorporation of a correction factor of tortuous flow and fracture wall roughness (f) and accounting for the irreducible flow (Q_o) at high normal stresses allows application of a modified cubic flow law to a wider range of fracture conditions.

Gale (1977), Elliott et al. (1985), Ryan et al. (1987) among others have shown that the basic cubic law (Eqn. 2.27), or slightly modified versions of it (Eqns. 2.29 and 2.30), accurately describe the flow through natural and induced fractures. The validity or appropriateness of the parallel plate flow model depends on the degree to which the fracture flow deviates from the assumptions listed in the previous section. Factors which can alter the cubic flow relationship include non-laminar flow, high normal stress, tortuous flow, and incorrect estimates of the fracture aperture.

2.6.2.1 Laminar Flow Assumption

Non-laminar flow has been detected in tests by some researchers indicating that the typically assumed laminar flow regimes may not exist in some engineering situations (Rissler, 1978; Cruz et al., 1982; Elliott et al., 1985; Jung, 1989). Elsworth and Doe (1986) demonstrated the effects of non-laminar flow on the interpretation of borehole pumping tests. Non-laminar and turbulent flow could potentially mask the appropriate relationships if not accounted for in the analysis of experimental data.

In a comprehensive review of laminar flow through fractures, Wilson and Witherspoon (1970) noted that the Reynolds number, R_e, at which flow passes from laminar to turbulent dropped from about 2000 to about 200 as the fracture wall roughness increased. However, they indicated that turbulent flow occurs only when abnormally large fractures are found in the vicinity of large hydraulic gradients. Witherspoon et al. (1980) conducted a review of various laboratory results and found that the assumption of laminar flow in fractures was found to be valid for Reynolds numbers less than about 2300. They also noted that the cubic flow relationship appeared applicable for fractures with apertures ranging from 250 down to 4 μm.

2.6.2.2 Aperture Determination

Validation of the cubic law fundamentally depends on the determination of the initial aperture at the start of a test or the irreducible flow at very high normal stresses. Barton et al. (1985) distinguished hydraulic apertures from mechanical apertures. Mechanical apertures can be determined from normal stress - fracture closure testing while hydraulic apertures are typically back-calculated from flow tests assuming a parallel plate flow model. Since the hydraulic aperture is back-calculated, it implicitly accounts for tortuous flow and fracture wall roughness. Bandis et al. (1983) presented empirical solutions for both the initial mechanical aperture and the hydraulic aperture. Initial apertures have also been estimated from the stress-deformation curves of fractured rock (Pratt et al., 1977; Kranz et al., 1979; Amadei and Goodman, 1981). The hydraulic aperture is smaller than the mechanical aperture due to the fracture roughness and tortuous flow. The hydraulic aperture may be estimated by application of the parallel plate model to hydraulic test data. Sundaram et al. (1987) determined the effective initial apertures from a regression analysis of experimental flow and deformation data. An alternative statistical approach based on experimental flow data is given by Witherspoon et al. (1980) where the true aperture is conceived to consist of the sum of the measured aperture change and the residual aperture remaining at the maximum stress level. The residual aperture may be estimated from the flow rate at the maximum applied normal stress by assuming the cubic law is valid at that stress level (Gale, 1982a). Gale (1982a) noted that by varying the stress level at which the residual aperture is determined, the correspondence of laboratory data to the cubic relation could be improved.

2.6.2.3 Normal Stress and Tortuosity

Field and laboratory studies (Gale, 1977; Pratt et al., 1977; Kranz et al., 1979; Carlsson and Olsson, 1983; Elliott et al., 1985; Raven and Gale, 1985; Gale, 1987b; Pyrak-Nolte et al., 1987; Ryan et al., 1987; Sundaram et al., 1987) indicate that fractures are highly deformable (stress dependent) and changes in effective normal stress can significantly alter fracture apertures, flow rates and fluid pressure distributions. Most tests of normal stress-closure behaviour of both natural and induced fractures have been conducted under effective normal stress ranges of about 0 to 20 MPa. Analysis of tests conducted below 20 MPa normal stress have generally concluded that the basic cubic relation adequately described the relationship between flow and measured closure. In some cases, adjustments of initial apertures and application of friction or fracture roughness factors were found to the improve the cubic fit.

Kranz et al. (1979) tested artificially prepared surfaces in granite at effective normal stresses up to about 140 MPa. These tests indicated that within the uncertainty of fracture aperture measurements, the parallel plate model was inadequate. The parallel plate did not account for the observed stress-path dependent nature of the fracture permeability. They noted that at higher normal stresses, asperities in contact increased the flow path length and tortuosity while inhibiting further fracture closure. Raven and Gale (1985) noted that changes in fracture contact areas with stress may play a major role in decreasing flow. Tsang and Witherspoon (1985) concluded that tortuosity and surface roughness greatly influence the flow, especially when contact area is greater than 30%. Flow tortuosity increases as a function of contact area. Laboratory tests by Gale (1982b), Raven and Gale (1985) and Gale (1987b) subjected natural fractures in granite to stress levels up to 30 MPa. In each series of tests, discrepancies with the cubic flow law were observed at the high stress levels. Pyrak-Nolte et al. (1987) tested the hydraulic-mechanical response in natural fractures in quartz monzonite at effective normal stresses up to 85 MPa and noted that at stresses greater than roughly 20 MPa a markedly non-cubic flow relation was observed.

These experimental investigations have shown that at normal stresses below 10 to 20 MPa (depending on the rock type), the contact area in the fracture is small and occurs in isolated patches such that fluid flow occurs through large void areas. Under these conditions, the fracture is very compliant, the voids reduce their sizes readily under applied stresses and the parallel plate model appears to adequately describe the relationship between changes in fluid flow and fracture closure. Correction factors (f) can account for effects of limited flow tortuosity (Cook et al., 1990).

At higher normal stresses, the contact area becomes large (> 25% to 30% of fracture surface) and the voids which remain do not deform easily. The flow becomes tortuous with the principal flow conduits consisting of tubes or orifices with roughly equidimensional cross section that do not diminish significantly with increasing stress. The mechanical closure at high levels of stress is accommodated by deformation of isolated or poorly interconnected voids. The parallel plate model is inadequate in these circumstances.

For the Room 209 fracture zone, normal stresses on the individual fractures should vary in the range of 10 to 20 MPa (see Section 5.4.2). Therefore, the parallel plate flow model should be suitable.

2.6.2.4 Limitations of the Cubic Flow Law

The basic parallel plate model and cubic flow law (Eqn. 2.27) fail to recognize the spatial heterogeneity in the fracture aperture. Flow in fractures inherently occurs through a network of channels (Pyrak-Nolte et al., 1987; Hakami, 1988; Kikuchi et al., 1989). Consequently, modifications to the basic cubic flow relation have been introduced to account for effects of fracture roughness and tortuous flow paths. When these effects become too large, the parallel plate model is no longer adequate. For example, in the analysis of fracture closure and fluid flow data, Pyrak-Nolte et al. (1987) noted that replacing the exponent '3' in Equation 2.27 with a value that ranged from 7.6 to 9.8 provided a best fit with their data. Clearly the cubic flow law was inappropriate and they suggested that the large exponents are indicative of a nonlinear relationship between changes in mechanical aperture and hydraulic aperture.

For conditions in which the flow is distinctively channelled, a parallel plate model will only be, at best, a rough approximation of reality. In these situations a completely different model is required. Yang et al. (1989) present a model where the flow is assumed to occur in tubes with elliptical cross-sections. Flow through numerical representations of networks of tubes (or channels) showed that flow was dependent on the 'apparent' fracture aperture to a much greater power than 3. Other channelled flow models have been proposed by Neuzil and Tracy (1981), Tsang and Tsang (1987), Tsang et al. (1988), and Shapiro and Nicholas (1989). One difficulty with channelled flow models is assessing the lengths of the flow paths as well as the aperture distribution along the channel.

Previous experimental results have shown that the flow is dependent on some measure of fracture aperture. The fracture aperture may include modifications for lengths of flow paths or tortuosity and fracture roughness. The flow is commonly assumed to be a function of the aperture cubed. Although the relationship may not be cubic for some fractures or correction factors are required to improve the fit with experimental data, the adoption of more complex relationships for the purpose of this thesis was not justified since the fracture aperture and spatial distribution of apertures are poorly quantified for real fractures.

2.7 Using Transmissivities in Finite Element Seepage Programs

Most finite element seepage programs were designed to model flow in porous media. These finite element programs require input of the elemental hydraulic conductivities. The finite element seepage program (SEEP) used in this research allows specification of anisotropic conductivities for each element. The program needs input of hydraulic conductivities in the major and minor principal conductivity directions as well as the orientation of the major conductivity axis with respect to the global coordinate system. Since SEEP is a two-dimensional finite element program, the flow quantities and gradients are calculated under the implicit assumption of unit thickness perpendicular to the mesh. However, when dealing with flow through fractures of variable aperture (or fracture zones with variable equivalent apertures) the unit thickness assumption is no longer valid. In order to account for the "thickness" of the flow regime, the input hydraulic conductivities are replaced by principal transmissivity terms. Fracture transmissivity (T) is defined as the product of fracture hydraulic conductivity and the width of the fracture:

$$T = K_f\, a \qquad [2.45]$$

When using transmissivities instead of hydraulic conductivities the specific discharges* calculated by the program have units of (m^2/s) rather than velocity units (m/s). Therefore, the flows or specific discharge calculated from the finite element model are total flows through the fracture zone and not flows per unit thickness. To calculate flows (m^3/s) one simply takes the product of specific discharge with the length of fracture (or fracture zone) perpendicular to the flow. Heads and fluid pressures and gradients remain the same as for the porous media case.

Although real fractures will have gradually varying apertures, only constant values of transmissivity may be assigned to each finite element. The representation of gradual changes in transmissivity (or aperture) improves as the finite element mesh becomes finer. Fortunately, finite elements with piece-wise constant aperture have shown satisfactory performance in representing tapering fractures (Elsworth, 1985).

Fractures intrinsically have directional transmissivity. The transmissivity of a fracture as given by the parallel plate model applies only in directions parallel to the fracture surface. The transmissivity perpendicular to the fracture is essentially zero since negligible flow can pass through the rock. All fracture seepage modelling presented in this thesis assumes 'in the fracture plane flow'. The transmissivity is also assumed to be isotropic in the plane of the fracture, i.e., transmissivity is not dependent on flow direction.

---

* The term 'specific discharge' is retained even though its dimensions are L^2/T.

3 SHEAR DISPLACEMENT - TRANSMISSIVITY RELATIONSHIP

3.1 Background

The hypothesis of shear-induced transmissivity reduction in a fracture zone calls for the development of a relationship between shear displacement and transmissivity change. There is little information available to suggest the form of this relationship. No published laboratory data of transmissivity changes associated with induced shear displacement in fracture zones have been found. Most laboratory testing of the hydro-mechanical response in fractures involved assessing the influence of normal closure or normal stress on the hydraulic behaviour of single, planar fractures of generally small areal extent (Jouanna, 1972; Gale, 1977; Pratt, et al., 1977; Kranz et al., 1979; Gale, 1982b; Raven and Gale, 1985; Sundaram, et al., 1987; Pyrak-Nolte, et al., 1987; Gale, 1987b; Ryan et al., 1987). Tests have also been conducted to examine the influence of shear-induced dilation at low normal stress. Some laboratory shear tests by Sun et al. (1985) and Ohnishi and Goodman (1974) have demonstrated aperture closure during the initial stages of shear. Almost all laboratory tests have been done on small scale, single fractures and the experimental results cannot be easily extrapolated to larger scale fracture zones.

The large size and complex geometry of fracture zones create extreme difficulties when determining their hydraulic properties. Testing must be conducted at the field scale and only a few field studies have been completed to date. These tests fall into two general categories: 1) hydrological characterization and 2) hydro-mechanical characterization.

Studies by Gale et al. (1985), Neuman et al. (1985), Raven et al. (1985), Dverstorp and Andersson (1989), Kikuchi et al. (1989), and Shapiro and Nicholas (1989) involved the hydrological characterization of fractured rock. Such studies are primarily done with packer and tracer tests. Whereas these experiments may describe the hydraulic properties of fractured rock, they can only indirectly determine the hydro-mechanical behaviour of rock fractures. Direct measurement of fracture closure and application of controlled stresses or displacements to the fracture are not possible.

Field studies in which the fracture is mechanical deformed by application of normal or shear stress during hydraulic testing have been performed by Pratt et al. (1977), Carlsson and Olsson (1983, 1986), Sour et al. (1987), and Gertsch (1990). These tests have been predominantly concerned with the influence of normal stress on closure of individual fractures. The volumes of rock tested have been small due to constraints on techniques for applying sufficient load to the rock. It is unclear whether data from these tests could be extrapolated to much larger scales and to fracture zones. These studies have also demonstrated the difficulties in designing and interpreting the experimental data.

A special packer system which allows measurement of normal displacements across a fracture has allowed hydro-mechanical fracture characterization without the use of externally applied loads (Hesler et al., 1990; Martin et al., 1990a). This method is being extended to include shear displacements (Thompson et al., 1989) and holds promise for in situ hydro-mechanical characterization of fractures and fracture zones.

The field studies mentioned above do not address the influence of excavation-induced changes in stress or displacement on the conductivity of single fractures, fractured rock masses, or fracture zones. Simmons (1989) presented a review of the causes and possible effects of excavation disturbances. Jakubick et al. (1989) discussed the characteristics of excavation response zones as determined with vacuum permeability techniques.

Lieb et al. (1989) summarized Swiss investigations on excavation effects. At the Nagra Grimsel test site, excavation by tunnel boring increased the permeability of steeply inclined schistose fracture zones. Further ventilation and heater tests at Grimsel (Schneefuss et al., 1989) found no significant effects on the permeability in granitic rock due to the induced thermal stresses. The hydraulic monitoring program showed definite evidence for channelled flow in the fracture zones.

At the Colorado School of Mines' Edgar Mine research facility, Montazer et al. (1982) and Kelsall et al. (1982, 1984) have evaluated excavation-induced changes in rock permeability. A series of fractures and one 0.4 m thick shear zone were oriented approximately perpendicular to a long room excavated by careful smooth wall blasting (Fig. 3.1a). Permeability measurements in three boreholes parallel to the room and at varying radial distances from the room indicated a permanent drop in permeability towards the room. The permeability in the shear zone reduced by more than one order of magnitude near the opening. Similar trends were also noted in individual fractures. In contrast to these perpendicular features, permeability testing in radial boreholes showed that fractures parallel to the room increased in permeability. Montazer et al. (1982) speculated that the permeability distributions near the opening were due to excessive shear displacement along the fractures near the tunnel or closure of the fractures due to increase in normal stresses.

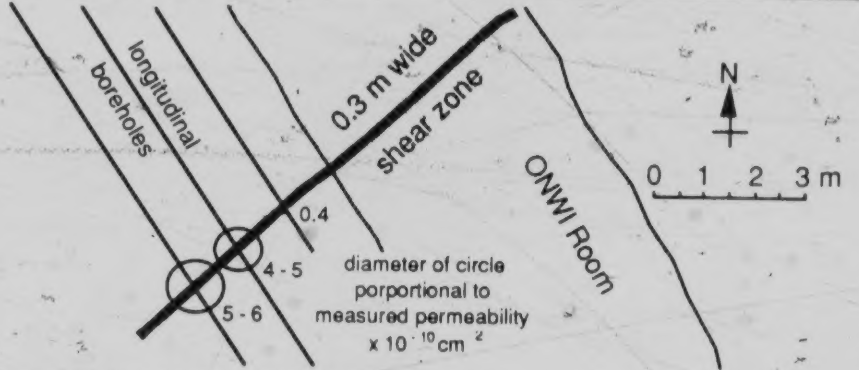

(a) Permeability decrease in shear zone near an excavation at the Colorado School of Mines' Experimental Mine

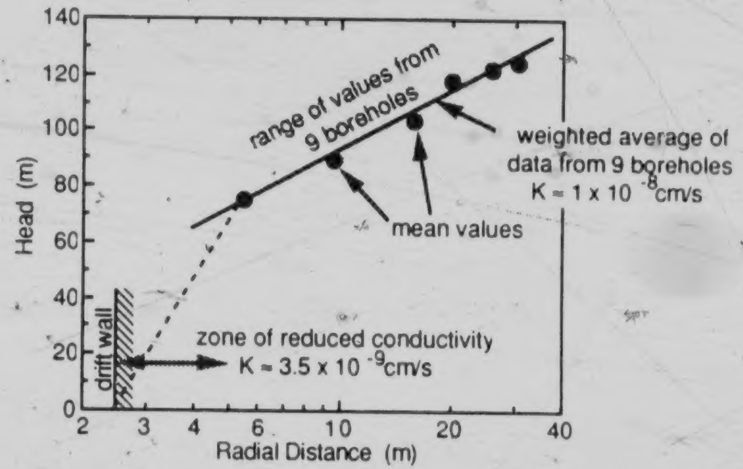

(b) Head profile showing the reduced conductivity zone near the walls of the Stripa Mine Ventilation Drift

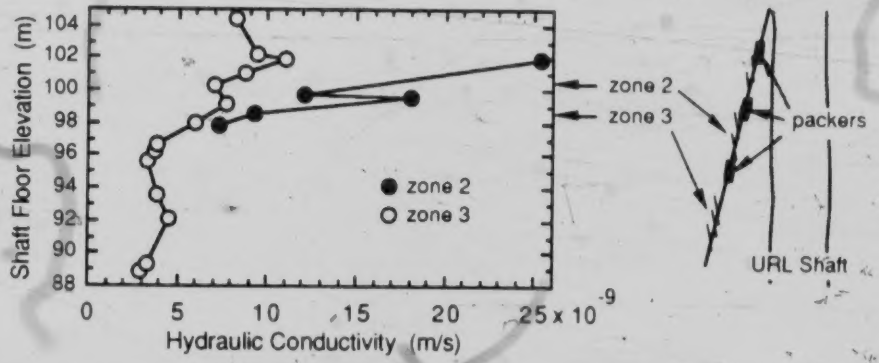

(c) Change in conductivity during shaft sinking at the URL

Figure 3.1 Examples of excavation-dependent fracture conductivity decreases

Field experiments at the Stripa research mine in Sweden (Kelsall et al., 1982; 1984) have been conducted to investigate the influence of excavation on the hydraulic conductivity of rock near the opening. Pressure gradients near a ventilation test drift (Wilson et al., 1983) indicated that a zone of lower radial permeability surrounded the drift (Fig. 3.1b). It was suggested that the permeability reduction was due to tangential stress concentration around the opening. Further testing at this site (Pusch, 1989; Pusch and Bergstrom, 1989) revealed an increase in axial permeability near the drift. Kelsall et al. (1982, 1984) showed stress redistributions around a circular opening would tend to close fractures oriented perpendicular to the axis of the opening, whereas the permeability of fractures oriented parallel to the opening tend to increase near the wall. These findings appear consistent with observations at the Edgar and Stripa mines, although, aside from the one shear zone at Edgar mine, the results apply only to discrete fractures.

Lang et al. (1987a) present results of the near-field mechanical and hydraulic response of a shaft excavated at the Underground Research Laboratory (URL) in Manitoba. The shaft was sunk with careful drill and blast techniques through a granitic rock mass containing near vertical fractures (Fig. 3.1c). Monitoring of fluid pressure and step withdrawal tests performed as the excavation proceeded past the fractures showed an excavation-induced reduction in fracture permeability near the shaft. Numerical modelling to determine the changes in normal stresses on the fractures predicted a decrease in normal stress and hence, an increase in fracture permeability. The observed permeability decrease could not be explained by traditional normal stress-permeability and shear dilation-permeability relationships (Lang et al., 1987a).

An excavation response experiment at Room 209 of the URL provided an opportunity to measure the transmissivity changes in a fracture zone oriented roughly perpendicular to a pilot and slash tunnel excavation (Lang et al. 1986; 1987b; Lang, 1989). The fracture zone transmissivity decreased near the tunnel during excavation. The permeability reduced both as the pilot and the slash excavations proceeded past the fracture zone (see Section 5; Fig. 5.6). The fracture zone also demonstrated a partial recovery in permeability as the excavation continued. Numerical modelling by Chan et al. (1987; 1988) and Kaiser et al. (1987; 1989) failed to predict the observed permeability changes. Application of a normal stress - fracture closure model only predicted permeability or transmissivity decreases in two quadrants around the tunnel whereas the field measurement indicated a consistent decrease in transmissivity at every location around the tunnel.

Kaiser et al. (1989) suggested that shear displacements in the Room 209 fracture zone may provide a mechanism for both the excavation-induced permeability reduction and the partial permeability recovery. The relief of pre-existing shear stresses in the fracture zone by the excavation would account for some component of the observed permanent permeability decrease. This case history is examined in more detail later in this thesis.

The field experiments at the Edgar and Stripa mines and at the URL provide evidence for excavation-induced changes in fracture permeability. However, there were no direct measurements of fracture deformation during the excavation procedure. Due to the lack of experimental evidence to guide or assist the establishment of relationships between shear displacement and permeability or transmissivity change, theoretical relationships were developed. Transmissivity changes are examined rather than permeability changes since transmissivity is a better parameter representing the fluid conducting capacity of a fracture. These relationships apply to fracture zones in crystalline rock and were established by: 1) replacing the real fracture zone by a physical model reflecting the salient geometric features; 2) adopting the parallel plate model for flow through individual fractures in the fracture zone; and 3) establishing the relationships between shear displacement and transmissivity change in the fracture zone.

3.2 Fracture Zone Flow Model

A fracture zone consisting of multiple smaller fractures establishes a very complex geometrical arrangement of flow paths. The general characteristics of fracture zones in crystalline rock were presented earlier. Fracture zones typically display en echelon fracture patterns created by a set of primary fractures oriented at an angle to the plane of the fracture zone. Secondary fractures or micro-fractures often connect the primary fractures. The evolution of the fracture zone flow model is schematically illustrated in Figure 3.2. The observed structure of a naturally occurring fracture (Fig. 3.2a) is represented by the parallel plate flow model (Fig. 3.2b). The observed structure of fracture zones occurring in crystalline rock (Fig. 3.2c) is represented by an arrangement of individual fractures which are in turn modelled by the parallel plate flow model (Fig. 3.2d). The fracture zone flow model is limited by the parallel plate representation for flow through individual fractures. A better representation would include flow channelling and tortuous flow (Fig. 3.2e). However, for this thesis, i.e., the assessment of shear-dependent transmissivity changes in a fracture zone, the simplicity of the parallel plate representation was considered adequate. Furthermore, it is nearly impossible to sufficiently characterize a naturally occurring fracture zone in order to apply a more complex flow model.

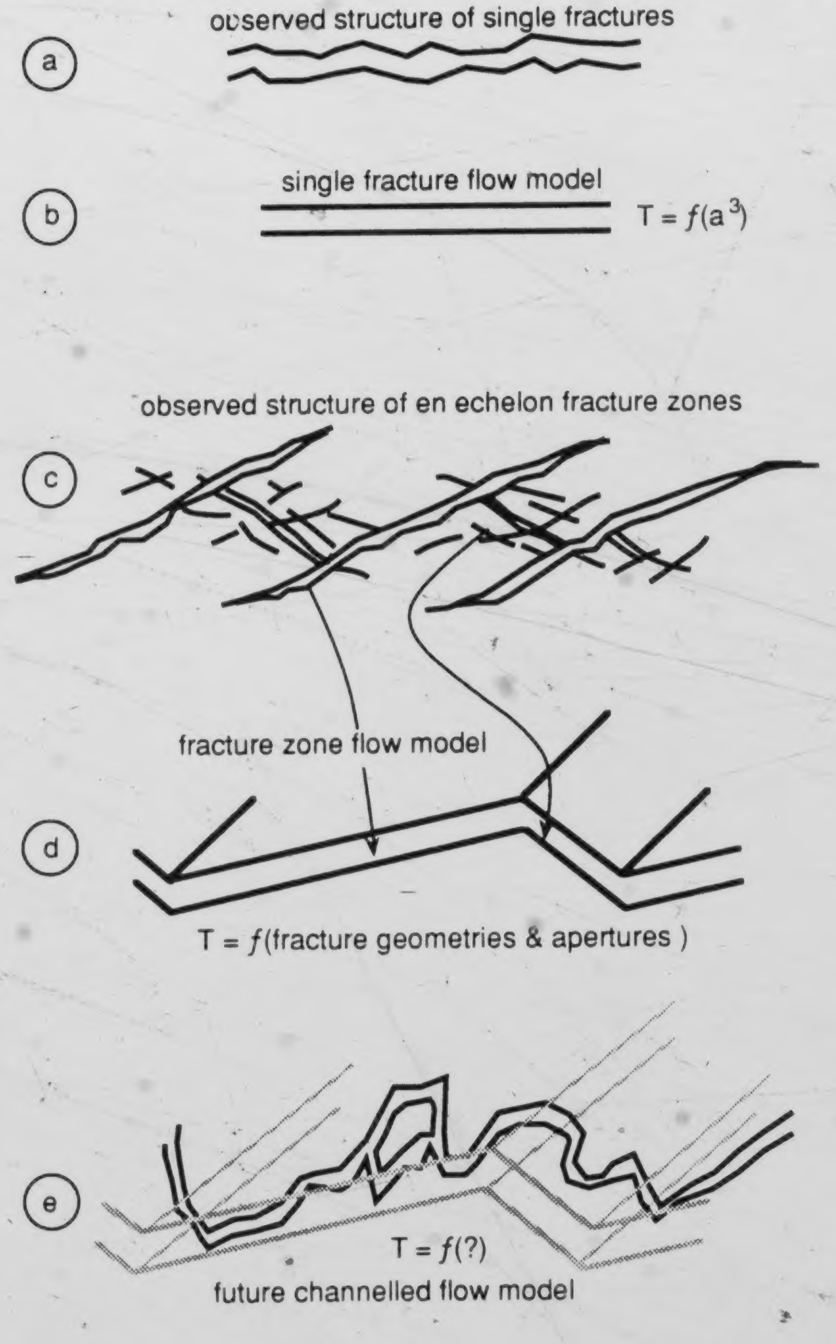
observed structure of single fractures
a
single fracture flow model
b
$T = f(a^3)$
observed structure of en echelon fracture zones
c
fracture zone flow model
d
$T = f$(fracture geometries & apertures)
e
$T = f(?)$
future channelled flow model

Figure 3.2 Evolution of fracture zone flow model

The geometric arrangement of fractures in a fracture zone may be represented by an idealized structure of a continuous, stepped, planar channel (Fig. 3.3a). The model shown in Figure 3.3b represents a conceptual model and is intended to portray the flow paths in a fracture zone rather than the structure of the fracture zone itself. For example, the dotted lines in Figure 3.3a show possible extensions of the en echelon primary fractures but since these form dead-end channels for flow they are not included in the flow model. Typically, a fracture zone contains more than one secondary fracture connecting the primary fractures, however, for the model these are consolidated into an equivalent secondary fracture. Furthermore, the secondary fractures are often nearly perpendicular to the primary fractures. However, the derivation of the shear displacement versus transmissivity change relationship is not limited to perpendicular secondary fractures.

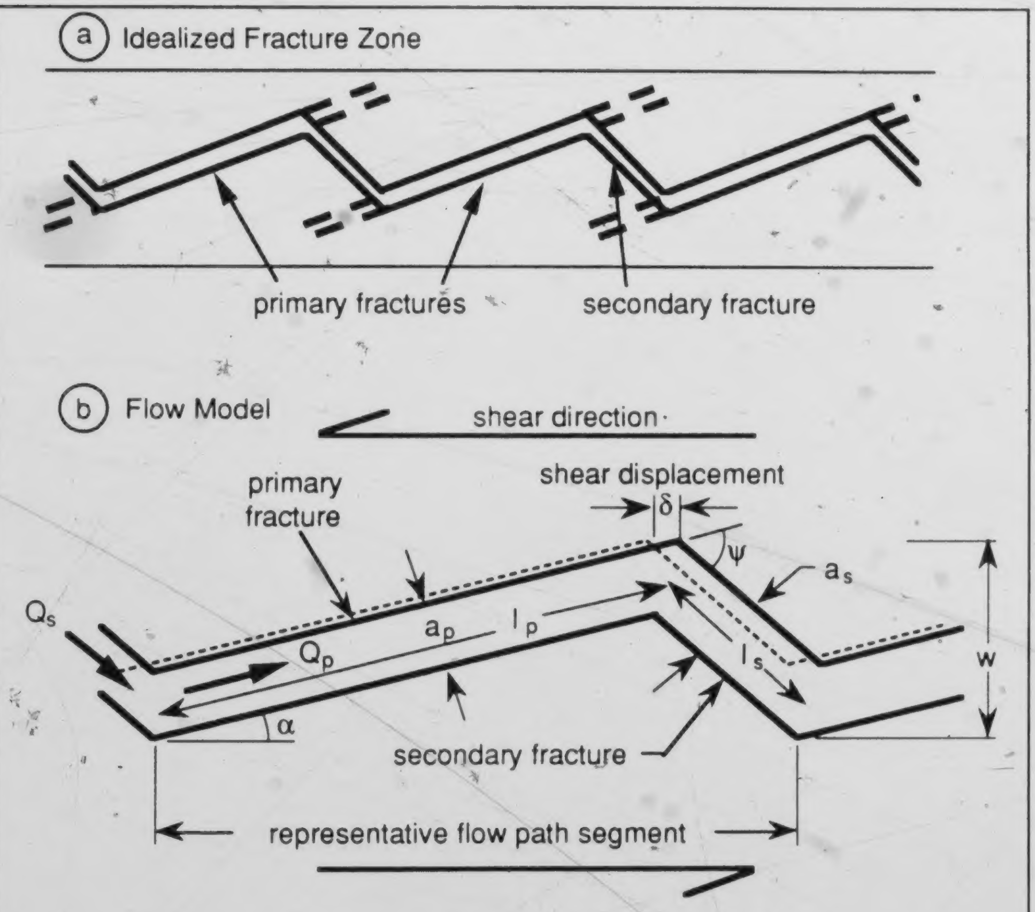

Figure 3.3 Fracture zone flow model

The fracture zone model presented in Figure 3.3b can be viewed as model which reflects the phenomenological hydraulic behaviour of a fracture zone subject to shear. It is analogous to the many spring and dash-pot models which can represent a wide variety of physical systems. For example, the stiffness of fractures may be represented by springs between opposing fracture faces. In reality there are no springs. However, the concept of springs between the fracture faces allows development of relationships between stresses and resulting displacements. These relationships describe the observed response of the fracture. In a similar manner, the fracture zone flow model allows development of a relationship between shear and transmissivity change.

The model is not an accurate representation of real flow paths in fracture zones. Instead it is intended to represent or model the effect of shear-induced decreases in transmissivity. The model does not allow consideration of directional dependent changes in transmissivity or shear in arbitrary directions. Flow is assumed to occur in the plane of the page. Shear displacements in the fracture zone cause changes in fracture apertures. The aperture of either the primary or secondary fracture decreases depending on the direction of shear displacement relative to the fracture orientation. While one fracture decreases in aperture the other increases. However, since the flow is confined to the fracture zone, the fractures with the smaller aperture tend to control the overall fracture zone transmissivity. The equivalent transmissivity of the fracture zone depends on the transmissivities, orientations, and lengths of the primary and secondary fractures.

3.3 Parallel Plate Flow Model and Fracture Zone Transmissivity

Before developing relationships between shear displacement and transmissivity in a fracture zone, the transmissivity of an individual fracture must be defined. A fracture may be considered as a single aquifer with its transmissivity described similar to a porous aquifer, by the product of fracture hydraulic conductivity (K_f) and hydraulic fracture aperture (a).

$$T = K_f \, a = \frac{\rho g}{\mu} k_f \, a \qquad [3.1]$$

If the fracture is filled, the K_f is the hydraulic conductivity of the infilling. For unfilled fractures, K_f is a measure of the frictional drag of flow along the fracture walls and the tortuousity of the flow paths in the fracture. Transmissivity (T) describes the capacity of a fracture (or an aquifer) to transmit a fluid, whereas, hydraulic conductivity (K_f) describes the conductive properties of the fracture (or material comprising the aquifer). Permeability (k_f) is only a function of the fracture aperture and not the fluid properties.

The parallel plate model for flow has been selected to describe the hydraulic conductivity of fractures (frictional aspect of fracture conductivity). In Section 2.6, the applicability and limitations of the parallel plate model for describing fracture flow were discussed. Appendix C presents the derivation of the parallel plate flow equations. The fracture hydraulic conductivity is:

$$K_f = \frac{\rho g}{12 \mu} a^2 \qquad [3.2]$$

where a is the fracture aperture, ρ is the fluid density, g is the gravitational acceleration, and μ is the fluid viscosity.

Multiplying Equation 3.2 by the fracture aperture gives the fracture transmissivity:

$$T = \frac{\rho g}{12 \mu} a^3 = c\, a^3 \qquad [3.3]$$

The fracture transmissivity depends on the aperture cubed.

The equivalent transmissivity in the transverse direction for the fracture zone model (in the plane of the page for Fig. 3.3b) may be calculated using the principle of continuity of flow and determining the head drops across each fracture. From Darcy's law, the flow (Q) per unit width through a fracture is given by:

$$Q = K \frac{\Delta h}{l} a = T \frac{\Delta h}{l} \qquad [3.4]$$

where $\Delta h / l$ is the head gradient. A system of connected fractures in a fracture zone must have equal flow through each fracture:

$$Q \quad = \quad Q_p = c\, a_p^{\,3} \frac{\Delta h_p}{l_p} \quad = \quad Q_s = c\, a_s^{\,3} \frac{\Delta h_s}{l_s} \qquad [3.5]$$

where the subscripts '*p*' and '*s*' refer to the primary and secondary fractures. Therefore, the total head loss through a fracture zone segment of a primary and secondary fracture is:

$$\Delta h_p + \Delta h_s = \left[\frac{l_p}{a_p^{\,3}} + \frac{l_s}{a_s^{\,3}} \right] \frac{Q}{c} \qquad [3.6]$$

If the flow paths represented in Figure 3.3b are replaced by a system which causes an equivalent head drop over the length of the fracture zone, then the flow is given as:

$$Q = T_{fz}\left[\frac{\Delta h_{fz}}{l_{fz}}\right] = T_{fz}\left[\frac{\Delta h_p + \Delta h_s}{l_p \cos\alpha + l_s \cos(\psi - \alpha)}\right] \qquad [3.7]$$

where Δh_{fz} is the total head loss in the fracture zone, l_{fz} is the length of the fracture zone, and T_{fz} is the equivalent transmissivity for the fracture zone. Back-substituting into Equation 3.7 the expressions for head loss in the primary and secondary fractures (Eqn. 3.5), eliminating Q, and solving for T_{fz} yields:

$$T_{fz} = c\left[\frac{l_p \cos\alpha + l_s \cos(\psi - \alpha)}{\dfrac{l_p}{a_p^{3}} + \dfrac{l_s}{a_s^{3}}}\right] \qquad [3.8]$$

An equivalent aperture of a fracture zone segment, a_{fz} can be calculated from the expression of fracture zone transmissivity (Eqn. 3.8):

$$a_{fz} = \left[\frac{l_p \cos\alpha + l_s \cos(\psi - \alpha)}{\dfrac{l_p}{a_p^{3}} + \dfrac{l_s}{a_s^{3}}}\right]^{\frac{1}{3}} \qquad [3.9]$$

3.4 Transmissivity - Shear Displacement Relationship

A relationship between shear displacement and changes in transmissivity can be established using the flow model presented in Figure 3.3b with the transmissivity of a fracture zone as expressed by Equation 3.8. Figure 3.3b shows the effect of shear displacement by a translation of the upper profile of the fracture to the left (dotted lines). For the given shear direction, the aperture of the primary fracture increases while the aperture of the secondary fracture decreases. If the shear were reversed, the opposite situation would prevail. The shear is assumed to occur parallel to the boundaries of the fracture zone. For the following, shear was assumed to cause neither contraction nor dilation of the fracture zone.

The angles α and ψ control the rate at which the aperture changes in the primary and secondary fractures. The change in fracture zone transmissivity due to an applied shear displacement (δ) is dependent on the angular interaction of the primary and secondary fractures as well as the lengths of their flow paths:

$$\Delta T = \mathrm{f}(\delta, \alpha, l_p, \psi, l_s) \tag{3.10}$$

The change in fracture zone transmissivity is:

$$\Delta T_{fz} = \left[\frac{l_p \cos\alpha + l_s \cos(\psi - \alpha)}{\dfrac{l_p}{a_p^{\,3}} + \dfrac{l_s}{a_s^{\,3}}} \right]_1 - \left[\frac{l_p \cos\alpha + l_s \cos(\psi - \alpha)}{\dfrac{l_p}{a_p^{\,3}} + \dfrac{l_s}{a_s^{\,3}}} \right]_2 \tag{3.11}$$

where the subscripts '1' refers to the initial condition and '2' refers to the condition after shear displacement, δ. For flow lengths much longer than fracture apertures ($l \gg a$), only changes in apertures of the primary and secondary fractures cause transmissivity changes. Therefore, a calculation of the apertures after a known shear displacement approximates fully the transmissivity change. For the assumed flow model (Fig. 3.3b), the aperture changes are only a function the shear displacement and the angles between the direction of shearing and the orientation of the primary and secondary fractures:

$$a_{p2} = a_{p1} + \delta \sin\alpha \quad \text{and} \quad a_{s2} = a_{s1} - \delta \sin(\psi - \alpha) \tag{3.12a}$$

If the direction of shearing reverses, then Equation 3.12a changes to:

$$a_{p2} = a_{p1} - \delta \sin\alpha \quad \text{and} \quad a_{s2} = a_{s1} + \delta \sin(\psi - \alpha) \tag{3.12b}$$

The transmissivity of the fracture zone after any shear displacement can be determined if the initial geometry and the magnitude and direction of shear displacements are known:

$$T_{fz2} = c \left[\frac{l_p \cos\alpha + l_s \cos(\psi - \alpha)}{\dfrac{l_p}{a_{p2}^{\,3}} + \dfrac{l_s}{a_{s2}^{\,3}}} \right] \tag{3.13}$$

where a_{p2} and a_{s2} are given by either Equation 3.12a or b. When either the primary or secondary fracture completely closes, the fracture zone transmissivity drops to zero.

An improvement to this relationship may be the consideration of a minimum or irreducible transmissivity (see Section 2.6.2) below which shear can cause no further transmissivity decrease. For simplicity however, Equation 3.13 was not modified.

3.5 Parametric Study of the Transmissivity - Shear Displacement Relationship

A series of figures have been produced to examine the sensitivity of Equation 3.13 to changes in various fracture zone parameters and magnitude of shear displacement. The following fracture zone parameters were assessed: 1) the orientation of the primary fracture (α); 2) the effect of shear direction i.e., which fracture, primary or secondary, closes under shear; 3) the effect of initial ratio of primary fracture aperture to secondary fracture aperture (a_p/a_s) under conditions of different shearing directions; and 4) the effect of secondary fractures not oriented perpendicular to the primary fractures.

The primary and secondary fractures are assumed to extend over a constant width of the fracture zone (see Fig. 3.3a). Therefore, the lengths of the primary or secondary fractures must change for different fracture orientations. The ratio of primary to secondary fracture lengths will also change.

The figures in the following sub-sections present data in various normalized forms. Transmissivity ratios are used because the absolute transmissivity in a fracture zone depends on (among other factors) the length of the representative fracture zone segment (l_{fz}) which in turn varies as a function of the orientation of the primary and secondary fractures (see Eqn. 3.7). By using transmissivity ratios this factor is eliminated from the following comparisons.

3.5.1 Primary Fracture Orientation

The influence of the primary fracture orientation on the shear displacement - transmissivity relationship is shown in Figure 3.4. The initial apertures of the primary and secondary fractures were assumed equal before shearing ($a_p/a_s = 1$) and the secondary fractures are oriented perpendicular to the primary fractures ($\psi = 90°$). The assumed shear direction is opposite to that indicated in Figure 3.3, i.e., the primary fractures close while the secondary fractures open. The transmissivity ratio is the ratio of transmissivity after shear to the initial transmissivity before shearing.

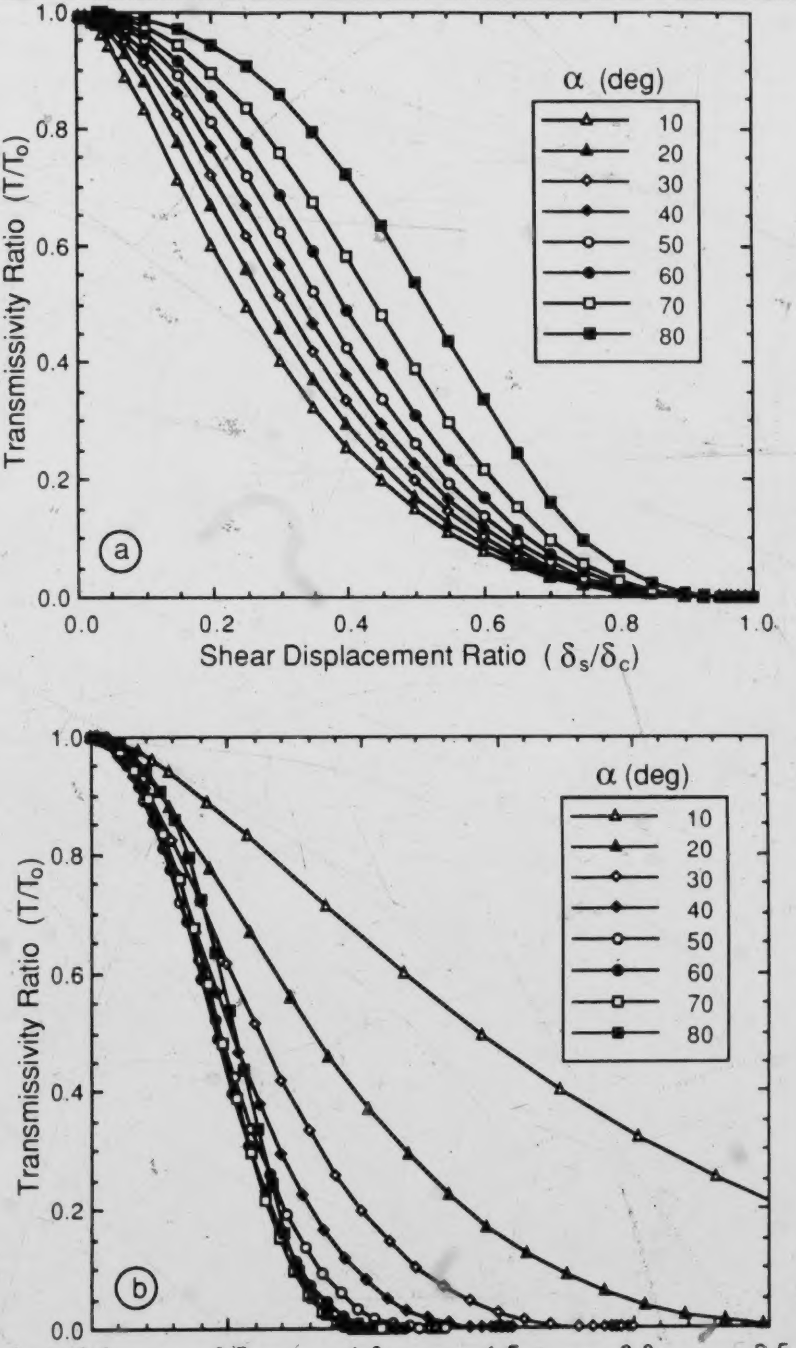

Figure 3.4 Effect of primary fracture orientation on transmissivities during shear

The shear displacement ratio in Figure 3.4a refers to the ratio of shear displacement (δ_s) to the shear displacement (δ_c) which causes complete closure of either of the fractures. In Figure 3.4b, the shear displacements are normalized by the initial fracture aperture (a_o).

Figure 3.4 demonstrates the nonlinear nature of Equation 3.13. The transmissivity changes at a slower rate during the initial and final stages of shearing. Figure 3.4a shows that most of the transmissivity reduction occurs for shear displacements between 0.2 and 0.6 times δ_c. From Figure 3.4a, it appears that fracture zones with a low primary fracture orientation ($\alpha = 10°$) close at the fastest rate. However, the shear displacements in Figure 3.4a are taken as ratios of shear required to completely close the fracture and δ_c depends on α. The shear required to close the fracture is much larger when $\alpha = 10°$ as compared to steeper orientations. Figure 3.4b shows the transmissivity ratios plotted against a normalized shear displacement and it is readily apparent that the shallower orientations lead to slower rates of transmissivity decrease. Fracture zones with primary fracture orientations of about 45° to 90° all give approximately the same rate of transmissivity decrease. Primary fractures in real fracture zones tend to be inclined at less than 45° to the boundary of the fracture zone (Appendix A), thus α may be an important parameter controlling flow.

3.5.2 Shear Direction

The influence of shearing direction relative to the orientation of the primary and secondary fractures is illustrated by Figure 3.5. The primary and secondary fractures have equal apertures prior to shearing, i.e., $a_p / a_s = 1$ when $\delta_s = 0$. Depending on the direction of shearing relative to the fracture zone geometry the primary or the secondary fractures will close. The figure shows the shear direction in which the primary fractures close with solid symbols. Shearing in the opposite direction in which the secondary fractures close is shown by open symbols. The curves are not symmetric about the zero shear axis except for fracture zone geometries where $\alpha = 45°$. However, the curve for $\alpha = 60°$ (secondary fractures closing) is a mirror image of a curve for $\alpha = 30°$ (90°-60°) with shear direction such that the primary fractures close (not shown).

Figure 3.5 shows that irrespective of the direction of shear, the overall transmissivity of the fracture zone decreases. The decrease in transmissivity is caused by the closure of critically oriented fractures. This behaviour reflects the same phenomenon that is observed in real fracture zones.

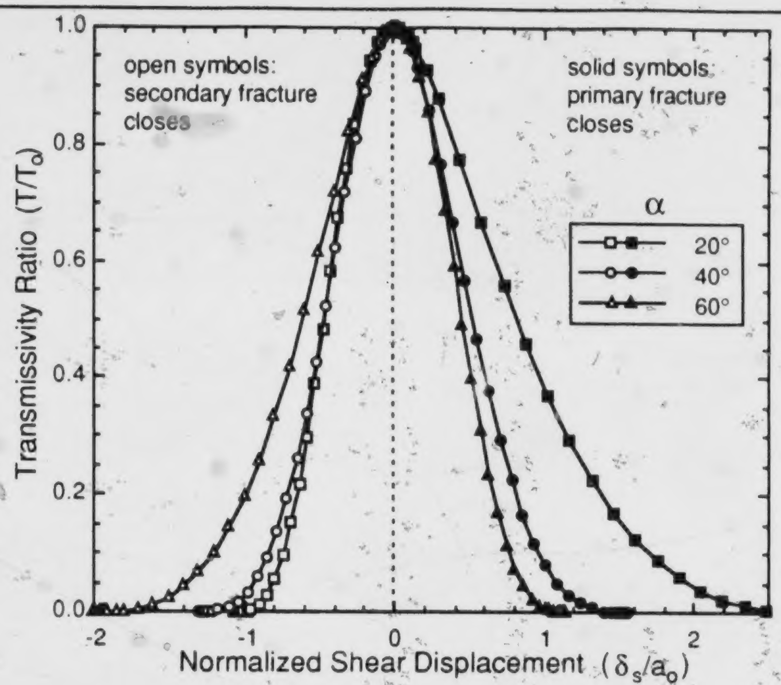

Figure 3.5 Effect of shear direction on transmissivity

3.5.3 Initial Ratio of Primary to Secondary Fracture Aperture

The shear direction is only important if the initial apertures of the primary and secondary fractures are not equal. Figure 3.6 presents the transmissivity ratios for three different initial configurations of fracture zone structure. The transmissivity is plotted against shear displacement which is normalized by the initial primary fracture aperture. The orientation of the primary fracture (α) was set at 20° and the secondary fractures were perpendicular to the primary fracture for all three cases. However, the ratio of initial primary aperture to initial secondary fracture (a_p/a_s) was varied from 1 to 4. The secondary fractures control the overall fracture zone transmissivity when their apertures are small relative to the primary fractures. The striking change in fracture zone transmissivity (either increase or decrease) at small shear displacements reflects primarily, the change in aperture of the secondary fractures. For example, if the aperture ratio is large ($a_p/a_s = 4$) and the shearing is such that the secondary fractures open, the increase in secondary fracture apertures greatly dominates the decrease in primary fracture apertures in terms of the net increase in the fracture zone transmissivity. Naturally, after a certain amount of shear, the primary fracture apertures become smaller than the secondary fracture apertures. Therefore, as the primary fracture approach full closure they take over control of the fracture zone transmissivity.

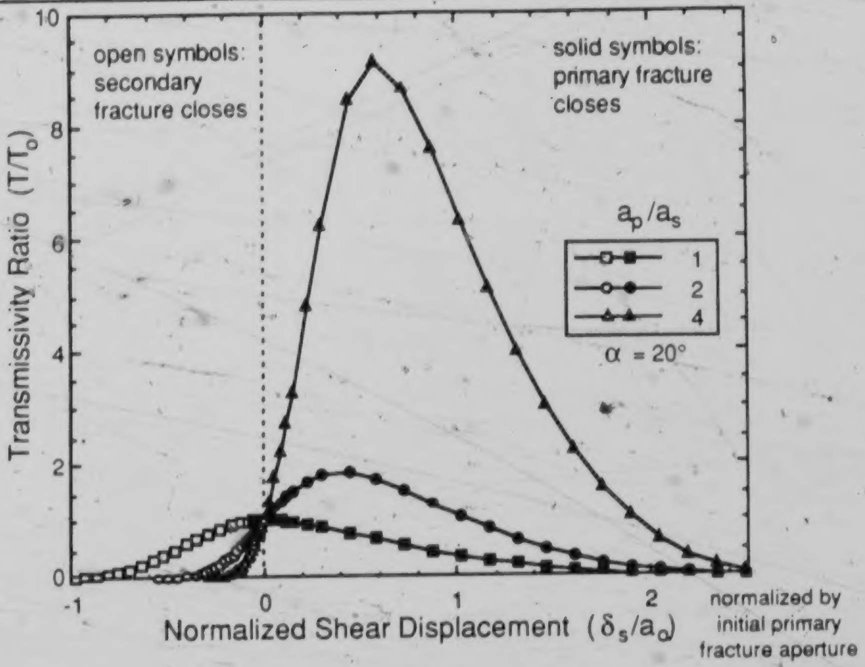

Figure 3.6 Effect of aperture ratio and shear direction on transmissivity

The peak or highest transmissivity ratios for the curves in Figure 3.6 occur when the apertures of the primary and secondary fractures become equal due to shear.

3.5.4 Angle Between Primary and Secondary Fractures

The secondary fractures were assumed perpendicular to the primary fractures in the previous examples. Figure 3.7 presents the transmissivity ratios for a fracture zone with a variable angle between the secondary fracture and the primary fracture (ψ = 60° to 120°). The orientation of the primary fracture was α = 20° and $a_p/a_s = 1$. This figure shows that Equation 3.13 is insensitive to ψ while the secondary fracture is oriented within ± 30° of the perpendicular to the primary fracture and the primary fracture closes during shear. For shear in the other direction, the transmissivity only becomes sensitive for angles near 60°.

A comparison of the curves in Figure 3.7 to those in Figures 3.5 and 3.6 suggests that realistic angles between primary and secondary fractures have less control over fracture transmissivity than do shear direction and aperture ratio. At angles greater than 120°, the length of the secondary fracture gets disproportionately large compared to the length of the primary fractures and hence, becomes unrealistic for natural fracture zones. Similarly, angles (ψ) less than 60° imply non-typical fracture zone geometries.

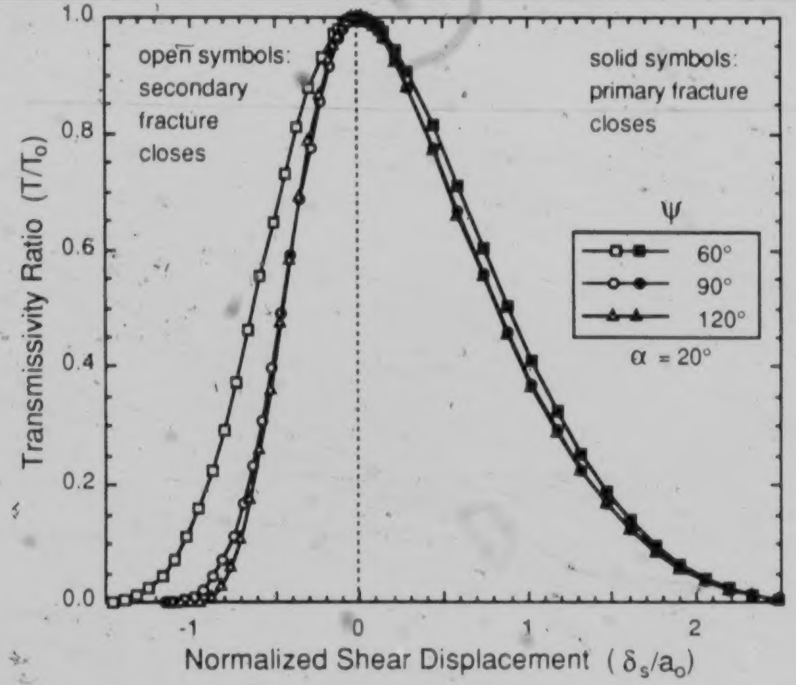

Figure 3.7 Effect of angle between primary and secondary fractures on transmissivity

3.5.5 Initial Aperture Ratios in Natural Fracture Zones

The assumed initial fracture zone structure largely controls the form of the transmissivity - shear displacement relationship and the starting point on the curves presented in Figures 3.4 to 3.7. This thesis introduces a hypothesis for the reduction in transmissivity with shear displacement. If the initial aperture ratio is not unity, Figure 3.6 appears to contradict this hypothesis by indicating that large increases in transmissivity may be just as probable as reductions depending on the direction of shearing. However, the flow conditions in a naturally occurring fracture zone establish, with geologic time, flow channels which are the most efficient system possible for a given fracture zone structure. This is accomplished by solution processes which increase the size of flow channels where sufficient flow exists while mineral deposition blocks channels where the flow rate is small. Therefore, flow through a natural, undisturbed, fracture zone is likely to establish with time, an initial condition where the cross-sectional areas of flow through the primary and secondary fractures are approximately equal. This condition corresponds to the highest point on the transmissivity - shear displacement curves. Any slight disturbance of this flow system, by shear in any direction, would reduce the transmissivity of the fracture zone system.

3.6 Conclusions

Relationships between shear displacement and transmissivity change have been presented and discussed. These equations may now be placed in a suitable overall perspective. Equation 3.13 is intended to reflect a first order approximation of the relationship between shear displacement and fracture zone transmissivity. It is based on a conceptual or phenomenological fracture flow model. The fracture zone flow model shown in Figure 3.3 must not be viewed as a physical model since it does not account for the difference between transverse and longitudinal flow and shear in one direction was assumed to cause the same transmissivity decrease in all directions (isotropic transmissivity change). The important phenomenon it predicts is the reduction in fracture zone transmissivity with increasing shear displacement. Although the channelled nature of flow in natural fractures is well recognized, the choice of a parallel plate model for fracture flow when combined with Equation 3.13 still captures the important aspect of channel pinching or cut-off during shear via the reduced apertures.

The fracture flow model may also be used to derive a relationship between normal fracture zone displacements and transmissivity. However, the model was chosen explicitly to represent the phenomenon of shear-induced transmissivity reductions. Without a careful assessment of the influence of normal stresses on fracture zone transmissivity it is not known whether the same model would adequately describe the observed responses to changes in normal stress.

The shear - transmissivity relationship allows recoverable transmissivity changes. A reverse in the direction of shearing would cause a decrease in the net shear displacement and hence, a recovery in transmissivity as predicted by Equation 3.13. The transmissivity would recover to the initial value as the net shear displacement reduced to zero. Continued shearing would again lead to a transmissivity decrease after the initial conditions had been reached.

The proposed relationship between shear and transmissivity is most valid in situations where the shearing does not approach the peak strength of the fractures. Consequently, the flow model is most appropriate for elastic fracture zone responses. The restriction to pre-peak fracture behaviour allows an elastic finite element joint model to adequately represent the fracture zone hydraulic response. If shearing were to continue in a real fracture zone model then dilation may eventually dominate the hydraulic response. A shear-transmissivity relationship restricted to pre-peak fracture behaviour may, initially, appear to limit the usefulness of such a relationship. This may be true when applied to the interpretation of laboratory shear tests on single fractures. Typical direct shear test results show that the pre-peak behaviour occurs over a limited (small) range of shear. However, most direct shear tests reported in the literature are primarily concerned with peak and post-peak fracture behaviour and shear displacements of 10's of millimetres are imposed on the rock specimens. In these situations, dilation probably dominates the hydraulic response in the fracture. Fortunately, many underground openings situated in crystalline rock (nuclear waste repositories, tunnels, liquid and solid storage facilities, and shallow mines) never exceed the yield strength of the rock or rock fractures. In these environments, shear displacements are small and in the pre-peak range. Essentially elastic behaviour dominates the excavation response. Fracture dilation does not control the hydraulic response and hence, the theory offered here should provide an explanation for observed hydraulic responses in some fracture zones intersected by excavations (see Section 5).

4 FLOW FROM A FRACTURE ZONE INTO A CIRCULAR OPENING

Excavation through a water-bearing fracture zone causes stress redistribution around the opening, induces shear displacements, and alters the hydraulic boundary conditions. A series of numerical simulations were performed to assess the effect of model parameters on transmissivity distributions and changes in boundary conditions on the flow and pressure distributions around a circular opening. In all cases, the fracture zone was assumed perpendicular to the axis of the opening (Fig. 4.1). The opening could be a vertical shaft with a horizontal fracture zone or a tunnel through a vertical fracture zone. These simulations used two different 2-D finite element models which represented the fracture zone and were designed to examine the influence of the following factors: 1) the relative importance of the fracture zone geometric parameters; 2) the influence of fracture orientation with respect to the assumed direction of shearing; 3) the effect of axisymmetric versus non-axisymmetric shear displacement distributions; 4) the hydraulic response of a fracture zone to changes in flow boundary conditions; and 5) the hydraulic response of the fracture zone to simulated fluid withdrawal (pumping) tests.

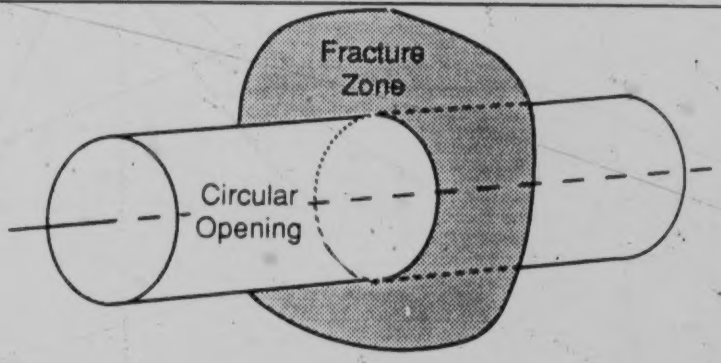

Figure 4.1 Fracture zone perpendicular to the opening axis

4.1 Shear Displacement and Transmissivity Determination

For the finite element seepage simulations, the transmissivity of the fracture zone and its dependence on shear was established in Section 3. The parameters describing this relationship were based on the idealized geometric model for shear-displacement induced transmissivity changes in a fracture zone. The internal fracture geometry defines the shear displacement - transmissivity change relationship (Eqn. 3.13). For the following simulations, the primary and secondary fractures were assumed to have the same initial apertures.

Having established a relationship between shear displacement and transmissivity change, the shear displacements were required. The Kirsch solution for radial displacements around a circular opening (Appendix D) was used to estimate shear displacements in the fracture zone. Displacements from the Kirsch formulae approximate the situation when an excavation proceeds to the point where it just intersects a fracture zone (lightly shaded part of excavation in Figure 4.1). The rock around the opening responds to the stress relief and if the shear stiffness of the fracture zone is relatively soft then the rock displacement on the excavated side of the fracture zone can be approximated by the Kirsch solution. If the rock ahead of the fracture zone is assumed to remain rigid (because it still fully supported by the unexcavated rock), then the Kirsch displacements may be taken as the shear displacements in the fracture zone. These shear displacements would represent an upper limit on shear displacements induced by the excavation. If the excavation advanced past the fracture zone the shear displacements would reduce towards zero. Obviously, this assumption neglects the three-dimensional face effects and the influence of the fracture zone itself on the displacement and stress distributions. (More realistic shear displacement distributions, obtained from three-dimensional finite element analyses, are used for the specific case study presented in Section 5.)

Kirsch's equation generates a strongly non-linear distribution of displacements (Fig. D.1, Appendix D). The shear displacements were converted to transmissivities by application of Equation 3.13. The displacements corresponding to the location of the nodes in the finite element mesh were averaged for each element and then the average displacement was used to calculate the elemental transmissivity. The change in transmissivity at each point in the fracture zone was assumed isotropic, i.e., shear in any direction at a point causes equal transmissivity reduction in all directions at that point. Therefore the two principal transmissivities required by the seepage program for each element were always equal.

4.2 Quarter Mesh Results

Different finite element models were built to explore the various factors introduced earlier. A 2-D quarter-mesh (Fig. 4.2) was designed to model a fracture zone oriented perpendicular to the axis of the opening (Fig. 4.1). This mesh was used to investigate the effects of: 1) the orientation of the primary fractures in a fracture zone; 2) the magnitude of shear displacement; 3) the shear direction dependency of the relationship between shear displacement and transmissivity change; and 4) the effect of both axisymmetric and non-axisymmetric shear displacement distributions on the fracture zone seepage.

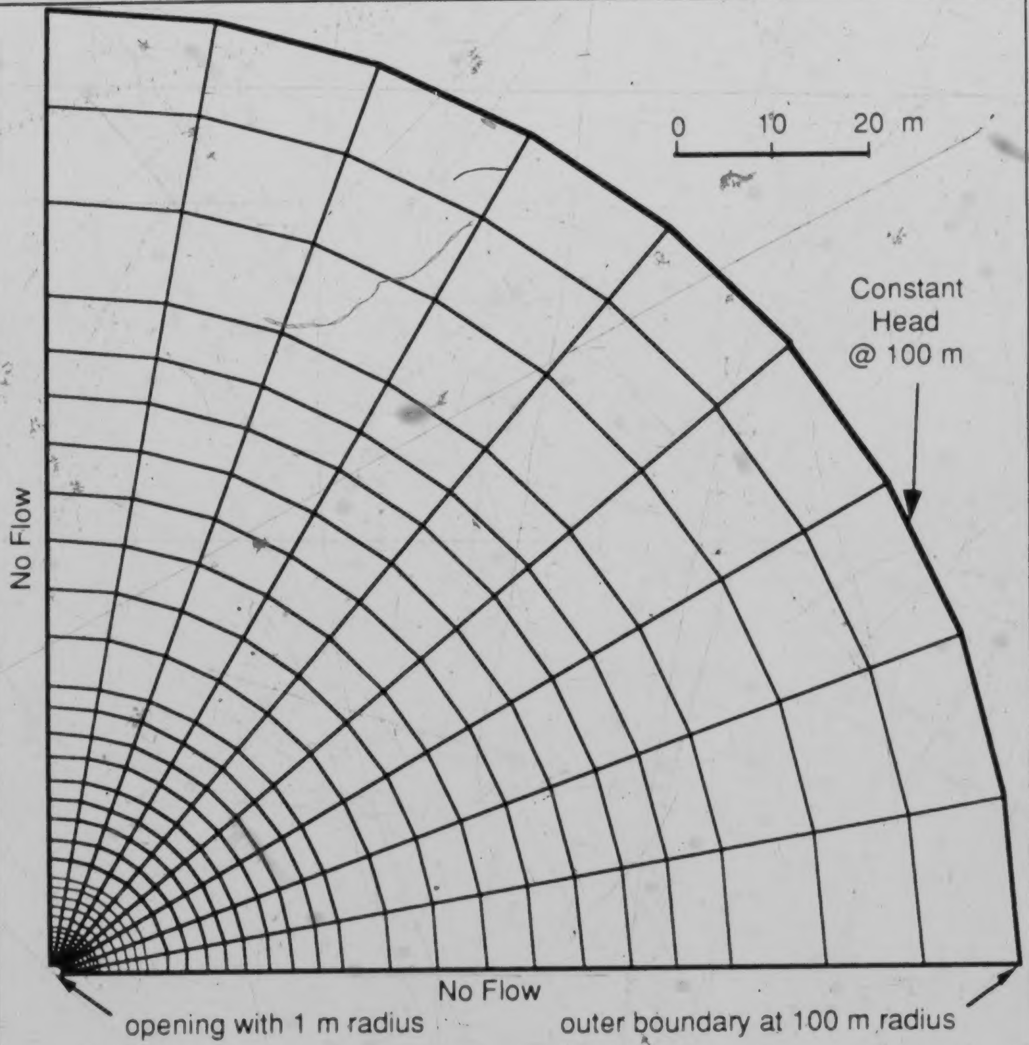

Figure 4.2 Quarter-mesh and boundary conditions

The mesh was constructed with 306 four-noded elements and 350 nodes (Fig. 4.2). The finite element program SEEP (Taylor and Brown, 1967; Kealy and Busch, 1971; Guther, 1972) was used to calculate the heads and flows. The program was run on a Macintosh II computer with 5 Megabytes of RAM. SEEP uses constant velocity elements in its formulation. Therefore, each element was automatically broken into four triangular elements by the finite element program before solving for the nodal heads. Each element was associated to a unique transmissivity set. Different transmissivity distributions in the mesh were created by changing the 306 different transmissivity sets to values specified by the shear-transmissivity relationship.

Since a two-dimensional finite element model was adopted to calculate flows and steady-state fluid pressures in a fracture zone with varying apertures, elemental hydraulic conductivity terms were replaced with transmissivity values which reflect both the changes in permeability and fracture aperture. The results from the modelling are presented using dimensionless parameters.

4.2.1 Constant Transmissivity Solution

A finite element simulation of radial flow into a circular opening through a fracture zone with constant transmissivity served as a base case. The opening has a radius of unity and is oriented perpendicular to the fracture zone. The boundary conditions are zero pressure at the opening and 100 % head at 100 radii from the axis. These fluid boundary conditions are an approximation for a tunnel and are correct for a vertical shaft.

The steady-state pressure distribution is presented in Figure 4.3 and compared with a closed-form solution. The boundary conditions create radial flow conditions. As the fluid approaches the opening, it is confined into a smaller and smaller area and this constriction in flow leads to larger flow gradients near the opening. The results of the numerical modelling and the closed-form solution (Appendix E) match well for this case (Fig. 4.3).

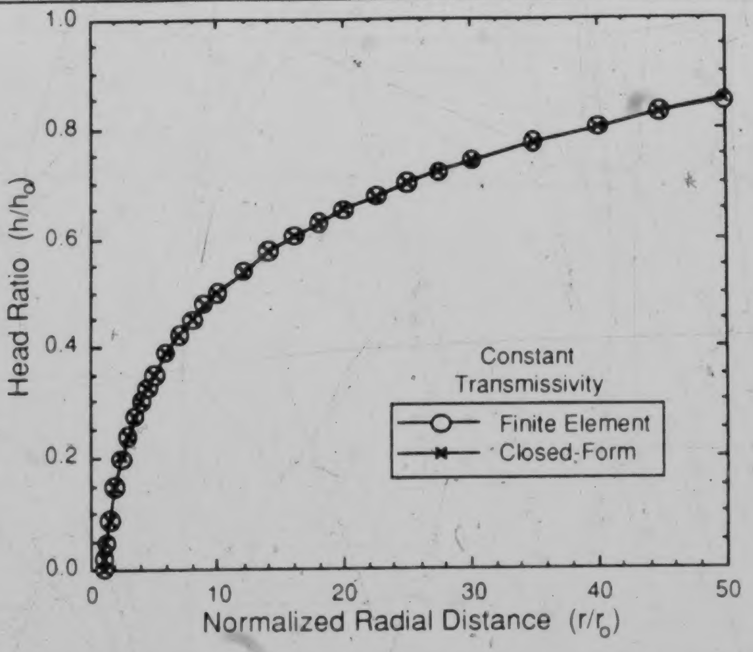

Figure 4.3 Head profile for constant transmissivity case

4.2.2 Effect of Internal Fracture Zone Structure

A series of finite element simulations were done assuming a hydrostatic stress field and an isotropic transmissivity response in the fracture zone. The isotropic transmissivity response implies that a given shear displacement in any direction causes the same transmissivity decrease, i.e., the transmissivities in any direction are independent of the fracture zone geometry. But since the shear displacement - transmissivity relationship was based on the internal geometry of the fracture zone, the magnitude of the transmissivity change at any point was governed by the internal fracture zone geometry.

The secondary fractures were assumed perpendicular to the primary fractures and hence, any change in the orientation of the primary fractures results in a corresponding change in the orientation of the secondary fractures. The primary fractures were angled at 20°, 40°, and 60° to the plane of the fracture zone (Fig. 3.3b). Hence, a different relationship between shear and transmissivity change was used for each set of runs.

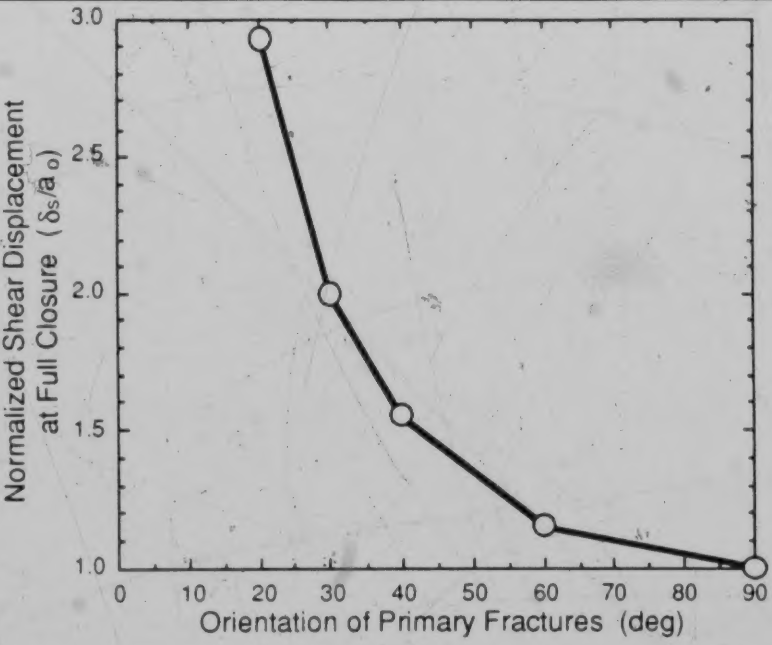

Figure 4.4 Shear displacement at full fracture closure versus primary fracture orientation

To facilitate comparison of results, the seepage simulations were performed such that the shear displacement ratios (the ratio of shear displacement to maximum shear displacement allowable before complete fracture closure, δ_S/δ_C) at the opening wall were equal for each fracture zone geometry. The shear displacement required to completely close the fracture at the wall, henceforth called the maximum shear displacement (δ_C), depends on the inclination of the fractures in the fracture zone relative to the direction of shearing. Shearing was assumed to cause primary fracture closure regardless of the orientation of the fracture zone with respect to the direction of shearing (isotropic response assumption). Figure 4.4 shows that fracture zones with low primary fracture orientations (small α) need more shear displacement to close than do fracture zones with steeply inclined fractures.

For the following set of analyses shear displacement ratios (δ_S/δ_C) of 0.3, 0.55, 0.75, and 0.9 were arbitrarily chosen. These were obtained by varying the ratio,

$$\frac{\sigma(1+\nu)}{2E}\ r_o/a_i \qquad [4.1]$$

which is found in the Kirsch formulae (Appendix D). Three fracture zone geometries were also analysed. Primary fractures were assumed oriented at 20°, 40°, and 60°, thereby giving three different shear - transmissivity relationships.

Figures 4.5a, b and c present the shear displacement distributions normalized by the maximum shear displacement. These shear displacements were then transformed into transmissivity changes using the proper relationship for each fracture orientation (Eqn. 3.13). Transmissivity profiles for the three different shear - transmissivity relationships are presented in Figures 4.5d, e and f. The shear displacements create concentric rings of rapidly decreasing transmissivity near the opening. These transmissivities were used in the finite element seepage program to produce the normalized head distributions shown in Figure 4.6. The axisymmetric transmissivity distributions resulted in purely radial flow. The fluid pressures reach steady-state equilibrium with high magnitudes and high pressure gradients near the opening. Flow rates into the opening decrease rapidly under increasing shear displacement as seen in Figure 4.7.

The angle of the primary fractures affects the shear displacement - transmissivity relationship. Therefore, the fracture zone geometry (for the idealized fracture-zone model) controls the rate of transmissivity reduction and hence, also influences the rate at which flow decreases with increasing shear. However, the nonlinearity of the shear displacement versus transmissivity change relationship (Eqn. 3.13) has much less effect on the seepage than does the strongly nonlinear shear displacement versus radial distance relationship (Kirsch) which was adopted for these simulations.

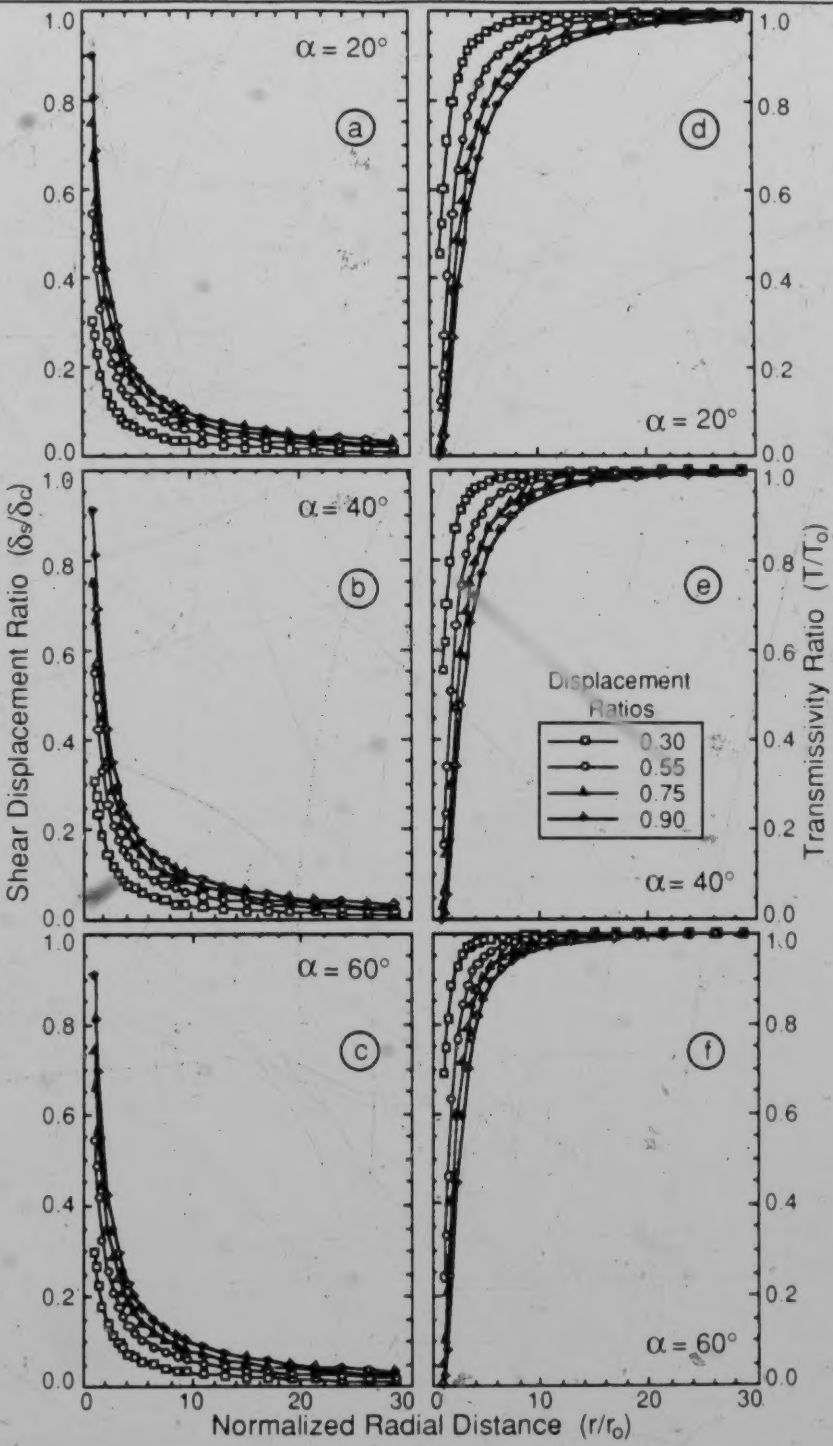

Figure 4.5 Shear displacement and transmissivity profiles for varying amounts of shear and hydrostatic stress conditions

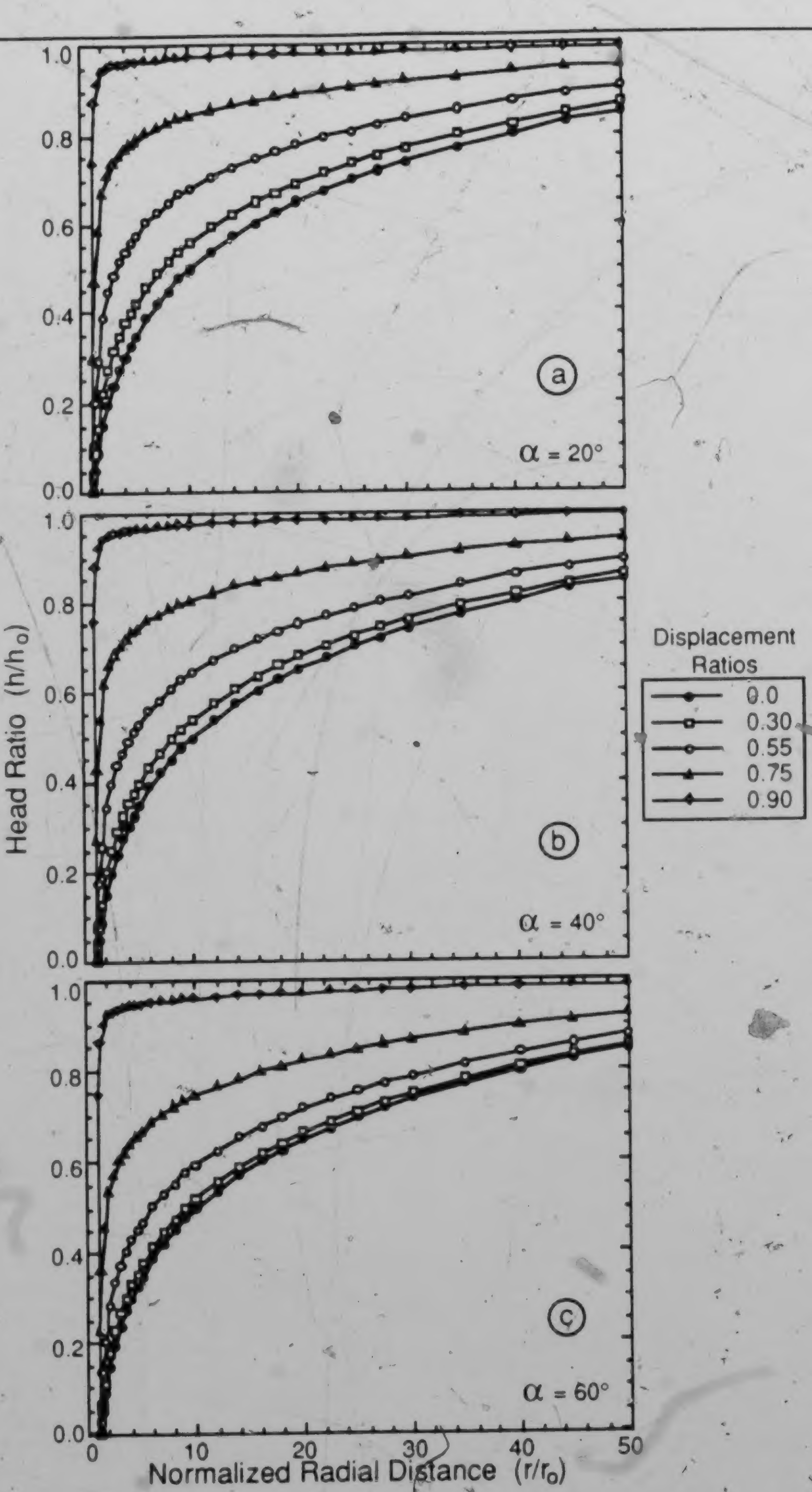

Figure 4.6 Head profiles for fracture zones with varying shear and different primary fracture orientations under hydrostatic stress conditions

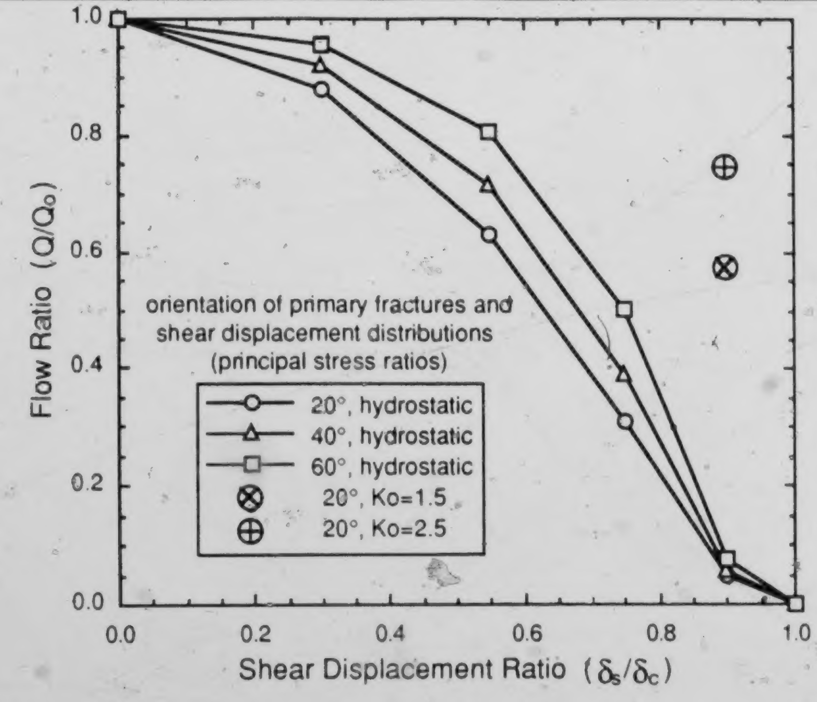

Figure 4.7 Effect of fracture zone geometry and shear displacement distribution on flows into a circular opening

4.2.3 Effect of Non-Axisymmetric Shear Displacement Distributions

The shear displacements used in the previous seepage analyses were based on Kirsch's equation with the principal stress ratio, $K_o = 1$. In this sub-section, K_o was varied to assess the influence of non-axisymmetric shear displacement distributions on the hydraulic response in a fracture zone. As before, the shear - transmissivity change relationship was assumed isotropic, but only one fracture zone geometry was selected. The angle of the primary fractures, α was 20°. K_o was arbitrarily set to 1.5 and 2.5 and the shear displacements were chosen such that the maximum shear displacement ratio was 0.9 at the excavation boundary. Consequently, the shear displacement ratio was less than 0.9 everywhere except at two points at the opening wall. Note that when $K \neq 1$, both radial and tangential displacements are generated. The maximum displacement (vector sum of the radial and tangential displacements) was used in the shear - transmissivity change relationship instead of just the radial displacements.

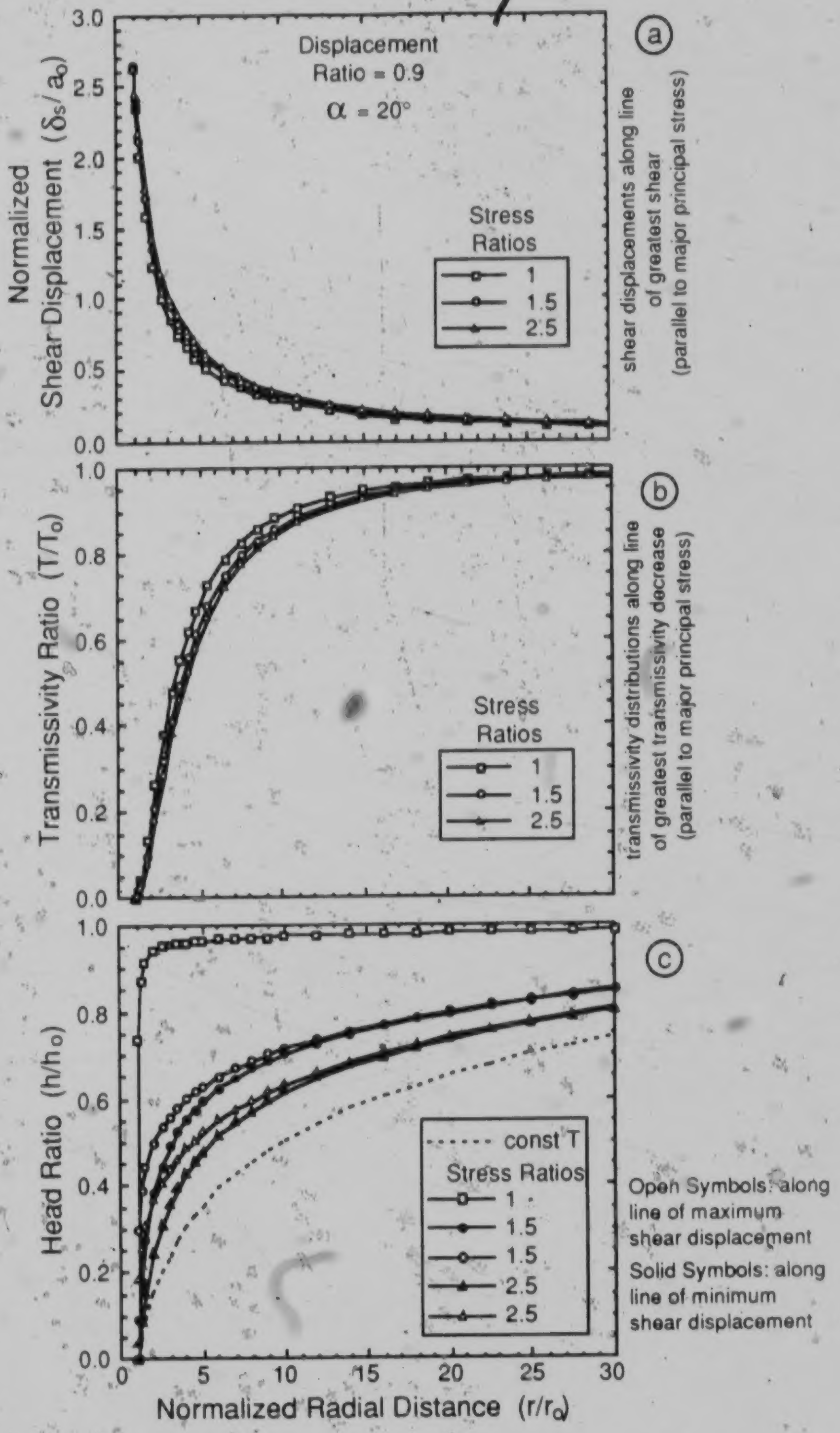

Figure 4.8 Effect of shear distribution on transmissivity and resulting head profiles

The shear displacement and transmissivity profiles (Figs. 4.8a and 4.8b) in the radial direction of the major principal stress are very similar for all three stress ratios. This is expected since the shear displacements along this line occur only in the radial direction and they were scaled by adjusting Equation 4.1 to ensure that shear displacement ratio was 0.9 at the tunnel wall. In other radial directions the shear distributions and hence, the transmissivity distributions vary greatly. The shear displacement is at a minimum parallel to the minimum principal stress. For $K_o > 1$, the shear displacements parallel to the minimum principal stress are smaller than those parallel to the maximum principal stress. For example, the maximum ratio of shear displacements near the opening are 1.6 for K_o = 1.5 and 18.4 for K_o = 2.5.

Head profiles along lines with the greatest extremes in shear displacements and transmissivities (for K_o = 1, 1.5, and 2.5) are shown in Figure 4.8c and are compared to the constant transmissivity case. Only a minor deviation from K_o = 1, i.e., K_o = 1.5 leads to a tremendous change in head distributions. The non-axisymmetric shear distributions for $K_o \neq 1$ lead to a non-axisymmetric transmissivity distribution which concentrates the flow into areas of higher transmissivity. These 'gaps' in the low transmissivity ring created by the non-axisymmetric shear displacement distribution have a dominant control over the seepage pattern. The head gradients are much lower near the opening and the inflows are higher.

The flows into the opening for a fracture zone with $\alpha = 20°$ and shear displacement ratio = 0.9 for K_o = 1.5 and 2.5 is plotted on Figure 4.7. The flow is very sensitive to the change from an axisymmetric (K_o = 1) to non-axisymmetric ($K_o \neq 1$) transmissivity distributions. The lack of continuity in the rings of low transmissivity around the opening leads to much higher inflows.

4.3 Circular Mesh Results

A full, circular mesh was built to model a fracture zone oriented perpendicular to the axis of a circular opening (Fig. 4.1). As before the opening can represent either a tunnel or a shaft. This model was used to investigate the hydraulic response inside a fracture zone in reaction to: 1) the drilling of a single and several free-draining boreholes; 2) simulated fluid withdrawal (packer) tests; 3) changes in flow boundary conditions; and 4) a low transmissivity ring around the opening. The specific effects due to shear displacements were not examined in this series of numerical simulations.

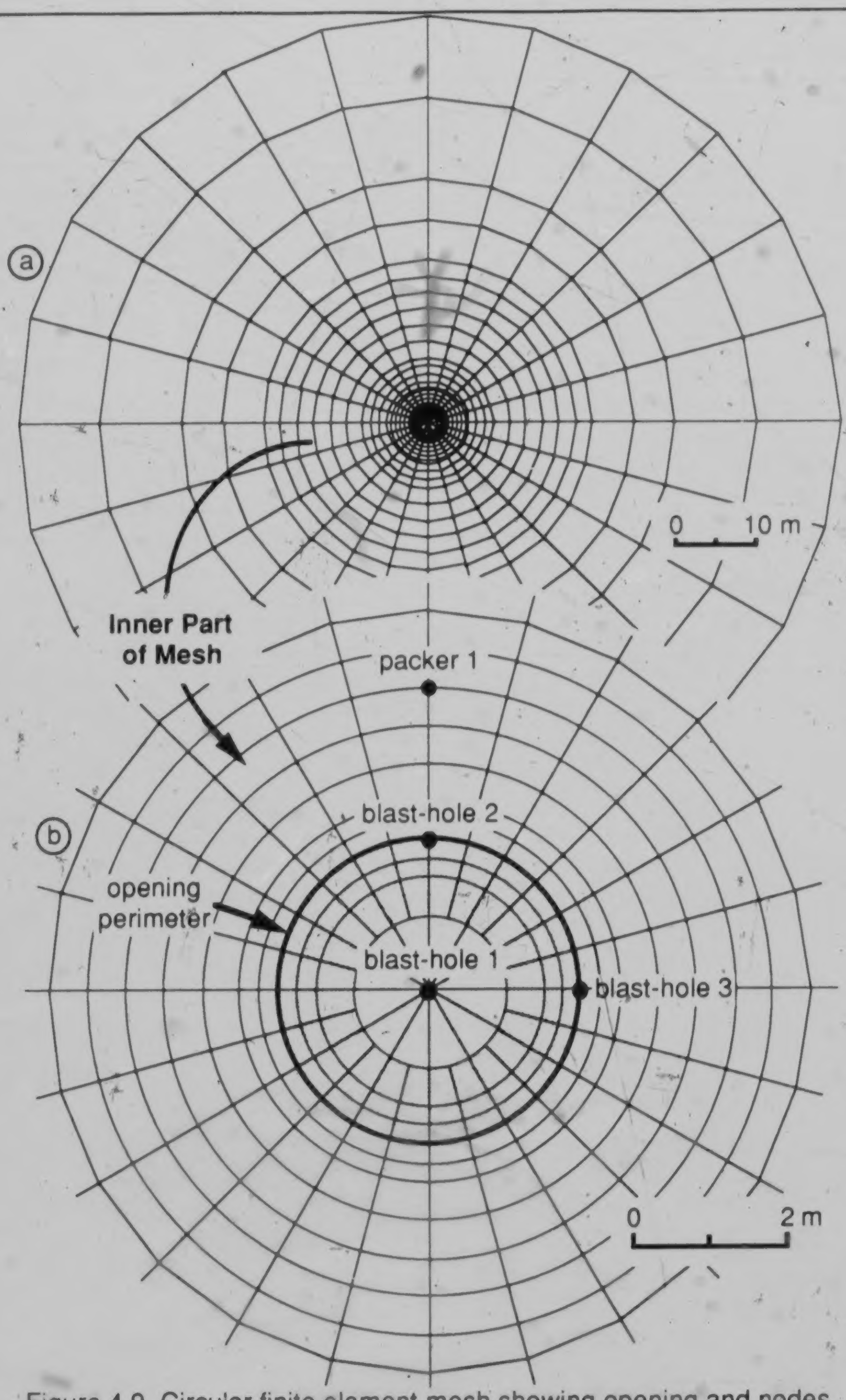

Figure 4.9 Circular finite element mesh showing opening and nodes representing blast-holes and packer

The circular mesh was constructed with 564 four-noded quadrilateral elements employing 577 nodes (Fig. 4.9). The mesh has an outer boundary at a radius of 50 m and the opening has a radius of 2 m. The head at the outer boundary was fixed at 100 m. An isotropic fracture-zone transmissivity of 6.2434 x 10^{-7} m^2/s was adopted. This transmissivity corresponds to an equivalent fracture aperture of 100 μm (assuming a parallel plate model). The modelling was conducted with SEEP on a Macintosh II computer.

Pumping tests were simulated by specifying either head drops at, or flow quantities from, a single node representing a packed-off borehole location. Similarly, free-draining boreholes intersecting the fracture zone were represented by a node with zero head. Only steady-state hydraulic responses were examined. The use of a single node to represent a borehole is convenient but the results are mesh dependent. A mesh which is fine near the node representing the borehole yields different results than a coarser mesh. If the mesh is very fine near the borehole location, then a borehole can be modelled with zero head (pressure) boundaries on the sides of the elements which surround the borehole in a manner similar to the much larger opening itself. However, this would lead to a much larger finite element mesh and the computational effort would approach the capacity of the computer. Furthermore, this series of simulations is only concerned with the general effects of boreholes and fluid withdrawal tests on the head and flow responses in a fracture zones. Therefore, a single node representation of a borehole location was judged appropriate.

4.3.1 Interpretation of Q/ΔH Measured from Packer Tests

Packer tests can provide valuable information on the changes in hydraulic behaviour as an excavation intersects and proceeds past a fracture zone. Both transient and steady-state testing may be performed in packed-off intervals of boreholes. The use of transient methods potentially provides more information including compressibility effects in the borehole, non-linear flow effects, influence of boundaries, and the influence of conductivity changes near the borehole due to drilling. However, to extract more information from the transient tests more complex equations and additional assumptions and parameters are needed. Steady-state packer test data are easier to interpret and provide a measurement of hydraulic conductivity or transmissivity which is as accurate as that obtained from transient test data. Reviews of packer test design, data interpretation, and sources of error are given by Grisak et al. (1985) and Doe et al. (1987). Steady-state packer tests measure the ratio of flow to head drop, Q/ΔH. Transmissivity is given by:

$$T = C_s \, Q/\Delta H \qquad [4.2]$$

where C_S is a shape factor which varies depending on the flow geometry. For steady-state, radial, laminar flow with a constant pressure boundary at a radius R, from the packed-off borehole of radius r_O, the shape factor is:

$$C_s = \frac{1}{2\pi} \ln(R/r_o) \qquad [4.3]$$

The radius to the constant pressure boundary or reach (R) is never precisely known (except for numerical models). However, since R appears as a logarithmic variable, large variations in R result in only small changes in T. For example, with a HQ borehole (r_O = 4.8 cm), varying the reach from 15 to 150 m only increases the calculated transmissivity by a factor of 1.4. This variation is insignificant compared to the many orders of magnitude that transmissivities typically vary.

Hydraulic conductivity and fracture aperture may be calculated from the transmissivity after making assumptions the nature of flow. For example, using the parallel plate model for flow, the fracture aperture and hydraulic conductivity may be calculated from Equation 4.2 by using Equations 3.2 and 3.3.

Steady-state packer testing at Room 209 showed decreases in Q/ΔH after the tunnel was excavated through the fracture zone (Fig. 1.2a; see also Section 5). A permeability or transmissivity decrease was assumed responsible for the measured drop in Q/ΔH (Lang et al., 1987b). However, the tunnel alters the hydraulic boundary conditions and these changes were not considered in the interpretation of the measured Q/ΔH. Changes in flow pattern due to the presence of the tunnel effectively alter the shape factor (C_S) in Equation 4.2. Before drops in Q/ΔH can be conclusively attributed to transmissivity decreases it is essential to determine whether C_S increases or decreases due to boundary condition changes. The following sub-sections address the influence that changes in boundary conditions and changes in transmissivity distribution have on the flow into an opening and the 'measured' Q/ΔH at packer locations.

4.3.2 Seepage Simulations with a Constant Transmissivity Distribution

4.3.2.1 Response to Borehole Drilling and Excavation

A series of computer runs was done to assess the fracture zone response to several boreholes penetrating the fracture zone before the opening had been excavated. The boreholes within the planned excavation perimeter represent holes drilled for blasting purposes while those outside the perimeter are those used for packer tests. Figure 4.9b shows the inner portion of the mesh, the perimeter of the opening, and the location of nodes representing both types of boreholes.

Figure 4.10a presents the normalized head (h/h_o) profiles near the opening for four situations: 1) a single free-draining hole (blast-hole 1) at the centre of the mesh; 2) a second free-draining hole (blast-hole 2) at the perimeter of the mesh; 3) a third free-draining hole (blast-hole 3) at the perimeter of the mesh; and 4) a fully excavated opening. The free-draining blast-holes were modelled by specifying zero head at the node representing the blast-hole. The head profiles are taken along a radial line passing through blast-hole 2 and packer 1. The heads are normalized by the fixed head (h_o) present at the outer boundary. The flows from the blast-hole nodes calculated from the elemental flows and the total inflow to the opening are shown in Figure 4.11. The flow into the excavation calculated from the finite element program (1.22×10^{-4} m^3/s) is equal to the flow calculated from the closed-form solution. Note that just three blast-holes account for 76 % of the total final flow into the opening.

As a check on the finite element seepage program, instead of specifying zero head at a blast-hole node, flow was specified and the resulting head at the node calculated by the program. The head at a node is extremely sensitive to the specified flow. However, the flow which corresponds to zero head was essentially the same as determined when the head was specified.

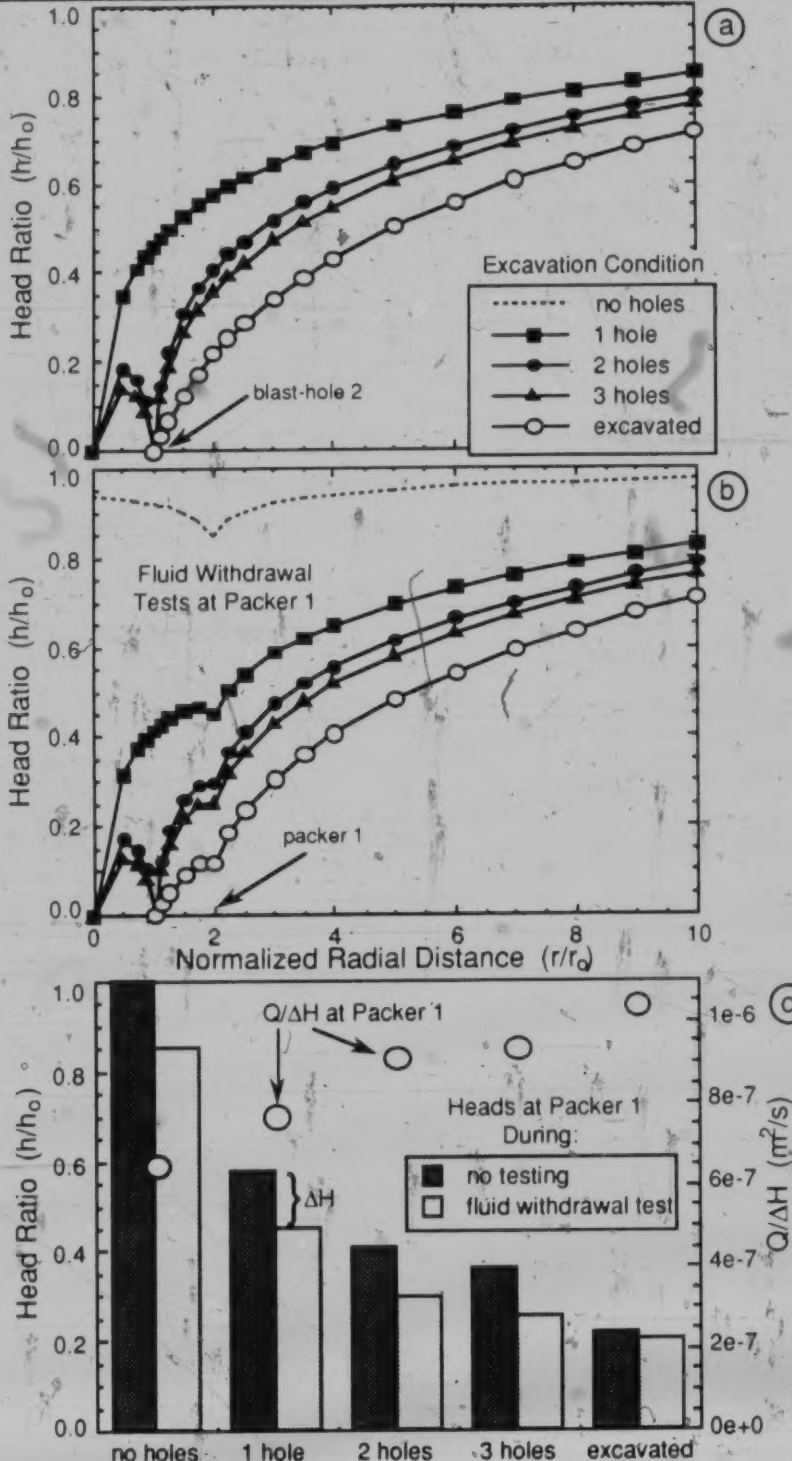

Figure 4.10 Head profiles after excavation of blast-holes and opening and during packer testing plus values of Q/ΔH from the packer tests

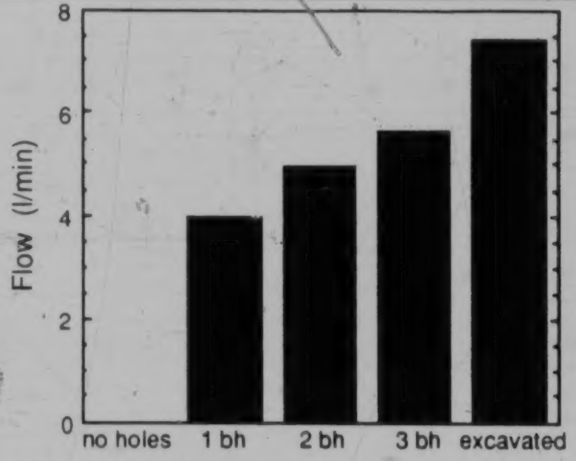

Figure 4.11 Flows into blast-holes and excavated opening

Closed-form solutions (Appendix E) may be compared with the results from the single borehole at the centre of the mesh. Knowing the flow from the node at a prescribed head drop, the 'effective radius' of the borehole represented by the node can be calculated. With the given boundary conditions and fracture zone transmissivity, the flow from the single borehole was 6.61×10^{-5} m^3/s. Using the closed-form solution for radial flow (Eqn. E.3) yields an effective borehole radius of 13 cm. As noted earlier, the use of a single node to represent a borehole is mesh dependent and so is the effective radius of a borehole at the node. Although the radius for this 'nodal' borehole is larger than most typical boreholes, it is still not an unreasonable dimension.

4.3.2.2 Effect of Blast-holes and Excavation Opening on Simulated Fluid Withdrawal Tests

Numerical simulations of fluid withdrawal (packer) tests were performed at the 'packer 1' location for drainage conditions with: zero, one, two, and three blast-holes. A packer test was also conducted for the fully excavated opening. The fluid withdrawal tests were done by specifying negative flows at the nodes representing the packer locations. Fluid withdrawal causes a head drop at the packer location. By repeating the analysis with different magnitudes for the flow, the relationship between flow and head drop was shown to be perfectly linear, as expected from the following relationship for radial flow into a well:

$$Q = 2\pi T \frac{\Delta H}{\ln(R/r)} \quad \text{or} \quad \frac{Q}{\Delta H} = \frac{2\pi}{\ln(R/r)} T = constant \qquad [4.4]$$

The value of Q/ΔH is essentially a measure of transmissivity. Another simulation with the head at the outer boundary reduced to 50 m showed that the ratio Q/ΔH is independent of the head at the outer boundary although the percentage head drop at a packer location does depend on the head at the outer boundary.

The influence of blast-holes and the opening on the response at the packer is shown by the steady-state heads (normalized by h_o) at 'packer 1' (Figs. 4.10b and c). The packer tests were simulated by withdrawing 1×10^{-5} m^3/s of fluid at the packer location. The radial head profiles through packer 1 are shown in Figure 4.10b and values of Q/ΔH, calculated at 'packer 1', are plotted in Figure 4.10c. Figure 4.10c shows that the first borehole causes the largest reduction in head (ΔH) at the packer location while each successive blast-hole has less and less effect. The head profiles during the fluid withdrawal or packers tests are superpositions of the drawdown profiles due to fluid withdrawal at the packer location (dashed curve labelled 'no holes') and the steady-state head distributions shown in Figure 4.10a.

The Q/ΔH ratios in Figure 4.10c demonstrate a most interesting behaviour. Each time an additional blast-hole intersects the fracture zone the value of Q/ΔH increases (circles; right axis). Increases in Q/ΔH under constant boundary conditions would normally signify corresponding increases in transmissivity. However, if the changes in Q/ΔH measured before and after the drilling of blast-holes are interpreted as changes in transmissivity, the interpretation would be in error. The blast-holes and the excavation itself cause a boundary condition alteration and this in turn results in different values for Q/ΔH. Therefore, the interpretation of Q/ΔH values from packer tests must account for both changes in flow boundary conditions and possible transmissivity changes.

The alteration of boundary conditions, by addition of boreholes or a tunnel, changes the flow pattern near a packer such that the shape factor (C_s) in Equation 4.2 decreases. Equation 4.2 implies that measured increases in Q/ΔH after an excavation (or borehole) intersects a fracture zone could be attributed to either boundary condition changes under constant transmissivity conditions or transmissivity increase and boundary condition changes. However, if measurements of Q/ΔH decrease, then the transmissivity must have also decreased. The boundary conditions changes due to additional openings near a packer location can only increase the measured Q/ΔH.

The effect of changed hydraulic boundary conditions on the determination of Q/ΔH at a packer location is also examined using closed-form equations in Appendix F. This

Appendix supports the findings from the finite element simulations that the presence of additional boreholes increases Q/ΔH measured at a borehole.

4.3.3 Rings of Low Transmissivity Around the Excavation

The effect of the proposed shear-dependent transmissivity reduction associated with an excavation through a fracture zone was examined by introducing a ring of lower transmissivity around the opening. A set of runs was performed with a single, low transmissivity ring 0.25 m in width (Fig. 4.12). Transmissivities of 7.8042×10^{-8}, 9.7552×10^{-9}, and 6.2434×10^{-10} m^2/s were arbitrarily assigned to this ring. Using the parallel plate model, these values correspond to fracture apertures of 50, 25, and 10 μm. The dramatic effect of the reduced transmissivity around the opening can be seen in Figure 4.13 by the increase in heads near the opening (Fig. 4.13a) and the reduction in total inflows (Fig. 4.13c).

Packer tests were then simulated at the 'packer 1' location shown in Figure 4.12. The head profiles near the opening for each low transmissivity-ring model are compared with the constant transmissivity case in Figure 4.13b. The presence of the low transmissivity ring reduces the values of Q/ΔH determined at the packer locations with the largest decrease associated with the ring with the smallest transmissivity (Fig. 4.13c).

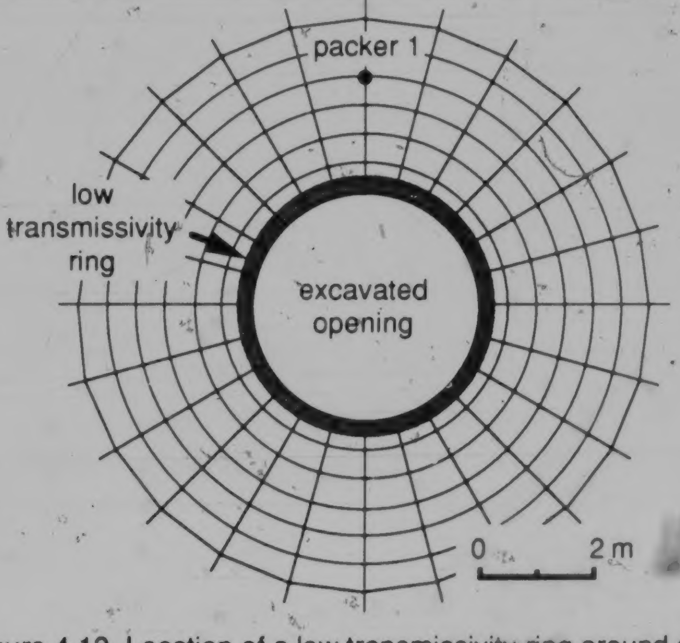

Figure 4.12 Location of a low transmissivity ring around opening

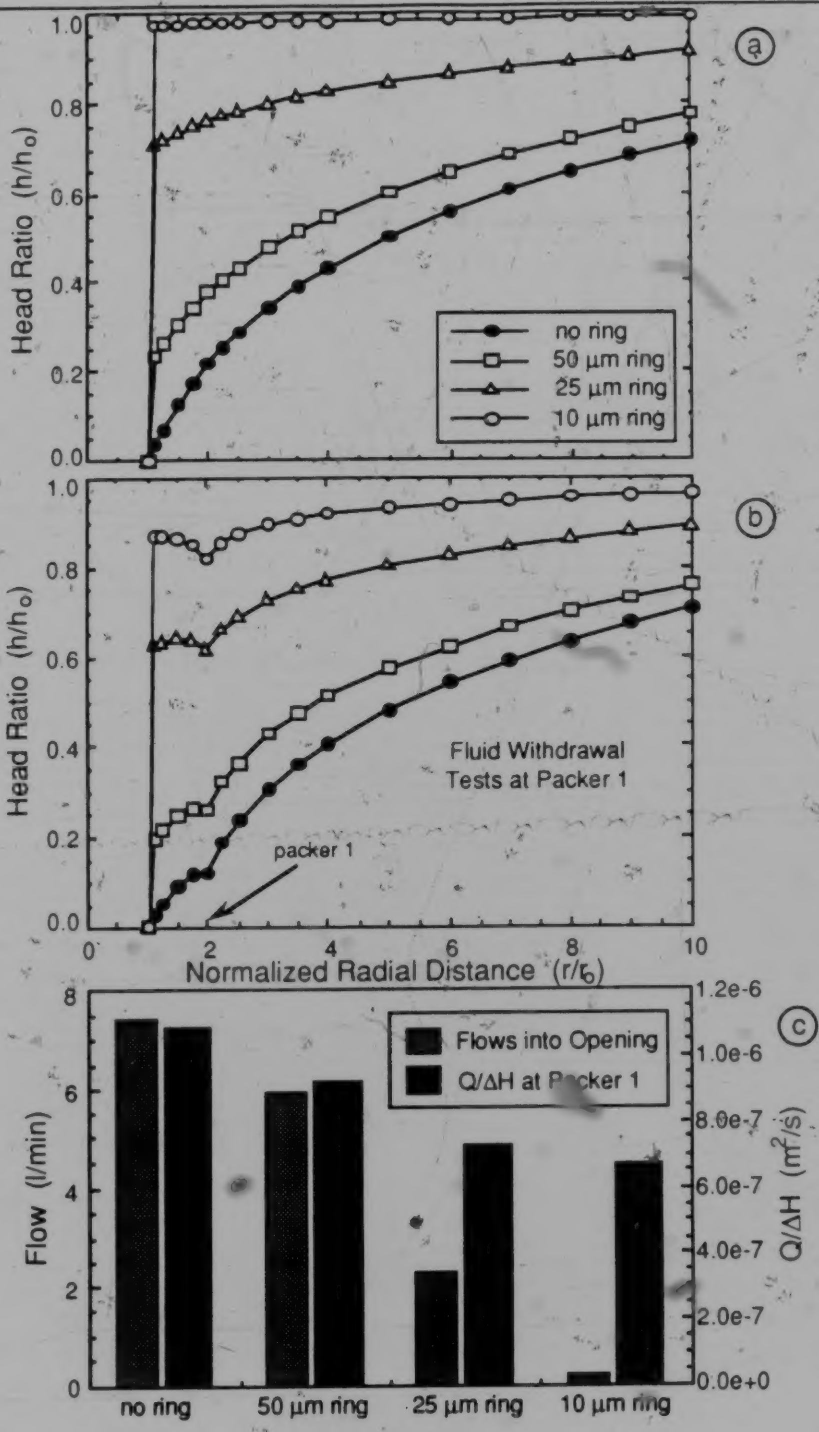

Figure 4.13 Head profiles and inflows for opening with different transmissivity rings and results from simulated packer tests

The seepage analyses presented here have shown that changes in flow boundary conditions and as expected, changes in transmissivity, affect the measured responses at packer locations. Therefore, it is important to differentiate boundary conditions effects from the changes in fracture transmissivity when interpreting values of Q/ΔH determined from fluid withdrawal tests. For example, if the value of Q/ΔH remained constant before and after excavation through a fracture zone, this would not necessarily imply a unchanged fracture zone transmissivity. If the packer location was close enough to the excavation perimeter to be affected by the change in flow boundary conditions, then the value of Q/ΔH would rise because of the boundary condition effect alone. Therefore, to measure a constant Q/ΔH, the transmissivity of the fracture zone must reduce (due to excavation-dependent changes in the fracture zone) to counteract the increase in Q/ΔH caused by boundary condition changes.

4.4 Summary

Two different finite element models were used to assess various factors controlling the hydraulic response in a fracture zone and interpretation of steady-state, packer test data The modelling with the quarter mesh was conducted on the premise that the idealized flow model presented in Section 3 could adequately approximate a fracture zone. The following observations were noted.

1) The internal geometry or more specifically, the orientation of the primary fractures was found to govern the shear displacement - transmissivity change relationship. Geometry also limited the shear displacement that the fracture zone could sustain before the fracture completely closed and the transmissivity reduced to zero.

2) The shear displacement - transmissivity relationship was nonlinear, however the adopted (Kirsch) shear displacements around the opening were strongly nonlinear. Therefore, the shear displacement distribution had a more dominant control over the resultant transmissivity distribution around an opening than did the form of the shear - transmissivity relationship.

3) When non-axisymmetric shear displacement distributions were considered, non-continuous, low transmissivity rings were created. This transmissivity distribution greatly influenced the resulting head profiles and inflows. The steady-state heads and head gradients were much lower near the opening than when a continuous low

transmissivity ring existed around the opening. Furthermore, the flows into the opening were much higher.

4) A very thin, continuous, low transmissivity ring at the opening wall will greatly reduce the flow into the opening and lead to very high head gradients and steady-state heads near the opening.

5) The value of Q/ΔH determined from a packer test is influenced by changes in boundary conditions in the fracture zone as well as changes in fracture zone transmissivity. The introduction of boreholes or the excavation of an opening increases the value of Q/ΔH measured at a packer location while a reduction in transmissivity decreases Q/ΔH.

5 HYDRO-MECHANICAL RESPONSE OF THE ROOM 209 FRACTURE ZONE

5.1 Introduction

An in situ excavation response experiment was conducted at Atomic Energy of Canada Limited's (AECL) Underground Research Laboratory (URL). The URL is located 100 km northeast of Winnipeg, Manitoba in the Lac du Bonnet Batholith (Fig. 5.1). The excavation response experiment was initiated after exploratory drilling at the 240-m level (Fig. 5.2) discovered a near-vertical water-bearing fracture zone (the Room 209 fracture zone) in an essentially unfractured rock mass. The discovery lead to the design and implementation of the Room 209 excavation response experiment. The experiment was designed to evaluate the response of the rock mass and the fracture zone to the excavation of a tunnel and to assess the effects of the excavation procedure, the instrumentation performance, and the predictive capabilities of numerical modelling codes. The rock mass around the Room 209 tunnel was monitored with a wide variety of instrumentation to achieve these goals. Thompson and Lang (1987), Lang et al. (1987b), and Thompson et al. (1989) describe the design of the experiment, the type of monitoring tools, and the instrumentation layout. A summary of the Room 209 excavation response experiment is given by Lang (1989) and a more detailed description of the experiment may be found in Lang et al. (1987b).

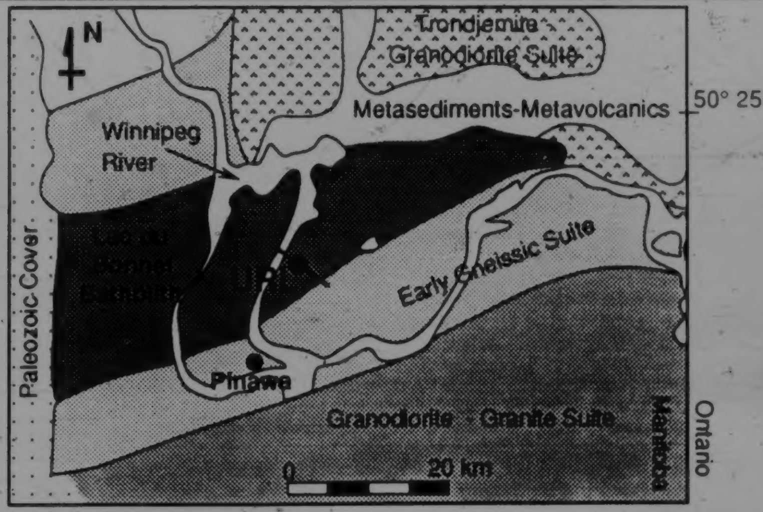

Figure 5.1 Location of the Underground Research Laboratory

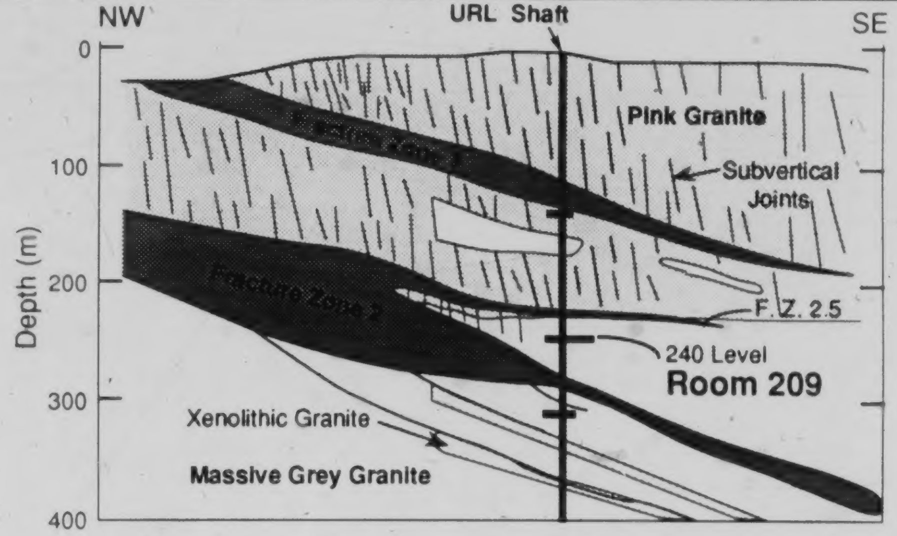

Figure 5.2 Cross-section through Lac du Bonnet Batholith

Finite element predictions of the excavation response were produced by Kaiser et al. (1987) and Chan et al. (1987). Evaluation of these predictions by the authors and subsequent analyses showed that the greatest deficiency of the numerical models was in their simulation of the hydraulic response in the fracture zone (Kaiser et al., 1989; Chan et al., 1988). These models both assumed that normal stress controlled the transmissivity of the fracture zone. The comparison of predictions with measurements showed that the measured trends in hydraulic response were not be consistently predicted. This thesis was motivated by the need to better understand and forecast the hydraulic response of the fracture zone. The approach adopted to examine the hydraulic response was divided into four phases: 1) numerical generation of shear displacement distributions in the fracture zone at different excavation stages, 2) matching the measured hydraulic response by a trial and error procedure of adjusting the transmissivity distributions, 3) estimation of transmissivity distributions using shear displacements, and 4) numerical simulation of the hydraulic response in the fracture zone.

5.2 Room 209 Excavation Response Experiment

5.2.1 Hydro-Geologic Setting

The Lac du Bonnet granitic batholith is representative of many granitic intrusions in the Precambrian Shield of Canada. The batholith has several granitic phases. At the URL shaft, a moderately fractured, pink granite grades downwards into a grey granite or quartz monzonite at about 220 m depth (Fig 5.2). The grey granite is generally much less fractured than the pink granite. There are three extensive, shallow-dipping, major fracture zones in the upper 500 m of the batholith at the URL site (Everitt, 1986). These fracture zones define the main aquifers at the site and they control the movement of groundwater within the rock mass. Except for these distinct fracture zones, the rock is relatively unfractured. The fracturing which is present is slightly more pronounced near the surface. There appears to be poor hydraulic connection between the three major fracture zones. In the fracture zones, near vertical fractures are the most common and a set striking about 030° is predominant. These fractures may be extensional in origin and have a zonal spacing. Some are water bearing and are probably responsible for the vertical hydraulic conductivity at the site.

An excavation response experiment was conducted in Room 209 at the 240-m level (Fig. 5.2). The predominant lithology of the immediate Room 209 area consists of a grey, unaltered, gneissic, medium grained granite. It is host to a variety of lensoid, semi-concordant, leucocratic segregations and to a swarm of granodiorite dikes. Room 209 and the entire 240-m level occur within a wedge shaped block whose edges are delineated by the #2 fracture zone below and a splay, the #2.5 fracture zone, above.

Cores obtained from holes drilled adjacent to the Room 209 drift as well as a hole down the axis of the tunnel, and geological mapping within Room 209, indicated that a minor fracture zone of hydrogeologic significance (Fig. 5.3) was located 4 m ahead of the Development Room face. The zone is near planar with orientation {(dip direction) dip} of (134°) 79° and is apparently unrelated to the regional, shallow dipping, major fracture zones. This fracture zone is almost perpendicular to the centerline of Room 209 which has an orientation of 120°. It is a composite feature consisting of one to six, discontinuous, en echelon fractures within a zone up to 0.4 m thick near Room 209. It cuts through a few granodiorite dykes (Fig. 5.4) and infillings are absent or very minor. It was impossible to determine, in detail, the internal structure of the fracture zone from the drill core or traces of fractures around the tunnel perimeter. However, the fracture zone is believed to exhibit en echelon fracture structure (Everitt, per. comm.).

The extent of the fracture zone is shown in Figure 5.4. On the northeast side of Room 209, the fracture zone thickens to about 1.5 m at a distance of 15 to 25 m from the tunnel while to the southwest, the fracture zones pinches out at roughly 15 m from Room 209.

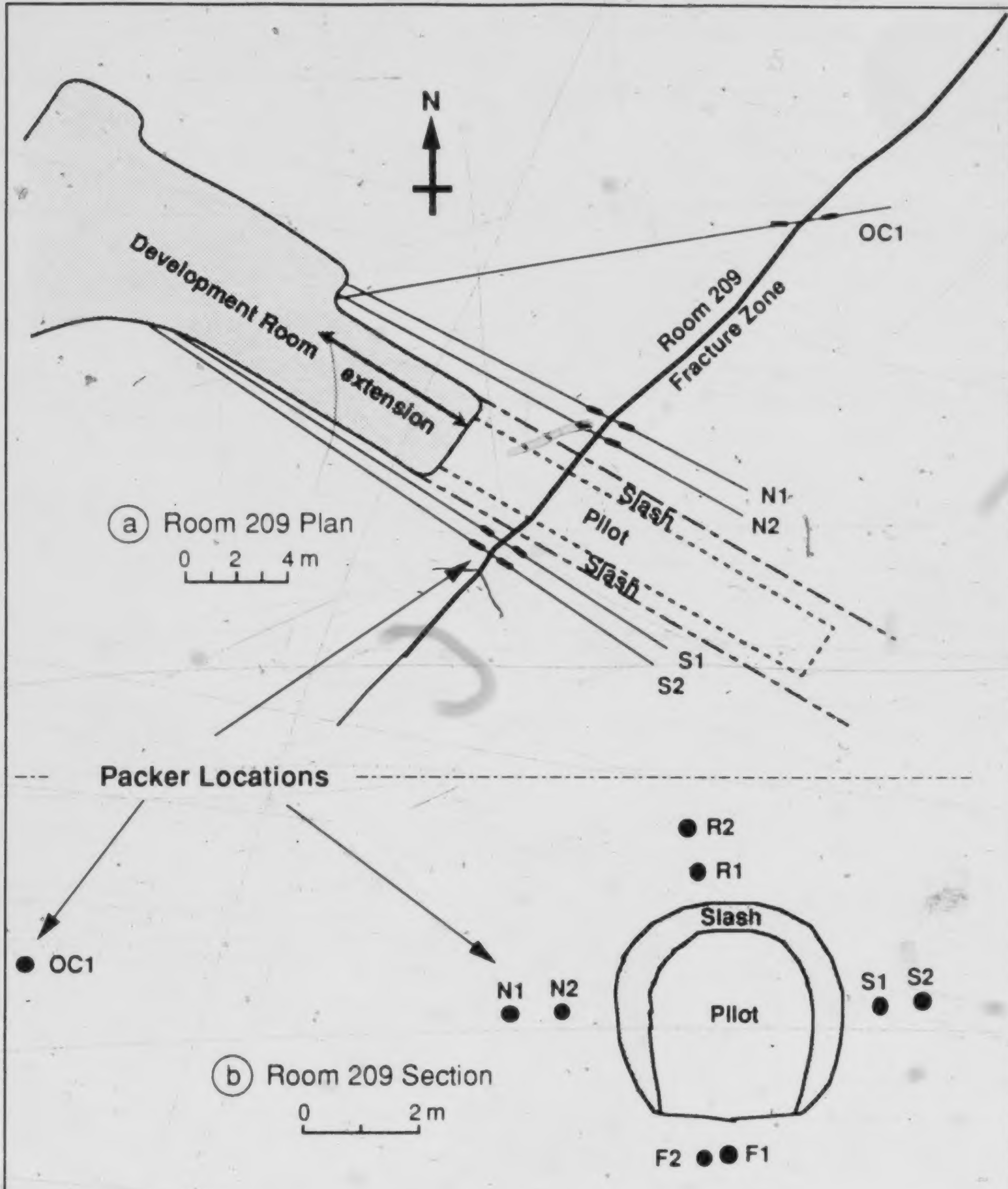

Figure 5.3 Plan and section of Room 209 showing fracture zone and packer locations

The Room 209 fracture zone is hydraulically connected to the #2.5 fracture zone-splay, situated 29 m above the excavation elevation. The fracture zone is thought to terminate immediately below the tunnel floor. Based on hydraulic monitoring, this zone appears more permeable above and northeast of Room 209 (Kozak and Davison, 1986).

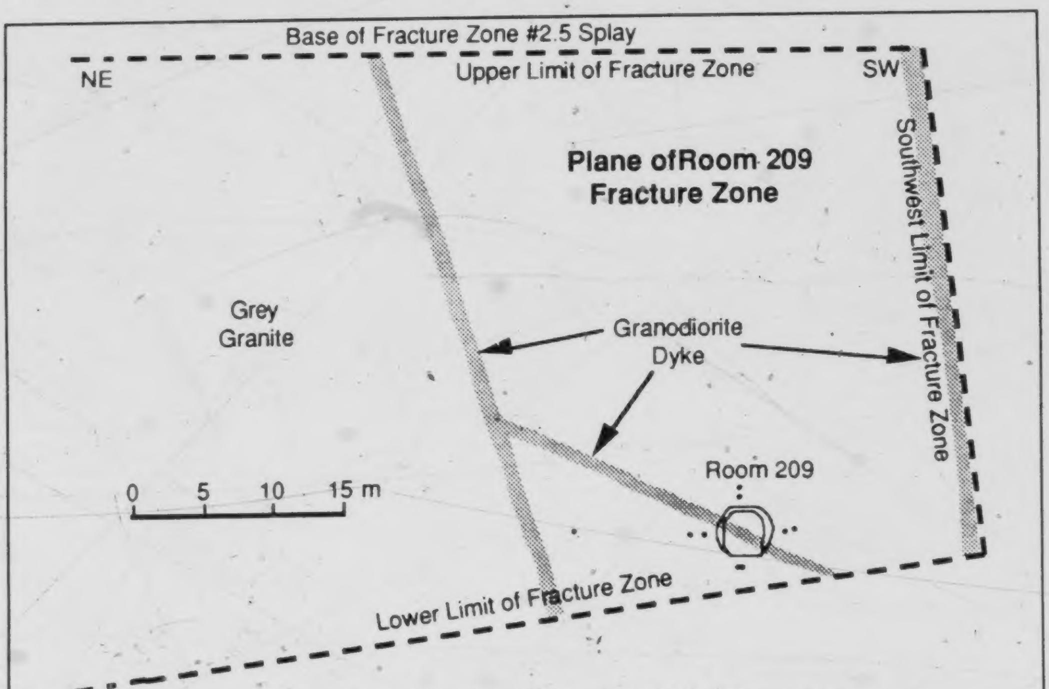
Base of Fracture Zone #2.5 Splay
NE
Upper Limit of Fracture Zone
SW
Plane ofRoom 209
Fracture Zone
Southwest Limit of Fracture Zone
Grey
Granite
Granodiorite
Dyke
Room 209
0
5
10
15 m
Lower Limit of Fracture Zone

Figure 5.4 Extent of Room 209 fracture zone

5.2.2 Instrumentation

The monitoring program for the Room 209 excavation response experiment involved instruments installed to measure displacements, stress changes, temperatures, and fluid pressures at different locations around the tunnel. The instrumentation was installed in two stages. A first set of boreholes (N1, N2, S1, S2, and OC1) was drilled before the Development Room extension was excavated. The extension goes from the collars of the north and OC1 packers to the end of the Development Room 4 metres from the fracture zone (Fig. 5.3a). Packers were placed in these holes to isolate and monitor the hydraulic behaviour in the Room 209 fracture zone using vibrating wire pressure transducers. The 7.5 m long extension to the Development Room was carefully excavated by drilling and blasting a pilot and slash. After the face was squared off, a second set of hydraulic monitoring holes (R1, R2, F1, and F2) were drilled from the end of the Development

Rooom (Fig. 5.3b). As before, packers and pressure transducers were installed to monitor the hydraulic pressure fluctuations. The packers systems used by AECL were described by Thompson et al. (1989). Eight boreholes, all within 2.5 m of the tunnel periphery were situated to measure the near-field hydraulic response. OC1 was drilled to intersect the fracture zone at 15 m to the northeast of the tunnel axis. This borehole was placed to provide a measurement point outside the near-field. In addition to the packers, thermistors and CSIRO triaxial strain cells were also installed in these boreholes. The CSIRO or 'stress' cells were installed before the packers. The CSIRO cells were placed near the ends of the boreholes, away from the influence of the fracture zone. All boreholes were accurately surveyed to establish the locations of the packed-off zones relative to the tunnel perimeter.

Nine additional boreholes were drilled in a plane perpendicular to the tunnel axis at a distance of about 0.5 m behind the Development Room face. Various types of extensometers combined with thermistors were placed in these radial boreholes. The instrumentation package was completed with convergence pins at the extensometer array and one other borehole which intersected the tunnel profile ahead of the Development Room face and contained a sliding micrometer (Lang et al., 1986b). The results from this additional instrumentation are not used in this thesis as they relate primarily to the closure and deformation of the tunnel at the location of the end of the Development Room.

5.2.3 Measured Response to Tunnel Excavation

Several hydraulic tests were performed before the tunnel was advanced. Fluid withdrawal tests were performed in boreholes (OC1, N1, N2, R1, R2, and F1). The results of these tests (Table G.1, Appendix G) are used in Section 5.6 to calibrate the numerical seepage model. By testing one borehole at a time, the hydraulic response at other boreholes was measured thereby providing an indication of the relative transmissivity distribution or connectivity between the boreholes. Figure 5.5 summarizes the findings of these tests (Kozak and Davison 1986). The band of low transmissivity cutting through Room 209 from the upper NE side to the lower SW side appears related to the presence of a cross-cutting granodiorite dyke (Fig. 5.4). This zone of reduced transmissivity was incorporated in the seepage models.

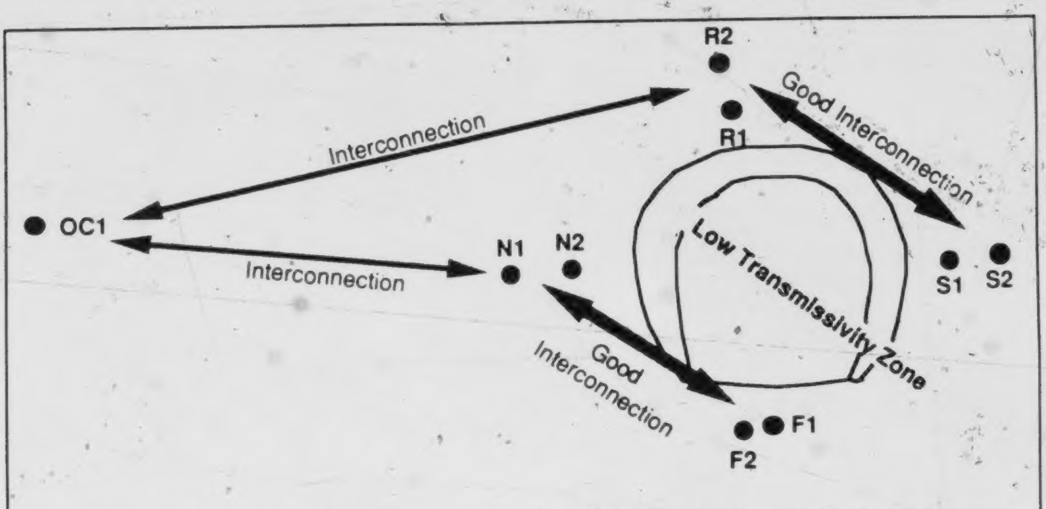

Figure 5.5 Hydraulic interconnection from borehole interference testing (after Kozak and Davison, 1986)

After initial fracture zone characterization, Room 209 was excavated by drill and blast techniques (Kuzyk et al., 1986; Lang et al., 1987b). A pilot tunnel was first advanced in 2.8 m rounds except for the first two rounds which were shortened to 1.5 m in length. The shorter rounds allowed the third round to intersect the fracture zone in the middle of the round and supplied more information during the rapid displacement transition as the face moved away from the extensometer array. The pilot was stopped after ten rounds at a distance of 25 m. The time between blast rounds ranged from 57 to 73 hours which allowed more than enough time to reach steady-state conditions in the fracture zone (Lang et al., 1987b). A slash excavation was then conducted in a similar manner. All slashes were 2.8 m in length except for the first which was 1.6 m long. Details of the excavation sequence and the as-excavated tunnel geometries are given in Lang et al. (1987b) and the blasting procedure is described by Kuzyk et al. (1986; 1987).

Displacements, stresses, temperatures, and fluid pressures were continuously monitored during the excavation of Room 209. In addition, fluid withdrawal tests were performed between blast rounds. All measurements are reported by Lang et al. (1987b). Although the entire suite of measurements produced by the experiment provides a general indication of the rock mass and fracture zone response, the hydraulic measurements from the boreholes intersecting the Room 209 fracture zone are of particular interest for this thesis. The deformation and stress records were analysed by the author and compared with numerical predictions (Kaiser et al., 1989). This work contributed to the development of the current numerical model but details of the comparison and analysis of deformation and stresses will not be fully reproduced in this thesis. Section 5.3 provides more information on previous numerical simulations.

The measurements related to the fracture zone response include: 1) steady-state fluid pressures as a function of time (or excavation stage); 2) the flow per unit head drop (Q/ΔH) obtained from single or multi-step fluid withdrawal tests; 3) the rate of flow from blastholes which intersected the fracture zone prior to blasting through the fracture zone; and 4) the rate of inflow into the pilot and the slash after excavation through the fracture zone. This data is summarized in Appendix G (Tables G.2 to G.6).

The measurements of Q/ΔH are graphically presented in Figure 5.6 relative to the excavation face position. The ratio of flow to head change (Q/ΔH) measured at the packed-off intervals, first dropped as the excavation face passed the fracture zone, then partially recovered as the excavation advanced. These characteristic drops and recoveries in Q/ΔH are similar to the variation in shear stress as an excavation face passes a measurement location (Fig. 5.7; Pelli, 1987; Chan et al., 1987). This similarity suggests that shear displacements as opposed to fracture zone closures (normal displacements) or other mechanisms must control the measured hydraulic response. The drop is partially recoverable at the packers during the pilot excavation. During the slash, the roof packers showed a drop in Q/ΔH which did not recover as the excavation proceeded. An interpretation of this behaviour relative to the hypothesis of shear-induced transmissivity reduction will be given later.

The two floor packers failed after the pilot intersected the fracture zone apparently due to blast damage arising from the higher explosive charge used at the floor. The S1 packer also failed at this time. The S2 packer continued to operate but showed signs of failure and data from this packer after the pilot had intersected the fracture zone is of questionable accuracy. All other packers performed well throughout the excavation response experiment and provided the most reliable data for comparison with measurements.

5.3 Previous Numerical Simulations of Room 209 (Elimination of Normal Stress - Fracture Closure Model)

The Room 209 excavation response experiment has been modelled by Kaiser et al. (1987; 1989) and Chan et al. (1987; 1988). The work presented by Kaiser et al. (1989) contributed to the development and validation of the finite element model used in this thesis. The 'Kaiser et al. (1989) model' was found to provide a reasonable prediction of displacements and stress changes (i.e., within or close to the range of confidence of the field measurements). The numerical representation of Room 209, introduced later in Section 5.4, is an improved version of the 'Kaiser et al. (1989) model'. It incorporates a better estimate for the rock mass modulus, in situ stresses, and tunnel and fracture zone geometries.

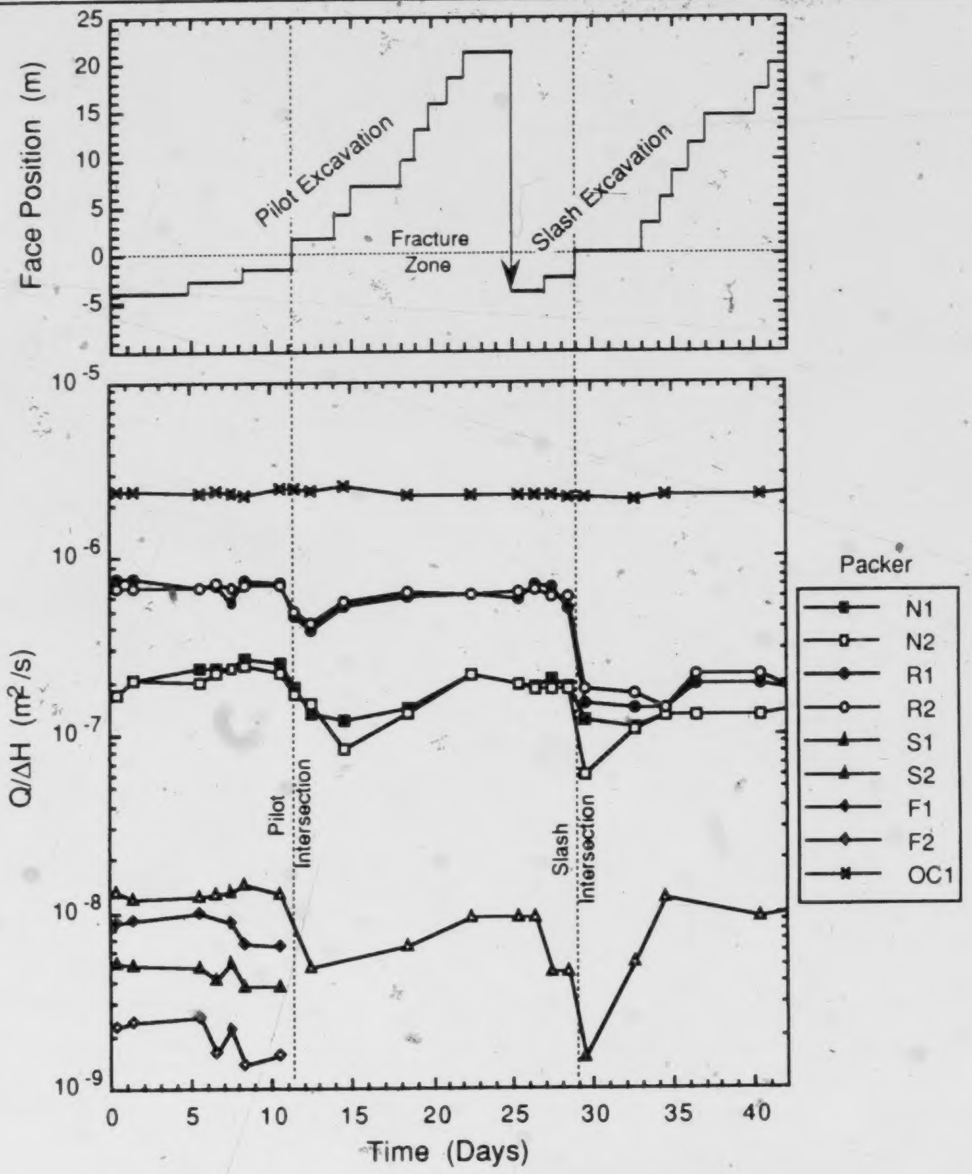

Figure 5.6 Measured Q/ΔH values at Room 209 packer locations

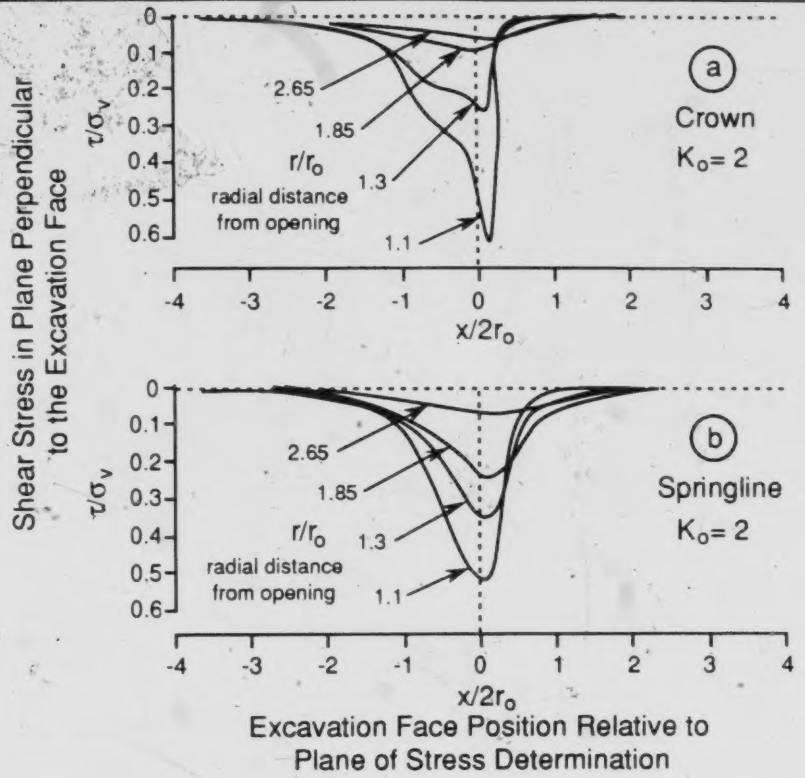

Figure 5.7 Development of shear stresses at the crown and springline as a function of the face position (after Pelli, 1987)

The finite element simulations by Kaiser et al. (1987) and Chan et al. (1987) failed to correctly predict the hydraulic response in the Room 209 fracture zone. The hydraulic response predictions assumed a normal-stress dependent fracture closure. Coupled fracture closure - fracture flow responses were also considered. The 'Kaiser et al. (1987) numerical model' used a high normal stiffness for the joint elements (5000 MPa/mm) to represent the fracture zone normal stiffness. This value was ten times higher than was used later by Kaiser et al. (1989). The fracture zone, which was oriented perpendicular to the Room 209, showed changes in equivalent fracture aperture that did not exceed 1.5 μm. This change was far less than the maximum 25 μm and 40 μm drops in equivalent fracture aperture inferred from measurements at the north and roof packer intervals (Lang et al., 1987b). However, a comparison of magnitudes is of minor value since the assumed fracture stiffness was higher than the in situ stiffnesses which were measured after these predictions were made (see Section 5.4.3). More important however, were the predicted trends. The normal stress - closure model predicted aperture increases at the north and south packer locations whereas obvious transmissivity reductions were measured. The numerical modelling conducted by Chan et al. (1987) showed a similar normal stress decrease near the north and south sides of the tunnel (Fig. 5.8). Again, a fracture closure model based on normal stress changes failed to explain the measured hydraulic response at these locations.

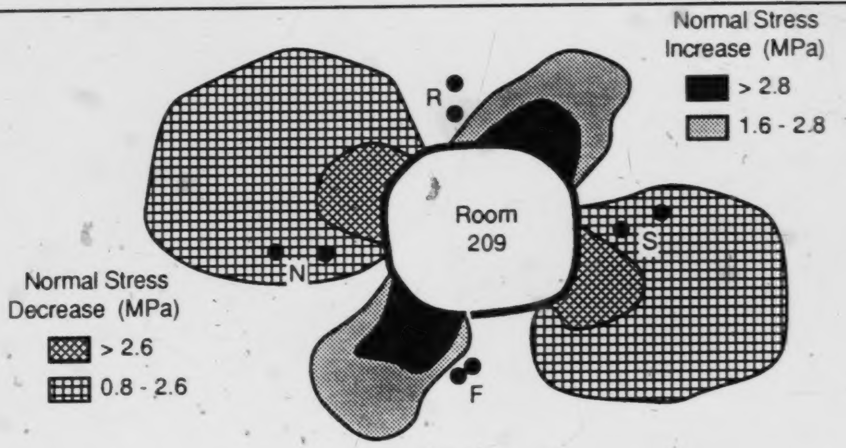

Figure 5.8 Normal stress changes in the plane of the Room 209 fracture zone after excavation of the slash (after Chan et al., 1987)

Since apertures were predicted to increase at some locations around the tunnel, a continuous low transmissivity ring near the tunnel was not generated by the normal stress - closure model. Without a continuous low transmissivity ring the steady-state predicted heads were much smaller than those measured. Figure 5.9 shows that the predicted heads were increasingly in error towards the tunnel.

The development of normal and shear stresses in the fracture zone as predicted by Chan et al. (1987) provide further evidence that normal stresses are not dominating the hydraulic response in the fracture zone. The maximum changes in normal stress occur when the excavation face is at the end of the pilot and the slash excavations and not when the excavation intersected the fracture zone. In contrast, the maximum changes in shear stress occur, as expected (Pelli, 1987; see Fig. 5.7), when the excavation face is near the fracture zone. The peaks in shear stress change correspond to the excavation stage when the fracture zone experienced the largest changes in transmissivity, i.e., when the face was near the fracture zone.

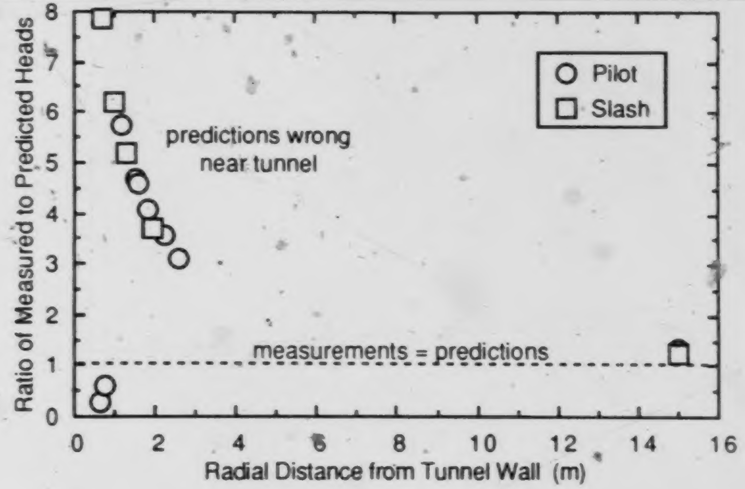

Figure 5.9 Comparison between measured heads at packer locations around Room 209 and heads predicted by a normal stress - fracture closure hydraulic model (after Kaiser et al., 1987)

Field measurements of stress change also support the proposition that the hydraulic response in the Room 209 fracture zone is not controlled by the traditional concept of normal-stress dependent fracture closure. An examination of measured axial (intermediate) stress changes (which are approximately equivalent to the normal stress changes in the fracture zone), demonstrated that normal-stress dependent fracture closure failed to predict the observed hydraulic response in a consistent manner (Kaiser et al., 1989). For example, the measured changes in intermediate principal stress consistently show a reduction in compressive stress as the pilot and the slash faces passed the stress change (CSIRO) cells. These measurements imply a decrease in normal stress at the fracture zone. Hence, a normal stress - closure model would predict opening of fractures or fracture dilation whereas the hydraulic monitoring showed a marked reduction in transmissivity near the tunnel wall.

Although a normal stress - closure model would predict the correct trends in transmissivity changes at the roof and floor where the normal stress increases (Fig. 5.8), the model does not provide consistent predictions for all hydraulic parameters at every location around the tunnel. Furthermore, the measured stress changes would imply an aperture increase everywhere around the tunnel. This does not mean that influence of normal stress on fracture closure is irrelevant. Instead, it appears that normal stress - fracture closure plays a subordinate role to other phenomena in the fracture zone. This section evaluates the role of shear-induced transmissivity decrease as the dominating influence in the Room 209 fracture zone.

5.4 Geomechanical Finite Element Model of Room 209

A major step in the process to evaluate the hypothesis of a fracture zone transmissivity reduction and partial recovery based on shear displacements is the prediction of shear displacements in the Room 209 fracture zone. Due to the complex geometry and in situ stresses which characterize the Room 209 experiment, a three-dimensional finite element model was needed to generate the shear displacements.

5.4.1 Finite Element Mesh and Coordinate System

A three-dimensional mesh was constructed to represent the area around the Room 209 fracture zone. The mesh contains 8161 nodes comprising 3680 isoparametric elements which form a nearly circular cylinder aligned parallel to the tunnel axis (Fig. 5.10a). The centre portion of the mesh is shown in Figure 5.10b. The geometry of the pilot and slash cross-sections were designed to reflect the as-excavated geometry near the Room 209 fracture zone. In the longitudinal direction (z-axis), the mesh consists of 20 'slices' of elements including the one slice of joint elements representing the fracture zone (Fig. 5.11). Most slices in the mesh were parallel to the fracture zone. However, three slices at each end of the mesh were progressively rotated until they were perpendicular to the tunnel axis. The three slices at each end of the mesh consisted of linear (8-noded) elements only. Quadratic elements were used in the other slices near the tunnel. The thickness of each slice varies. The slices are thinnest (0.5 m) near the fracture zone and thickest (7.0 m) at the two ends of the mesh. The slice of joint elements representing the fracture zone was 10 cm in thickness. However, the thickness of the joint elements is irrelevant since the joint element formulation is independent of element thickness.

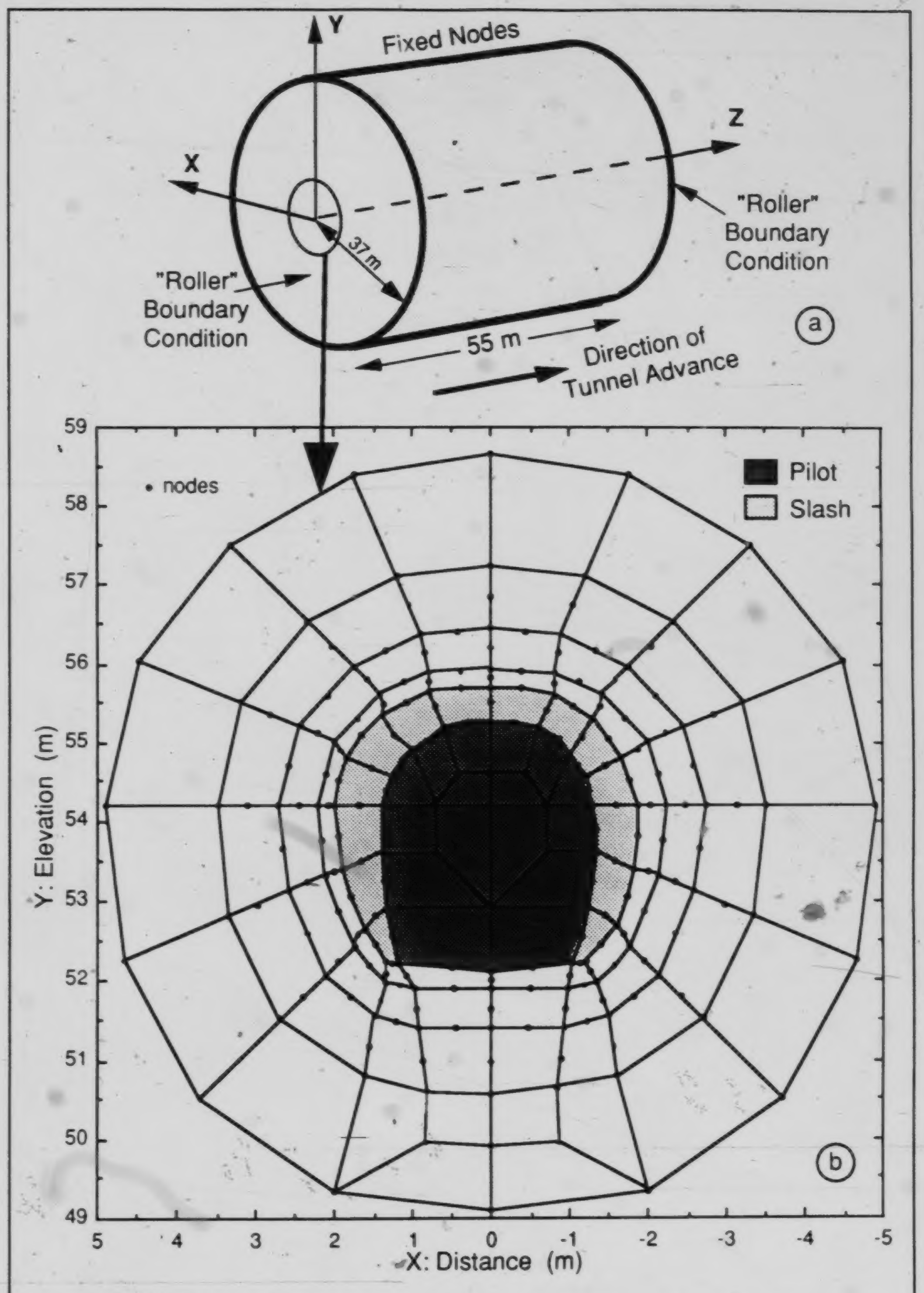

Figure 5.10 Three-dimensional finite element mesh and cross-section of the inner part of the mesh

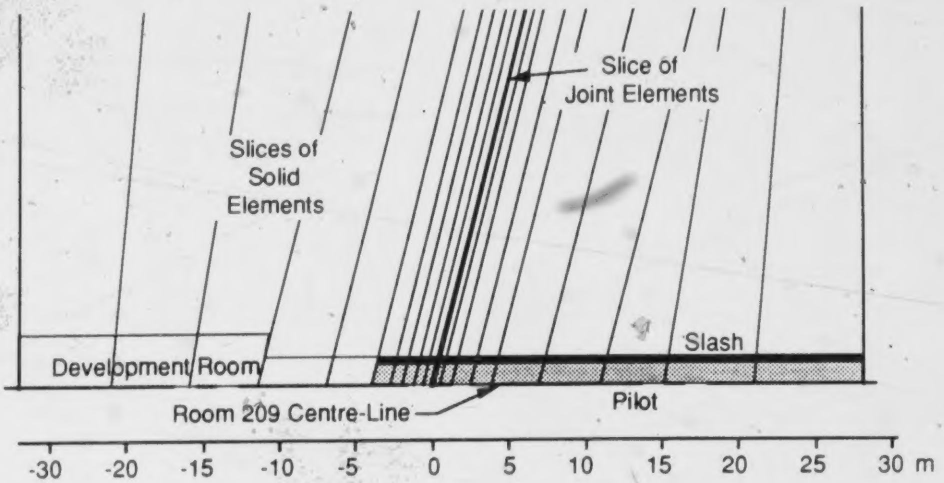

Figure 5.11 Longitudinal section through finite element mesh showing joint elements and slice orientations

Table 5.1 Orientation of Room 209 and fracture zone

Feature	Plunge	Trend
Room 209 Axis	0°	120°
Normal to Fracture Zone (slices)	-11°	134°

Specific locations and directions of positive displacement and stress change within the finite element mesh are based on the Cartesian coordinate system shown in Figure 5.10. The relationship between the finite element mesh coordinate system and the coordinate system used by AECL is as follows:

1. Elevations (Y) correspond; [5.1a]
2. $X = (E - E_o)\sin 30^\circ + (N - N_o)\cos 30^\circ$ m; [5.1b]
3. $Z = (E - E_o)\cos 30^\circ + (N - N_o)\sin 30^\circ + 1.75$ m; [5.1c]

where, N_O = 5570543.125 m, E_O = 295794.198 m, and N and E are the northing and easting.

The displacement boundary conditions imposed on the mesh were 'rollers' at each end of the mesh, i.e., on the two planes perpendicular to the tunnel axis, whereas the remaining nodes on the outer surface of the mesh were fixed. The radial distance to the outer boundary was about 37 m and the length of the mesh was 55 m (Fig.5.10).

The finite element analyses were done using SAGE (Chan, 1986; Chan and Chen, 1988) on a Cyber 205 computer located in Calgary. Before deletion of elements to simulate excavation, the mesh had over 20000 displacement degrees of freedom. The mesh had a stiffness matrix size of about 42 million words which was just manageable on the Cyber 205. Fortunately, recent improvements in the code SAGE allowed solution using only the upper half of the symmetric global stiffness matrix. This greatly reduced the execution time as well as the memory requirements on the Cyber 205. The bandwidth for this matrix was 1406. A typical run required about 12000 system time units. A single restart (output/input) file contained 43 Megabytes of data. The turn-a-round time was variable, ranging between six hours and 3 days.

Table 5.2 Resource usage on the Cyber computers

NOS/VE (Cyber 860)		
Resource	**Quantity**	**Charges ($)**
Catalog-kilobyte-months	129.09	3.61
File-kilobyte-months	24325.58	681.12
Connect-hours	33.92	43.31
Interactive-cpu-seconds	2297.34	355.65
		1083.69
VSOS (Cyber 205)		
Disk storage (kchars/day)	45820.234	2291.01
CPU-Express (kilo-STU)	0.021	9.66
CPU-LPrime (kilo-STU)	0.260	109.20
CPU-LNPrime (kilo-STU)	0.460	96.60
CPU-LDefer (kilo-STU)	183.274	25658.36
		28164.83
	Total	29248.52

Many difficulties were encountered while using the Cyber 205 and its front end computer, a Cyber 860. Most delays and problems were related to insufficient memory, either virtual memory on the Cyber 205 or permanent storage for files on the Cyber 860 and the Cyber 205. Table 5.2 gives a summary of the computer resources used to run the full analysis and the associated dollar costs at academic rates. This summary does not include time and resources used to develop and test the finite element mesh or efforts taken to implement the joint element formulation and in situ stress subroutines into the code SAGE.

5.4.2 In Situ State of Stress

The first step in the finite element analysis was to initialize the stress field. This was accomplished by specifying a uniform in situ stress state at every Gauss point in the mesh prior to removal (simulated excavation) of any elements. A 3x3 Gauss integration scheme was adopted for this analysis. The following stress tensor was taken as the best representation of the in situ stress state near Room 209 (Martin, per. comm., 1990; Martin et al., 1990b):

Table 5.3 In situ stresses

Principal Stress	**Magnitude** (MPa)	**Plunge** (deg)	**Trend** (deg)
σ_1	-27.5	25	213
σ_2	-14.4	48	092
σ_3	-9.8	31	320

Note that tunnel axis does not correspond to any of the principal stress directions. This state of stress was transformed into a stress tensor in terms of the mesh coordinate system before specification at the Gauss points. This stress tensor is given below with compressive stress taken as negative and the shear stresses following the right-hand rule.

$$\begin{bmatrix} \sigma_{xx} & \tau_{xy} & \tau_{xz} \\ \tau_{yx} & \sigma_{yy} & \tau_{yz} \\ \tau_{zx} & \tau_{zy} & \sigma_{zz} \end{bmatrix} = \begin{bmatrix} -24.79 & -5.68 & -1.54 \\ -5.68 & -15.46 & 1.71 \\ -1.54 & 1.71 & -11.45 \end{bmatrix} \quad \text{(MPa)} \qquad [5.2]$$

This stress field when transformed into normal and shear stresses in the plane of the fracture zone gave the following in situ stresses:

Table 5.4 In situ fracture zone stresses

Normal Stress	-10.5 MPa
Maximum Shear Stress	2.1 MPa

5.4.3 Material Properties

The material properties of the solid elements were chosen to represent rock that is homogeneous, isotropic and linear elastic. The rock mass around the Room 209 fracture zone has been extensively tested for physical properties (Lang et al. 1986b, 1989; Katsube and Hume, 1987; Koopmans and Hughes, 1988, 1989a,b). The measured rock mass modulus (E) is slightly anisotropic and heterogeneous. Although some modulus anisotropy has been noted near Room 209, there was insufficient information to assign spatial variations in modulus to the finite elements. Therefore, a homogeneous, isotropic rock mass modulus was adopted for the numerical model. Based on the modulus data and previously reported back-analyses, an isotropic rock mass modulus of 60 GPa and Poisson ratio of 0.25 were selected.

In situ testing after the tunnel was excavated (Koopmans and Hughes, 1989a,b) indicated lower moduli near the tunnel walls. This modulus reduction was probably caused by blast damage or is the result of a stress dependence. Thus, the modulus of finite elements located adjacent to the tunnel walls was decreased to 40 GPa and the next 'ring' of elements was assigned an intermediate modulus of 50 GPa (Fig. 5.12). The modulus of elements directly ahead of the face was also reduced to 50 GPa.

Elastic joint elements were chosen to represent the Room 209 fracture zone. The normal and shear stiffnesses used in the Kaiser et al. (1987) and (1989) numerical models were based on the Barton and Bandis empirical equations (see Section 2 and Appendix B). However, since the excavation of Room 209, in situ normal stiffness measurements in the Room 209 fracture zone have indicated a stiffness range between 50 and 635 MPa/mm (Martin et al., 1990a). It is well recognized that the fracture stiffness is sensitive to the normal stress on the fracture. However, given the measured variation in normal stiffness and the in situ virgin normal stress on the fracture zone (10.5 MPa) a linear elastic fracture stiffness seemed as appropriate as a nonlinear or Barton-Bandis type hyperbolic stiffness (Section 2.4.1). The Barton-Bandis hyperbolic normal displacement versus normal stress relationship can be approximated by a linear relationship when the normal stress level is high and the perturbations to the normal stress vary only over a small range. Both of these conditions apply in the Room 209 fracture zone, except perhaps immediately next to the tunnel wall where higher normal stress changes may be expected (Fig. 5.8).

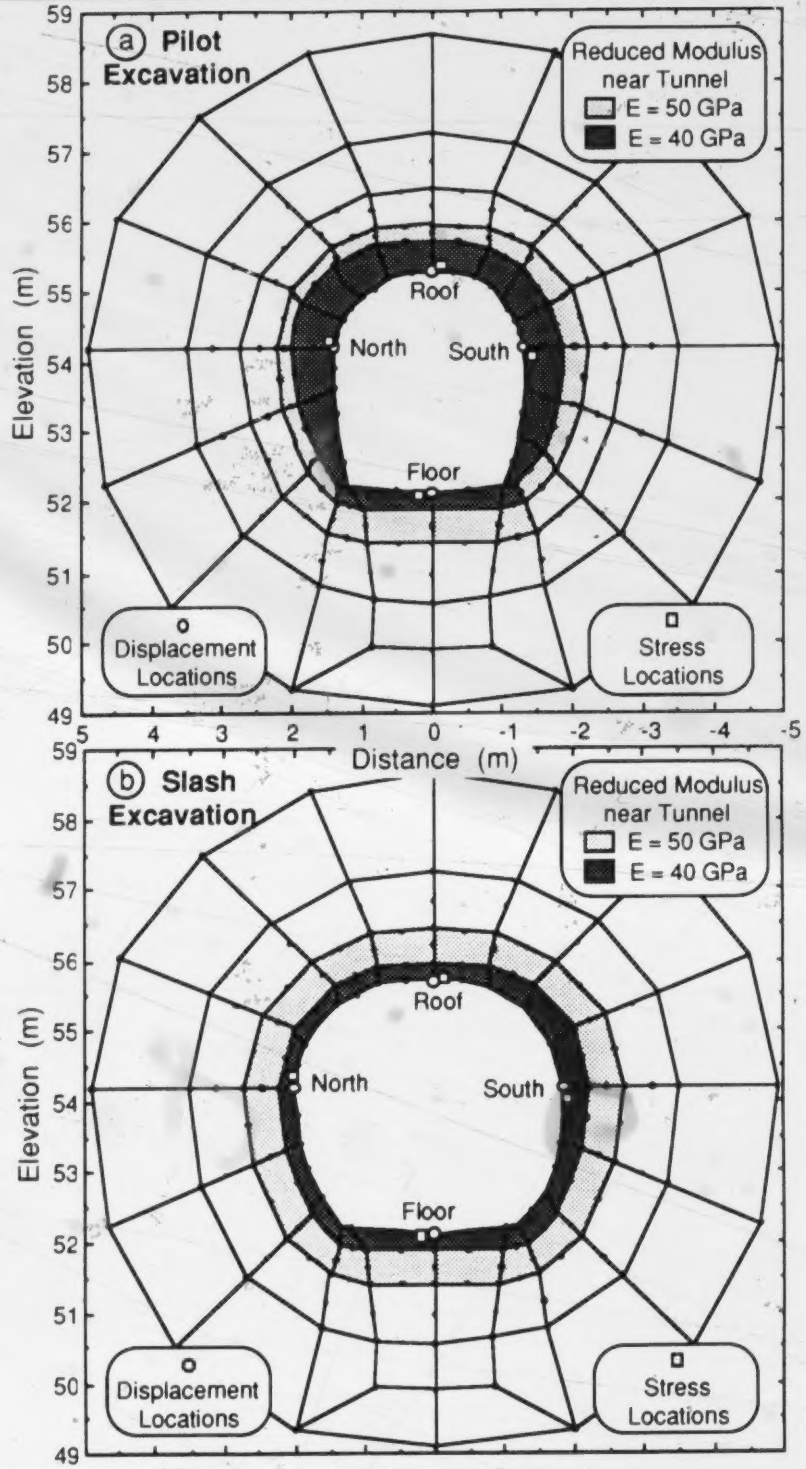

Figure 5.12 Reduced modulus zones and locations for displacement and stress determination

The fracture zone appears softer near the tunnel at least at the north side of Room 209 (Martin et al., 1990a). Unfortunately, stiffness measurements were only taken at two locations in the fracture zone (N1 and OC1). These measurements were not sufficient to define a spatial distribution in fracture stiffness. Therefore, a single representative normal stiffness of 300 MPa/mm was chosen to represent the normal stiffness of the whole fracture zone. This value is reduced from the stiffness of 500 MPa/mm used by Kaiser et al. (1989) for numerical modelling of the Room 209 area prior to the availability of in situ stiffness measurements.

The choice of shear stiffness for the joint elements was more subjective. No in situ measurements of shear stiffness for the Room 209 fracture zone are available. Laboratory testing of rock fractures from the URL (Makurat, 1989) involved some shear testing. However, it must be noted that fracture stiffnesses are extremely sensitive to normal stress level and in laboratory environments, sample disturbance. The testing at the Norwegian Geotechnical Institute (Makurat, 1989) was not designed to measure shear stiffness. Nevertheless, relationships between shear stress and shear displacements induced under nearly constant normal stresses similar to those experienced by the Room 209 fracture zone (10 to 11 MPa) gave a wide range of shear stiffnesses, typically less than 1 to more than 1000 MPa/mm. These stiffnesses are for single fractures and it is not known how they would relate to a system of fractures with unknown geometry composing the fracture zone at Room 209. Other laboratory work (Goodman and Dubois, 1972; Sun et al., 1985; Chappell, 1990) has shown that the shear stiffness of fractures is less than the normal stiffness at a given normal stress. The ratio between shear and normal stiffness for single fractures in crystalline rock ranged between 4.2 (Goodman and Dubois, 1972) and roughly 20 to 50 (Sun et al., 1985). Also, it is likely that a fracture zone is softer in shear than a single fracture. The Barton and Bakhtar (1983) empirical shear stiffness relationship predicted a stiffness of about 2 MPa/mm (Appendix B). For the numerical model, the ratio of fracture zone normal stiffness to fracture zone shear stiffness was assumed at 100:1. This gave a fracture zone stiffness of 3 MPa/mm which was the same stiffness used in the 'Kaiser et al. (1989) numerical model'. The chosen value of shear stiffness equals the value used by Rutqvist et al. (1990) for crystalline rock fractures subject to 10.2 MPa normal stress.

5.4.4 Excavation Sequence

The analysis had three main excavation stages: 1) Development Room, 2) Pilot, and 3) Slash. The excavations of the Pilot and the Slash were further subdivided into numerous steps. These excavation steps correspond roughly with the blast rounds on either side of the fracture zone. In addition, both the pilot and the slash were excavated to the fracture zone. The excavation sequence is summarized in Table 5.5.

Table 5.5. Excavation sequence

Excavation Step	Designation	Face Distance from Fracture Zone
Development Room	DR	- 4 m
Pilot	P1	-1.2
Pilot (FZ)	P2	0
Pilot	P3	1.2
Full Pilot	P4	28 m
Slash	S1	-2.0
Slash (FZ)	S2	0
Slash	S3	0.5
Full Slash	S4	28 m

The pilot and slash face positions reflect the as excavated average face positions. However, the actual excavation of Room 209 did not have excavation rounds corresponding to the modelled steps of P2 and S2. These steps were added to capture the high stress and displacement gradients which exist near the excavation face. This has no effect on the ultimate solution as all materials are linear elastic.

5.5 3-D Finite Element Results

The finite element program provides displacements at the nodes and stresses at each Gauss point. The output file from each excavation step was about 43 Megabytes in size. Since only specific displacements and stresses were needed, a program was written to extract: 1) the nodal displacements in the fracture zone (slice of joint elements); 2) normal and shear stresses in the joint elements; and 3) nodal displacements along the springlines, roof, and floor (Fig. 5.12).

5.5.1 Tunnel Wall Displacements

Displacements on either side of the fracture zone were plotted to verify the performance of the numerical model and to assist in understanding the shear displacements generated in the fracture zone. Total radial displacements at the north, south, roof, and floor tunnel wall locations are plotted against distance from the fracture zone along the tunnel axis (Figs. 5.13 and 5.14). These plots show displacements for each of the four pilot and slash excavation steps. Radially inward displacement is positive. Figure 5.12 shows the location where wall displacements were determined. Note that due to removal of the slash, the north, south, and roof locations are shifted to a different location during the Slash excavation (Fig. 5.12b).

Figure 5.13 shows the radial displacements during the Pilot excavation. The face position at steps P1, P2, and P3 are indicated along the axial distance axis; the face position at P4 (full pilot) is well off the scale of the plots. The excavation faces are close to the fracture zone (Table 5.5) and hence, the joint elements influence the displacement profiles. At step P1, the displacements show that the typical S-shaped closure curve is disrupted by shear at the fracture zone. At step P2, when the excavation face is at the fracture zone, the tunnel closure on the excavated side is comparatively independent of displacements on the other side. The difference in displacements on either side of the fracture zone is due to the relatively low shear stiffness in the joint elements.

When the excavation advances to P3 the shear displacements in the joint elements reduce and the closure curve approaches an S-shape again. However, even after the full pilot is excavated (P4), some non-recoverable shear displacements remain in the joint elements. The shear displacements would be expected to return to zero with full excavation if the following conditions were satisfied: 1) linear elastic model; 2) joint elements oriented perpendicular to the tunnel; and 3) in situ principal stresses perpendicular and parallel to the orientation of the tunnel. As these conditions are not satisfied at Room 209, the numerical model predicts non-recoverable shear displacements in the fracture zone at P4.

Profiles of radial displacements at the tunnel wall when the Slash was excavated are presented in Figure 5.14. In contrast to the Pilot excavation, the largest shear displacements in the joint elements do not occur when the face is at the fracture zone for the north and floor locations. In Figures 5.14a and 5.14d, the S2 shear displacements at the north and floor locations are nearly zero with the larger shear displacements at steps S1 and

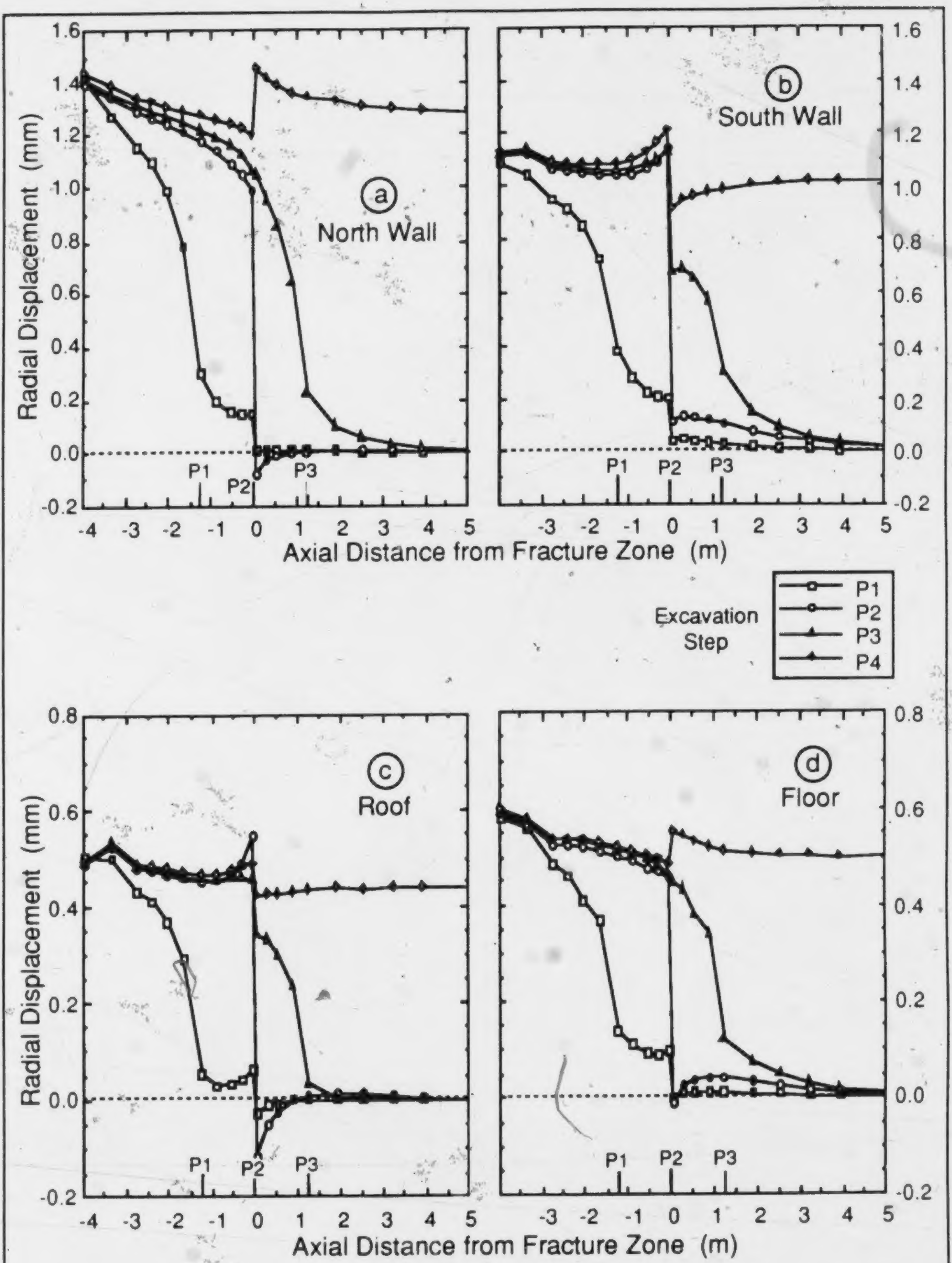

Figure 5.13 Radial displacements along the tunnel at the north and south walls and the roof and floor during pilot excavations

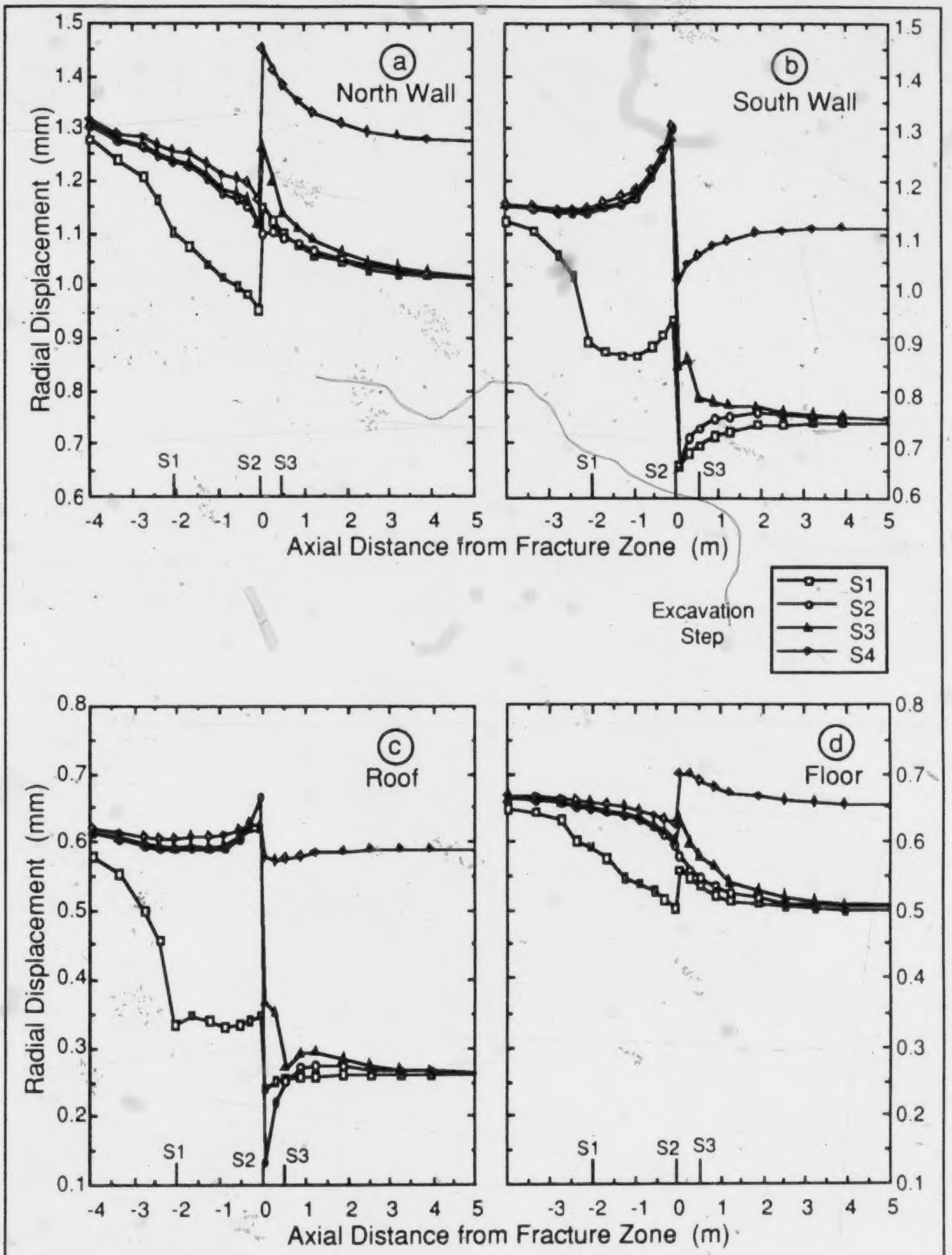

Figure 5.14 Radial displacements along the tunnel at the north and south walls and the roof and floor during slash excavations

S4. The combination of fracture zone orientation relative to the tunnel geometry and in situ stresses determines the distribution of shear displacements.

5.5.1.1 Closures and Convergence

The closures or radial wall displacements taken at 0.5 m behind the Development Room face are compared to predictions made by Kaiser et al. (1989) in Table 5.6. These are incremental displacements relative to conditions after the excavation of the Development Room. The numerical model used in this thesis gave closures significantly larger than those predicted by Kaiser et al. (1989). This is attributed to the incorporation of the reduced modulus zone around the tunnel. A previous analysis of the displacements around Room 209 (Kaiser et al., 1989) and in situ modulus measurements after the excavation of Room 209 (Koopmans and Hughes, 1989a,b) indicated that consideration and implementation of a zone of reduced modulus near the tunnel would improve the fit with measurements. Hence, the model used in this thesis adopted a reduced modulus zone, the influence of which can be seen by the increased closures. The 'Kaiser et al. (1989) model' also differs slightly from the present model in terms of in situ stresses, tunnel geometry, and mesh layout. Each of these factors may also partially account for the difference in closures.

Table 5.6 Wall closures and convergence

* Closure or Convergence	Excavation Step	Location			
		North	South	Roof	Floor
K	Full Pilot P4	0.29	0.41	0.10	0.15
T		0.59	0.47	0.18	0.32
K		0.70		0.25	
T		1.06		0.50	
L		1.04		0.63	
K	Full Slash S4	0.38	0.61	0.25	0.19
T		0.74	0.64	0.35	0.38
K		0.99		0.44	
T		1.38		0.73	
L		1.36		1.01	

* K = Kaiser et al. (1989) numerical model.
T = Thesis model.
L = Lang et al. (1987b) field measurements.

The closures (or one-sided wall movements) were added to determine the tunnel convergence along a north-south and a roof-floor line and are compared in Table 5.6 with the measured convergences (Lang et al., 1987b) and convergences predicted by Kaiser et al. (1989) at the same locations. The numerical model used in this thesis provides a better fit with the measured closures. The fit was extremely good at the north-south line. The current model still under-predicted the tunnel convergence along the roof-floor line. This may indicate that the zone of reduced modulus is larger than assumed or that the modulus reduction is larger than that which was adopted in the vicinity of the roof or floor. Nevertheless, the comparison of measured and predicted convergences gives confidence that the numerical model is generating an accurate displacement field in the rock mass near the Room 209 fracture zone.

5.5.2 Shear Displacements in the Fracture Zone

At Room 209, most field monitoring, including the hydraulic testing, was conducted after the Development Room had been excavated. Test data obtained after excavation of the Development Room and before the Pilot excavation were used to establish the initial fracture zone conditions. Therefore, the fracture zone displacements were calculated relative to the conditions after the excavation of the Development Room.

Shear displacements in the fracture zone were determined in the following manner:

1) The x-, y- and z-nodal displacements at an excavation step were adjusted by subtracting displacements due to the excavation of the Development Room.

2) The relative displacements in the fracture zone were calculated by subtracting the nodal displacements at one side of the fracture zone (joint elements) from displacements at the other side.

3) The magnitudes of the relative normal displacements were found by taking the dot product of the relative displacement vectors and the unit normal vector to the fracture zone.

4) The maximum shear displacements were found by subtracting the normal displacement vectors from the relative displacement vectors.

Manually created contour plots of the maximum shear displacements after each of the Pilot and the Slash excavation steps are presented in Figures 5.15 and 5.16. These plots clearly show the evolution of shear displacements as the excavation face approaches, intersects,

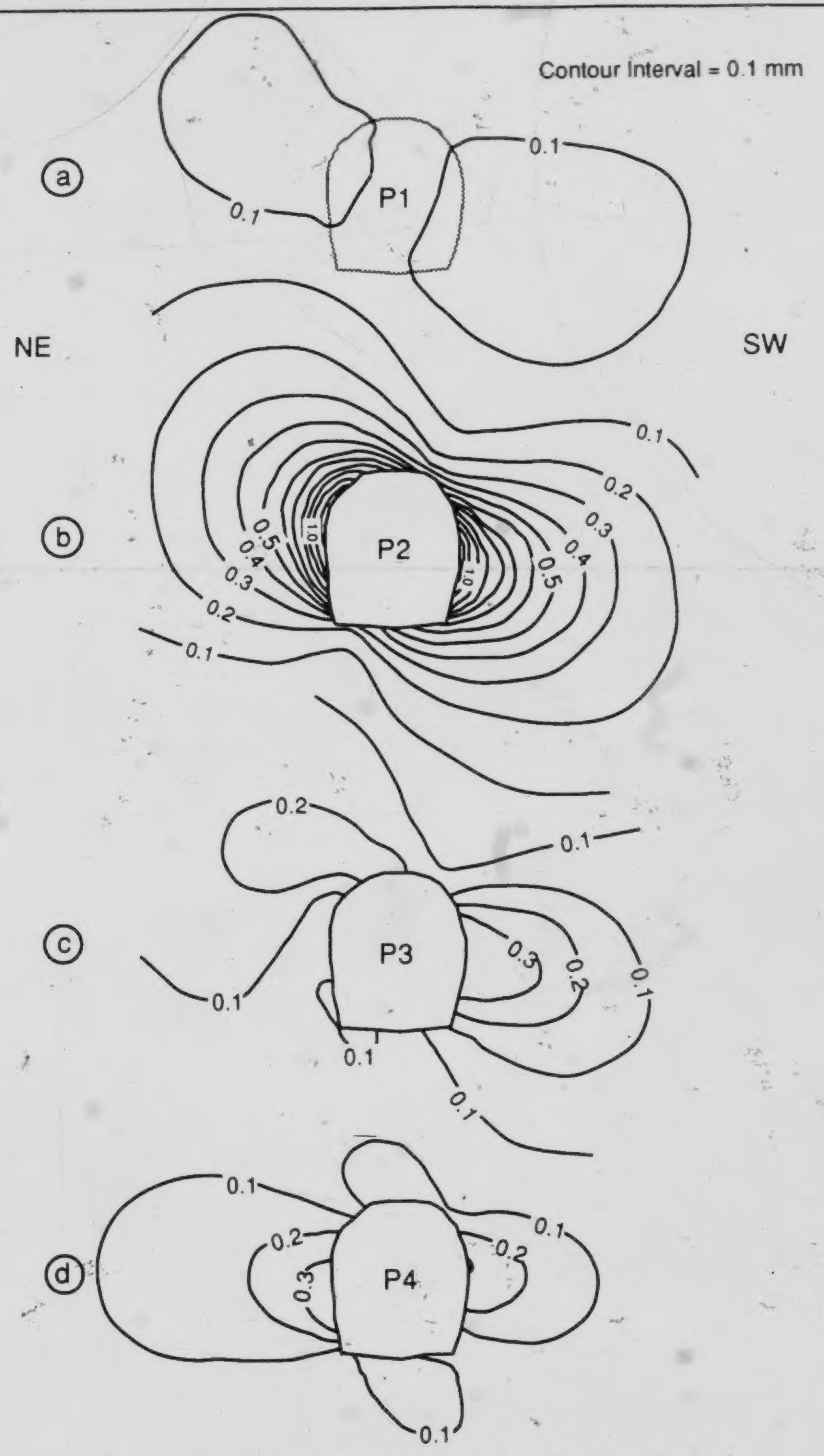

Figure 5.15 Maximum shear displacement magnitudes in the fracture zone during pilot excavations

and then passes the fracture zone. The shear displacements at step P1 (Fig. 5.15a), are generally less than 0.1 mm and only just beginning to develop. However, an advance of 1.2 m (P2) intersects the fracture zone and establishes much larger shear displacements (Fig. 5.15b). The shear displacement distribution is strongly non-axisymmetric because of the in situ stress field, fracture zone orientation, and tunnel geometry. Figures 5.15a and 5.15b indicate a plane of near symmetry extending from the upper-north to the lower-south of the fracture zone. The orientation of this plane is similar to the orientation (in the plane of the fracture zone) of the major principal in situ stress.

After the Pilot proceeded beyond the fracture zone, the shear displacements rapidly decrease (Fig. 5.15c) and then approach a stable distribution (Fig. 5.15d). The shear displacements at P4 adopt a pattern of distribution which is different from P1 and P2. Whereas the first two distributions showed two opposing lobes of higher displacement, the distribution at P4 shows four lobes. The four lobes are arranged in two pairs. The pair with largest shear displacements is located to the north and south sides of the tunnel. Profiles of maximum shear displacement extend nearly horizontally from the north and south walls. The other pair is located at the roof and floor of the tunnel. This pattern of displacement is somewhat characteristic of all the remaining slashing steps.

The shear displacements at S1 (Fig. 5.16a) are very similar to P4 with a slight increase in magnitude. However, as the fracture zone is intersected by the Slash (Fig. 5.16b), shear displacements increase at the roof and south side. The Slash at S2 generates approximately half the shear displacements as the Pilot created at P2 although the total volume excavated is 150% of the Pilot. Again, as the face passes the fracture zone the shear displacements decrease (Fig. 5.16c) and approach stable distributions (Fig. 5.16d).

A comparison of the shear distributions at steps P2 and S2 shows that the high shear displacement lobe on the upper-north side of the tunnel at P2 shifts upwards to the roof. The other lobe of high shear displacement remains in roughly the same position and orientation (south wall and inclined about 15° to 17° downwards away from the tunnel). The upwards shift in one lobe of shear displacements may be a result of slashing only the roof and side-walls.

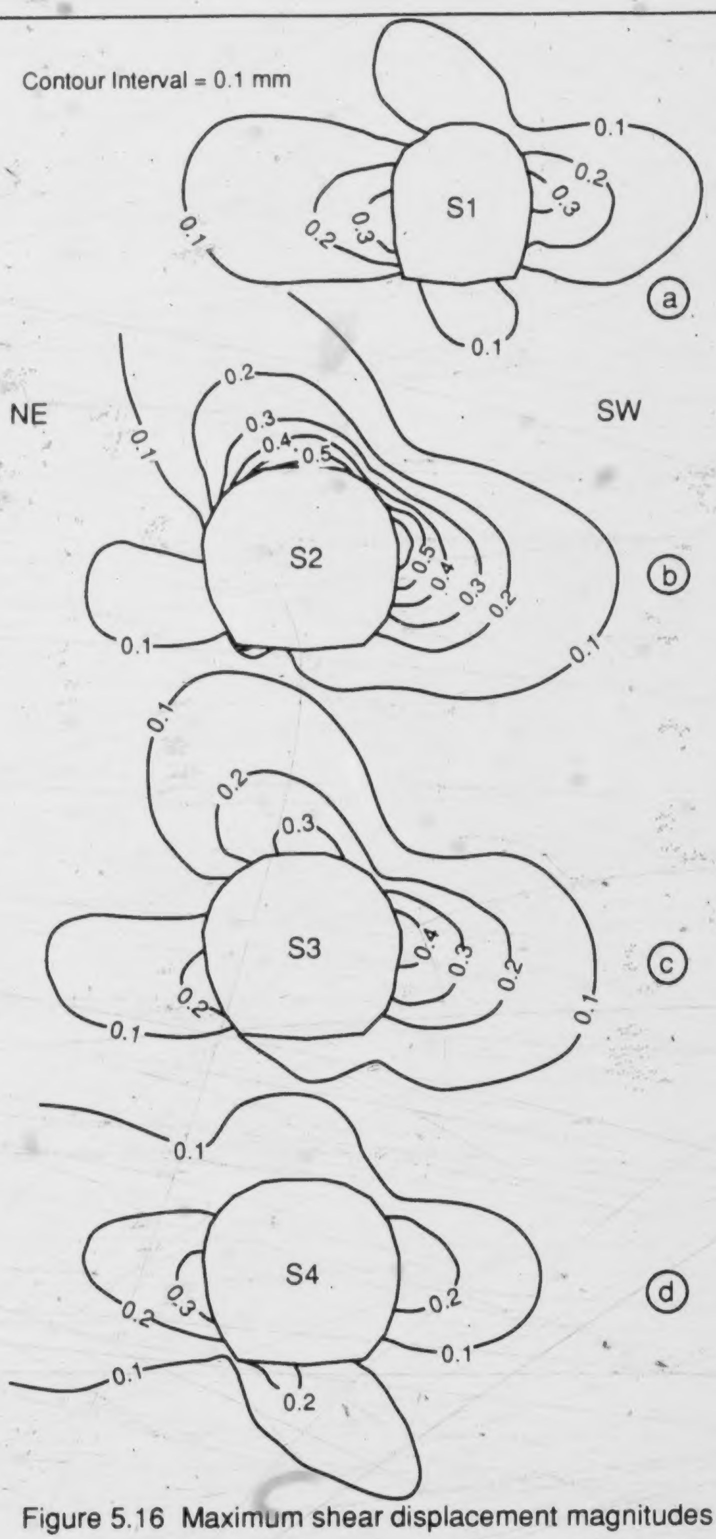

Figure 5.16 Maximum shear displacement magnitudes in the fracture zone during slash excavations

The shear displacement distributions, plotted in Figures 5.15 and 5.16, were used to determine shear-dependent transmissivity changes for fracture zone seepage modelling. The seepage analysis required elemental displacements, i.e., one representative shear displacement per element. These displacements were obtained by taking the x-, y- and z-relative displacement components at nodes belonging to the element and calculating the average or elemental shear displacement. The elemental shear displacements were then used to calculate transmissivity changes for each element. The seepage modelling and associated calculations of transmissivity distributions are discussed in the next section.

5.6 Room 209 Seepage Modelling

Finite element techniques were chosen as a means of modelling the hydraulic response in the Room 209 fracture zone. This analysis was conducted in two phases. In the first phase, a series of finite element seepage analyses was done in an attempt to match the measured hydraulic response in the Room 209 fracture zone. The transmissivity distributions in the mesh were arbitrarily varied to obtain the best match between the numerically modelled and measured responses. Simulations were run for conditions before and after excavation of the pilot, and after the slash excavation.

The second phase of modelling used the shear displacements determined from the geomechanical modelling (Section 5.5) to generate transmissivity distributions at different excavation steps. Predictions from seepage analyses using these transmissivity distributions were compared to the field measurements. The results from this phase allowed evaluation of the shear-dependent transmissivity hypothesis.

5.6.1 Finite Element Mesh and Boundary Conditions

The finite element mesh presented in Figures 5.17 and 5.18 was based on the mesh used by Kaiser et al. (1989) for modelling the geomechanical response of Room 209. The mesh consisted of 193 four-noded quadrilateral elements containing 205 nodes. The finite element program SEEP was used on a Macintosh II computer to determine the heads and flows. Each element was associated with a unique transmissivity set. Therefore, different transmissivity distributions were created by altering the 193 different transmissivity sets. The trial and error procedure which was used to match the field measurements entailed repeated simulations with slightly altered transmissivity distributions. Literally hundreds of simulations were performed.

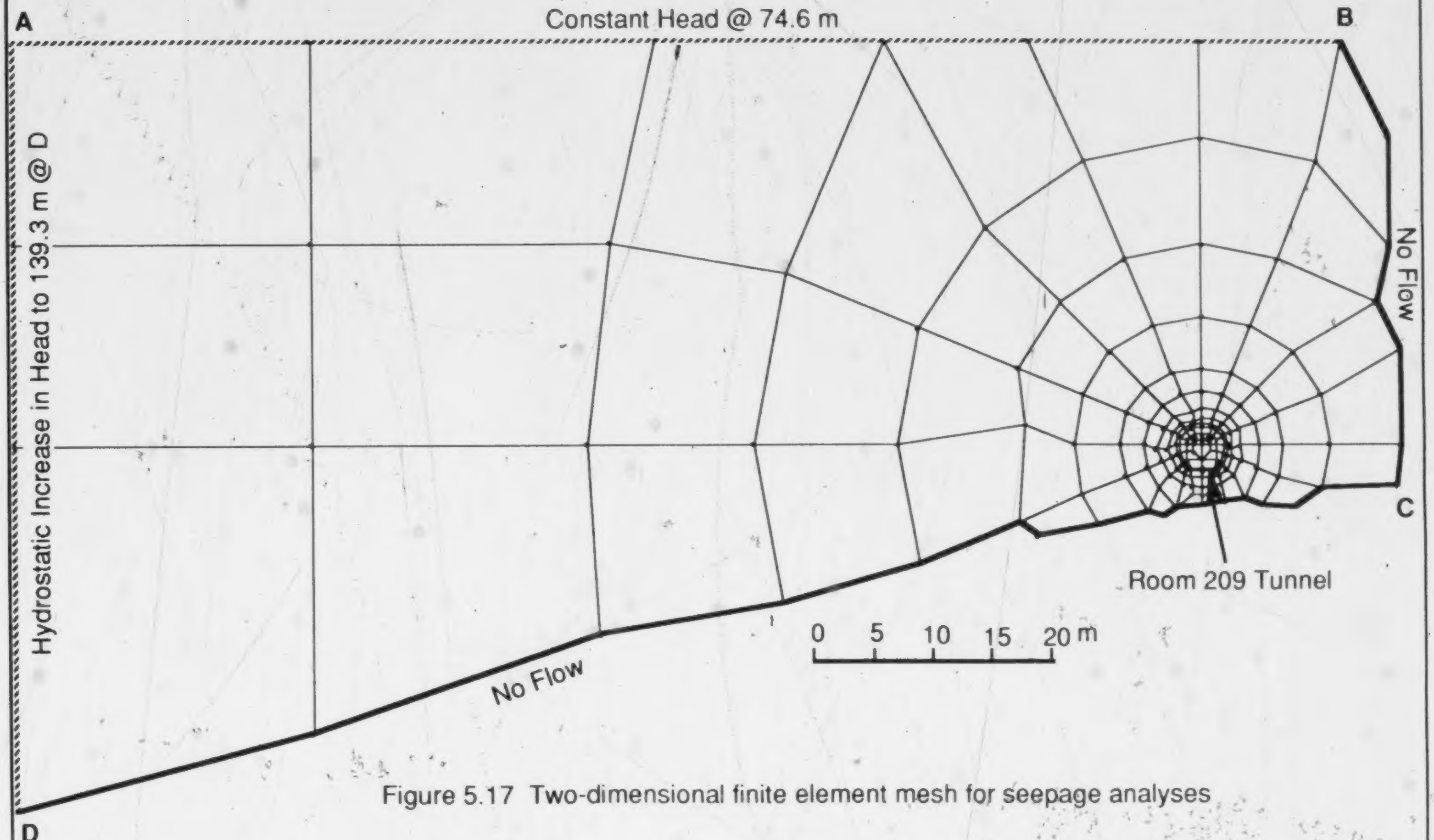

Figure 5.17 Two-dimensional finite element mesh for seepage analyses

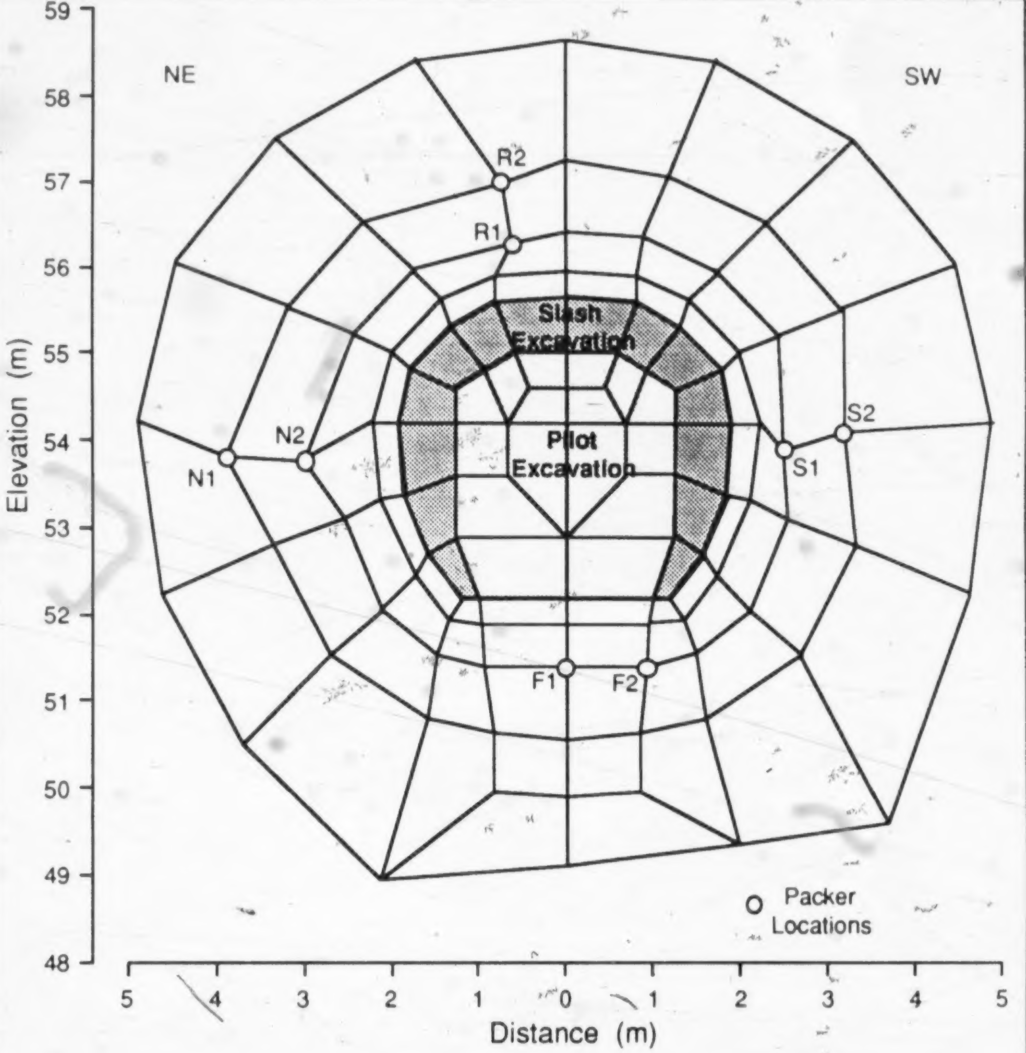

Figure 5.18 Inner part of finite element seepage mesh showing nodes representing packer locations and excavation perimeter

The boundary conditions for the mesh shown in Figure 5.17 are: 1) no-flow at the right and lower peripheries of the mesh representing the disappearance or pinching out of the fracture zone; 2) a prescribed head at the upper and left peripheries of the mesh reflecting the contact with a major fracture zone above Room 209 and a zone of greater fracture zone storativity and permeability about 100 m to the northeast of Room 209. The prescribed head of 74.6 m along the upper mesh boundary corresponds to the steady-state pre-excavation head (108.6 m or 1065 kPa fluid pressure) measured at the elevation of Room

209 (Lang et al., 1986b, 1987b). The heads along the left mesh boundary were specified to increase hydrostatically with depth from a head of 74.6 m at the upper northeast corner (pt. A) to 139.3 m at the lower northeast corner (pt. D). These boundary conditions are based on the hydro-geologic features near the Room 209 fracture zone as depicted in Figure 5.5.

5.6.2 Transmissivity Models

The seepage simulations were conducted by varying the transmissivity distributions in the following sequence:

1) initial analysis with a constant transmissivity distribution;
2) the transmissivities were altered until a best fit was established for pre-excavation conditions, including the presence of blast-holes;
3) the pilot was removed without changing the transmissivity distribution;
4) the transmissivities were altered until a best fit was established for the pilot excavation;
5) the slash was removed without changing the transmissivity distribution and finally;
6) the transmissivities were adjusted until a best fit was established for the slash excavation.

Since different transmissivity values can be specified for each element, the transmissivity distributions were dependent on the shape of the mesh and element sizes. The transmissivities were specified such that the two principal transmissivity values for each element were equal, i.e., isotropic flow was assumed within each element. The best fit was judged by a qualitative assessment of inflows, heads, and Q/ΔH at the packer locations.

Fluid withdrawal tests were conducted at the nodes representing the packers (Fig. 5.18). A packer test was simulated by specifying a negative flow at a node and allowing the program to determine the corresponding head. The head drop resulting from the prescribed flow could then be calculated. The head response at other nodes during a packer test was used for cross-hole interference analysis. Flow quantities into the pilot and slash were calculated from the flows in the elements around the opening.

The quality of fit between the mesh transmissivities and actual fracture zone transmissivities is influenced by the size of elements in the mesh, the available field data, and the variability and reliability in the measured values.

The 'matched' transmissivity distributions were obtained by a trial and error process of altering transmissivities, performing a seepage analysis, and comparing predictions with measurements. These best-fit solutions are not unique in that others could be found to provide an equal match. However, based on a qualitative assessment considering all available information and the limitations of the numerical model, the matched transmissivities represent a best fit condition. The fit was establish by minimizing the difference between measurements and predictions. No statistical analyses were performed. The transmissivity distributions are also similar to those used by Winberg (1988) who revised the AECL Room 209 fracture zone finite element flow model.

The six transmissivity models are summarized below.

5.6.2.1 Constant Transmissivity Distribution

Results from the constant transmissivity model are used as a reference for later numerical models and are compared to the measured responses. A transmissivity of 7.80×10^{-8} m^2/s (corresponding to an equivalent parallel plate aperture of 50 μm) was assigned to all elements. This aperture lies between the measured equivalent single-fracture apertures which ranged from 16 to 104 μm at the eight packers located near the tunnel perimeter. The model was used to determine values of $Q/\Delta H$ at the packer locations under pre-excavation conditions and for the pilot and slash excavation stages. Only heads and inflows were determined at the pilot and the slash stages.

5.6.2.2 Pre-Excavation Transmissivity Match

The transmissivity distribution was adjusted to better match field measurements of $Q/\Delta H$ at the packers and flow rates from the blast-holes. The best-fit transmissivity distribution (with transmissivities converted to equivalent parallel-plate apertures for presentation) is shown in Figure 5.19a. Only the near-field elemental apertures are shown in this figure. The transmissivity distribution accounts for the hydro-geologic features noted in the vicinity of Room 209 (Fig. 5.5). For example, the band of low transmissivity elements extending from the lower right to the upper left of the tunnel corresponds to the presence of a granodiorite dyke. The lower transmissivity of the dyke is inferred from borehole pressure interference tests which were done before the pilot excavation (Kozak and Davison, 1986). The low transmissivities in the lower right part of the mesh conform to a disappearance of the fracture zone at this location.

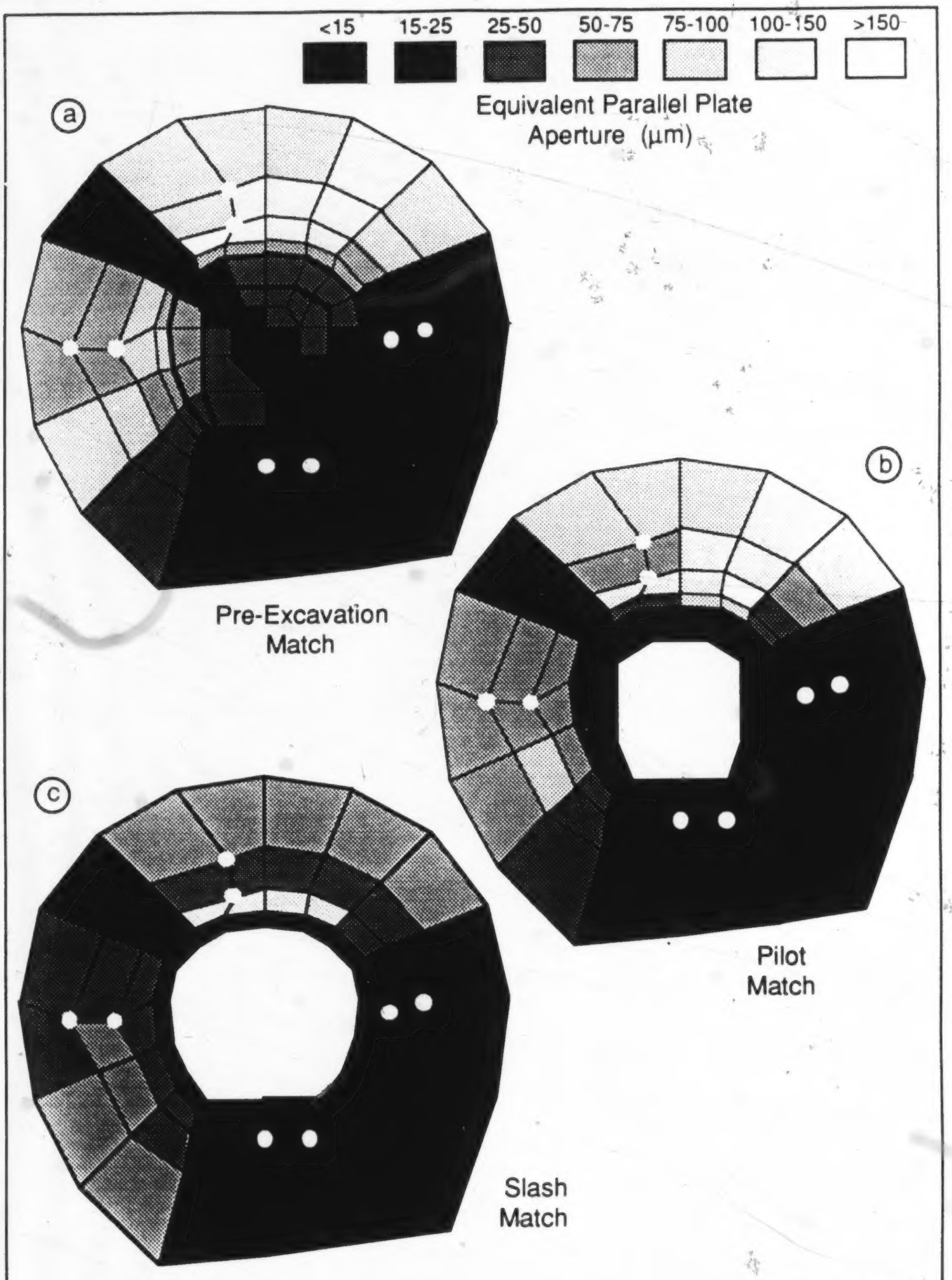

Figure 5.19 Trial and error matched transmissivity (aperture) distributions

5.6.2.3 Pilot Excavation with Pre-Excavation Transmissivities

The pilot tunnel was excavated and the hydraulic response in the fracture zone was simulated. Head distributions, Q/ΔH values at the packers, and the flow into the pilot tunnel were calculated.

5.6.2.4 Matching Post-Pilot Transmissivities

The pre-excavation transmissivity distribution was adjusted to achieve a better match with field measurements of head and Q/ΔH at the packers and the flow rate into the pilot. The best-fit transmissivity distribution (with transmissivities converted to parallel-plate apertures for presentation) is shown in Figure 5.19b. The transmissivity distribution shows a significant reduction near the pilot. The strongest transmissivity reduction occurs in the area between the pilot walls and the north and roof packers. The maximum transmissivity reduction was 7×10^{-6} m^2/s (or an equivalent aperture decrease of 117 μm). The transmissivity beyond about 2 m from the pilot walls shows little or no reduction. There were two small areas were the transmissivity increased. These are located at the upper right about 0.5 m from the pilot wall and about 0.5 m from the lower left corner of the pilot.

By comparison with the measured displacements in Room 209 (Lang et al., 1987b), the areas of greatest transmissivity reduction coincides with the extensometers showing the larger convergences. The area of little change or aperture increase coincides with the extensometers showing very small convergence (and possibly outward displacements).

5.6.2.5 Slash Excavation with Pilot Transmissivities

The slash was excavated and the hydraulic response in the fracture zone was calculated.

5.6.2.6 Matching Post-Slash Transmissivities

The transmissivity distribution which matched the pilot data was adjusted to better match field measurements of head and Q/ΔH at the packers and the flow rate after the slash. The best-fit transmissivity distribution (with transmissivities converted to parallel-plate apertures for presentation) is illustrated in Figure 5.19c. The transmissivity distribution shows an additional reduction near the slash. As with the pilot, the transmissivity decreases the most near the north and roof walls. The maximum transmissivity reduction was 2 x 10^{-6} m^2/s (or an aperture decrease of 99 µm). Again, a transmissivity increase occurs at the lower left and upper right corners of the tunnel.

5.6.3 Hydraulic Response in the Fracture Zone

The finite element results are compared to the measured hydraulic responses in the fracture zone in a series of figures. Figure 5.20 presents a comparison of steady-state heads at the packers. Figure 5.21 compares values of $Q/\Delta H$ determined from fluid withdrawal tests at the packers. The flows into the blast-holes and pilot and slash opening are given in Figure 5.22. The measured data presented in these figures represents most data taken during the excavation response experiment at Room 209 (Lang et al., 1987b). As nearly always, there are inherent uncertainties in the field measurements and instrumentation failures reduced the available data from some packers. For example, the two floor packers (F1 and F2) and the S1 packer failed after the pilot had intersected the fracture zone. Therefore, no head or packer test data is available for comparison and no figures are presented for these packers.

Figures 5.20 to 5.22 are designed to compare measured and predicted data at different excavation stages and for different transmissivity models. The 'pre-excavation' and 'blast holes' excavation stages correspond to transmissivity model 2. The 'blast holes' excavation stage refers to the drainage conditions created by the drilling of blast holes through the fracture zone. Since fluid inflows and heads were monitored during and after the drilling of these holes, a comparison with numerically simulated drainage at blast hole locations was possible. The 'pilot' and 'pilot fit' excavation stages corresponds to transmissivity models 3 and 4 respectively. The 'slash' and 'slash fit' excavation stages corresponds to transmissivity models 5 and 6 respectively. The constant transmissivity model (1) data is plotted for comparison with the 'fitted' transmissivity data at the appropriate excavation stages. The field data showed fluctuations with time. The measured 'low' and 'high' values plotted in the figures represent the extreme values which were measured and give an indication of the variability in field data.

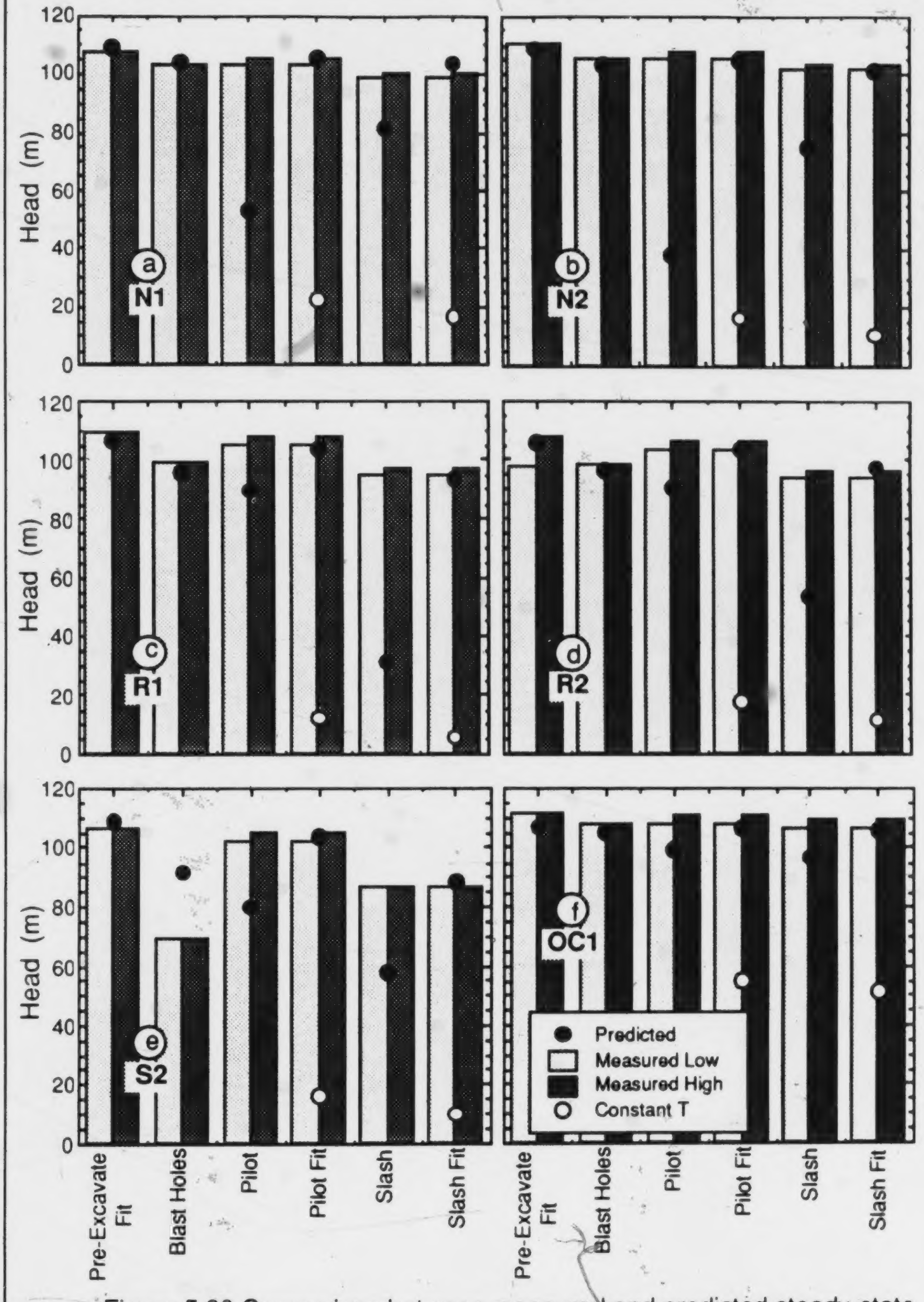

Figure 5.20 Comparison between measured and predicted steady-state heads at the packer locations for different transmissivity distributions

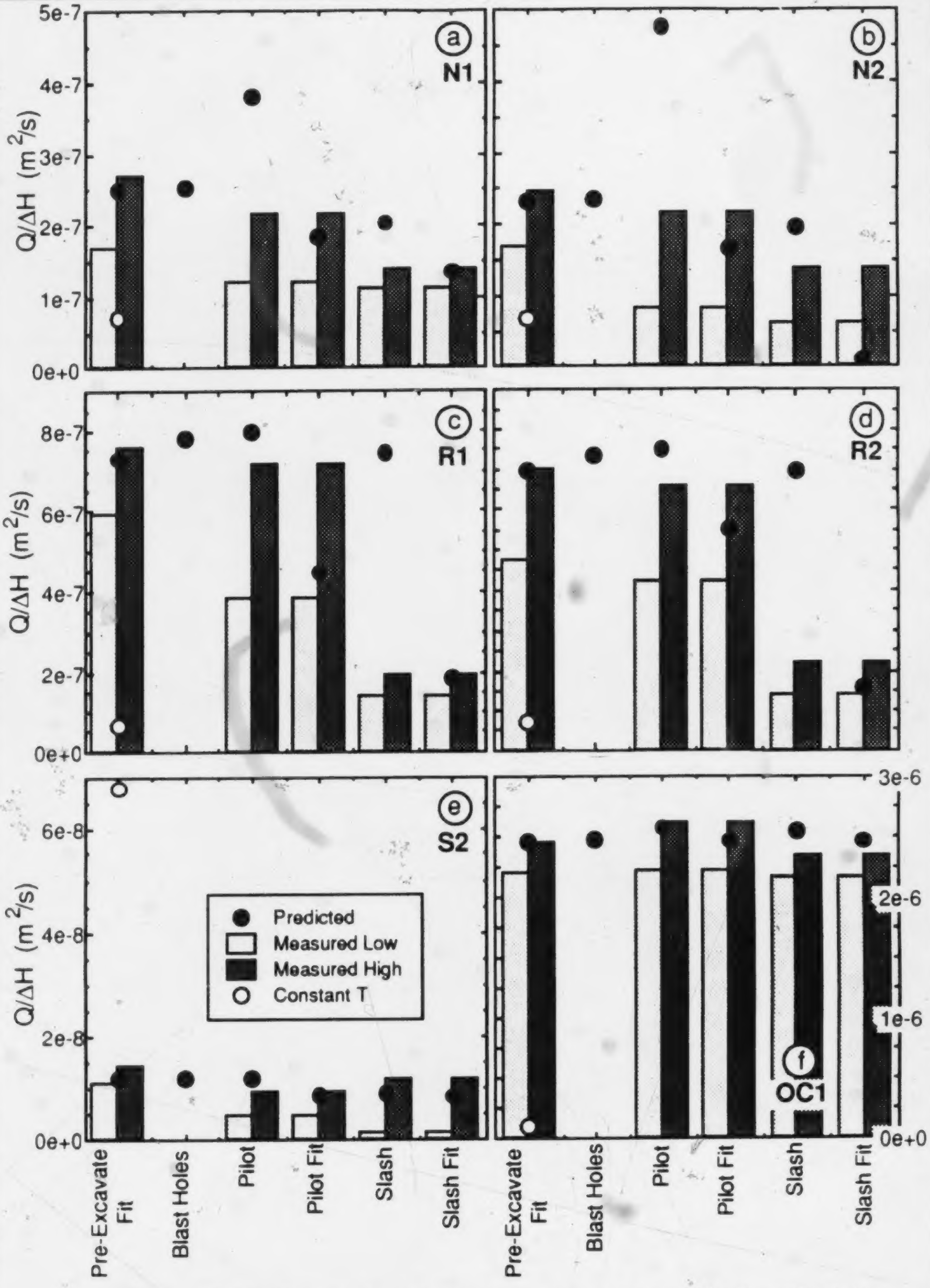

Figure 5.21 Comparison between measured and predicted Q/ΔH at the packer locations for different transmissivity distributions

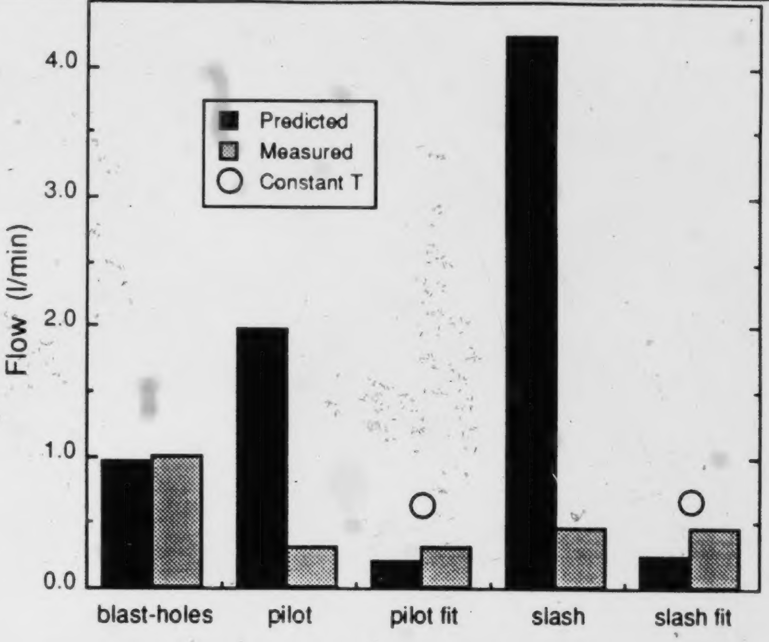

Figure 5.22 Predicted and measured (estimated) inflows into the Room 209 tunnel from the fracture zone

5.6.3.1 Steady-State Heads at Packers

In Figure 5.20, the calculated and measured steady-state heads at the nine packers are compared. Note that for pre-excavation conditions (with no blast-holes) the heads are independent of the transmissivity distribution. The pre-excavation heads are close to those measured implying that the boundary conditions specified for the mesh are appropriate. In contrast, the striking difference between measured and calculated heads for the 'unmatched' pilot and slash models reveals inadequacies in the transmissivity distributions of these models. It also demonstrates that the transmissivity changed during each excavation stage.

The three 'fitted' models provided good agreement with the measured heads, even when modelling the blast-holes. Since the packers are located close to the openings, the measured heads are very sensitive to the local transmissivities around each packer. A ring of low transmissivity between the packer and the opening greatly increases the steady-state head at the packer. The measured heads were all much higher than heads predicted from the constant transmissivity model (shown by open circles in the figures). Therefore, the head data alone indicate a zone or ring of reduced transmissivity around both the pilot and the slash openings. Furthermore, as the excavation proceeds, the transmissivities required to match the field data during the slash must be reduced near the opening from those of the pilot.

5.6.3.2 Packer Test Q/ΔH Values

Figure 5.21 displays the values of Q/ΔH determined from fluid withdrawal tests performed at the packers. There is considerable difference between the measured and predicted values for the constant transmissivity model. This is understandable because Q/ΔH reflects the transmissivity around a packer and it is improbable that the fracture zone initially had a constant transmissivity. The transmissivity distributions near the tunnel have a significant effect on the predicted values of Q/ΔH at the north and roof packer locations. By neglecting the excavation dependent change in transmissivity, the pilot and slash values of Q/ΔH are much higher than those measured. Incorporation of a reduced transmissivity near the tunnel (pilot-fit and slash-fit) reduces the values of Q/ΔH to the range which was measured.

There are time or excavation dependent changes in the measured values of Q/ΔH. This variation appears as the range between the low and high values in Figure 5.21. Nevertheless, the measured Q/ΔH values show one consistent feature. They tend to drop after the pilot is excavated and again after the slash is excavated. For example, note the large decrease in Q/ΔH at the two roof packers (R1 and R2) from the pilot to the slash stage. As discussed in Section 4, the change in flow boundary conditions caused by an excavation should increase Q/ΔH measured at a packer (other conditions being constant). The fact that the measured values of Q/ΔH dropped (Fig. 5.6) after the excavation intersected the fracture zone is strong evidence for a transmissivity reduction at Room 209. The reduction must have been large enough to counteract the boundary condition effect. Furthermore, the transmissivity must be excavation dependent since the drop in Q/ΔH only happens as the excavation passes the fracture zone.

5.6.3.3 Flows into the Blast-Holes, Pilot, and Slash

Figure 5.22 shows the predicted and measured flows. The blast-hole flows were measured by capturing the discharge after the holes were drilled. Only a few holes in the upper right (southwest) quadrant of the blast pattern had measurable discharge. No flow was observed from the floor. However, any flow from the floor may have been obscured by muck and rubble. The measured flows after the pilot and the slash excavations are rough estimates based on the observed seepage along the exposed fracture traces (Lang et al., 1987b).

Although the measured flows may be inaccurate, they still indicate a large flow reduction associated with the pilot intersecting the fracture zone. The 'fitted' transmissivity models, by virtue of their reduced transmissivities near the tunnel walls, also show a prominent decrease in flow after each excavation intersects the fracture zone.

5.6.3.4 Summary

The different transmissivity models and the numerical modelling results (pressure heads, packer test results, and flow rates) convincingly demonstrate that zones of reduced transmissivity are consistent with the observed hydraulic response in the Room 209 fracture zone. Furthermore, the transmissivity reduction must have occurred during excavation past the fracture zone. This analysis did not presuppose any mechanism for transmissivity reduction. However, the association between excavation and resulting transmissivity change and the locations of the greatest transmissivity changes are consistent with the hypothesis of shear-induced transmissivity changes in a fracture zone. The driving force for the shear displacements must come from the stresses released by the excavation process.

A 'fitted' transmissivity distribution may be obtained after any excavation stage using the hydraulic monitoring data to calibrate the numerical model. However, this distribution will not predict the hydraulic response in the fracture zone after additional excavation stages since the excavation modifies the transmissivity distribution. Therefore, one needs to know how the transmissivity changes, i.e., the mechanism for excavation induced change, before predictive capabilities are possible.

5.6.4 Transmissivity Distributions Based on Shear Displacements

The hydraulic response in the fracture is analysed in this section assuming that shear displacements cause the change in transmissivity distributions. Whereas in Section 5.6.2 and 5.6.3 the transmissivity distributions were created by a trial and error process which matched the measured hydraulic responses, in this section, shear displacements from Section 5.5 are used to calculate transmissivity changes in the fracture zone. By comparing the modelled and measured hydraulic responses in the Room 209 fracture zone, the hypothesis of shear-induced transmissivity changes is evaluated.

The finite element model was similar to the one used in Section 5.6.1 except that the excavation shape was slightly modified to better represent the intersection between the

Room 209 fracture zone and the excavation. Figure 5.23 shows the inner part of the seepage mesh and the locations of the packers. The boundary conditions imposed on the mesh were identical to those illustrated in Figure 5.17.

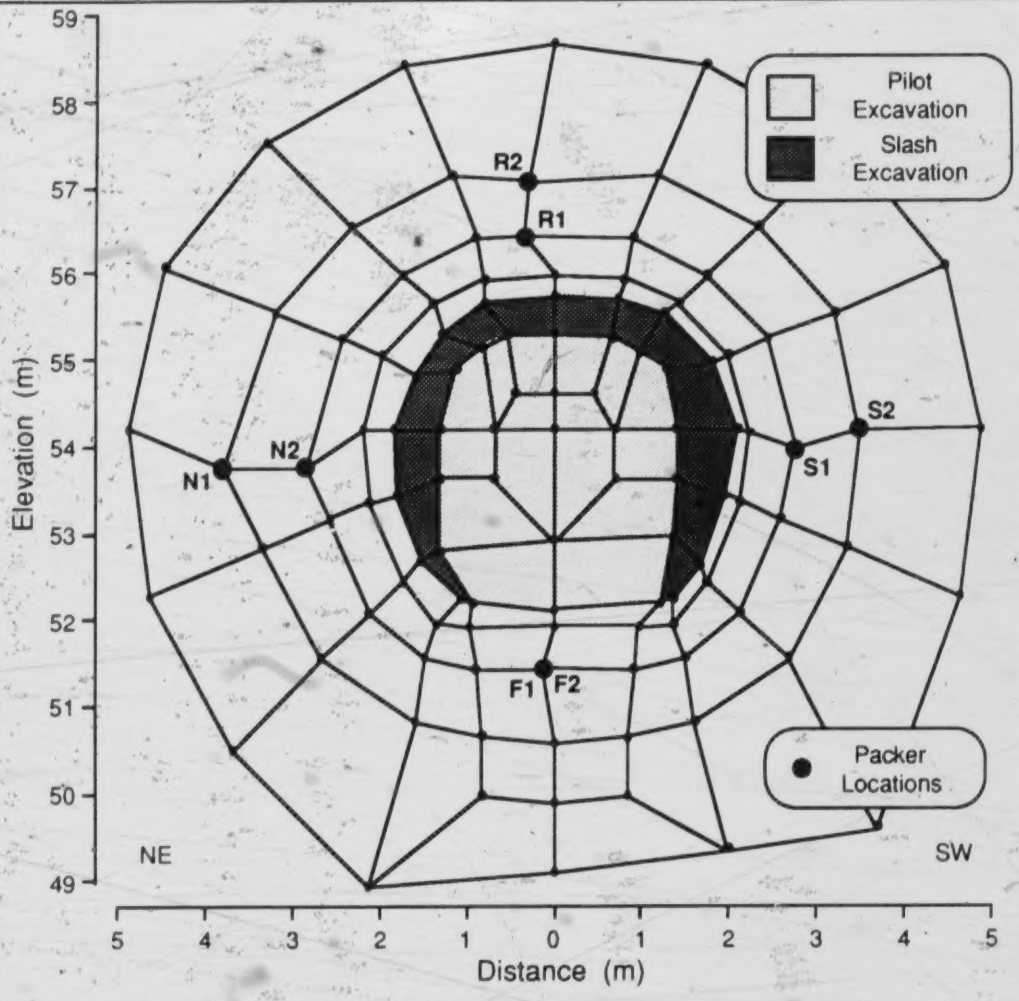

Figure 5.23 Modified inner part of finite element seepage mesh showing pilot and slash and nodes representing packer locations

The shear displacements relative to excavation of the Development Room are used to calculate transmissivity changes in the elements. Since shear displacements are taken relative to the Development Room, transmissivities were also taken relative to the Development Room. The initial (or Development Room) transmissivities were based on the transmissivity distribution obtained from the 'fitted' pre-excavation distribution found in Section 5.6.2. However, the geometric modifications associated with the new mesh necessitated some further trial and error fitting of transmissivities to obtain a better pre-excavation transmissivity distribution. This distribution is presented in Figure 5.24. The transmissivity distribution is similar to the distribution in Figure 5.19a. A zone of low transmissivity extends from the lower south side to the upper north side of the tunnel. The transmissivities also reflect the pinching out of the fracture zone below the tunnel.

All changes in fracture zone transmissivity resulting from excavation-induced shear displacements are taken relative to the initial distribution (Fig 5.24). The changes in transmissivity for each excavation step were calculated from the shear displacements assuming the following conditions:

1) The primary fractures are inclined 45° to the fracture zone.

2) The secondary fractures are perpendicular to the primary fractures.

3) The initial apertures of the primary and secondary fractures were equal, but varied in location throughout the fracture zone as reflected in the initial transmissivity distribution.

4) The relationship between shear displacement and transmissivity change was assumed isotropic, i.e., the orientation of the fracture zone was disregarded.

5) The shear displacements were reduced by a factor of five prior to use in the shear-transmissivity change relationship.

The geometric structure of the fractures in the Room 209 fracture zone could not be determined. Therefore the least complicated form of the shear-transmissivity relationship was adopted. Assumptions 1 to 3 define the form of the relationship (Eqn. 3.13). The selected orientations of the primary and secondary fractures creates a relationship which is independent of the direction of shear displacement. Note, the fracture zone flow model presented in Figure 3.3 is a phenomenological model used to derived the shear-transmissivity change relationship. This model does not represent, in a physical sense, the real fracture structure in the Room 209 fracture zone since it does not account for the three-dimensional nature of the flow paths or direction dependent changes in transmissivity. Assumption 4 is used to generalize the relationship to all directions in the fracture zone.

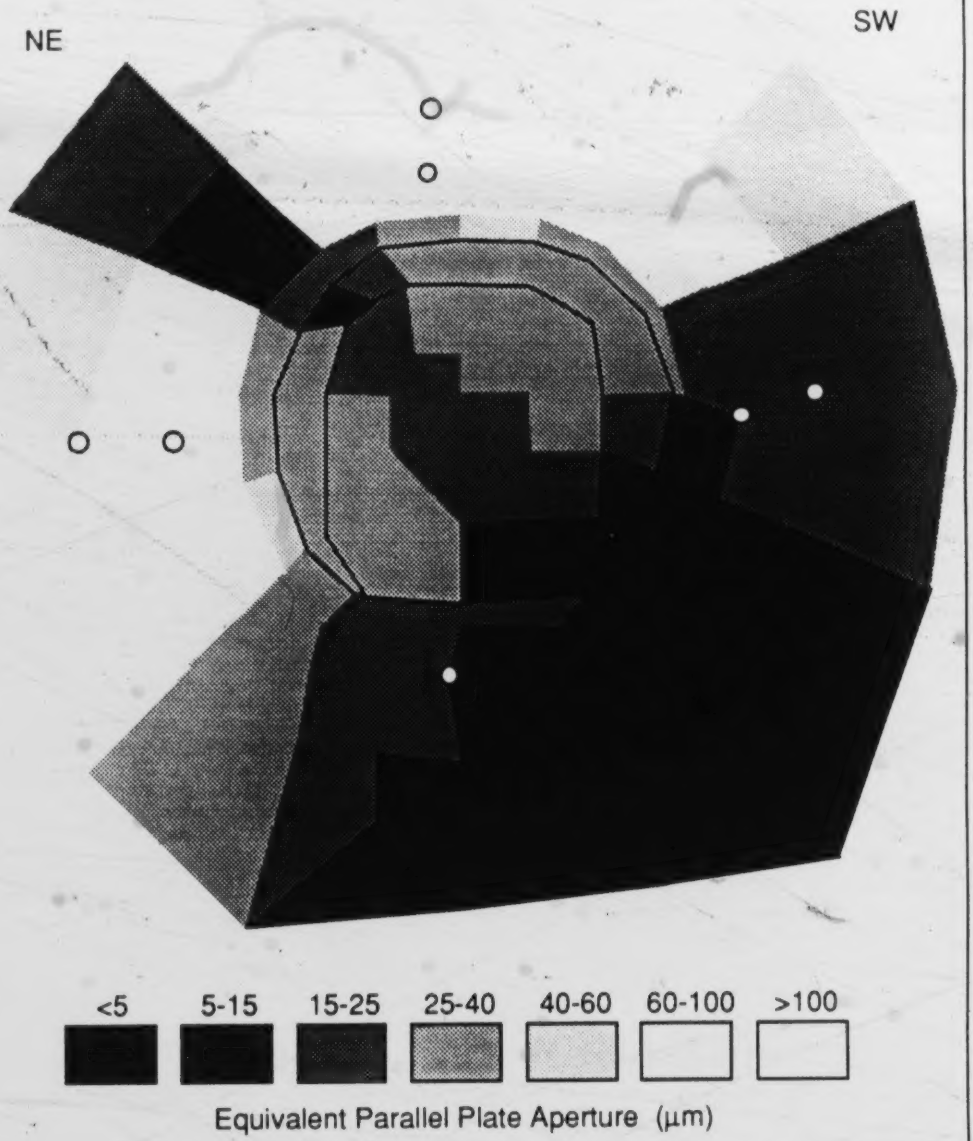

Figure 5.24 Initial or Development Room transmissivity (aperture) distribution

As initial application of the shear displacement - transmissivity change relationship with the shear displacements obtained in Section 5.5.2 yielded excessive transmissivity reductions and since the choice of shear stiffness for the joint elements was somewhat subjective, condition 5 was assumed in order to reduce the shear displacements. Alternatively, the form of the shear displacement - transmissivity change relationship could have been altered such that the initial shear displacements would cause more realistic transmissivity changes. Assumption 5 should be roughly equivalent to increasing the shear stiffness of the joint elements by a factor of five. An increase in shear stiffness to 15 MPa/mm would make the normal stiffness to shear stiffness ratio equal to 20 which is comparable to the minimum ratios of 10 to 20 suggested by Bandis (1990). Computing cost limitations precluded re-analysis using higher shear stiffnesses.

5.6.4.1 Transmissivity Distributions and Seepage Modelling

The transmissivity distributions near the tunnel for the different excavation steps are depicted by showing the equivalent single fracture apertures in Figures 5.25 and 5.26. The high shear displacements associated with step P2 cause a continuous ring of low transmissivity (aperture) around the opening. The transmissivity or aperture distributions at the other excavation steps vary as a function of the shear displacements. For example, the increase in shear displacements at the north wall from step P3 to P4 (Figs. 5.12c and d) results in a corresponding decrease in aperture at the wall (Figs. 5.25c and d). It is worthwhile noting that the low transmissivity ring present when the pilot face is at the fracture zone (Fig. 5.25b) partially opens when the face passes the fracture zone (Figs. 5.25c and d)

During the Slash excavation, large shear displacements were generated at step S2 (Fig. 5.13b). The higher shear displacements occurred at the roof and south wall. Hence, a band of low transmissivity extends from the roof to the floor along the south side of the tunnel (Fig. 5.26b).

The distribution of transmissivity near the opening has a dominant control on the hydraulic response in the fracture zone. The steady-state heads and tunnel inflows were determined by series of finite element seepage analyses using the transmissivity distributions presented in Figures 5.25 and 5.26. In addition, fluid withdrawal tests were simulated at each packer location for each transmissivity configuration.

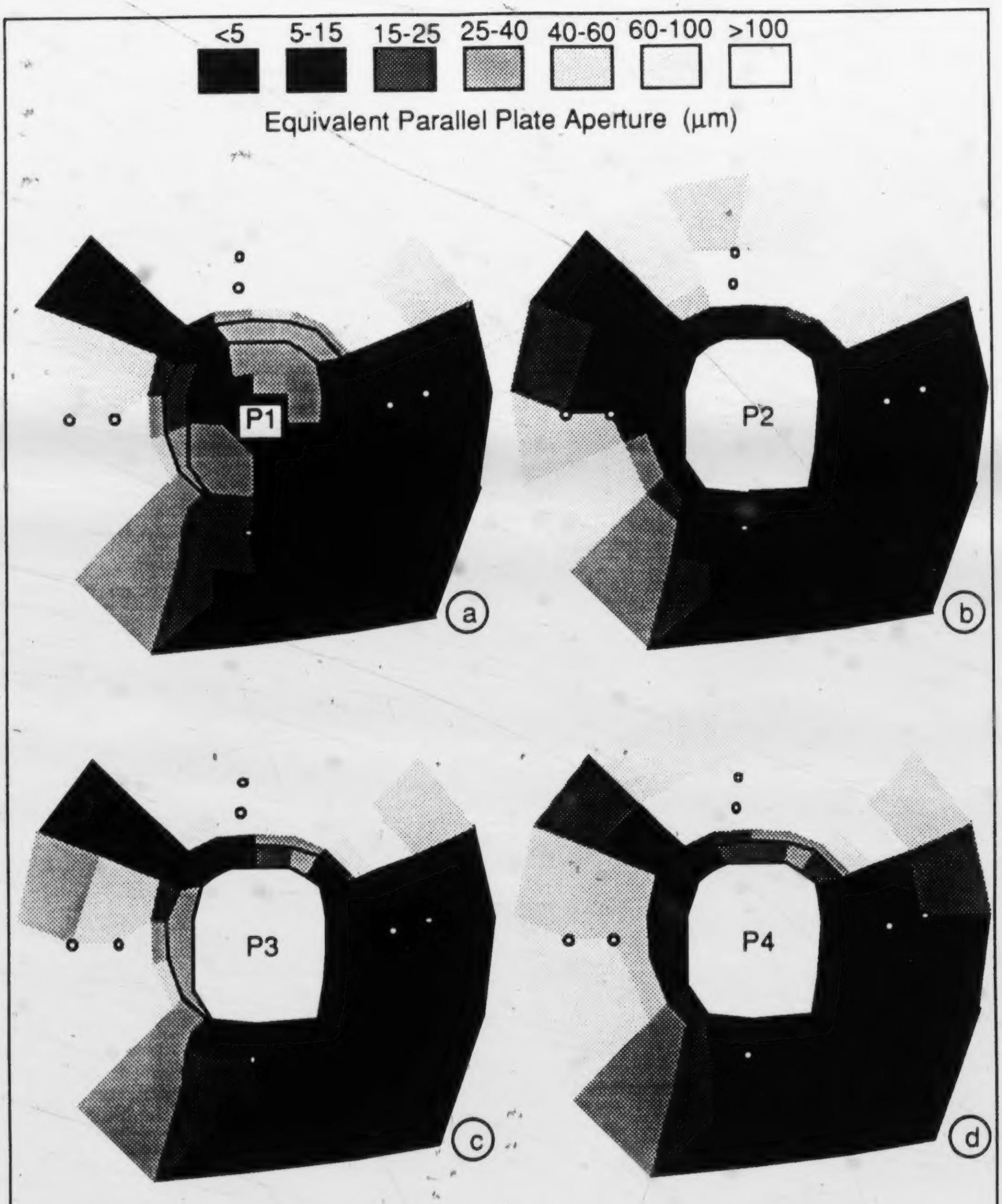

Figure 5.25 Transmissivity (aperture) distributions during pilot excavation based on shear displacements

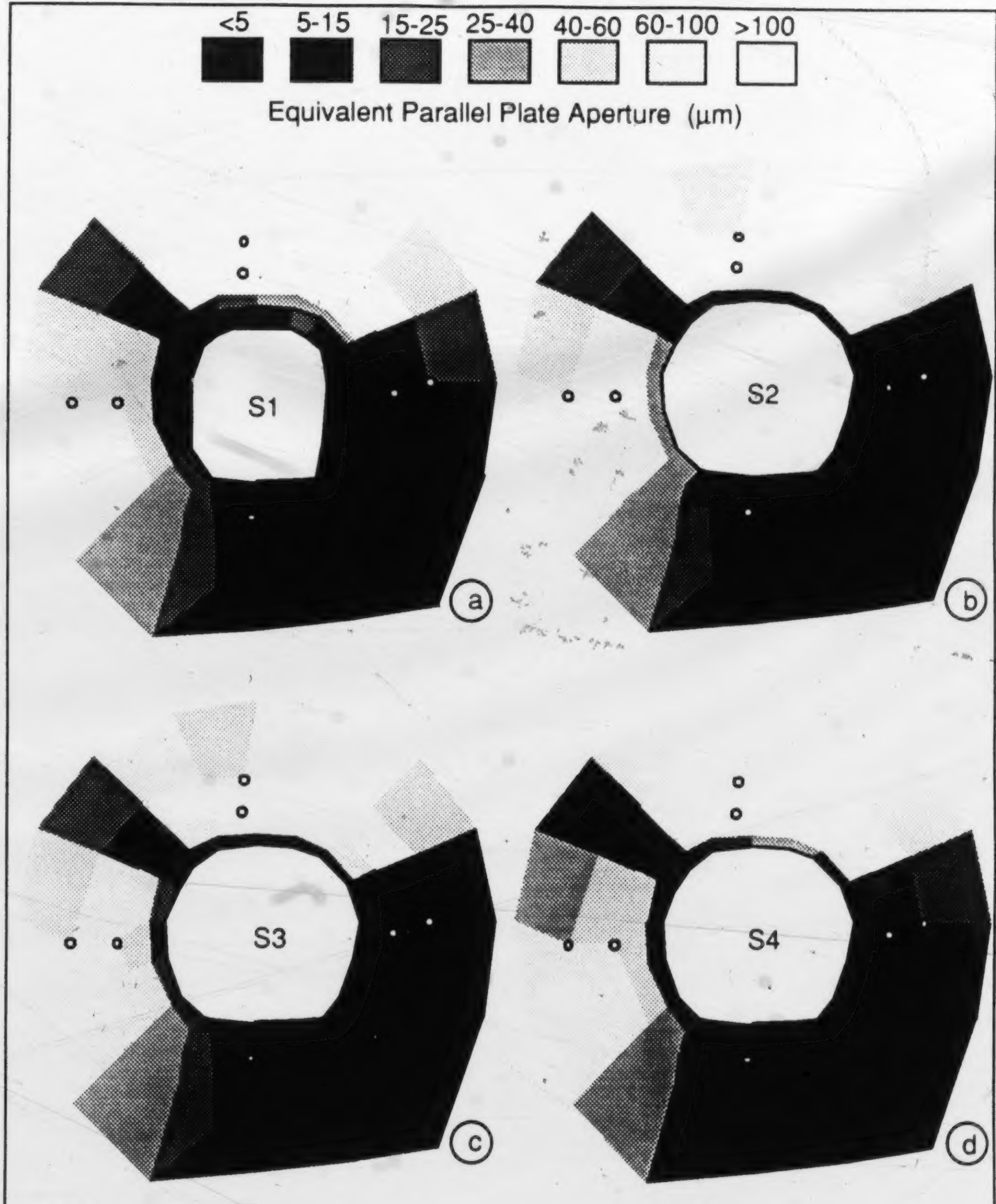

Figure 5.26 Transmissivity (aperture) distributions during slash excavation based on shear displacements

5.6.4.2 Flows into the Tunnel

The fracture zone specific discharge is graphically presented in Figure 5.27. It was calculated from the elements around the perimeter of the tunnel. The length of the arrows in Figure 5.27 corresponds to the discharge magnitude while the orientation of the arrows gives the direction of flow at different locations around the tunnel. The locations of highest inflow are situated where the ring of low transmissivity has gaps. The gaps or regions of higher transmissivity exist at varying locations at the north wall and roof. No significant flow occurs through the floor or south wall at any excavation step. At excavation step P1 the fracture zone had not yet been intersected by the pilot and hence, no flows are calculated. When the pilot excavation intersects the fracture zone at step P2 the high shear displacements generated a complete ring of very low transmissivity around the tunnel. This ring of low transmissivity essentially prevented any inflow. The location and directions of inflow at the other excavation steps are presented in Figure 5.27.

The measured inflow after the pilot was roughly 300 ml/min and after the slash 450 ml/min (Lang et al., 1987b). These measurements are only approximate yet they compare favourably with the total inflows predicted from the seepage modelling. The predicted total inflows into pilot and slash tunnels are given in Figure 5.27 and average 272 ml/min for the pilot (steps P3, P4, and S1) and 513 ml/min for the slash (steps S2, S3, and S4).

5.6.4.3 Steady-State Heads

The head distributions or heads at the packer locations are not controlled by the transmissivity magnitudes but by the spatial distribution of the transmissivities around the tunnel. This is in contrast to the values of $Q/\Delta H$ which are more sensitive to the magnitude of transmissivities in the area near the packer. Figure 5.28 presents a comparison between measured and predicted heads at all packer locations for all excavation steps. For a perfect fit, all points would lie on the dashed line. Most points fall within a range of ± 10 % to the dashed line. A difference of less than 10 % between measurements and predictions is considered a good fit. The points of S1 (P2), N2 (P3 and S2), and N1 (P3 and S2) show larger deviations. However, data from steps P2 and S2 are subject to the greatest uncertainty due to face effects, non-linear rock responses, and high stress and displacement gradients. The predicted heads after the pilot (P4) and the slash (S4) show good correspondence with the measured heads. Measured heads which are higher than those predicted suggest an under estimation of the shear - transmissivity dependency.

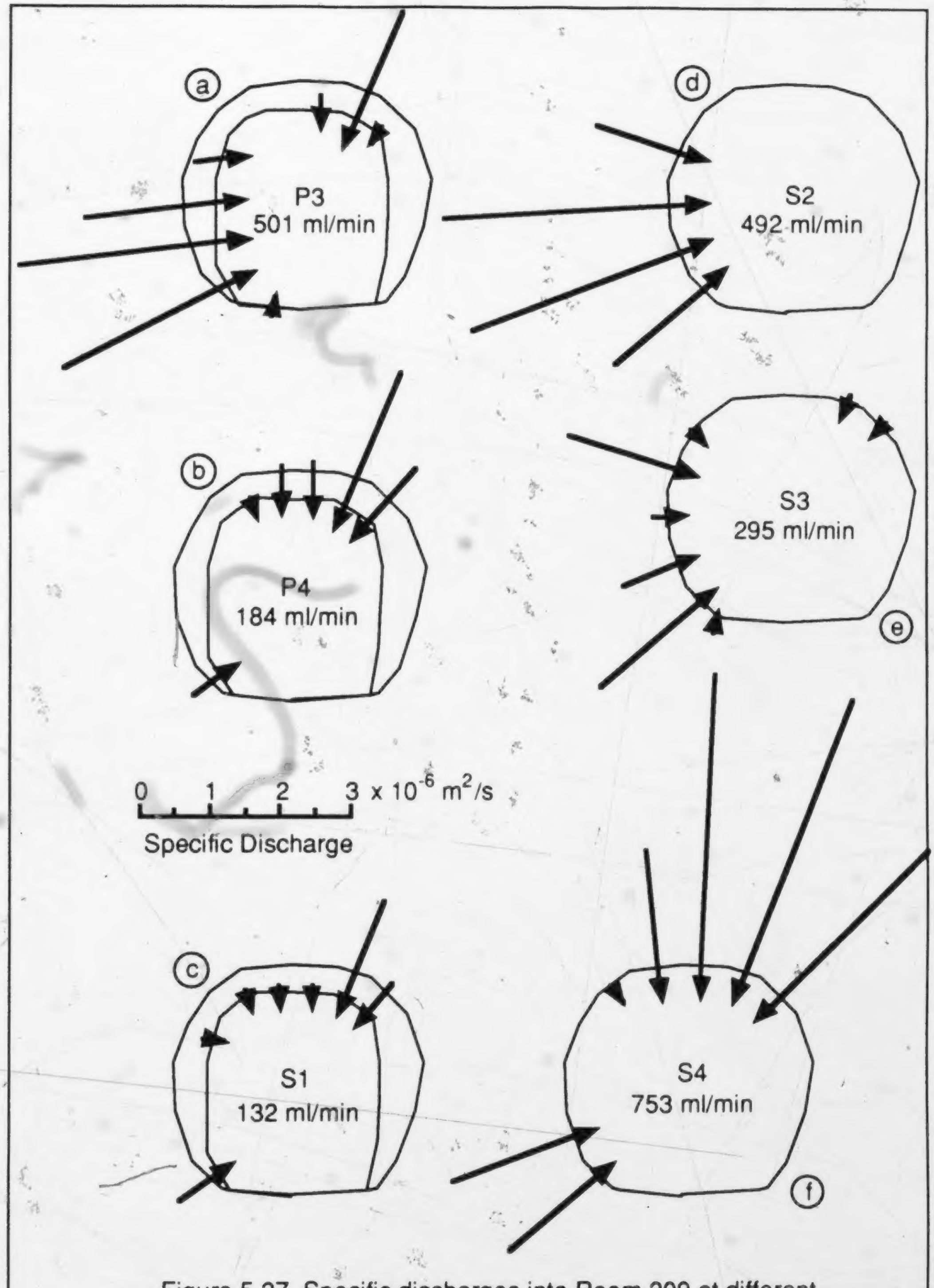

Figure 5.27 Specific discharges into Room 209 at different excavation steps and total inflows

Figure 5.29 compares the heads at the N1, N2, R1, R2, S2, and OC1 packer locations for the different excavation steps. These packer locations supplied the most reliable field measurements of steady-state heads around the tunnel. Excavation steps where measurements are not available for packer S2 are indicated by a question mark. These figures compare the measured heads with heads predicted using the transmissivity distributions presented in Section 5.6.4.1 (labelled 'predicted') and with heads predicted using the best-fit initial transmissivity distribution (Fig. 5.24) but assuming no shear-dependent transmissivity change (labelled 'no shear').

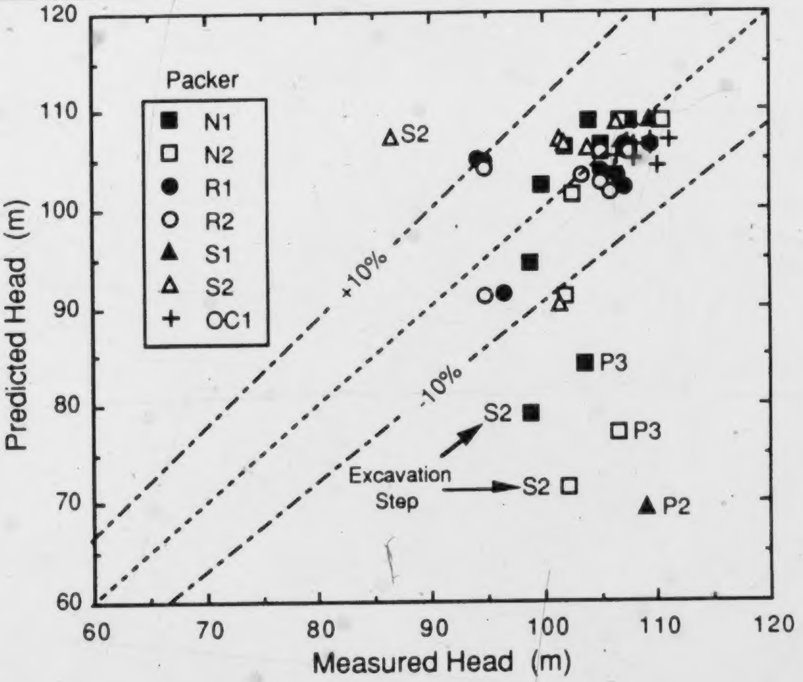

Figure 5.28 Measured and predicted steady-state heads at all packers for all excavation steps

The differences between the 'predicted' and the 'no shear' heads are due solely to the influence of shear-dependent transmissivity changes. The 'no shear' heads show the head changes caused by the altered hydraulic boundary conditions resulting from the tunnel excavation. The transmissivity distribution remained constant for the 'no shear' runs. The 'no shear' heads are consistently less than the measured and predicted heads at all excavation steps after the pilot intersected the fracture zone. The incorporation of shear-dependent transmissivities causes an increase in steady-state heads. These heads are much closer to the measured heads when compared to the heads obtained from the unchanged (no shear) transmissivity distribution.

The head profiles at the north side (horizontal profile) and above the tunnel (vertical profile) after excavation of the pilot (P4) and the slash (S4) are given in Figure 5.30. This figure clearly shows the improvement in predicted heads when shear-dependent transmissivity is taken into account. The head gradient must be extremely high near the tunnel to match the measured heads at about 1 to 2 m from the wall. A high pressure gradient is strong evidence for a band of low transmissivity existing around the tunnel between the wall and the packer locations. These simulations demonstrate that an overall transmissivity decrease near the tunnel (dependent on excavation advance) is needed for correspondence between measurements and predictions. Furthermore, a shear-dependent transmissivity reduction is consistent with changes in measured hydraulic response.

5.6.4.4 Fluid Withdrawal Tests

Fluid withdrawal tests were numerically simulated at the various packer locations in the finite element seepage mesh. Values of Q/ΔH were determine by withdrawing a known quantity of fluid at a packer node and determining the corresponding drop in head relative to the steady-state head prior to the packer test. As noted earlier, this technique for simulating packer tests is mesh dependent. Although the magnitude of Q/ΔH at any node depends on the mesh refinement near that node, the changes in Q/ΔH (increases or decreases) are valid indications of changed hydraulic conditions in the fracture zone.

Figure 5.31 compares the measured and modelled values of Q/ΔH at all packers as a function of time. The days when the pilot and the slash intersected the fracture zone are shown on the figure. The wide range in values for Q/ΔH necessitated separation of the figure into two parts. The north, roof, and OC1 packers were situated in a region of relatively high transmissivity and hence, the values of Q/ΔH are high (Fig. 5.31a). The predictions best match the measured responses at these packers. This is encouraging since these packers also provided the most reliable field measurements.

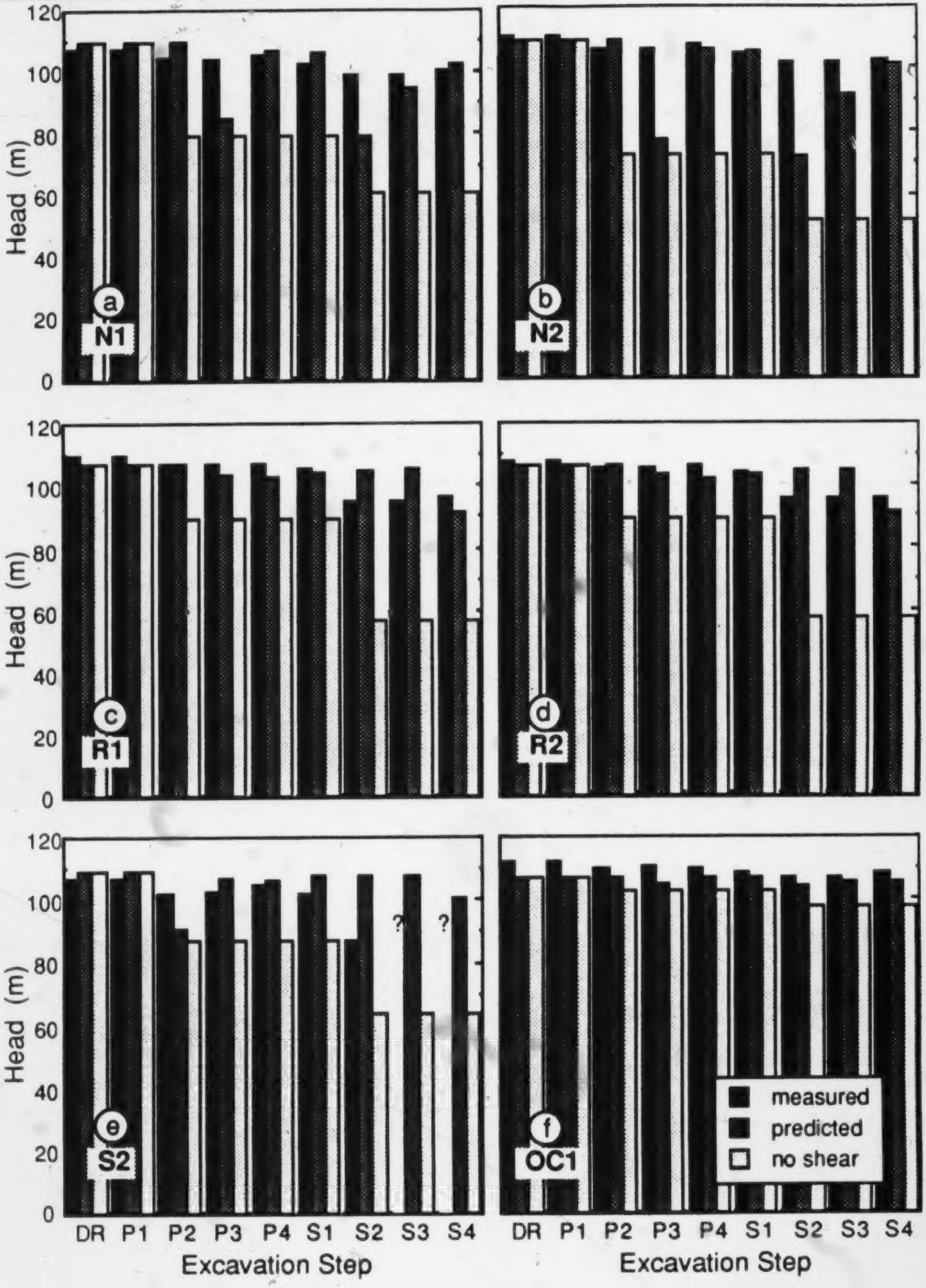

Figure 5.29 Measured and predicted heads at packer locations versus excavation step

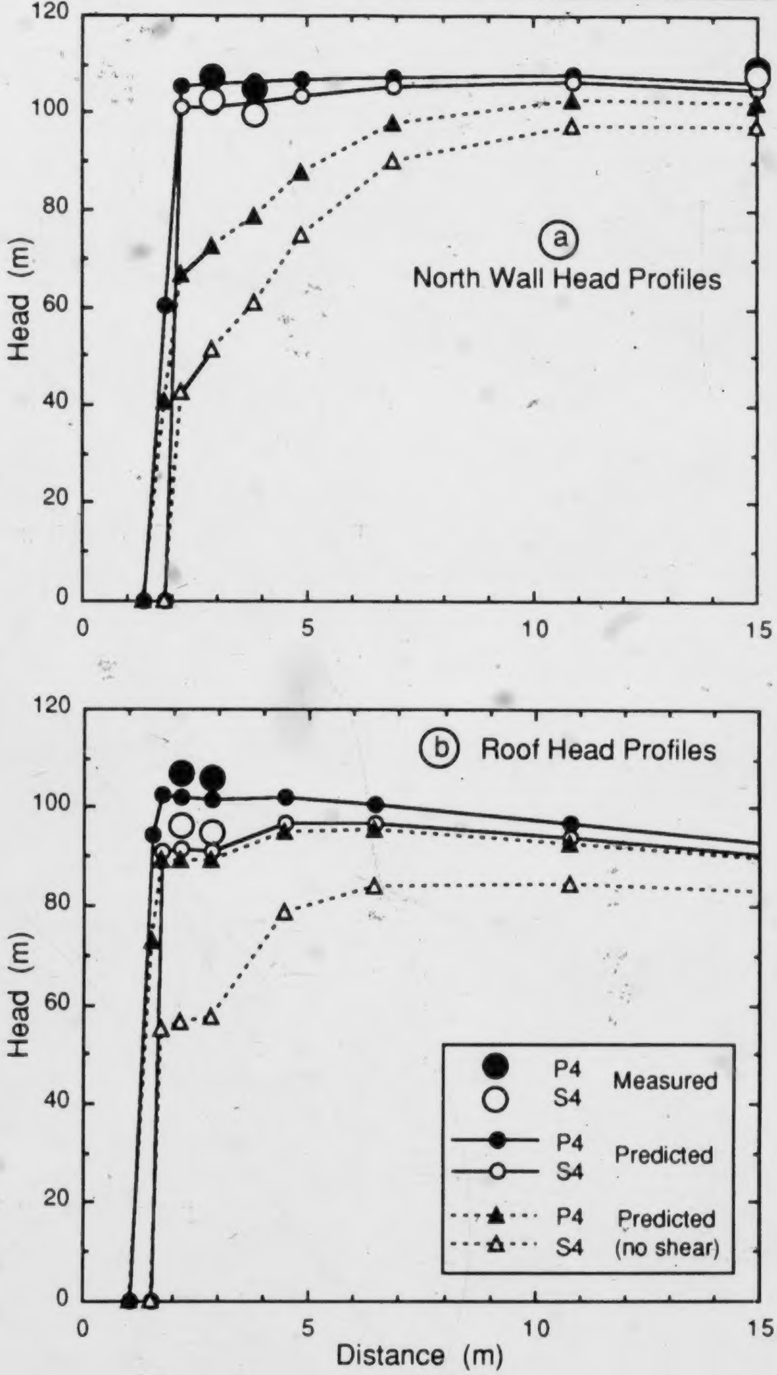

Figure 5.30 North and roof predicted head profiles

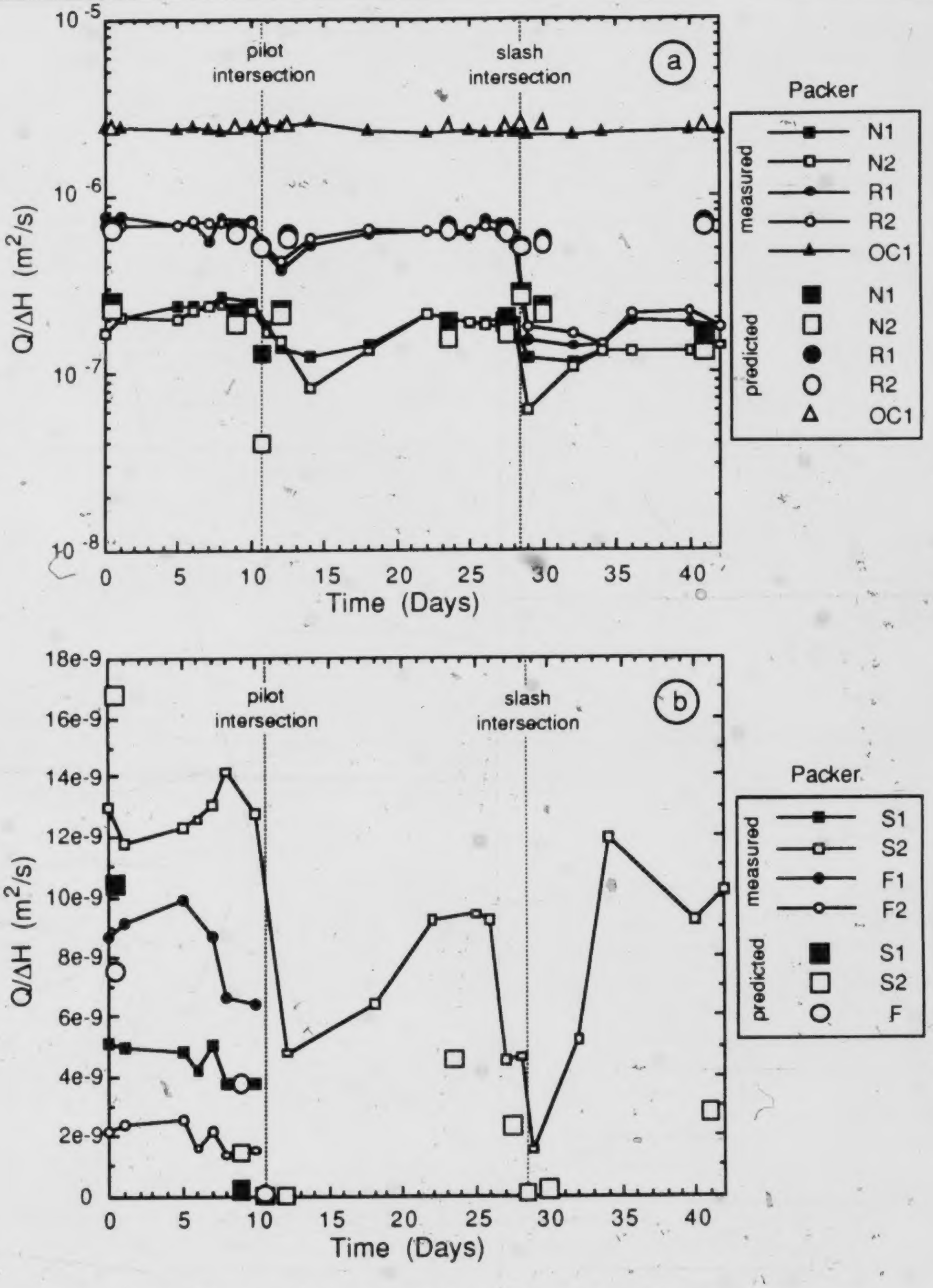

Figure 5.31 Measured and predicted values of Q/ΔH versus time or excavation sequence

The floor and south packers were in a region of low transmissivity and near the boundary of the fracture zone. In areas of low transmissivity, slight shear displacement can completely close the fracture. Hence, the transmissivity and Q/ΔH are extremely sensitive to any shear. The floor and S1 packers failed after the pilot had intersected the fracture zone (Fig.5.31b). Predicted data for these packers are only shown until the P2 excavation steps. The predicted Q/ΔH at S2 displays the same trend as the measured values except the that the predicted values vary over a wider range. The most important feature with the measurements and the predictions is the drop in values as the face passes the fracture zone and then the recovery in Q/ΔH as the excavation proceeds.

The predicted Q/ΔH values drop essentially to zero when the excavation face intersects the fracture zone for all packers in Figure 5.31b. The measured values did not drop to zero indicating that perhaps the shear-transmissivity process is less dominant at low initial transmissivities. This seems reasonable since experimental evidence has shown that even when fractures are subject to extremely high normal stresses there is usually a component of irreducible flow (Raven and Gale, 1985; Pyrak-Nolte et al., 1987). Similarly, under shear it is unlikely that a fracture can be completely closed off; there will always be a small, residual amount of flow. This implies that an improved shear-transmissivity change relationship should account for the initial transmissivity and place a certain minimum below which the transmissivity can not be reduced by shear alone.

Figure 5.32 shows only the data from the north and roof packers. Fluid withdrawal tests at the north and roof packers and OC1 provided the best field data for comparison with modelling results. Since the OC1 packer was beyond the zone influenced by the tunnel excavation there was essentially no change in transmissivity near the packer and hence, both measured and modelled values of Q/ΔH are nearly constant during the excavation (Fig. 5.31a). The predicted values of Q/ΔH obtained using the transmissivity distributions generated by the excavation-induced shear displacements are plotted on Figure 5.32 with individual square and circular symbols. The influence of a hydraulic boundary condition change each time the excavation intersected the fracture zone is shown by the predictions of Q/ΔH which assumed no transmissivity changes after the Development Room step (solid and dashed lines).

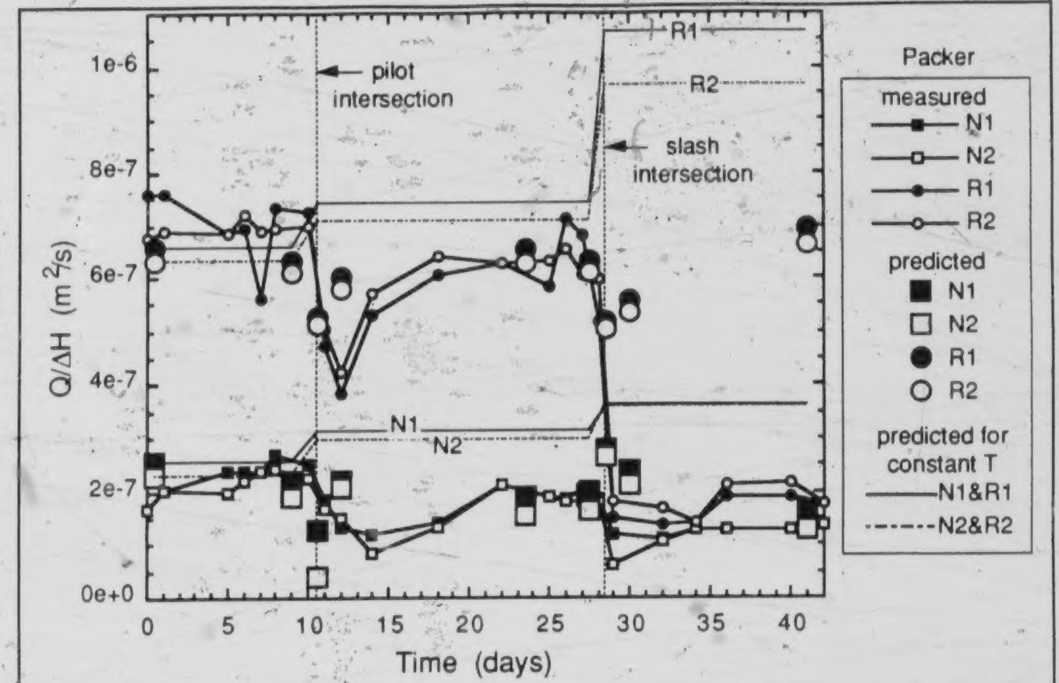

Figure 5.32 Measured and predicted values of Q/ΔH at the north and roof packers (showing the predicted Q/ΔH if there were no transmissivity changes due to excavation)

The north and roof packers are situated close to the tunnel and Q/ΔH is influenced in the following manner:

1) Intersection of the pilot and then the slash with the fracture zone changes the hydraulic boundary conditions (solid and dashed lines). Numerical modelling in Section 4 has shown that the imposition of a zero pressure boundary condition near a packer location causes an increase in Q/ΔH determined from fluid withdraw tests. This effect is not dependent on the position of the excavation face once the fracture zone intersection has occurred.

2) Shear displacements generated near the tunnel are assumed to cause an associated transmissivity reduction. The resulting zone of reduced transmissivity near the tunnel causes Q/ΔH to decrease. Since the shear displacements vary depending on the position of the excavation face, the transmissivity distribution and Q/ΔH also display excavation dependency.

Superposition of these two factors in combination with the initial transmissivity distribution determines the final values of Q/ΔH as the excavation proceeds past the fracture zone. Figure 5.32 shows that the measured Q/ΔH decreases as the excavation face intersects the fracture zone (except during the slash for the north packers). This implies that the transmissivity reduction has a greater influence than the altered boundary conditions. The increase in Q/ΔH at the north packers during intersection of the slash and the fracture zone is caused by the shift in shear displacements to the roof and south sides for step S2 (Fig. 5.14b). This shift resulted in temporarily higher transmissivities at the north wall of the tunnel for step S2.

The fit between measured and modelled packer results is best for the pilot excavation steps. Predictions of Q/ΔH based on the shear-dependent reductions in transmissivity are lower than the constant transmissivity predictions and are close to the measured responses. Figure 5.32 clearly demonstrates that shear-dependent transmissivity changes provide a mechanism to explain the observed excavation-dependent Q/ΔH response at Room 209.

For the pilot excavation, the measured Q/ΔH nearly recovers to the pre-intersection values. Therefore, the transmissivity distribution is excavation dependent. Keeping in mind that without a transmissivity reduction the values of Q/ΔH would abruptly increase when the excavation face intersected the fracture zone (boundary condition effect), the predicted Q/ΔH show behaviour similar to the measurements.

For the slash excavation, the final predictions at the north packers are very close to those measured. The predictions with shear-dependent transmissivity changes are much closer to the measurements than are constant transmissivity predictions. The greatest disagreement between predictions and measurements occurs at the roof packers.

The correspondence between predicted and measured Q/ΔH is poorest at the roof packers for steps S3 and S4. The fact that the measured values of Q/ΔH do not recover after the slash intersection indicates the possibility that shear-induced displacements caused non-recoverable damage to the flow paths. This damage would prevent the values of Q/ΔH from recovering at the roof after the face passed the fracture zone. The assumption of fully recoverable (elastic) shear-transmissivity reduction may require modification to better predict the measure responses. Alternatively, the increase in normal stress at the roof (see Fig. 5.8) which remains after the tunnel is excavated may have induced non-recoverable fracture closure. Using data from the roof packers only, one can not distinguish between these alternative explanations or determine which is more likely.

It is recognized that normal stresses have an influence on fracture transmissivity and certainly normal stresses are playing a minor role in the Room 209 fracture zone. However, the shear-induced transmissivity reduction mechanism provides a consistent explanation for the observed response at all locations around the tunnel for all excavation stages. Simple modifications of the shear-induced transmissivity model to account for irreducible flow at very small apertures and non-recoverable reductions in aperture under certain conditions of high shear would improve the model. This does not exclude the possibility that normal stress and fracture closure are contributing to the observed hydraulic response, rather it suggests that shear dominates the hydraulic response.

6 CONCLUSIONS AND RECOMMENDATIONS

This thesis presents results from an examination of the hydro-mechanical behaviour of fracture zones in crystalline rock masses subject to excavation-induced shear displacements which respond in an elastic manner. Civil engineering projects and some mine openings excavated in competent crystalline rock commonly induce stresses below the yield strength of fractures. Hence, an underground environment exists where the elastic response of fracture zones is of primary interest. Experimental evidence indicates that within this environment there exists a class of problems where the measured hydraulic response is dominated by shear displacements induced in fracture zones.

Flow through fracture zones is intrinsically complex. Any application of simplified idealizations and models to represent fracture flow will inevitably have shortcomings. The complexity is further magnified when openings are excavated through these fracture zones. The excavation alters the hydraulic boundary conditions, changes the stress regime, and induces displacements in the fracture zone. Models which capture some of the important phenomenological aspects of flow in fracture zones can provide insight into the complex behaviour of fracture zones subject to shear. However, it cannot be expected that any one model will be applicable to all fracture zones in all situations.

It is recognized that normal stress - fracture closure can play a controlling role in the hydraulic response of fractures and certain fracture zones. However, this thesis concentrates on the influence of shear displacements. This does not imply that normal stress effects are irrelevant in all fracture zones. Instead, it was suspected that shear displacements could in certain circumstances dominate the hydraulic response of a fracture zone. Therefore, a hypothesis of shear-dependent transmissivity reduction in fracture zones was proposed. This concept differs fundamentally from the traditional notions of fracture dilation and associated transmissivity increase resulting from shear displacements and changes in fracture zone transmissivity due to changes in normal stresses. The research presented in this thesis supports the hypothesis and provides a new mechanism for interpreting the hydraulic behaviour of fracture zones. By examining the influence of shear displacements alone, a conclusive assessment of shear-induced transmissivity changes was made without additional uncertainties and complexities introduced by examining simultaneously both shear and normal stress - fracture closure.

The transmissivity - shear displacement relationship and flow model presented in this thesis are only a first order approximation of fracture zone hydraulic behaviour under shear. The flow model is intended to only represent the phenomenological characteristics of the influence of shear on fracture zone transmissivity. Although the flow model is based on commonly observed en echelon fracture zone structure it is not intended to replace real fracture zone flow paths since these are intrinsically complex and the model is only conceptual.

The research was not directed to verify the accuracy of the adopted relationship between shear displacements and transmissivity changes because insufficient experimental data is available. Instead, the concept or mechanism for shear-dependent transmissivity changes was evaluated and confirmed by predictions of hydraulic response which agreed with monitoring data from an excavation through a fracture zone at Room 209. Other relationships which predict a fully or partially, recoverable, shear-dependent, transmissivity decrease may be equally appropriate and would not alter the conclusions of this thesis.

Extensive numerical modelling was undertaken to simulate the mechanical-hydraulic response in the Room 209 fracture zone. The following points summarize the findings from the numerical modelling.

6.1 Shear - Transmissivity Relationship

- For undisturbed fracture zones, the shear displacement - transmissivity change relationship predicts a transmissivity reduction regardless of the direction of shear.

- When the direction of shearing reverses (net shear displacement decreases) the shear displacement - transmissivity change predicts a recovery of transmissivity.

- The orientation of fractures within a fracture zone controls the rate at which the transmissivity changes.

- The shear - transmissivity relationship does not work well for fracture zones with initially small apertures (less than roughly 20 to 50 μm). At least two factors provide an explanation: 1) Fractures with small apertures tend to have large areas of contact between opposing fracture walls. This induces significant tortuosity into the fracture flow and hence the parallel plate assumption for flow is invalid. 2) The relationship predicts complete closure after a small shear. However, experimental evidence shows there is usually a small but irreducible flow through fractures which exists regardless of increased stress on the fracture.

- The shear - transmissivity relationship does not account for potential damage to flow paths caused by large shear displacements and hence neglects potential non-recoverable transmissivity reductions.

6.2 Shear Displacement Distributions

- Shear displacements generated in a fracture zone can have a complex spatial distribution. The distribution depends on many factors including fracture zone orientation and properties, rock mass properties, in situ stresses, and opening geometry.

- Shear displacements have a greater effect on the resulting hydraulic response than does the exact form of the shear - transmissivity relationship because excavation through a fracture zone generates high shear displacement gradients near the opening.

- The spatial distribution of shear displacements combined with initial transmissivity distributions control the resulting pressure distributions and flow into an opening.

- Shear displacements and initial transmissivities which combine to create continuous rings of low transmissivity around an opening will have a profound effect on flow and pressure head distributions. Heads will be extremely high near the opening and flows will be small.

- Shear displacements and initial transmissivities which combine to create discontinuous rings of low transmissivity have less effect on flow and pressure heads. Just one 'gap' in the ring will moderate the influence of the transmissivity reduction.

6.3 Interpretation of Field Hydraulic Monitoring Data

- Steady-state heads at points near an opening provide an indication of the overall flow pattern into the opening. $Q/\Delta H$ measured at these same points provides a measure of the local transmissivities near the packer locations.

- Boundary conditions must be considered when interpreting $Q/\Delta H$ measurements. The change in hydraulic boundary condition resulting from an opening intersecting a fracture zone will cause an increase in values of $Q/\Delta H$ measured at nearby packers.

- Measurements of $Q/\Delta H$ which do not change as an excavation passes a fracture zone imply a reduction in transmissivity near the opening.

- Measurements of Q/ΔH which vary as the excavation proceeds past a fracture zone are indicating time or excavation-dependent changes in both boundary conditions and fracture zone transmissivity.

6.4 Recommendations

6.4.1 Field Work

The flow through fracture zones is extremely complex. Even if it were possible to conquer the enormous numerical and mathematical difficulties involved in solving problems of flow through fracture zones and the influence of excavations on these flows, it is not possible to determined the configuration of the fracture zone and flow system with any degree of reliability and realism. Nevertheless, to better understand the response of fracture zones subjected to shear displacements, the transmissivity - shear displacement relationship needs refinement. Real, in situ fracture zones need to be examined and tested. In situ testing and fracture zone characterization are prerequisites for interpretation of hydraulic fracture zone response. The characterization should involve flow tests and careful excavation to reveal the actual flow paths.

Given the hydraulic response after excavation through a fracture zone, one may calibrate a numerical model to simulate or back-analyze the measured behaviour. However, current understanding of fracture flow is still a long way from providing accurate predictive capabilities. The greatest obstacle to precise modelling of fracture flow is a lack of knowledge about the geometrical configuration of the flow paths. This thesis has used the distinctive en echelon fracture patterns which typically occur in crystalline rock masses as a basis for a conceptual flow model. However, the exact nature of flow through these fractures is not known. Since it is nearly impossible to know the flow configuration before a fracture zone is excavated, any predictive models for fracture flow must be based on idealized fracture zone geometries and flow channels. For better numerical representation of flow, a more complex model would be required. This model must account for flow tortuosity in three-dimensions. The orientations of fractures with respect to shear directions and reversal in shear displacements need to be considered. Shear displacements in one direction would most likely induce anisotropic changes in transmissivity.

6.4.2 Numerical Models

This thesis demonstrates that there is still a role for simple, elastic, finite element models for analyzing and improving our understanding of hydro-mechanical fracture flow. Too often researchers adopt a much more complex numerical model than is required to facilitate an understanding of physical behaviour. The choice of parameters for these models is then subject to uncertainty and it may be impossible to determine whether the numerical model is an accurate representation of the physical process or whether the parameters for the numerical model have been fortuitously chosen to allow an improper numerical model to make seemingly valid predictions. Use the simplest possible numerical model which allows adequate representation of reality. In the case of hydro-mechanical fracture flow, ‘reality’ is still poorly defined and hence, the physical model must be better characterized before complex numerical models can be formulated (see Section 6.4.1).

One observation for those considering the use of ‘super’ computers for numerical modelling deserves comment. Working on a computer that is beyond an individual’s control, i.e., a computer with multiple users and a complex system of resources sharing, can create many problems. Although the computer may be theoretically capable of doing the necessary calculations and storing the data, in practice there may be many unexpected constraints and short-comings. Performing finite element simulations on a personal computer or work station, although more limited in capabilities, has well defined limits which are in the complete control of the computer user. Fortunately, the capabilities and speed of personal computers or work stations is rapidly increasing and quite complex problems may be solved without resorting to super computers. A numerical model tailored to the capabilities of a personal computer may, in practice, provide more information, more quickly, and with less frustration than a larger, more complex model run on a super computer.

7 REFERENCES

Atkinson, B.K. (ed.) *Fracture Mechanics of Rock:* Academic Press, 1987.

Amadei, B. and Goodman, R.E. A 3-D constitutive relation for fractured rock masses. *Proceedings of International Symposium on the Mechanical Behaviour of Fractured Media*, Ottawa, 1981.

Andersson, J. and Dverstorp, B. Conditonal simulations of fluid flow in three-dimensional networks of discrete fractures. *Water Resources Research*, 1987; **23**(10): 1876-1886.

Bandis, S.C. Mechanical properties of rock joints. *Proceedings of the International Symposium on Rock Joints*, 1990: 125-140.

Bandis, S.C., Lumsden, A.C. and Barton, N.R. Experimental studies of scale effects on the shear behaviour of rock joints. *International Journal of Rock Mechanics and Mining Sciences & Geomechanics Abstracts*, 1981; **18:** 1-21.

Bandis, S.C., Lumsden, A.C. and Barton, N.R. Fundamentals of rock joint deformation. *International Journal of Rock Mechanics and Mining Sciences & Geomechanics Abstracts*, 1983; **20**(6): 249-268.

Bandis, S.C., Barton, N.R. and Christianson, M. Application of a new numerical model of joint behaviour to rock mechanics problems. *Proceedings of the International Symposium on Fundamentals of Rock Joints;* Sweden, 1985a: 345-355.

Bandis, S.C., Makurat, A. and Vik, G. Predicted and measured hydraulic conductivity of rock joints. *Proceedings of the International Symposium on Fundamentals of Rock Joints;* Bjorkliden, 1985b: 269-280.

Barton, N.R. Rock mechanics review: the shear strength of rock and rock joints. *International Journal of Rock Mechanics and Mining Sciences & Geomechanics Abstracts*, 1976; **13:** 255-279.

Barton, N.R. Deformation phenomena in jointed rock. *Geotechnique*, 1986; **36**(2): 147-167.

Barton, N. and Bakhtar, K. *Rock joint description and modeling for the hydro-thermo-mechanical design of nuclear waste repositories.* CANMET, Mining Research Laboratories, report TRE83-10, 1983: 258p.

Barton, N. and Choubey, V. The shear strength of rock joints in theory and practice. *Rock Mechanics*, 1977; **10**(1-2): 1-54.

Barton, N. and Makurat, A. Modelling excavation responses in jointed rock. *Proceedings of a NEA Workshop on Excavation Responses in Geological Repositories for Radioactive Waste;* Winnipeg, 1989: 225-232.

Barton, N., Bandis, S. and Bakhtar, K. Strength, deformation and conductivity coupling of rock joints. *International Journal of Rock Mechanics and Mining Sciences & Geomechanics Abstracts*, 1985; **22**(3): 121-140.

Bear, J. *Dynamics of Fluids in a Porous Media*, American Elsevier Pub. Co., 1972: 764p.

Beer, G., Cowling, R., and Bywater, S. A novel three-dimensional joint element with application to the modelling of mining excavations. *Proceedings of the International Symposium on Fundamentals of Rock Joints;* Bjorkliden, 1985: 357-365.

Blanford, M.L., Key, S.M. and Chieslar, J.D. A general 3-D model for a jointed rock mass. in *Constitutive Laws for Engineering Materials - Theory and Applications*, 1987; **1:** 35-46.

Bock, H. A simple failure criterion for rough joints and compound shear surfaces. *Engineering Geology*, 1979; **14:** 241-254.

Bonilla, M.G. Historic surface faulting - map patterns, relation to subsurface faulting, and relation to preexisting faults. *Proceedings of Conference VIII Analysis of Actual Fault Zones in Bedrock, USGS Open-File Report 79-1239*, 1979: 36-65.

Brown, S.R. and Scholz, C.H. Broad bandwidth study of the topography of natural rock surfaces. *Journal of Geophysical Research*, 1985; **90**(B14): 12575-12582.

Brown, S.R. and Scholz, C.H. Closure of rock joints. *Journal of Geophysical Research*, 1986; **91**(B5): 4939-4948.

Carlsson, A. and Olsson, T. Rock stress influence on water flow in fractures. *Proceedings of 5th Congress of the International Society for Rock Mechanics;* Melbourne, 1983; **2:** 31-34.

Carlsson, A. and Olsson, T. Large scale in-situ tests on stress and water flow relationships in fractured rock. Vattenfall - Swedish State Power Board; 1986.

Carol, I. and Alonso, E.E. A new joint element for the analysis of jointed rock. *Proceedings of 5th Congress of the International Society for Rock Mechanics;* Melbourne, 1983; **2:** 147-151.

Carol. I., Genso, A. and Alonso, E.E. A three dimensional elastoplastic joint element. *Proceedings of the International Symposium on Fundamentals of Rock Joints;* Sweden, 1985: 441-451.

Carr, J.R. A note on the implementation of a continuum finite element approach for stress analysis of jointed rock. *Proceedings of the 26th U.S. Symposium on Rock Mechanics;* Rapid City, 1985: 613-620.

Chan, D.H. *Analysis of Strain Softening Material.* Ph.D. thesis, University of Alberta, 1986.

Chan, D.H. and Chen, Z.H. A *Computer Program for Soil Analysis by Finite Element,* Dept. of Civil Engineering, University of Alberta, 1988: 192p.

Chan, T., Griffiths, P., and Nakka. B. *Finite element modelling of geomechanical and hydrogeological responses to the Room 209 heading extension excavation response experiment - I. pre-test modelling.* AECL, Applied Geoscience Branch, Whiteshell Nuclear Research Establishment, Pinawa, 1987.

Chan, T., Griffiths. P., and Nakka.B. *Finite element modelling of geomechanical and hydrogeological responses to the Room 209 heading extension excavation response experiment - II. post-excavation analysis of experimental results.* AECL, Applied Geoscience Branch, Whiteshell Nuclear Research Establishment, Pinawa, 1988.

Chappell, B.A. Rock mass characterization for dam foundations. *Journal of Geotechnical Engineering , ASCE,* 1990; **116**(GT4): 625-646.

Chen, D.W., Zimmerman, R.W. and Cook, N.G.W. The effect of contact area on the permeability of fractures. *Proceedings of the 30th U.S. Symposium on Rock Mechanics;* West Virginia, 1989: 81-88.

Cook, A.M., Myer, L.R., Cook, N.G.W., and Doyle, F.M. The effect of tortuosity on flow through a natural fracture. *Proceedings of the 31st U.S. Symposium on Rock Mechanics;* Golden, 1990: 371-378.

Cruz, P.T., Quadros, E.F., Correa, F. and Marrano, A. Evaluation of opening and hydraulic conductivity of rock discontinuities. *Proceedings of the 23rd U.S. Symposium on Rock Mechanics;* Berkeley, 1982: 769-777.

Cundall, P.A. Distinct element models of rock and soil structure. Chapt. 4 in *Analytical and Computational Methods in Engineering Rock Mechanics,* 1987.

Cundall, P.A. and Fairhurst, C. Correlation of discontinuum models with physical observations - an approach to the estimation of rock mass behaviour. *Journal for Geomechanics and Engineering Geology in Construction and Mining, (Felsbau)*, 1986; **4**(4): 197-202.

Deng, Q., Wu, D., Zhang, P. and Chen, S. Structure and deformational character of strike-slip fault zones. *Pure and Applied Geophysics*, 1986; **124**(1/2): 203-223.

Dershowitz, W.S. and Einstein, H.H. Three dimensional flow modeling in jointed rock masses. *Proceedings of 6th Congress of the International Society for Rock Mechanics;* Montreal, 1987; **1:** 87-92.

Desai, C.S. Unified approach for constitutive modelling for geologic materials and discontinuities. Swoboda. *Numerical Methods in Geomechanics;* Innsbruck, 1988: 45-54.

Desai, C.S. and Fishman, K.L. Constitutive models for rocks and discontinuities (joints). *Proceedings of the 28th U.S. Symposium on Rock Mechanics;* Tucson, 1987: 609-620.

Desai, C.S., Zaman, M.M., Lightner, J.G., and Siriwardane, H.J. Thin-layer element for interfaces and joints. *International Journal for Numerical and Analytical Methods in Geomechanics*, 1984; **8:** 19-43.

Detournay, E. Hydraulic conductivity of closed rock fractures: an experimental and analytical study. *Proceedings of 13th Canadian Rock Mechanics Symposium: Underground Rock Engineering;* Toronto, 1980: 168-173.

Doe, T.W., Osnes, J., Kenrick, M., Geier, J. and Warner, S. Design of borehole testing programs for waste disposal sites in crystalline rock. *Proceedings of 6th Congress of the International Society for Rock Mechanics*, Montreal, 1987; **3**: 1377-1398.

Dverstorp, B. and Andersson, J. Application of the discrete fracture network concept with field data: possibilities of model calibration and validation. *Water Resources Research*, 1989; **25**(3): 540-550.

Egger, P. Field study of rock damage around a gallery. *Proceedings of 2nd International Symposium on Numerical Methods in Geomechanics*, 1988; **2:** 625-634.

Elliott, G.M., Brown, E.T., Boodt, P.I. and Hudson, J.A. Hydromechanical behaviour in joints in the Carnmenellis granite, S.W. England. *Proceedings of International Symposium on Fundamentals of Rock Joints;* Bjorkliden, 1985: 249-258.

Elsworth, D. *Laminar and Turbulent Flow in Rock Fissures and Fissure Networks*. Ph.D. thesis, Berkeley: University of California, 1984. 192 p.

Elsworth, D. Coupled finite element/boundary element analysis for nonlinear fluid flow in rock fissures and fissure networks. *Proceedings of the 26th U.S. Symposium on Rock Mechanics*, 1985; Rapid City, 1985; **1:** 633-641.

Elsworth, D. and Doe, T.W. Application of non-linear flow laws in determining rock fissure geometry from single borehole pumping tests. *International Journal of Rock Mechanics and Mining Sciences & Geomechanics Abstracts*, 1986; **23**(3): 245-254.

Everitt, R. *Geology of the Room 209 area and its planned extension*. Atomic Energy of Canada Limited, report GSEB-86-168, 1986.

Gale, J.E. *A numerical, field and laboratory study of flow in rocks with deformable fractures*. Scientific Series #72, Inland Waters Directorate, Water Resources Branch, Environment Canada, 1977: 145p.

Gale, J.E. Assessing the permeability characteristics of fractured rock. *Geological Society of America Special Paper - Recent Trends in Hydrogeology*, 1982a; **189:** 163-181.

Gale, J.E. The effects of fracture type (induced versus natural) on the stress-fracture closure-fracture permeability relationships. *Proceedings of the 23rd U.S. Symposium on Rock Mechanics*, 1982b: 290-298.

Gale, J.E. Comparison of coupled fracture deformation and fluid flow models with direct measurements of fracture pore structure and stress-flow properties. *Proceedings of the 28th U.S. Symposium on Rock Mechanics*, 1987a: 1213-1222.

Gale, J.E. *Roughness, contact area and pore structure, under given normal stress conditions, of selected natural fractures in the Lac du Bonnet granite*. report submitted to Atomic Energy of Canada Limited, Pinawa, 1987b.

Gale, J.E., Rouleau, A. and Atkinson, L.C. Hydraulic properties of fractures. *Hydrogeology of Rocks of Low Permeability, Memoires of 17th International Congress of the International Association of Hydrogeologists;* Tucson, 1985; **1:** 1-16.

Gamond, J.F. Displacement features associated with fault zones: a comparison between observed examples and experimental models. *Journal of Structural Geology*, 1983; **5**(1): 33-45.

Gamond, J.F. Bridge structures as sense of displacement criteria in brittle fault zones. *Journal of Structural Geology*, 1987; **9**(5/6): 609-620.

Gangi, A.F. Variation of whole and fractured porous rock permeability with confining pressure. *International Journal of Rock Mechanics and Mining Sciences & Geomechanics Abstracts*, 1978; **15:** 249-257.

Gay, N.C. and Ortlepp, W.D. Anatomy of a mining-induced fault zone. *Geological Society of America Bulletin*, 1979; **90**(1): 47-58.

Gerrard, C.M. Formulation for the mechanical properties of rock joints. *Proceedings of the International Symposium on Fundamentals of Rock Joints;* Bjorkliden, 1985: 405-422.

Gerrard, C. Shear failure of rock joints: appropriate constraints for empirical relations. *International Journal of Rock Mechanics and Mining Sciences & Geomechanics Abstracts*, 1986; **25**(6): 421-429.

Gertsch, L.S. Changes in in situ rock joint flow characteristics caused by mechanical displacement. *Proceedings of the 31th U.S. Symposium on Rock Mechanics*, Golden, 1990: 363-370.

Ghaboussi, J., Wilson, E.L. and Isenberg, J. Finite element for rock joints and interfaces. *Journal of the Soil Mechanics Engineering Division, ASCE Engineering Division*, 1973; **99**(SM10): 833-848.

Goodman, R.E. The deformability of joints. *Determination of the In Situ Modulus of Deformation of Rock, ASTM STP 477:* ASTM, 1969: 174-196.

Goodman, R.E. The mechanical properties of joints. *Proceedings of 3rd Congress of the International Society for Rock Mechanics;* Denver, 1974; **1A:** 127-140.

Goodman, R.E. *Methods in Geological Engineering in Discontinuous Rock*, West, 1976: 472p.

Goodman, R.E. *Introduction to Rock Mechanics*, 2nd edition, J. Wilely & Sons, 1989: 562p.

Goodman, R.E. and Dubois, J. Duplication of dilatancy in analysis of jointed rocks. *Journal of the Soil Mechanics and Foundations Division, ASCE*, 1972; **98**(SM4): 399-422.

Goodman, R.E. and St. John, C. Finite element analysis for discontinuous rocks. Chapt. 4 in *Numerical Methods in Geotechnical Engineering*. New York: McGraw-Hill, 1979: 148-175.

Goodman, R.E., Taylor, R. and Brekke, T.L. A model for the mechanics of jointed rock. *Journal of the Soil Mechanics and Foundations Division, ASCE*, 1968; **94**(SM3): 637-659.

Greenwood, J.A. and Williamson, J.B.P. Contact of nominally flat surfaces. *Proceedings of the Royal Society of London, Series A. Mathematical and Physical Sciences*, 1966; **295:** 300-319.

Grisak, G.E., Pickens, J.F., Avis, J.D., Belanger, D.W., Thury, M. and Schneider, A. Principles of hydrogeologic investigations at depth in crystalline rock. *Hydrogeology of Rocks of Low Permeability, Memoires of 17th International Congress of the International Association of Hydrogeologists;* Tucson, 1985; **1**: 52-71.

Guther, H. *Some Problems in Non-Homogeneous Seepage*. MSc. thesis, University of Alberta, 1972: 174p.

Hakami, E. Water Flow in Single Rock Joints. Licentiate thesis, Luleå University of Technology, Sweden, 1988.

Hempton, M.R. and Neher, K. Experimental fracture, strain and subsidence patterns over en echelon strike-slip faults: implications for the structural evolution of pull-apart basins. *Journal of Structural Geology*, 1986; **8**(6): 597-605.

Herrmann, L.R. Finite element analysis of contact problems. *Journal of the Engineering Mechanics Division, ASCE*, 1978; (EM5): 1043-1057.

Hesler, G.J., Zeng, Z. and Myer, L.R. In-situ fracture stiffness determination. *Proceedings of the 31st U.S. Symposium on Rock Mechanics;* Golden, 1990: 405-411.

Heuze, F.E. Dilatant effects of rock joints. *Proceedings of 4th Congress of the International Society for Rock Mechanics;* Montreux, 1979; **1:** 169-175.

Heuze, F.E. and Barbour, T.G. New models for rock joints and interfaces. *Journal of the Geotechnical Engineering Division, ASCE*, 1982; **108**(GT5): 757-776.

Heuze, F.E., Goodman, R.E., and Bornstein, A. Numerical analyses of deformability tests in jointed rock - "joint perturbation" and "no tension" finite element solutions. *Rock Mechanics*, 1971; **3:** 13-24.

Hopkins, D.L., Cook, N.G.W. and Myer, L.R. Fracture stiffness and aperture as a function of applied stress and contact geometry. *Proceedings of the 28th U.S. Symposium on Rock Mechanics;* Tucson, 1987: 673-680.

Hungr, O. and Coates, D.F. Deformability of joints and its relation to rock foundation settlements. *Canadian Geotechnical Journal*, 1978; **15:** 239-249.

Jaeger, J.C. Friction of rocks and stability of rock slopes. *Geotechnique*, 1971; **21**(2): 97-134.

Jaeger, J.C. and Cook, N.W.W. *Fundamentals of Rock Mechanics.* 2nd edition, J. Wiley &Sons, Inc., 1976: 585p.

Jakubick, A.T., Klein, R. Gray, M.N. and Keil, L.D. Characteristics of the excavation response zone as applied to shaft sealing. *Proceedings of a NEA Workshop on Excavation Responses in Geological Repositories for Radioactive Waste;* OECD, Winnipeg, 1989: 157-174.

Janardhanam, R. and Kane, W.F. A constitutive law for shear behaviour of rock joints. *Proceedings of the 26th U.S. Symposium on Rock Mechanics;* Rapid City, 1985; **1:** 395-402.

Johnson, B. Permeability of a simulated-fracture as a function of normal stress. *Proceedings of 24th U.S. Symposium on Rock Mechanics*, 1983: 519-523.

Jones, F.O. Jr. A laboratory study of the effects of confining pressure on fracture flow and storage capacity in carbonate rocks. *Journal of Petroleum Technology*, 1975: 21-27.

Jouanna, P. Laboratory tests on the permeability of micaschist samples under applied stresses. *Proceedings of ISRM International Symposium on Percolation Through Fissured Rock*, 1972; **T2-F:** 1-11.

Jung, R. Hydraulic in situ investigations of an artificial fracture in the Falkenburg Granite. *International Journal of Rock Mechanics and Mining Sciences & Geomechanics Abstracts*, 1989; **26**(3/4): 301-308.

Kafritsas, J., Gencer, M., and Einstein, H.H. Coupled deformation/flow analysis with the distinct element method. *Proceedings of the 25th U.S. Symposium on Rock Mechanics;* Evanston, 1984: 239-247.

Kaiser, P.K. *Time-Dependent Behaviour of Tunnels.* Ph.D. thesis, University of Alberta, 1979: 395p.

Kaiser, P.K., Chan, D.H., Tannant, D.D., Pelli, F., and Neville, C. *Numerical Simulation of Room 209 Instrument Ring* - Technical report to AECL, Pinawa, 1987: 200p.

Kaiser, P.K., Tannant, D.D., Chan, D.H., and Zou, D.H. *Numerical Simulations of Room 209 Instrument Array* - Technical report on data comparison and back analysis for AECL, Pinawa, 1989: 217p.

Katsube, T.J. and Hume, J.P. *Geotechnical studies at Whiteshell Research Area (RA-3).* CANMET report MRL 87-52, 1987.

Kealy, C.D and Busch, R.A. Determining seepage characteristics of mill-tailings dams by the finite element method. *U.S. Bureau of Mines, Report of Investigations*, No. 7477, 1971.

Kelsall, P.C., Case, J.B. and Chabannes, C.R. *A preliminary evaluation of the rock-mass disturbance resulting from shaft, tunnel, or borehole excavation.* Office of Nuclear Waste Isolation, 1982. 154 p.

Kesall, P.C., Case, J.B. and Chabannes, C.R. Evaluation of excavation-induced changes in rock permeability. *International Journal of Rock Mechanics and Mining Sciences & Geomechanics Abstracts*, 1984; **21**(3): 123-135.

Kemeny, J.M. and Long, J.C.S. The formation and properties of fault zones in brittle rock. *Proceedings of the 30th U.S. Symposium on Rock Mechanics;* West Virginia, 1989: 115-122.

Kikuchi, K., Mito, Y. and Okuno, T. Experimental study for groundwater flow in an actual jointed rock mass. *Proceedings of ISRM-SPE International Symposium on Rock at Great Depth;* Pau, 1989; **1**: 457-464.

Koopmans, R. and Hughes, R.W. *Determination of Excavation Disturbance in Room 209 Underground Research Laboratory.* Ontario Hydro research division, 1988; 88-65-K.6.

Koopmans, R. and Hughes, R.W. The assessment of excavation disturbance surrounding underground openings in rock. *Proceedings of a NEA Workshop on Excavation Responses in Geological Repositories for Radioactive Waste;* Winnipeg, 1989a: 283-294.

Koopmans G. and Hughes, R.W. *Reassessment of excavation disturbance in Room 209 - Underground Research Laboratory*. Ontario Hydro research division, 1989b; 89-308-K.27

Kozak, E.T. and Davison, C.C. *Hydrogeological Conditions in a Vertical Fracture Intersecting Room 209 of the 240 m Level of the Underground Research Laboratory*. Atomic Energy of Canada Limited report, Pinawa; 1986.

Kranz, R.L. Crack-crack and crack-pore interactions in stressed granite. *International Journal of Rock Mechanics and Mining Sciences & Geomechanics Abstracts*, 1979; **16:** 37-47.

Kranz, R.L., Frankel, A.D., Engelder, T. and Scholz, C.H. The permeability of whole and jointed Barre granite. *International Journal of Rock Mechanics and Mining Sciences & Geomechanics Abstracts*, 1979, **16:** 225-234.

Kulhawy, F.H. Stress deformation properties of rock and rock discontinuities. *Engineering Geology*, 1975; **9:** 327-350.

Kuzyk, G.W., Babulic, P.J., Lang, P.A. and Morin, R.A. *Blast design and quality control procedures at Atomic Energy of Canada Limit's Underground Research Laboratory*. Atomic Energy of Canada Limited report, Pinawa; 1987.

Kuzyk, G.W., Lang, P.A. and Bel, G. Le. Blast design and quality control at the second level of Atomic Energy of Canada's Underground Research Laboratory. *Proceedings of the International Symposium on Large Rock Caverns*, Helsinki, 1986: 147-158.

Ladanyi, B. and Archambault, G. .Simulation of shear behavior of a jointed rock mass. *Proceedings of the 11th U.S. Symposium on Rock Mechanics*, 1969; Berkeley, 1970: 105-125.

Ladanyi, B. and Archambault, G. Direct and indirect determination of shear strength of rock mass. *Society of Min. Eng. of AIME*, #80-25; 1980.

Lang, P.A. Room 209 excavation response test in the Underground Research Laboratory. *Proceedings of a NEA Workshop on Excavation Responses in Geological Repositories for Radioactive Waste*; Winnipeg, 1989: 295-329.

Lang, P.A. and Thompson, P.M. *Geomechanics experiments during excavation of the URL shaft*. Atomic Energy of Canada Limit report, Pinawa; 1986a.

Lang, P.A., Everitt, R.A., Kozak, E.T., Davison, C.C. *Room 209 Instrument Array - Pre-excavation information for modellers.* Atomic Energy of Canada Limited, report AECL-9566-1, 1986b.

Lang, P.A., Chan, T., Davison, C.C., Everitt, R.A., Kozak, E.T. and Thompson, P.M. Near-field mechanical and hydraulic response of a granitic rock mass to shaft excavation. *Proceedings of the 28th U.S. Symposium on Rock Mechanics;* Tucson, 1987a: 509-516.

Lang, P.A., Kuzyk, G.W., Babulic, P.J., Bilinsky, D.M., Everitt, R.A., Spinney, M.H., Kozak, E.T., and Davison, C.C. *Room 209 Instrument Array: Measured Response to Excavation.* Atomic Energy of Canada Limited TR-433, Whiteshell Nuclear Research Establishment, 1987b.

Lee, M.F. Shear mechanics of bedding planes at Mount Isa Mines, Queensland. *Proceedings of a Workshop on Rock Joints;* Melbourne, 1983: 18p.

Lemos, J.V., Hart, R.D., and Cundall, P.A. A generalized distinct element program for modelling jointed rock mass. *Proceedings of the International Symposium on Fundamentals of Rock Joints;* Bjorkliden, 1985: 335-343.

Lieb, R.W., Zuidema, P. and Gysel, M. Excavation responses in developing underground repositories in fractured hard rock in Switzerland. *Proceedings of a NEA Workshop on Excavation Responses in Geological Repositories for Radioactive Waste;* Winnipeg, 1989: 91-101.

Long, J.C.S., Endo, H.K., Karasaki, K., Pyrak, L., McLean, P. and Witherspoon, P.A. Hydrogeologic behaviour of fracture networks. *Hydrogeology of Rocks of Low Permeability, Memoires of 17th International Congress of the International Association of Hydrogeologists;* Tucson, 1985; **2:** 449-462.

Louis, C. and Maini, Y.N. Determination of in situ hydraulic parameters in jointed rock. *Proceedings of 2nd Congress of the International Society for Rock Mechanics;* Belgrade, 1970; **1:** 235-245.

Mahtab, M.A. and Goodman, R.E. Three dimensional finite element analysis of jointed rock slopes. *Proceedings of 2nd Congress of the International Society for Rock Mechanics;* Belgrade, 1970; **3:** 353-360.

Maini, T. and Hocking, G. *An Examination of the Feasibility of Hydrologic Isolation of a High Level Waste Repository in Crystalline Rock.* Geological Disposal of High-level Radioactive Waste Session, Annual Meeting of the Geological Society of America, Seattle, 1977.

Makurat, A. The effect of shear displacement on the permeability of natural rough joints. *Hydrogeology of Rocks of Low Permeability, Memoires of 17th International Congress of the International Association of Hydrogeologists;* Tucson, 1985; **1**: 90-106.

Makurat, A. *Coupled shear flow temperature tests (CSFT) on URL joint.* Norwegian Geotechnical Institute, report 876058, 1989.

Malina, H. The numerical determination of stresses and deformations in rock taking into account discontinuities. *Rock Mechanics*, 1970; **2**: 1-16.

Martin C.D., Davison, C.C. and Kozak, E.T. Characterizating normal stiffness and hydraulic conductivity of a major shear zone in granite. *Proceedings of the International Symposium on Rock Joints*, 1990a: 549-556.

Martin C.D., Read R.S. and Lang P.A. Seven years of in situ stress measurement at the URL - an overview. *Proceedings of the 31th U.S. Symposium on Rock Mechanics*, Golden, 1990b: 15-26.

McGarr, A., Pollard, D., Gay, N.C. and Ortlepp, W.D. Observations and analysis of structures in exhumed mine-induced faults. *Proceedings of Conference VIII Analysis of Actual Fault Zones in Bedrock, USGS Open-File Report 79-1239*, 1979: 101-120.

Montazer, P., Chitombo, G., King, R. and Ubbes W. Spatial distribution of permeability around CSM/ONWI Room, Edgar Mine, Idaho Springs, Colorado. *Proceedings of the 23rd U.S. Symposium on Rock Mechanics*, 1982: 47-56.

Morgenstern, N.R. and Tchalenko, J.S. Microscopic structures in kaolin subjected to direct shear. *Geotechnique*, 1967; **17**: 309-328.

Naylor, M.A., Mandl, G. and Sijpesteijn, C.H.K. Fault geometry in basement-induced wrench faulting under different initial stress states. *Journal of Structural Geology*, 1986; **8**(7): 737-752.

Neuman, S.P., Simpson, E.S., Hsieh, P.A., Jones, J.W. and Winter, C.L. Statistical analysis of hydraulic test data from fractured crystalline rock near Oracle, Arizona. *Hydrogeology of Rocks of Low Permeability, Memoires of 17th International Congress of the International Association of Hydrogeologists;* Tucson, 1985; **1**: 289-300.

Neuzil, C.E. and Tracy, J. V. Flow through fractures. *Water Resources Research*, 1981; **17**(1): 191-199.

Obert, L. and Duvall, W.I. *Rock Mechanics and the Design of Structures in Rock*. J. Wiley & Sons, Inc., 1967: 650p.

Ohnishi, Y. and Goodman, R.E. Results of laboratory tests on water pressure and flow in joints. *Proceedings of 3rd Congress of the International Society for Rock Mechanics;* Denver, 1974; **2 (A)**: 660-666.

Olofsson, T. A non-linear model for the mechanical behaviour of continuous rock joints. *Proceedings of the International Symposium on Fundamentals of Rock Joints;* Bjorkliden, 1985: 395-404.

Pande, G.N. A constitutive model of rock joints. *Proceedings of the International Symposium on Fundamentals of Rock Joints;* Bjorkliden, Sweden, 1985: 429-439.

Patton, F.D. Multiple modes of shear failure in rock. *Proceedings of 1st Congress of the International Society for Rock Mechanics*, Lisbon, 1966; **1**: 509-513.

Pelli, F. *Near Face Behaviour of Deep Tunnels in Rock*. Ph.D. thesis, Dept. of Civil Engineering, University of Alberta, 1987: 406p.

Petit, J.-P. Criteria for the sense of movement on fault surfaces in brittle rocks. *Journal of Structural Geology*, 1987; **9**(5/6): 597-608.

Petit, J.-P. Normal stress dependent rupture morphology in direct shear tests on sandstone with applications to some natural fault surface features. *International Journal of Rock Mechanics and Mining Sciences & Geomechanics Abstracts*, 1988; **25**(6): 411-419.

Plesha, M.E. Constitutive modeling of rock joints with dilation. *Proceedings of the 26th U.S. Symposium on Rock Mechanics;* Rapid City, 1985; **1**: 387-394.

Plesha, M.E. Constitutive models for rock discontinuities with dilatancy and surface degradation. *International Journal for Numerical and Analytical Methods in Geomechanics*, 1987; **11**: 345-362.

Polubarinova-Kochina, P. Ya. *Theory of ground water movement*. translated from Russian by J.M. Roger De West: Princeton University Press, 1962: 613 p.

Pollard, D.D. and Aydin, A. Progress in understanding jointing over the past century. *Geological Society of America Bulletin*, 1988; **100**: 1181-1204.

Pratt, H.R., Swolfs, H.S., Brace, W.F., Black, A.D. and Handin, J.W. Elastic and transport properties of an in situ jointed granite. *International Journal of Rock Mechanics and Mining Sciences & Geomechanics Abstracts*, 1977; **14:** 35-45.

Pusch, R. Alteration of the hydraulic conductivity of rock by tunnel excavation. *International Journal of Rock Mechanics and Mining Sciences & Geomechanics Abstracts*, 1989; **26**(1): 79-83.

Pusch, R. and Bergstrom, A. Alteration of the conductivity of rock from excavations as indicated by the Stripa plugging and backfilling tests. *Proceedings of a NEA Workshop on Excavation Responses in Geological Repositories for Radioactive Waste;* Winnipeg, 1989: 143-156.

Pyrak-Nolte, L.J., Myer, L.R., Cook, N.G.W. and Witherspoon, P.A. Hydraulic and mechanical properties of natural fractures in low permeability rock. *Proceedings of 6th Congress of the International Society for Rock Mechanics*, 1987; **1:** 225-231.

Raven, K.G. and Gale, J.E. Water flow in a natural rock fracture as a function of stress and sample size. *International Journal of Rock Mechanics and Mining Sciences & Geomechanics Abstracts*, 1985; **22**(4): 251-261.

Raven, K.G., Smedley, J.A., Sweezey, R.A., and Novakowski, K.S. Field investigations of a small groundwater flow system in fractured monzonitic gneiss. *Hydrogeology of Rocks of Low Permeability, Memoires of 17th International Congress of the International Association of Hydrogeologists;* Tucson, 1985; **1:** 72-86.

Rissler, P. *Determination of the Water Permeability of Jointed Rock*. Ph.D. thesis, Aachen: RWTH, 1978.

Rutqvist, J., Ljunggren, C., Stephansson, O., Noorishad, J. and Tsang, C.F. Theoretical and field investigations of fracture hydromechanical response under fluid injection. *Proceedings of the International Symposium on Rock Joints*, 1990: 557-564.

Ryan, T. M., Farmer, I.W. and Kimbrell, A.F. Laboratory determination of fracture permeability. *Proceedings of the 28th U.S. Symposium on Rock Mechanics;* Tucson, 1987: 593-600.

Schneefuss, J., Kull, H. and Brasser, Th. Stress and temperature effects on the permeability in granitic rock around a gallery excavated by continuous mining. *Proceedings of a NEA Workshop on Excavation Responses in Geological Repositories for Radioactive Waste;* Winnipeg, 1989: 119-130.

Segall, P. and Pollard, D.D. Mechanics of discontinuous faults. *Journal of Geophysical Research*, 1980; **85**(B8): 4337-4350.

Segall, P. and Pollard, D.D. Joint formation in granitic rock of the Sierra Nevada. *Geological Society of America Bulletin*, 1983a; **94**: 563-575.

Segall, P. and Pollard, D.D. Nucleation and growth of strike slip faults in granite. *Journal of Geophysical Research*, 1983b; **88**(B1): 555-568.

Serrano Gonzalez, A.A., and Soriano, A. Numerical model for jointed media. *Proceedings of 2nd International Symposium on Numerical Methods in Geomechanics;* Ghent, 1986: 855-862.

Shapiro, A.M. and Nicholas, J.R. Assessing the validity of the channel model of fracture aperture under field conditions. *Water Resources Research*, 1989; **25**(5): 817-828.

Sibson, R.H. Brecciation processes in fault zones: inferences from earthquake rupturing. *Pure and Applied Geophysics*, 1986; **124**(1/2): 159-175.

Simmons, G.R. Accounting for excavation responses in developing an underground repository in hard crystalline rock. *Proceedings of a NEA Workshop on Excavation Responses in Geological Repositories for Radioactive Waste;* Winnipeg, 1989: 47-66.

Skinas, C.A., Bandis, S.C. and Demiris, C.A. Experimental investigations and modelling of rock joint behaviour under constant stiffness. *Proceedings of the International Symposium on Rock Joints*, 1990: 301-308.

Smith, L., Mase, C.W., Schwartz, F.W. and Chorley, D. A numerical model for transport in networks of planar fractures. *Hydrogeology of Rocks of Low Permeability, Memoires of 17th International Congress of the International Association of Hydrogeologists;* Tucson, 1985; **2**: 666-675.

Sofianos, A.I. and Watson, J.O. Analysis of excavations in jointed rock of infinite extent. *International Journal for Numerical and Analytical Methods in Geomechanics*, 1986; **10**: 125-136.

Sour, L.E., Richardson, A.M., Brown, S.M., Hustrulid, W.A. and Lindner, E.N. A field study of coupled thermo-mechanical processes in fractured crystalline rock. *in Coupled Processes Associated with Nuclear Waste Repositories*, 1987: 699-712.

Sun, Z., Gerrard, C. and Stephansson, O. Rock joint compliance tests for compression and shear loads. *International Journal of Rock Mechanics and Mining Sciences & Geomechanics Abstracts*, 1985; **22**(4): 197-213.

Sundaram, P.N., Watkins, D.J. and Ralph, W.E. Laboratory investigations of coupled stress-deformation-hydraulic flow in a natural rock fracture. *Proceedings of the 28th U.S. Symposium on Rock Mechanics*, 1987: 585-592.

Swan, G. Determination of stiffness and other joint properties from roughness measurements. *Rock Mechanics and Rock Engineering*, 1983; **16**: 19-38.

Taylor, R.L. and Brown C.B. Darcy flow solutions with free surface. *ASCE Journal Hydraulics Division*, 1967; **92(HY2)**: 25-33.

Tchalenko, J.S. Similarities between shear zones of different magnitudes. *Geological Society of America Bulletin*, 1970; **81**: 1625-1640.

Teufel, L.W. Permeability changes during shear deformations of fractured rock. *Proceedings of the 28th U.S. Symposium on Rock Mechanics;* Tucson, 1987: 491-500.

Thompson, P.M., Kozak, E.T. and Martin, C.D. Rock displacement instrumentation and coupled hydraulic pressure/rock displacement instrumentation for use in a stiff crystalline rock. *Proceedings of a NEA Workshop on Excavation Responses in Geological Repositories for Radioactive Waste;* Winnipeg, 1989: 257-270.

Thompson, P.M. and Lang, P.A. Geomechanical instrumentation applications at the Canadian Underground Research Laboratory. *Proceedings of the 2nd International Symposium on Field Measurements in Geomechanics*, Kobe, 1987.

Tsang, Y.W. and Tsang, C.F. Channel model of flow through fractured media. *Water Resources Research*, 1987; **23**(3): 467-479.

Tsang, Y.W. , Tsang, C.F., Neretnieks, I., and Moreno, L. Flow and tracer transport in fractured media: a variable aperture channel model and its properties. *Water Resources Research*, 1988; **24**(12): 2049-2060.

Tsang, Y.W. and Witherspoon, P.A. Hydromechanical behaviour of a deformable rock fracture subject to normal stress. *Journal of Geophysical Research*, 1981; **86**(B10): 9287-9298.

Tsang, Y.W. and Witherspoon, P.A. Correlations between fracture roughness characteristics and fracture mechanical and fluid flow properties. *Proceedings of the 23rd U.S. Symposium on Rock Mechanics;* Berkeley, 1982: 560-567.

Tsang, Y.W. and Witherspoon, P.A. The dependence of fracture mechanical and fluid flow properties on fracture roughness and sample size. *Journal of Geophysical Research*, 1983; **88**(B3): 2359-2366.

Tsang, Y.W. and Witherspoon, P.A. Effects of fracture roughness on fluid flow through a single deformable fracture. *Hydrogeology of Rocks of Low Permeability, Memoires of 17th International Congress of the International Association of Hydrogeologists*, 1985; **2:** 683-694.

Van Dillen, D.E. and Ewing, R.D. BMINES - a finite element code for rock mechanics applications. *Proceedings of the 22nd U.S. Symposium on Rock Mechanics;* Boston, 1981: 373-378.

Verruijt, A. *Theory of Groundwater Flow*. Macmillan, 1970: 190p.

Vik, G. and Johansen, P.M. Determination of shear strength of rock joints at two dam sites and at Stripa Research Mine. *Proceedings of the International Symposium on Rock Joints*, 1990: 329-334.

Wallace, R.E. and Morris, H.T. Characteristics of faults and shear zones as seen in mines at depths as much as 2.5 Km below the surface. *Proceedings of Conference VIII Analysis of Actual Fault Zones in Bedrock*, USGS Open-File Report 79-1239, 1979: 79-100.

Walsh, J.B. and Grosenbaugh, M.A. A new model for analyzing the effect of fractures on compressibility. *Journal of Geophysical Research*, 1979; **84**(B7): 3532-3536.

Wei, Z.Q. and Hudson, J.A. The influence of joints on rock modulus. *Proceedings of International Symposium on Engineering in Complex Rock Formations;* Beijing, 1986: 54-62.

Wilson, C.R. and Witherspoon, P.A. An investigation of laminar flow in fractured rocks. *Geotechnical Report No. 70-6*, Berkeley, 1970.

Wilson, C.R., Witherspoon, P.A., Long, J.C.S., Galbraith, R.M., DuBois, A.O., and McPherson, M.J. Large-scale hydraulic conductivity measurements in fractured granite. *International Journal of Rock Mechanics and Mining Sciences & Geomechanics Abstracts*, 1983; **20**(6): 269-276.

Wilson, E. L. Finite elements for foundations, joints and fluids. in *Finite Elements in Geomechanics*. London: J. Wiley and Sons, 1977: 319-350.

Winberg, A. *Post-excavation analysis of a revised Room 209 hydraulic fracture model.* report to Atomic Energy of Canada Limited, Pinawa; 1988.

Witherspoon, P.A., Amick, C.H., Gale, J.E. and Iwai, K. Observations of a potential size effect in experimental determination of the hydraulic properties of fractures. *Water Resources Research*, 1979; **15**(5): 1142-1146.

Witherspoon, P.A., Tsang, Y.W., Long, J.C.S. and Noorishad, J. New approaches to problems of fluid flow in fractured rock masses. *Proceedings of the 22nd U.S. Symposium on Rock Mechanics;* Boston, 1981: 3-22.

Witherspoon, P.A. and Long, J.C.S. Some recent developments in understanding the hydrology of fractured rocks. *Proceedings of the 28th U.S. Symposium on Rock Mechanics;* Tucson, 1987: 421-432.

Witherspoon, P.A., Wang, J.S.Y., Iwai, K. and Gale, J.E. Validity of cubic law for fluid flow in a deformable rock fracture. *Water Resources Research*, 1980; **16**(6): 1016-1024.

Yang, G., Cook, N.G.W. and Myer, L.R. Network modelling of flow in natural fractures. *Prpceedings of the 30th U.S. Symposium on Rock Mechanics;* West Virginia, 1989: 57-64.

Yoshinaka, R. and Yamabe, T. Joint stiffness and the deformation behaviour of discontinuous rock. *International Journal of Rock Mechanics and Mining Sciences & Geomechanics Abstracts*, 1986; **23**(1): 19-28.

Zienkiewicz, O.C., Best, B., Dullage, C. and Stagg, K.G. Analysis of non-linear problems in rock mechanics with particular reference to jointed rock systems. *Proceedings of 2nd Congress of the International Society for Rock Mechanics;* Belgrade, 1970; **3**: 501-509.

Appendix A - Killarney Fracture Zones

Typical fracture zone geometries and orientations of the primary and secondary fractures within fracture zones were established by mapping a series of small fracture zones in the field. All the fracture zones are located near the mouth of Chlkanishing River in Killarney Provincial Park. The park is located on the north shore of Georgian Bay in Ontario. The host rock is a massive, cataclastic quartz monzonite of the Grenville Front pluton. The rock is middle to late Precambrian in age. It is possible that the formation of the fracture zones was related to a major fault which is located approximately 800 to 900 meters southeast of the mapped area.

The fracture zones are scattered along the shore of Georgian Bay at approximately 300 to 500 m east of the mouth of the Chlkanishing River. Wave erosion has removed all soil and vegetation leaving well exposed traces of the fracture zones. Field mapping was performed with a Clar compass and tape measure. Orientations of the fracture zones and the numerous primary and secondary fractures within these zones were recorded. These measurement were all of the true fracture orientations. Additional measurements of fracture length, offset, offset direction, overlap, and fracture aperture were also taken. The fracture zones displayed multiple, subparallel, en echelon primary fractures ranging in length from a few centimetres to 1 or 2 metres. The fracture traces are straight or gently curved. The primary fractures consistently stepped to the right. The length of the offset (step distance) varied from a few millimetres to 10's of centimetres .

Trace maps for two fracture zones (Figs. A.1 and A.2) were made with the assistance of a sheet of 15 cm by 15 cm welded wire mesh which was used as a reference grid when drawing the traces. The thickness of the lines in these figures represents the relative apertures of the the fractures. The primary fractures are distinguished by their longer traces, wider apertures, and consistent orientation. Secondary fractures may be more numerous, but are short and have smaller apertures. Secondary fractures rarely cut through more than one primary fracture. Instead, they tend to connect between primary fractures. Short fractures which have similar orientation to the larger primary fractures are also classified as primary fractures.

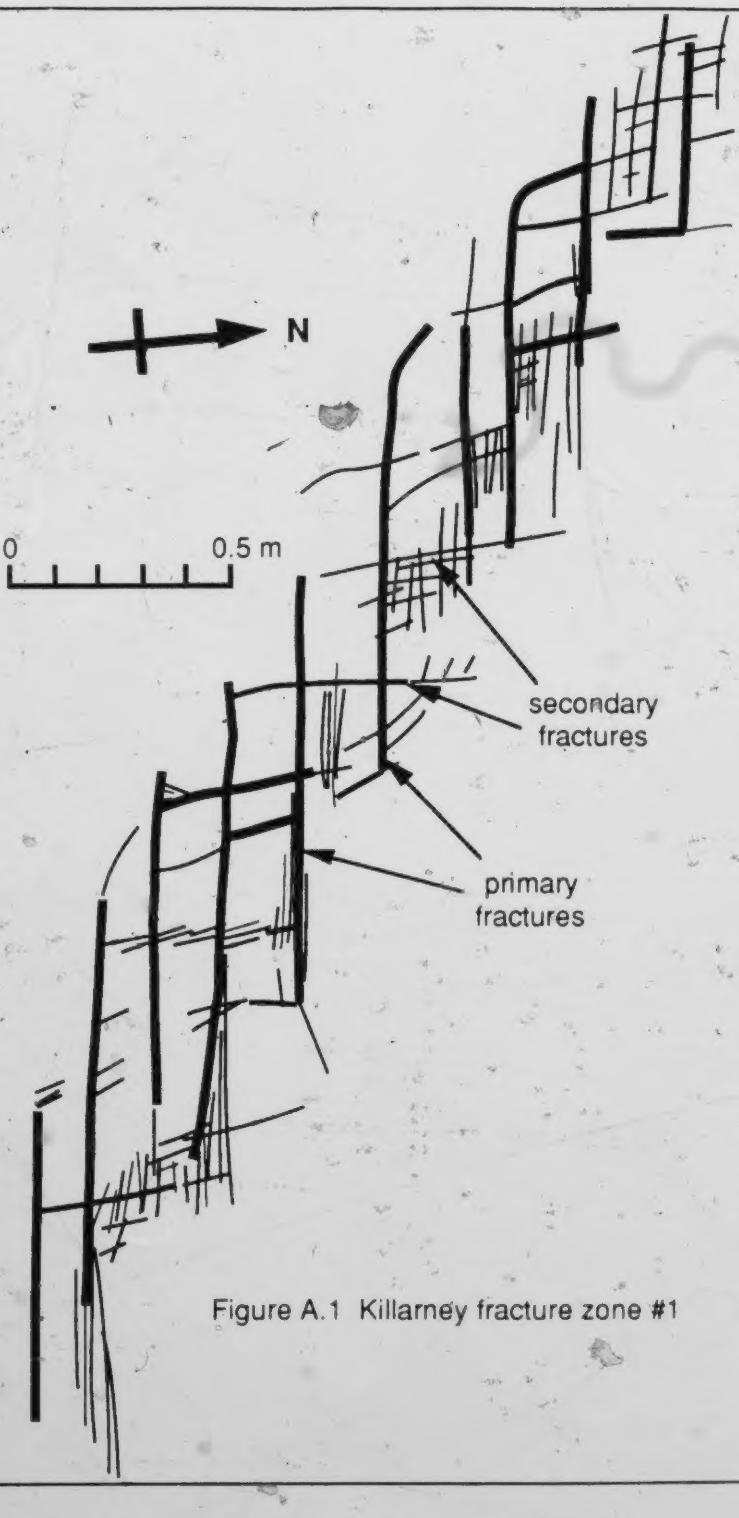

Figure A.1 Killarney fracture zone #1

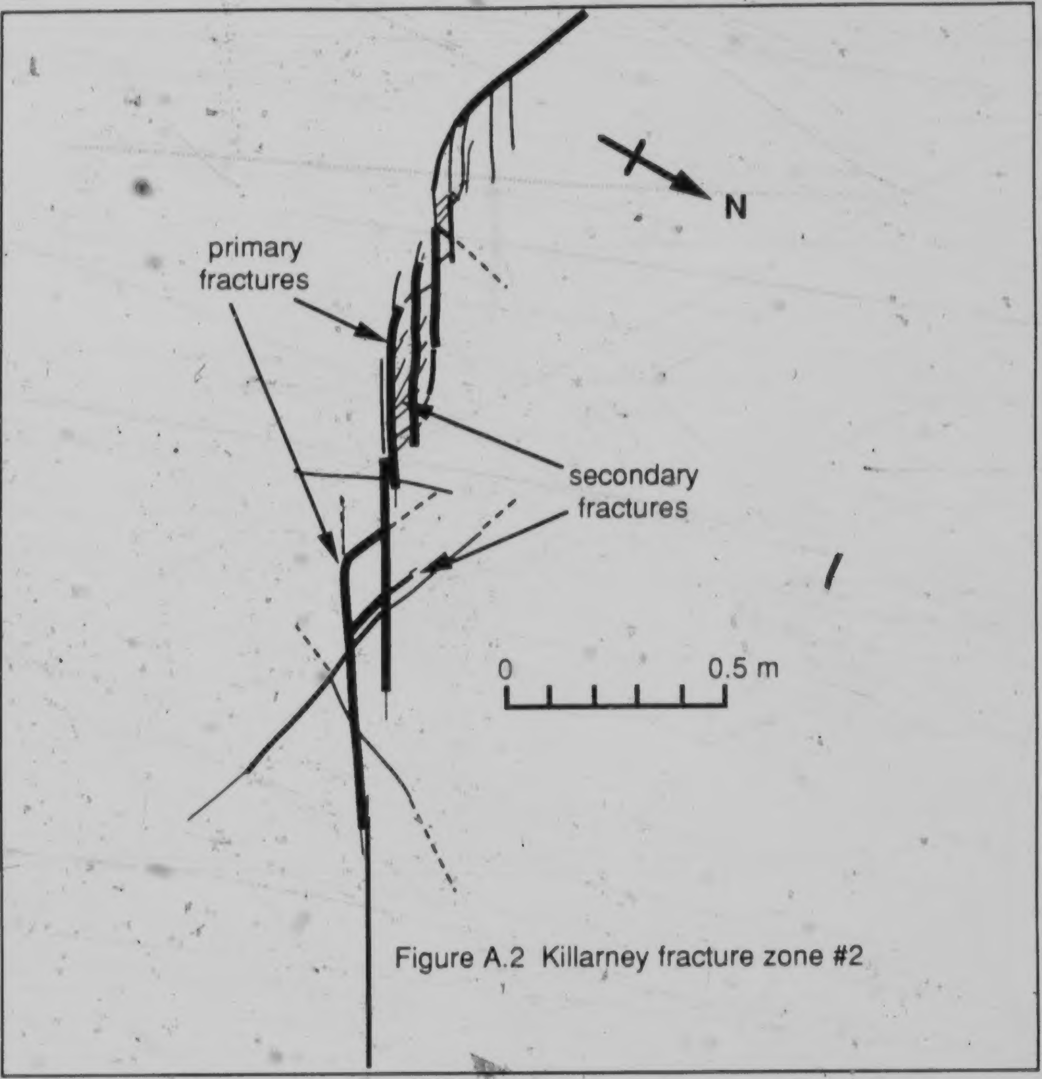

Figure A.2 Killarney fracture zone #2

The orientation data was entered into a stereonet computer program from which the mean poles to the primary and secondary fractures in each fracture zone were determined. Figures A.3 and A.4 present stereonet plots of the mean orientations of the primary and secondary fractures as well as the approximate orientation of the steeply dipping fracture zones. It is likely that the fracture zones did not all dip at exactly 90°. However, it was not possible to accurately determine the dips of the fracture zones and hence, they are plotted at 90°. Table A.1 present a compilation of the angles between the primary and secondary fractures and the fracture zone as well as the mean primary fracture lengths, offsets, and overlaps.

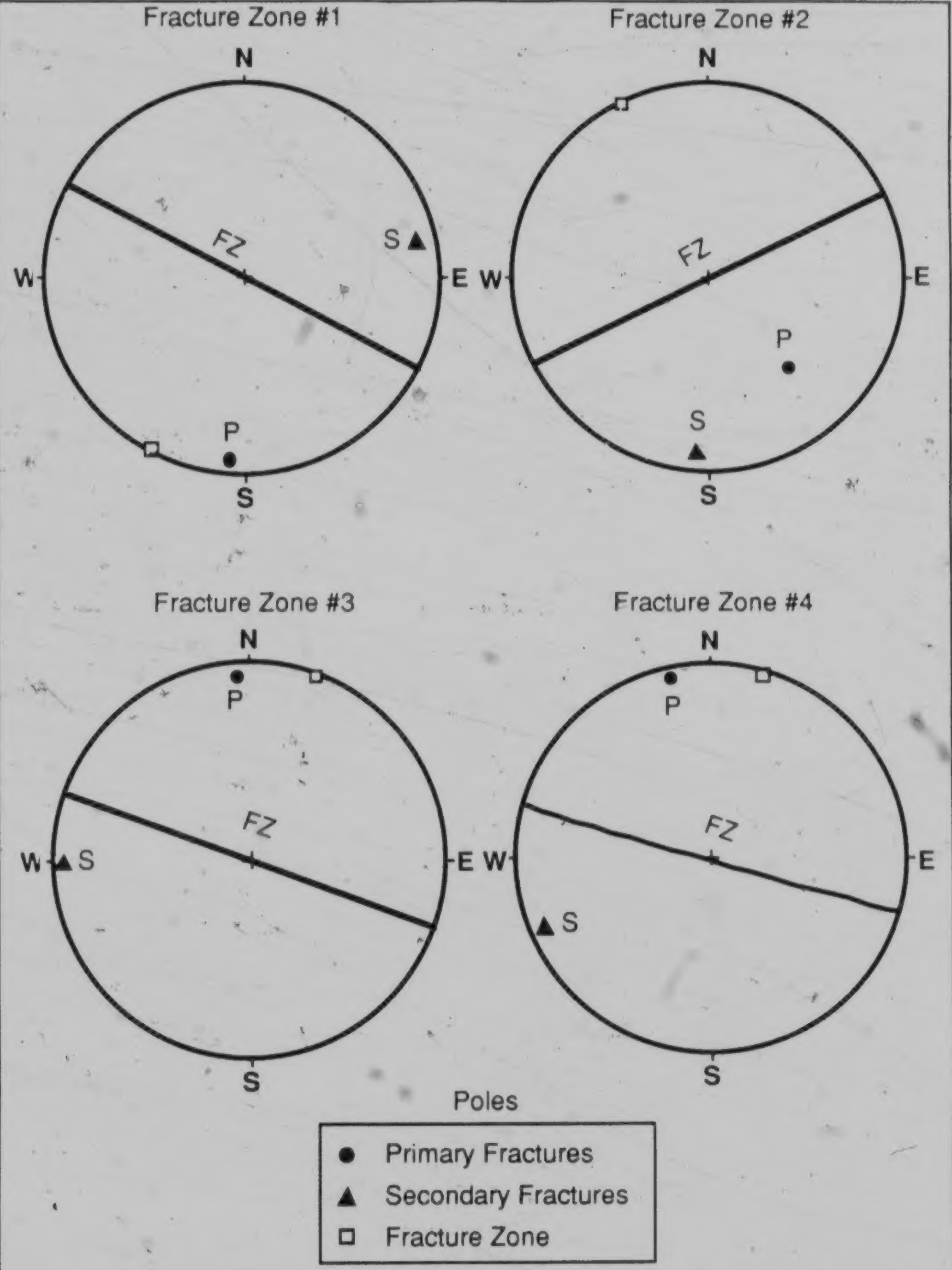

Figure A.3 Mean fracture orientations of Killarney fracture zones 1 to 4

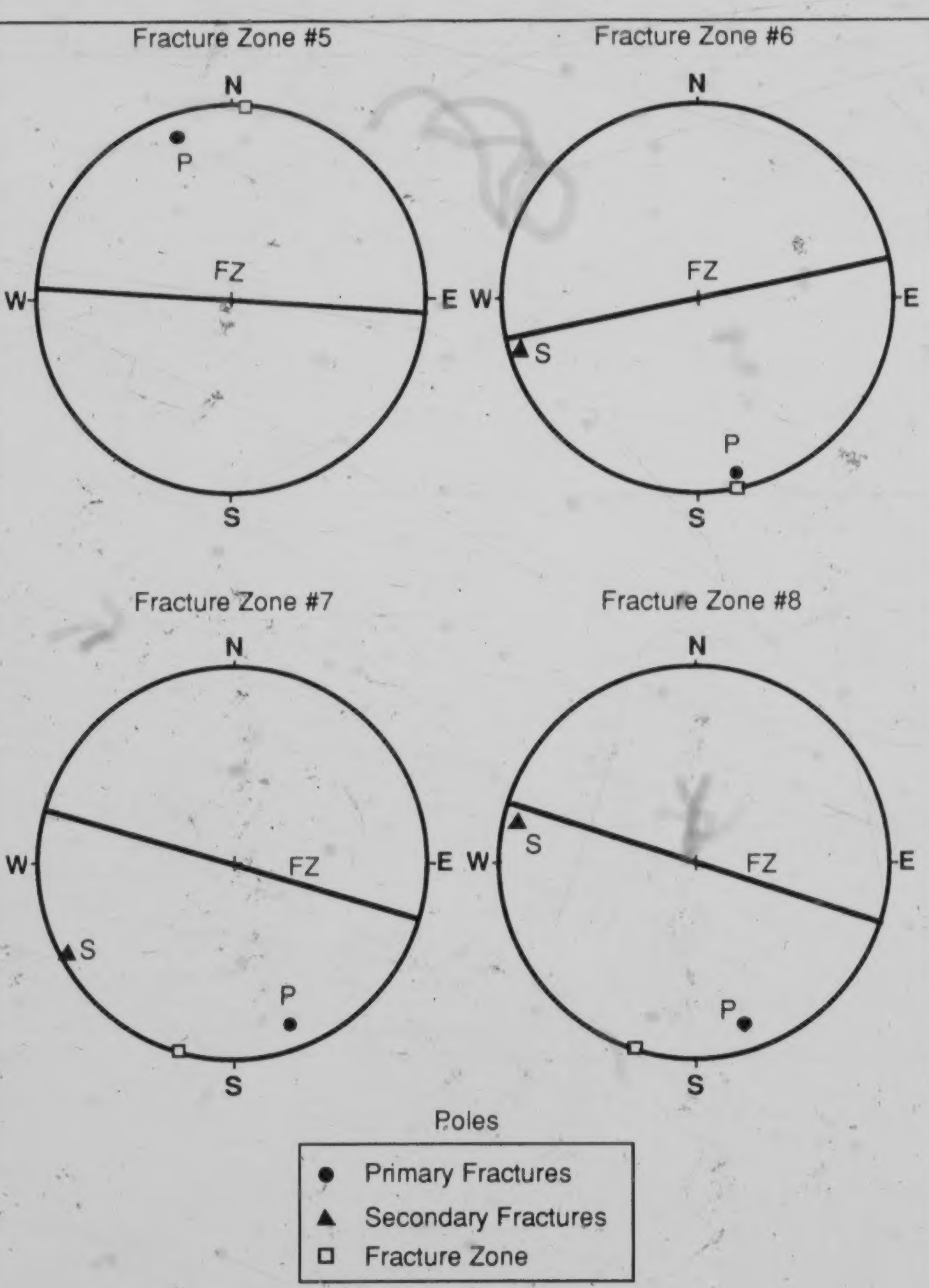

Figure A.4 Mean fracture orientation of Killarney fracture zones 5 to 8

Table A.1 Summary of fracture zone characterization

Fracture Zone	Angles Between: Primary and Fracture Zone	Angles Between: Secondary and Fracture Zone	Angles Between: Primary and Secondary	Primary Fracture Dimensions: Fracture Length [cm]	Primary Fracture Dimensions: Fracture Offset [cm]	Primary Fracture Dimensions: Fracture Overlap [cm]
1	25°	50°	74°	30.7	3.3	24.1
2	41°	33°	49°	45.7	4.1	-
3	25°	70°	86°	52.1	3.8	26.8
4	28°	54°	82°	-	-	-
5	25°	-	-	70	1.5	65
6	9°	87°	87°	55.5	2.7	36.4
7	38°	47°	82°	44.4	1.0	-
8	36°	86°	62°	54.5	1.4	24.7
average	28°	61°	75°	50.4	2.5	35.4

The stereonets and Table A.1 show that the primary fractures are inclined at less than 45° to the trend of the fracture zone whereas the secondary fractures are more steeply oriented (generally greater than 45°) relative to the fracture zone trend. The angle between the primary and secondary fracture is typically close (within 15°) to perpendicular. The fracture lengths and offset vary for each fracture zone. Fracture overlap is generally high, commonly over 70% of the primary fracture length.

When considering flow through a fracture zone, connected fractures will control the flow pattern. For example, by eliminating dead-end flow paths (fracture traces which do not connect to other fractures) a map of the flow paths (in 2-D) may be obtained. Figure A.5 presents the flow paths for fracture zone #1 (Fig. A.1). The longer primary fractures and the near perpendicular secondary fractures can be seen to dominate the flow pattern. It is this type of flow pattern that is represented by the flow model in Section 3 (Figs. 3.2 and 3.3). By combining the connecting secondary fractures into a single connecting fracture a stepped flow model may be realized. The single connecting fracture which represents one or more secondary fractures would have an aperture approximately equal to the primary fracture aperture. The equivalence in aperture allows the shear - transmissivity relationship to initially start at the peaks as shown in Figures 3.5 to 3.7.

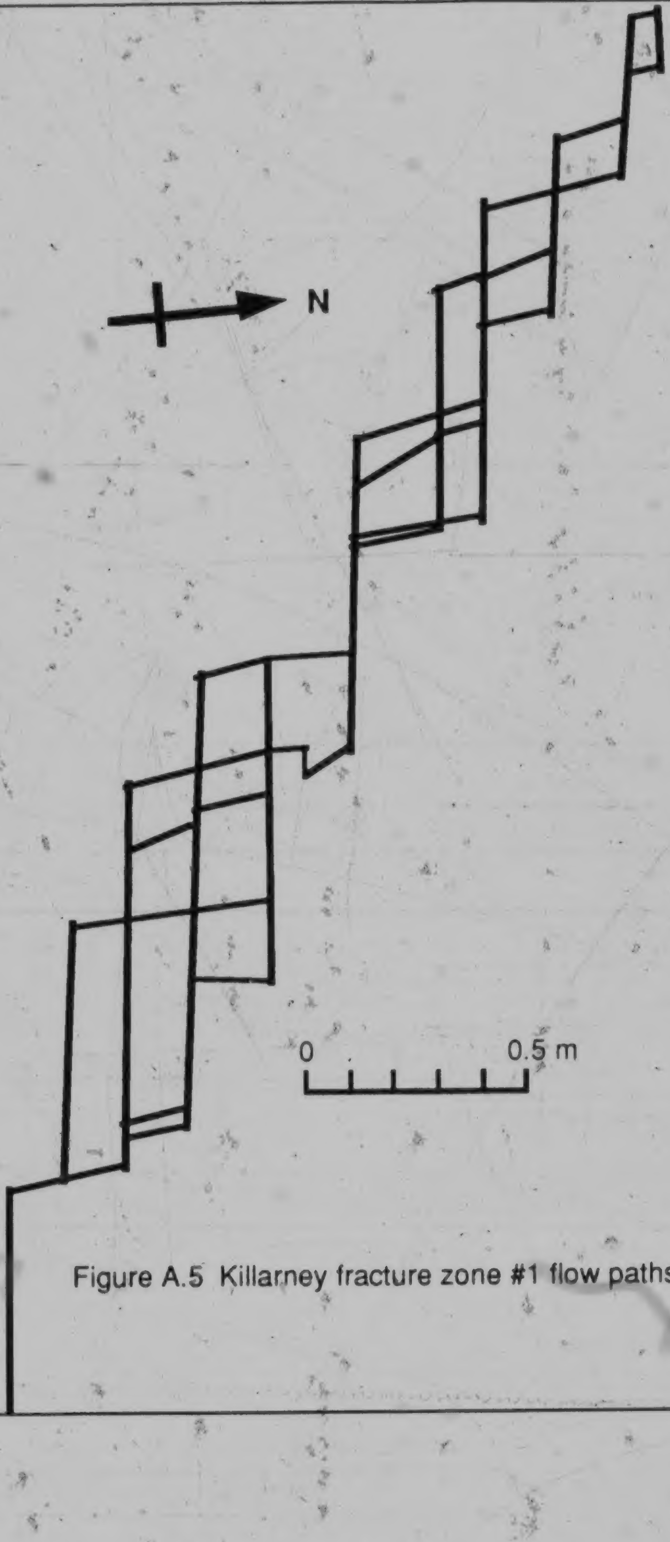

Figure A.5 Killarney fracture zone #1 flow paths

Appendix B - Application of Barton-Bandis Equations to Data from Room 209

Typical data obtained from rock and fractures near Room 209 illustrates the application of the Barton-Bandis group of empirical equations (Section 2.4). The procedure highlighted here may be used to estimate normal and shear stiffness for individual fractures if no actual measurements of stiffness are available. The empirical equations describing the fracture stress-deformation response are listed in Table B.1. Barton and Bakhtar, (1983) provided additional empirical equations for determining some of the parameters needed for the equations in Table B.1. These additional equations may easily be replaced by experimental values if they are available. The measured rock and fracture parameters required for these equations and their values are list in Table B.3.

Table B.1 Barton-Bandis empirical equations

No.	Relationship	Empirical Relationship	Reference
B.1	Normal Stress versus Closure	$\sigma_n = \dfrac{\delta_n}{\dfrac{1}{K_{ni}} - \dfrac{\delta_n}{V_m K_{ni}}}$	Bandis et al., 1983
B.2	Normal Stiffness versus Closure	$K_n = \dfrac{K_{ni}}{\left(1 - \dfrac{\delta_n}{V_m}\right)^2}$	Bandis et al., 1983
B.3	Normal Stiffness versus Normal Stress	$K_n = \dfrac{K_{ni}}{\left(1 - \dfrac{\sigma_n}{V_m K_{ni} + \sigma_n}\right)^2}$	Bandis et al., 1983
B.4	Shear Stress (Strength) versus Normal Stress	$\tau_p = \sigma_n \tan\left[JRC \log\left(\dfrac{JCS}{\sigma_n}\right) + \phi_r\right]$	Barton, 1976
B.5	Shear Stiffness versus Normal Stress	$K_s = \dfrac{\sigma_n}{\delta_{(peak)}} \tan\left[JRC \log\left(\dfrac{JCS}{\sigma_n}\right) + \phi_r\right]$	Barton and Bakhtar, 1983

Table B.2 Additional empirical relationships (after Barton and Bakhtar, 1983)

No.	Empirical Relationship	
B.6	size dependent JCS	$JRC = JRC_o \left(\frac{L}{L_o} \right)^{-0.02 JRC_o}$
B.7	size dependent JRC	$JCS = JCS_o \left(\frac{L}{L_o} \right)^{-0.03 JRC_o}$ MPa
B.8	shear displacement to mobilize peak strength	$\delta_{(peak)} = \frac{L}{500} \left(\frac{JRC}{L} \right)^{0.33}$ m
B.9	initial normal stiffness	$K_{ni} = 0.02 \left(\frac{JCS_o}{a_o} \right) + 1.75\, JRC_o - 7$ MPa/mm
B.10	fracture aperture at low (1 kPa) normal stress	$a_o = \frac{JRC_o}{5} \left(0.2 \frac{\sigma_c}{JCS_o} - 0.1 \right)$ mm

Table B.3 Rock and fracture parameters

Parameter	Value	Reference
JCS_o (6.1 cm core)	132.7 MPa	Martin et al., 1990a
JRC_o (6.1 cm core)	6.4	Martin et al., 1990a
σ_c	167 MPa	Martin et al., 1990a
σ_n	10.5 MPa	Section 5.4.2
ϕ_r	30°	assumed
L	1 m	assumed
in situ apertures	16 to 104 μm	Lang et al., 1987b

B.1 Determination of Normal and Shear Stiffnesses

1) Determine values for JRC and JCS:

$$JRC = 6.4 \left(\frac{1}{0.061} \right)^{-0.02(6.4)} = 4.5$$

$$JCS = 132.7 \left(\frac{1}{0.061} \right)^{-0.03(6.4)} = 77.6 \text{ MPa}$$

2) Estimate the amount of shear displacement required to mobilize peak shear strength:

$$\delta_{(peak)} = \frac{1}{500} \left(\frac{4.5}{1} \right)^{0.33} = 3.3 \text{ mm}$$

Note: the maximum closures measured at Room 209 were less than 2 mm. Since 2 mm would be an upper bound on the shear displacements in the fracture zone, the assumption of pre-peak fracture response is valid.

3) Estimate the aperture at low normal stress:

$$a_o = \frac{6.4}{5}\left(0.2\frac{167}{132.7} - 0.1\right) = 0.19 \text{ mm}$$

4) Estimate the maximum fracture closure:

Since the 'measured' initial apertures vary over a wide range it is difficult to estimate the maximum fracture closure. Certainly the maximum closure must be less than the estimated initial aperture from step 3 and hence, a value of 90% of initial aperture is assumed.

$$V_m = 0.17 \text{ mm}$$

Comparing a_o and V_m with the 'measured' apertures would indicate that the fractures are closed as far as possible at some locations. Hence, the in situ fractures are represented by points well up the normal stress - closure curve. This implies that a constant normal stiffness assumption may be adequate.

5) Estimate the initial normal stiffness (at low σ_n):

$$K_{ni} = 0.02\left(\frac{132.7}{0.19}\right) + 1.75(6.4) - 7 = 18 \text{ MPa/mm}$$

B.1.1 Normal Stiffness

6) Determine the expression for normal fracture stiffness:

$$K_n = \frac{18}{\left(1 - \frac{\sigma_n}{0.17(18) + \sigma_n}\right)^2} = 18\left(1 - \frac{\sigma_n}{3.0 + \sigma_n}\right)^{-2} \quad \text{MPa/mm}$$

This relationship is plotted in Figure B.1 The in situ normal stiffness is given by the normal stress of 10.5 MPa. The maximum range in normal stresses expected as Room 209 is excavated (Fig. 5.7) is indicated by the shaded area. This figure indicates that the normal stiffness should vary between 245 and 520 MPa/mm.

B.1.2 Shear Stiffness

7) Determine the fracture shear stiffness:

$$K_s = \frac{10.5}{3.3}\tan\left[4.5\log\left(\frac{77.6}{10.5}\right)+30\right] = 2.1\ \mathrm{MPa/mm}$$

The shear stiffness is calculated with the in situ normal stress. For the calculation, this normal stress is assumed to be equivalent to the normal stress present in the fracture if the fracture were sheared to peak. However, the normal stress should be higher at peak and hence, the shear stiffness as calculated will be a lower bound.

B.2 Implications

This Appendix demonstrates the many assumptions and empirical relationships which are required for the calculation (estimation) of fracture stiffnesses when stiffness measurements are not available. Each assumption and empirical equation introduces potential error to the final stiffness values. Hence, the stiffnesses determined from these empirical relationship should be used with caution and serve only to provide rough guidelines on the in situ fracture stiffnesses. Naturally, measurements of fracture stiffness would be preferred to values determined from these equations.

The uncertainty associated with determining the fracture stiffnesses leads to the question of whether complex or nonlinear relationships for fracture stiffness are necessary. For example, at Room 209 the estimated maximum normal stiffness range generated by the changes in normal stress as the excavation passes the fracture zone was only 245 to 520 MPa/mm. The error associated with determining the parameters which defined the hyperbolic normal stress-stiffness relationship for Room 209 probably induce as much variation as does the hyperbolic relationship itself. Therefore, in cases where the normal stress range is limited and starts at a fairly high level, linear relationships between fracture closure and normal stress should be sufficient for most modelling purposes. Naturally when modelling closure from an initial unstressed state, the hyperbolic relationship becomes more important.

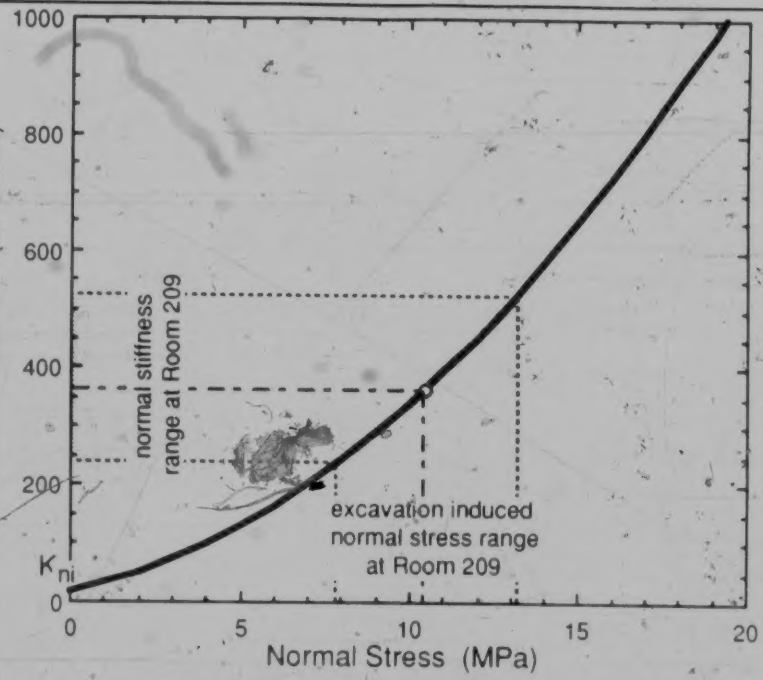

Figure B.1 Normal stiffness versus normal stress for fractures in the Room 209 fracture zone

Appendix C - Parallel Plate Analogy for Flow in a Single Fracture

The equations for one-dimensional (plane, irrotational) laminar flow of a Newtonian fluid between two parallel plates have been derived by Polubarinova-Kochina (1962), Bear (1972) and others. The derivations presented by these authors were based on the Navier-Stokes equation for the flow of a viscous incompressible fluid. A different derivation can be obtained by examination of forces on elemental volumes of fluid between the parallel plates. Laminar flow between parallel plates is caused by a difference in piezometric pressure and for laminar flow there is no movement of fluid in any direction perpendicular to the flow, and thus the piezometric pressure varies only in the direction of flow. A coordinate system can be set up with the origin at a point on the lower plate with the *x* axis along the plane parallel to the flow, and the *y* axis perpendicular to the plane (Fig. C.1a). The distance between the parallel plates or aperture is *a*. The requirement of zero fluid velocity at the two plate boundaries (no slip condition) produces a variation of velocity in the *y* direction.

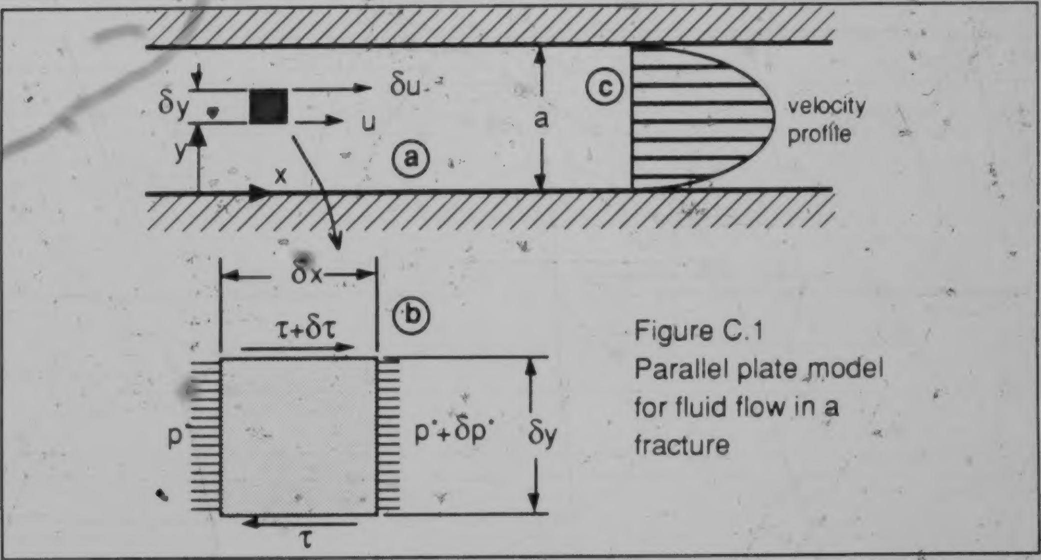

Figure C.1
Parallel plate model for fluid flow in a fracture

The viscous stresses resisting flow may be related to the forces arising from the difference of piezometric pressure by considering a small rectangular element of fluid as shown in Figure C.1b. Let the lower face of the element be distance *y* from the lower boundary and here let the velocity be *u*. At the upper face of the element, a distance $y+\delta y$ from the lower boundary, with velocity $u+\delta u$. If δu is positive, the faster-moving fluid just above the element exerts a forward force on the upper face of the element. Similarly, the slower-moving fluid adjacent to the lower face tends to retard the element. Thus there are stresses of magnitude τ on the lower face and $\tau+\delta\tau$ on the upper face in the direction shown in Figure C.1b. Let the piezometric pressure be p^* at the left end face, and $p^*+\delta p^*$ at the right end face. For unit width, the total force acting on the element towards the right is:

$$\{\, p^* - (\, p^* - \delta p^*)\}\,\delta y + \{(\tau + \delta\tau) - \tau\}\delta x \qquad [C.1]$$

But for steady-state flow there is no acceleration, so this force must be zero, therefore:

$$-\delta p^*\,\delta y + \delta\tau\,\delta x = 0 \qquad [C.2]$$

Dividing by $\delta x \delta y$ and proceeding to the limit $\delta y \to 0$, we get:

$$\frac{\partial p^*}{\partial x} = \frac{\partial \tau}{\partial y} \qquad [C.3]$$

We now need an expression for τ. The basic law of viscous resistance in laminar flow was described by Newton in 1687:

$$\tau = \mu\frac{\partial u}{\partial y} \qquad [C.4]$$

where μ represents the dynamic viscosity of the fluid. Note that kinematic, or molecular viscosity, v is the ratio μ/ρ. Using Equation C.4, Equation C.3 becomes:

$$\frac{\partial p^*}{\partial x} = \frac{\partial}{\partial y}\left(\mu\frac{\partial u}{\partial y}\right) \qquad [C.5]$$

Since p^* nowhere varies in the y direction, $\partial p^*/\partial x$ is independent of y and Equation C.5 may be integrated with respect to y to yield:

$$\frac{\partial p^*}{\partial x}\,y = \mu\frac{\partial u}{\partial y} + A \qquad [C.6]$$

For constant μ, a further integration with respect to y gives:

$$\left(\frac{\partial p^*}{\partial x}\right)\frac{y^2}{2} = \mu u + Ay + B \qquad [C.7]$$

The constants A and B are independent of x and may be determined by consideration of boundary conditions. If both plates are stationary the velocity of the fluid in contact with each boundary must be zero. Thus for $u = 0$ at $y = 0$ and $y = a$ yields $B = 0$ and $A = \left(\frac{\partial p^*}{\partial x}\right)\frac{a}{2}$.

Therefore, the fluid velocity at any distance y from the lower plate may be found from:

$$u = \frac{1}{2\mu}\left(\frac{\partial p^*}{\partial x}\right)(y^2 - a\,y) \qquad [C.8]$$

Equation C.8 shows that the velocity profile is in the form of a parabola with a vertex mid-way between the plates (Fig. C.1c). The total volume flow rate (Q) between the two plates may be found by considering an elemental strip, of thickness δy and unit width. The total discharge through the strip is:

$$Q = \int_0^a u\,dy = \int_0^a \frac{1}{2\mu}\left(\frac{\partial p^*}{\partial x}\right)(y^2 - a\,y)\,dy = -\frac{a^3}{12\mu}\left(\frac{\partial p^*}{\partial x}\right) \qquad [C.9]$$

In terms of hydraulic head, (h)the total flow per unit length of plate plate is given by:

$$Q = -\frac{\rho g}{12\mu}a^3 \nabla h \qquad [C.10]$$

It can be seen that Equation C.10 describing the flow between two parallel plates is analogous to Darcy's Law and thus for flow in a planar smooth-walled fracture the hydraulic conductivity is defined by:

$$K_f = \frac{\rho g}{12\mu}a^2 \qquad [C.11]$$

where a is the plate separation or, in the case of fractures, is the hydraulic aperture.

Equation C.9 is the well known cubic flow law for parallel plates separated by distance a. This flow law was derived from consideration of one-dimensional flow and may not be equally applicable to cases of divergent or convergent radial flow. However, Rissler (1978) shows that the flow velocity distribution between parallel plates for divergent radial flow differs slightly from the parabolic distribution for one-dimensional flow. Fortunately, Tsang and Witherspoon (1981) show that a correction factor which accounts for the geometric effects associated with radial flow becomes negligible as the ratio of outer radius to well bore radius becomes large (greater than about 7). Therefore, the flow equations valid for one-dimensional flow are taken as reasonable approximations for describing radial flow into openings such as tunnels and shafts.

Appendix D - Displacements Around a Circular Opening

Derivations for the displacements around a circular hole in a homogeneous plate subject to plane strain conditions have been presented by many researchers (Obert and Duvall, 1967; Jaeger and Cook, 1976; Kaiser, 1984; Goodman, 1989). The displacements are calculated by subtracting the displacements due to installation of the initial stresses on a plate without a hole from the displacements generated around a circular hole in a plate which is subject to a biaxial stress field.

Under $K_0 = 1$ conditions the displacements occur only in the radial direction and are given by:

$$u = \frac{\sigma(1 + \nu)}{E} r\left(\frac{a}{r}\right)^2 \qquad [D.1]$$

Under $Ko \neq 1$ conditions displacements occur in both the radial and tangential directions and the displacements are also a function angular location as well as radius. The radial displacements are given by:

$$u_r = \frac{\sigma_v(1 + \nu)}{2E} r\,[A + B] \qquad [D.2]$$

where the parameters *A* and *B* are:

$$A = (1 + K_o)\left(\frac{a}{r}\right)^2 \qquad [D.3]$$

$$B = -(1 - K_o)\cos 2\theta\left[4(1 - \nu)\left(\frac{a}{r}\right)^2 - \left(\frac{a}{r}\right)^4\right] \qquad [D.4]$$

The tangential displacements are given by:

$$v_\theta = \frac{\sigma_v(1 + \nu)}{2E} r\,C \qquad [D.5]$$

where *C* is:

$$C = (1 - K_o)\sin 2\theta\left[2(1 - 2\nu)\left(\frac{a}{r}\right)^2 + \left(\frac{a}{r}\right)^4\right] \qquad [D.6]$$

The maximum displacement and direction is given by the vector sum of the radial and tangential components.

$$u_m = \left(u_r^2 + v_\theta^2\right)^{\frac{1}{2}} \; ; \quad \beta = \theta - \arctan\left(\frac{v_\theta}{u_r}\right) \qquad [D.7]$$

The symbols used in these equations are as follows:

E = Young's Modulus
ν = Poisson Ratio
σ_v = vertical stress
Ko = principal stress ratio
a = opening radius
r = radial distance
θ = angular location
β = maximum displacement vector orientation
u_r = radial displacement (positive inwards)
v_θ = tangential displacement (positive counter-clock wise)
u_m = maximum displacement

Note: angles are measured counter-clock wise from the major principal stress direction.

Figure D.1 presents plots of radial displacement versus radial distance from the centre of a circular opening subject to four different initial stress fields. The displacements are plotted against distance along lines parallel to the principal stress directions.

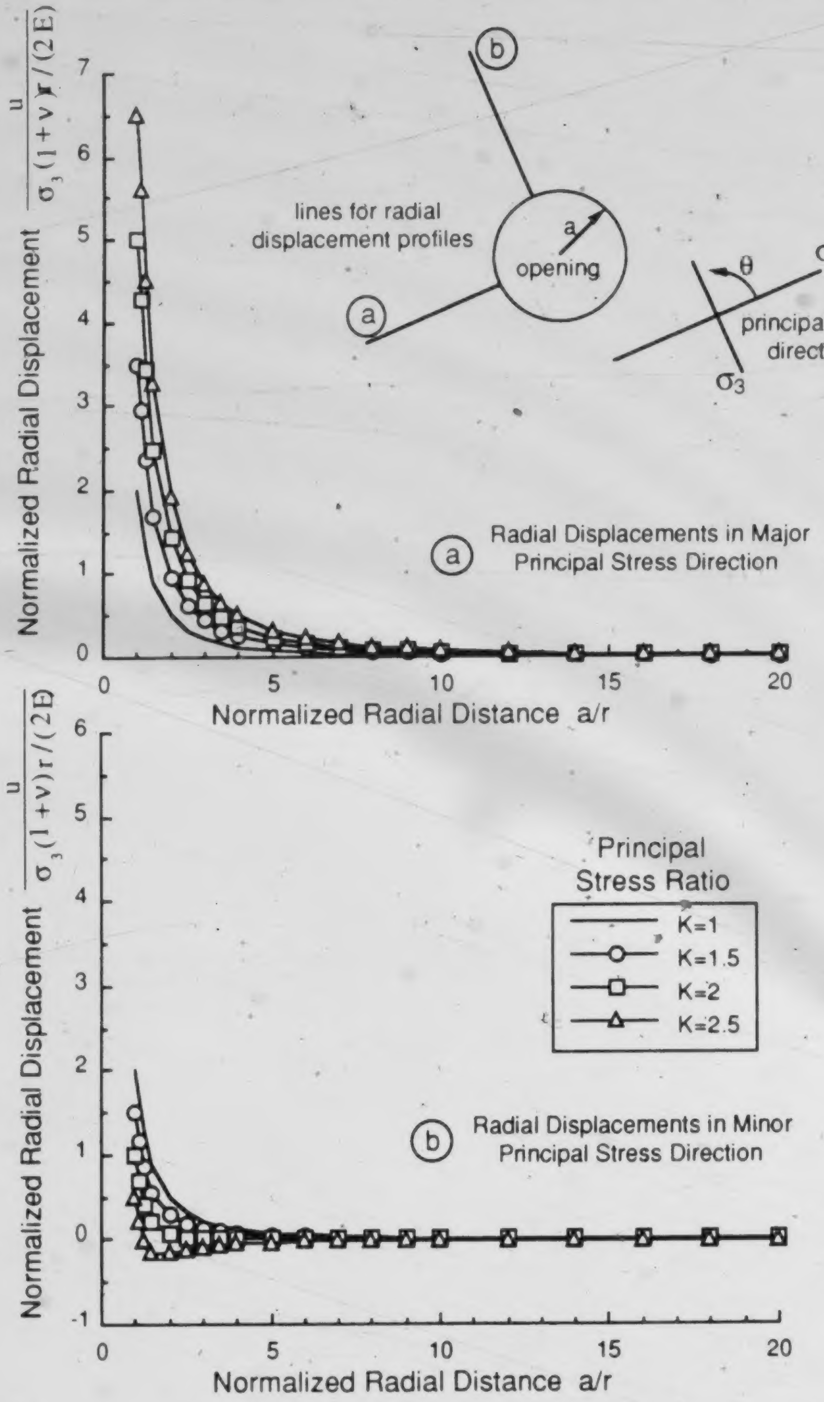

Figure D.1 Radial displacements around a circular opening

Appendix E - Steady-State Radial Flow into a Circular Opening

For radial flow in a fracture zone, the analogy to radial flow in a confined aquifer may be used. The following equations apply for two-dimensional flow into a opening centred in an area bounded by a constant pressure. The transmissivity (T) of the fracture zone (or confined aquifer) is assumed homogeneous and isotropic. Due to two-dimensional flow conditions, the Dupuit assumptions apply without error. For steady-state radial flow, using polar coordinates with the centre of the opening as the origin, the discharge (Q) at any radial distance (r) equals:

$$Q = -2\pi r T \frac{\partial h}{\partial r} \qquad [E.1]$$

Rearranging, integrating, and application of known boundary conditions at the opening, $h=h_o$ at $r=r_o$, and at the outer boundary, $h=H$ at $r=R$, yields:

$$H - h_o = -\frac{Q}{2\pi T} \ln \frac{r_o}{R} \qquad [E.2]$$

or

$$Q = 2\pi T \frac{H - h_o}{\ln(R/r_o)} \qquad [E.3]$$

with the negative sign neglected.

Equation E.3 can be extend to more complex transmissivity distributions. Using conservation of flow, when the opening lies in the middle of two concentric rings of different transmissivities, the head at the opening is given by:

$$h_o = H + \frac{Q}{2\pi T_1} \ln \frac{r_o}{r_i} + \frac{Q}{2\pi T_2} \ln \frac{r_i}{R} \qquad [E.4]$$

where r_i is the radial distance to the interface between the zones with transmissivities T_1 and T_2.

Appendix F - Effect of Additional Boreholes on Q/ΔH Determined at a Borehole

The solution for head drop at a single well (a sink) in the centre of a circular confined aquifer with fixed head at its outer boundary is (Appendix E; Verruijt, 1970):

$$\Delta h = \frac{-Q}{2\pi T} \ln \frac{r}{R} \qquad \text{[F.1]}$$

where r is the radial distance from the well, R is the outer radius to the fixed head, H, and T is the aquifer transmissivity. The principle of superposition allows the solution of drawdown anywhere in the aquifer for two (or more) wells. For two wells spaced at a distance $2p$, the head drop anywhere in the aquifer (except at the singularity points of the wells themselves) is given as:

$$\Delta h = \Delta h_1 + \Delta h_2 \qquad \text{[F.2]}$$

$$\Delta h = \frac{-Q_1}{2\pi T} \ln \frac{\left((x-p)^2 + y^2\right)^{\frac{1}{2}}}{R} + \frac{-Q_2}{2\pi T} \ln \frac{\left((x+p)^2 + y^2\right)^{\frac{1}{2}}}{R} \qquad \text{[F.3]}$$

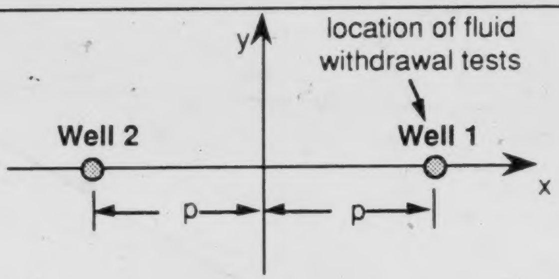

Figure F.1 Two wells in a circular confined aquifer

Let's use one well to simulate a fluid withdrawal test. Then the values of $Q/\Delta h$ can be determined both with and without the presence of an additional well using Equations F.1 and F.3. Note the location of all values will be taken at the radius of the borehole.

1) Initialize the parameters (note parameters are typical for a fracture zone):

$R = 100$ m
$H = 100$ m @ R
$T = 1 \times 10^{-6}$ m^2/s
$p = 2$ m
$r = 0.01$ m (the radius of borehole)
$Q_1 = 1 \times 10^{-5}$ m^3/s

2) Perform a fluid withdrawal test at well 1 without the presence of well 2:

$$\Delta h_1 = \frac{-1\text{x}10^{-5}}{2\pi\left(1\text{x}10^{-6}\right)} \ln\frac{0.01}{100} = 14.66 \quad \text{m} \qquad [\text{F.4}]$$

Therefore, **$Q/\Delta h = 6.82 \times 10^{-7}$ m²/s**.

3) Add well 2. Calculate the steady state head at the well 1 location due to the presence of well 2 fixed at a zero head. (Note, well 2 is free-draining and well 1 is only monitoring head).

3a) Determine the flow from well 2 which results in zero head at well 2:

$$Q_2 = 2\pi\left(1\text{x}10^{-6}\right)\frac{100}{\ln(100/0.01)} = 6.82\text{x}10^{-5} \quad \text{m}^3/\text{s} \qquad [\text{F.5}]$$

3b) Calculate the steady-state head at well 1 due to flow from well 2:

$$\Delta h_1 = \frac{-6.82\text{x}10^{-5}}{2\pi\left(1\text{x}10^{-6}\right)} \ln\frac{4}{100} = 34.95 \quad \text{m} \qquad [\text{F.6}]$$

Therefore, the steady state head at well 1 while well 2 is free-draining is 100 - 34.95 = 65.05 m.

4) Now perform a fluid withdrawal test at well 1.

4a) Recalculate the flow from well 2 which gives zero head at well 2 (now with well 1 withdrawing Q_1)

$$\Delta h_2 = 100 = \frac{-1.0\text{x}10^{-5}}{2\pi\left(1\text{x}10^{-6}\right)} \ln\frac{4}{100} + \frac{-Q_2}{2\pi\left(1\text{x}10^{-6}\right)} \ln\frac{0.01}{100} \qquad [\text{F.7}]$$

Solving for flow at well 2 gives $Q_2 = 6.47 \times 10^{-5}$ m³/s. Note that Q_2 is smaller than before since the packer test at well 1 is also contributing to the drawdown at well 2.

4b) Using the new Q_2, calculate the drawdown at well 1 due to flows from both well 1 and 2.

$$\Delta h_1 = \frac{-1.0 \times 10^{-5}}{2\pi\left(1 \times 10^{-6}\right)} \ln\frac{0.01}{100} + \frac{-6.47 \times 10^{-5}}{2\pi\left(1 \times 10^{-6}\right)} \ln\frac{4}{100} = 47.82 \quad \text{m} \qquad [\text{F.8}]$$

Since Δh_1 is relative to H = 100 m, the head at well 1 is 100 - 47.82 = 52.18 m. Therefore, the head drop solely due to the fluid withdrawal test at well 1 is 65.05 - 52.18 = 12.87 m. Now **$Q/\Delta h = 7.77 \times 10^{-7}$ m^2/s**.

This example shows that the altered flow conditions (boundary conditions) caused by the addition of another well increased the 'measured' $Q/\Delta h$ at well 1 from 6.82×10^{-7} m^2/s to 7.77×10^{-7} m^2/s (14% increase) even though the transmissivity remained constant.

Appendix G - Measured Hydraulic Response at Room 209

The following tables present a compilation of the measured hydraulic responses in the Room 209 fracture zone. The term 'stage' as used in these tables refers to either the position of the excavation face relative to the fracture zone as measured along the centerline of the tunnel or activities related to blasting through the fracture zone.

Table G.1 Borehole interference test results (after Lang et al., 1986)

Test Borehole	**Q** (l/min)	**Head Drop** (m) N1	N2	R1	R2	S1	S2	F1&F2	OC1	**Q/ΔH** (m^2/s)
OC1	3.42	22.2	22.3	17.7	17.6	7.6	17.0	19.2	25.3	2.25E^{-6}
OC1	3.48	2.22	22.2	17.7	17.6	8.4	17.1	19.0	25.4	2.28E^{-6}
OC1	3.42	22.4	22.5	17.9	17.9	8.2	17.3	19.4	25.4	2.24E^{-6}
N1	0.8	107.3	98.9	5.6	5.8	-	5.5	72.8	5.8	1.24E^{-7}
N1	0.8	107.3	99.3	5.4	5.5	-	5.3	70.4	5.5	1.24E^{-7}
N2	0.78	99.9	93.4	5.7	6.0	-	5.8	74.4	5.4	1.39E^{-7}
N2	0.74	99.7	93.4	5.6	5.8	-	5.6	73.7	5.2	1.32E^{-7}
R1	2.05	14.5	14.7	102.9	60.8	46.2	55.3	21.9	10.1	3.32E^{-7}
R1	2.07	14.0	14.0	103.0	62.2	38.7	55.6	19.1	9.7	3.35E^{-7}
R2	1.77	-	11.8	54.7	102.8	35.4	49.9	17.9	8.9	2.87E^{-7}
R2	1.71	12.1	9.2	53.0	103.0	38.5	48.5	16.2	8.7	2.77E^{-7}
F1	0.04	3.3	3.3	1.2	1.6	-	-	94.9	1.1	7.0E^{-9}

Note: The borehole interference testing was performed after the Development Room was excavated and well before excavation of the pilot started.

Table G.2 Steady-state pressure heads at packed-off locations during pilot excavation (after Lang et al., 1987b)

Stage (m)	Heads (m)								
	N1	N2	R1	R2	S1	S2	F1	F2	OC1
-4.0	107.1	110.6	109.1	107.1	109.1	106.0	-	-	111.1
-2.8	107.6	110.6	109.6	107.6	109.6	106.6	-	-	111.1
-1.25	107.6	110.6	109.6	107.6	109.6	106.6	-	-	111.1
before blast	107.6	110.4	109.6	107.5	109.6	106.6	106.0	107.1	111.1
bh #5	103.2	105.8	98.9	97.7	91.3	88.7	35.7	38.7	108.1
bh #19	102.8	105.5	98.9	97.4	91.3	88.2	35.7	38.2	107.6
all bh	102.8	105.4	99.4	98.2	71.4	69.3	29.6	31.6	108.1
after blast	104.0	106.7	107.1	105.0	109.1	101.5	-	-	109.6
1.75	103.7	106.6	106.6	105.0	102.0	102.0	-	-	110.1
4.3	103.0	106.0	107.1	105.5	-	103.0	-	-	110.6
7.25	103.5	106.0	107.6	106.0	-	103.5	-	-	110.1
9.9	104.0	107.1	107.1	106.0	-	103.5	-	-	110.1
13.1	104.5	107.6	107.1	106.0	-	103.0	-	-	110.1
15.75	105.0	107.6	107.1	106.0	-	104.5	-	-	110.1
18.45	105.0	107.6	107.1	106.0	-	104.0	-	-	109.6
21.15	103.0	106.6	105.0	104.0	-	102.0	-	-	108.1

Table G.3 Steady-state pressure heads at packed-off locations during slash excavation (after Lang et al., 1987b)

Stage (m)	Head (m)					
	N1	N2	R1	R2	S2	OC1
-4.0	102.0	105.5	105.0	103.5	102.0	108.1
-2.4	102.0	105.2	105.0	103.5	101.5	108.1
before blast	102.0	105.2	105.0	103.5	102.0	107.8
after drilling	97.3	100.2	24.0	30.6	41.8	104.0
after blast	98.9	100.5	92.8	94.3	86.7	106.3
0.35	98.9	102.0	94.3	94.8	86.7	106.6
3.3	99.4	102.5	95.8	95.8	-	106.6
6.05	98.9	102.0	94.8	94.3	-	106.6
8.8	98.9	101.5	96.4	95.3	-	106.6
11.65	99.4	102.0	96.9	95.8	-	107.1
14.45	99.4	102.0	96.4	95.3	-	107.6
17.3	99.9	102.5	96.4	95.3	-	107.6
20.0	99.9	102.5	96.4	94.8	-	108.1
23.55	99.9	103.0	95.3	94.3	-	108.6
26.1	99.9	103.0	94.3	93.3	-	109.1
28.25	99.9	103.0	92.8	91.8	-	109.6

Table G.4 Fluid withdrawal test data during pilot excavation (after Lang et al., 1987b)

Date	Stage (m)	Q/ΔH (m^2/s)								
		N1	N2	R1	R2	S1	S2	F1	F2	OC1
09/16	-4.0	$1.71E^{-7}$	$1.71E^{-7}$	$5.93E^{-7}$	$4.74E^{-7}$	$1.61E^{-9}$	$1.11E^{-8}$	$7.58E^{-9}$	$1.04E^{-9}$	$2.19E^{-6}$
10/16	-4.0	$1.68E^{-7}$	$1.68E^{-7}$	$7.6E^{-7}$	$6.75E^{-7}$	$5.1E^{-9}$	$1.3E^{-8}$	$8.7E^{-9}$	$2.2E^{-9}$	$2.4E^{-6}$
10/17	-4.0	$2.04E^{-7}$	$2.04E^{-7}$	$7.58E^{-7}$	$6.87E^{-7}$	$4.97E^{-9}$	$1.18E^{-8}$	$9.1E^{-9}$	$2.4E^{-9}$	$2.4E^{-6}$
10/21	-2.8	$2.37E^{-7}$	$1.99E^{-7}$	$6.83E^{-7}$	$6.83E^{-7}$	$4.85E^{-9}$	$1.23E^{-8}$	$9.87E^{-9}$	$2.53E^{-9}$	$2.35E^{-6}$
10/22	-2.8	$2.37E^{-7}$	$2.21E^{-7}$	$6.94E^{-7}$	$7.18E^{-7}$	$4.19E^{-9}$	$1.26E^{-8}$	-	$1.59E^{-9}$	$2.45E^{-6}$
10/23	-2.8	$2.37E^{-7}$	$2.37E^{-7}$	$5.59E^{-7}$	$6.9E^{-7}$	$5.07E^{-9}$	$1.31E^{-8}$	$8.7E^{-9}$	$2.17E^{-9}$	$2.36E^{-6}$
10/24	-1.25	$2.7E^{-7}$	$2.42E^{-7}$	$7.35E^{-7}$	$6.94E^{-7}$	$3.79E^{-9}$	$1.42E^{-8}$	$6.64E^{-9}$	$1.35E^{-9}$	$2.28E^{-6}$
10/26	-1.25	$2.51E^{-7}$	$2.25E^{-7}$	$7.23E^{-7}$	$6.99E^{-7}$	$3.79E^{-9}$	$1.28E^{-8}$	$6.4E^{-9}$	$1.52E^{-9}$	$2.46E^{-6}$
10/27	1.75	$1.84E^{-7}$	$1.69E^{-7}$	$4.74E^{-7}$	$5.02E^{-7}$	-	-	-	-	$2.51E^{-6}$
10/28	1.75	$1.34E^{-7}$	$1.5E^{-7}$	$3.84E^{-7}$	$4.24E^{-7}$	-	$4.8E^{-9}$	-	-	$2.44E^{-6}$
10/30	4.3	$1.2E^{-7}$	$8.2E^{-8}$	$5.29E^{-7}$	$5.69E^{-7}$	-	-	-	-	$2.6E^{-6}$
11/3	9.9	$1.42E^{-7}$	$1.33E^{-7}$	$6.06E^{-7}$	$6.42E^{-7}$	-	$6.4E^{-9}$	-	-	$2.29E^{-6}$
11/7	21.15	$2.14E^{-7}$	$2.14E^{-7}$	$6.26E^{-7}$	$6.26E^{-7}$	-	$9.2E^{-9}$	-	-	$2.25E^{-6}$
11/10	21.15	$1.89E^{-7}$	$1.89E^{-7}$	$5.85E^{-7}$	$6.3E^{-7}$	-	$9.4E^{-9}$	-	-	$2.28E^{-6}$

Table G.5 Fluid withdrawal test data during slash excavation (after Lang et al., 1987b)

Date	Stage (m)	Q/ΔH (m^2/s)					
		N1	N2	R1	R2	S2	OC1
11/11	-4.0	$1.87E^{-7}$	$1.82E^{-7}$	$7.11E^{-7}$	$6.56E^{-7}$	$9.2E^{-9}$	$2.24E^{-6}$
11/ 12	-2.4	$2.02E^{-7}$	$1.8E^{-7}$	$6.8E^{-7}$	$6.04E^{-7}$	$4.5E^{-9}$	2.26E-6
11/ 13	-2.4	$1.87E^{-7}$	$1.8E^{-7}$	$5.17E^{-7}$	$5.97E^{-7}$	$4.6E^{-9}$	$2.22E^{-6}$
11/ 14	0.35	$1.19E^{-7}$	$6E^{-8}$	$1.51E^{-7}$	$1.8E^{-7}$	$1.5E^{-9}$	$2.18E^{-6}$
11/ 17	0.35	$1.11E^{-7}$	$1.07E^{-7}$	$1.39E^{-7}$	$1.67E^{-7}$	$5.2E^{-9}$	$2.16E^{-6}$
11/ 19	6.05	$1.28E^{-7}$	$1.28E^{-7}$	$1.42E^{-7}$	$1.42E^{-7}$	$1.19E^{-8}$	$2.24E^{-6}$
11/ 21	11.65	$1.29E^{-7}$	$1.29E^{-7}$	$1.92E^{-7}$	$2.14E^{-7}$	-	-
11/ 25	17.3	$1.3E^{-7}$	$1.3E^{-7}$	$1.89E^{-7}$	$2.16E^{-7}$	$9.2E^{-9}$	$2.28E^{-6}$
11/ 27	23.55	$1.38E^{-7}$	$1.38E^{-7}$	$1.78E^{-7}$	$1.78E^{-7}$	$1.02E^{-8}$	$2.32E^{-6}$

Table G.6 Estimated flow rates (after Lang et al., 1987b)

Stage (m)	**Flow** (ml/min)
Blast holes	~990
Pilot	~300
Slash	~450